Sustainable hydrogen and value-added chemical production:

Pyrolysis oil enhancement methods and electrolysis of the by-products

by

©Tobias Michael Brueckner

A thesis submitted to the School of Graduate Studies
in partial fulfillment of the requirements for the degree of

Doctor of Philosophy

Process Engineering
Faculty of Engineering and Applied Science
Memorial University of Newfoundland

April 26, 2019

St. John's, Newfoundland and Labrador,
Canada

Supervisory Committee:
Prof. Dr. Peter Pickup
Prof. Dr. Kelly Hawboldt
Prof. Dr. Salim Ahmed

Abstract

Pyrolysis oils of forest residues can be used as renewable fuels for burner applications. However, some produced oils do not meet the ASTM standard for pyrolysis oil in boiler applications and must be upgraded. The scope of this work was to enhance pyrolysis oils via distillation and pervaporation to improve its properties as a fuel and produce value-added by-products. The main value still remains in the burner fuel, however the separated by-product can be used for a sustainable hydrogen production via electrolysis or the value-added chemicals can be used for other applications [1]. Distillation and pervaporation have been studied. Distillation was used as a reference case to compare with the pervaporation results. To find the optimal pervaporation process conditions to separate water from the aqueous phase of bark pyrolysis oil a 2^3 factorial design experiment study with commercial polyacrylonitrile-supported polyvinyl alcohol membranes was carried out. The conditions of 80 °C and a feed flow rate of 0.1 mL min^{-1} resulted in an enhancement of the pyrolysis bark oil aqueous phase from an incomplete combustion to a heating value of 16.07 MJ kg^{-1} and lowered the water content from 70.2 to 21.4 mass% to meet the ASTM D7544-12 standard in the investigated lab-scale pervaporation unit. Simultaneously low molecular weight components were isolated in the permeate. Electrolysis of these low molecular weight organics, such as methanol, ethanol, ethylene glycol, and glycerol can produce hydrogen at much lower potentials than water electrolysis, and yields useful oxidation products such as acetic acid and glyceric acid [2]. Efficient use of biofuels in electrolysis and fuel cells requires anode catalysts with both high activities and high

selectivity for the preferred product. A catalyst screening was carried out to identify a highly selective catalyst for the complete oxidation of the fuel to carbon dioxide. A novel experimental method for determining catalyst activities based on transferred electrons was developed.

Keywords: PEM fuel cell; electrolysis cell; fast pyrolysis; pervaporation; renewable energy; bark-pyrolysis oil; pyrolysis oil enhancement; dehydration; design of experiments

---

[1] Ong BC, Kamarudin SK, Basri S. Direct liquid fuel cells: A review. Int J Hydrogen Energy 2017;42:10142–57. doi:10.1016/j.ijhydene.2017.01.117.

[2] Baranton SC, Christophe Baranton S. Electrochemical conversion of alcohols for hydrogen production: a short overview. Wiley Interdiscip Rev Energy Environ 2016;5(4):388–400.

Acknowledgements

This research would not have been possible without the financial support of the National Science and Engineering Research Council of Canada (NSERC), the Centre for Forest Science and Innovation (CFSI, NL Provincial Government), and the Memorial University of Newfoundland's (MUN) School of Graduate Studies and Faculty of Engineering and Applied Science in St. John's Canada.

At this point, I would like to express my sincere gratitude towards my supervisors Prof. Dr. Peter Pickup and Prof. Dr. Kelly Hawboldt for their suggestions and their valuable advice and guidance during my PhD.

Moreover, I would like to express appreciation towards MUN technical service for their technical support, CREAIT staff member Dr. Celine Schneider for her help identifying the components in the pyrolysis oil samples by NMR, and Prof. Dr. Robert Helleur for his help and guidance with his pyrolysis knowledge. Thank you to my supervisory committee member Prof. Dr. Salim Ahmed for his guidance. I would also like to thank Craig Martin, Jon Howell, Jenny Kim, and all my friends in Newfoundland who have created this fantastic work-life balance with all the great adventures we have had together. Most importantly, I extend my deepest appreciation to my partner Anke Krutof and my family who encouraged me during my PhD.

Last but not least, I would like to thank the work term students that have contributed to this research project: Sam Byrne, Mareike Serra, and Brittany Traverse.

Table of contents

List of figures

List of tables

List of abbreviations

AEM	Anion exchange membrane
ANOVA	Analysis of variance
ASTM	American Society for Testing and Materials
C	Carbon
CEM	Cation exchange membrane
CFSI	Centre for Forest Science and Innovation
CO	Carbon monoxide
CO_2	Carbon dioxide
DEFC	Direct ethanol fuel cell
DEMS	Differential electrochemical mass spectroscopy
DHE	Dynamic hydrogen electrode
DMC	Dimethyl carbonate
DMFC	Direct methanol fuel cell
DoE	Design of experiment
F	Fraction
FCEV	Fuel cell electric vehicles
GC	Gas chromatography
GHG	Greenhouse gas
GHS	Globally harmonized system
H_2	Hydrogen
HHV	Higher heating value
MEA	Membrane electrode assembly
MeOH	Methanol
MTBE	Methyl tert-butyl ether
$NaHSO_3$	Sodium bisulfite
NaOH	Sodium hydroxide
NMR	Nuclear magnetic resonance
NSERC	Natural Sciences and Engineering Research Council of Canada
PAA	Polyacrylic acid
PAN	Polyacrylonitrile
Pb	Lead
PEM	Proton exchange membrane
PEMFC	Proton exchange membrane fuel cell
Pt	Platinum
PTFE	Polytetrafluoroethylene
PVA	Polyvinyl alcohol
Rh	Rhodium
RT	Room temperature
Ru	Ruthenium
SEM	Scanning electron microscopy
Sn	Tin
TAN	Total acid number

List of symbols

A	Ampere
A	Area
A	Membrane type
α	Electron transfer coefficient
C	Coulomb
C	Concentration
ca.	Approximately
E	Potential
e^-	Electron
E^0	Standard potential
F	Faraday constant
h	Hour
i	Current
i_k	Kinetic current
j	Current density
J	Flux
J_A	Flux of membrane selective component out of the bulk
J_B	Flux out through the boundary layer
j_{lim}	Limiting current density
j_{max}	Maximal current
k^0	Standard rate constant
m	Mass transport coefficient
min	Minute
n	Electrons transferred in the reaction
n_{av}	Average number of electrons transferred
ppm	Parts per million
Q	Permeate
R	Gas constant
s	Second
T	Temperature
U	Feed flow rate
u	Flow rate
V	Voltage
X_f	Molar fraction of the targe component in the feed
X_s	Molar fraction of the target component on the separation layer
Y	Yield

Chapter 1

Introduction

1 Introduction

The term climate change describes amongst others the issue of increasing atmosphere and oceans temperatures of the Earth [1]. To mitigate the overall temperature increase, the UN climate conference in Morocco in November 2016 agreed not to exceed a maximum of 2 °C temperature increase in order to contain man-made climate change [2]. To reach this goal, the release of greenhouse gases must be reduced significantly. This could be possible with the use of renewable fuels for energy production. In addition to a reduction in greenhouse gas emissions, renewable fuels for energy production are increasingly important with regard to other environmental concerns and pollution caused by fossil fuels. Most biofuels currently produced are made from sugar, starch and oil-rich crops such as soybeans, corn, canola, and wheat. However, use of these food crops competes with their use as food sources for humans and animals. This issue is addressed with second-generation biofuels. These biofuels are produced from non-food materials such as energy crops on marginal land, municipal solid waste, and forest and agriculture residues. These biomass resources provide liquid, gaseous, and solid fuels via thermal, chemical, biological and physical conversion processes [3–5]. One useful process is fast pyrolysis of biomass, which produces an energy-rich liquid that can be easily transported from remote locations. Therefore, the focus for this study was to enhance the fuel quality of pyrolysis oil through removal of the water and light ends and investigating the potential of light ends in the electrochemical production of hydrogen in electrolysis cells.

Fast pyrolysis is the rapid heating of biomass to 450 to 550 °C in the absence of oxygen, producing organic vapours (condensable and non-condensable gases) and char. The condensed phase produces a liquid pyrolysis oil consisting of 1000 plus different organic compounds [6]. Different process conditions favour different product yields and composition. Typically 50-70 mass% of the dry biomass feedstock is converted into oil under fast pyrolysis conditions (450-550 °C and seconds residence time) [7,8]. In addition to a fuel source as a whole oil, components of the oil can be a source of renewable chemicals and liquid fuels [7–9]. Some of these fuels can be used in fuel cells for transportation or energy production applications [10]. In addition, a catalyst screening for electrochemical oxidation of bio-fuels (from pyrolysis oil) was carried out.

This chapter is split into three parts, background and production of pyrolysis oil, purification and water separation from the pyrolysis oil by pervaporation and distillation, and use of separated fractions and components as fuels in electrolysis/fuel cell applications.

1.1 Pyrolysis

As indicated above, in general pyrolysis is a thermochemical conversion of biomass at 300–900 °C in the absence of air into pyrolysis oil, char, and syngas. The technique was historically used in ancient China to prepare charcoal and by indigenous Amazonians to generate biochar three to five thousand years ago [11]. The technology is well established in the conversion of biomass with plants operating at up to 200 kg h^{-1} feedstock, using wood biomass into pyrolysis oil. These plants use different reactor

systems from fluidized bed reactors (DynaMotive, UK and Canada; ENEL, Italy; Ensyn, USA; Bioware Technologia, Brazil), rotating cone reactors (BTG, The Netherlands), vacuum reactors (PyroVac Inc., Canada; Ecosun, The Netherlands), ablative reactors (PYTEC, Germany), auger reactors (AbriTech, Canada; Renewable Oil International, USA, KIT/Lurgi, Germany) , among other reactors (Compact Power, UK; PKA, Germany; Chemviron Carbon, Germany; Lambiotte, Belgium; Novasen, Senegal; BEST Energies, Australia) [9,12].

1.1.1 Pyrolysis oil

During pyrolysis, the vapours are condensed to generate pyrolysis oil and non-condensable gases that can be combusted to produce heat for the pyrolysis process [13]. Liquid pyrolysis oil is of particular interest for this work as it is potentially a source of a renewable fuel for fuel cell applications [8]. The product distribution depends on several factors. Pyrolysis is grouped into slow, moderate, and fast pyrolysis processes and gasification. Char is the main product if the heating rate and process temperatures are low (below 500 °C) and the vapour residence time is long (10 to 60 min) [8,14]. This process is called slow pyrolysis, carbonization, or torrefaction. High temperatures (750 to 900 °C) and longer residence times favour the conversion to gas via gasification [8]. To produce high yields of pyrolysis oil the temperature must be moderate (around 500 °C) and the vapour residence time short (seconds to minutes) to prevent cracking reactions. This process is referred to as moderate to fast pyrolysis. Intermediate and fast pyrolysis have fast heating rates, short vapour residence times of 10s of seconds, and a temperature of 450–550 °C [8,15,16].

Fast pyrolysis is the most favourable pyrolysis technology for this work because of its high liquid yield of up to 75 mass% of the dry biomass [8,16]. The oil mostly contains carbon, hydrogen, and oxygen [17], despite being called an "oil" it contains little to no hydrocarbons. The high yield is due to the high heating rate and short vapour residence time limiting secondary reactions such as cracking in the gas phase [8]. The oil produced is a complex mixture of acids, alcohols, aldehydes, esters, ketones, sugars, phenols, guaiacols, syringols, furans, and lignin-derived phenols [16]. It has a high water content of 15-30 mass% and a high oxygen content of 35-40 mass% [16]. The oxygen is distributed in more than 300 components in the pyrolysis oil. The oil contains large amount of organic acids, such as acetic and formic acids, resulting in low pH values of 2 to 3. Pyrolysis oil from softwood tends to be slightly more acidic than oil from hardwood [16].

One of the challenges for pyrolysis oil is the high water content, as it reduces the heating value and can act as a catalyst poison in subsequent refining [16]. The high water content in the pyrolysis oil reduces viscosity increasing feasibility for fuel applications [18]. Pyrolysis oil has low sulphur, nitrogen, and ash content compared to heavy fuel oil and other bio-fuels, and therefore, combustion results in lower emissions of SO_2, NO_x, and particulates [13,16,17]. Additionally, living plants recycle the CO_2 emissions of the biomass combustion, and thereby, the process potentially has a zero net CO_2 emission profile [16]. The energy demand of fast pyrolysis is low compared to gasification and biochemical processes to produce ethanol [19]. Huber and Corma have

introduced the bio-refinery concept, replacing crude petroleum with biomass/pyrolysis oil as a feedstock for transportation fuels and chemicals [20,21].

1.1.2 Purification methods for pyrolysis oil

Crude pyrolysis oil can be used in industrial scale combustion systems [12,22]. However, upgrading is necessary for use as a petrol fuel replacement. The high moisture and acid content of pyrolysis oil needs to be reduced to improve heating value, handling, and storage stability [11]. Over the past decades, various pyrolysis oil upgrading techniques such as hydrodeoxygenation, esterification, catalytic cracking, distillation, supercritical fluidization, steam reforming, emulsification, and blending have been investigated [11,23–26]. The focus of this work is to enhance the oil quality for higher quality fuel in heating and power applications, but not to meet transport fuel quality. As such, we are exploring non-catalytic distillation methods as a reference process to membrane separation methods.

1.1.2.1 Distillation

Distillation techniques such as atmospheric, vacuum, fractional, and molecular distillation technologies have been investigated to upgrade pyrolysis oil [27–31]. Results of the fractionating distillation process (at temperatures ≤100 °C, 100-180 °C, and 180-250 °C) showed significant reduction of the water content in the remaining pyrolysis oil fraction and consequently higher heating value of the remaining oil [28]. This method allowed separation of the pyrolysis oil into a light and middle distillate fraction (15-20 mass%) and a phenolic-rich heavy distillate fraction (53 mass%) [28]. The fractions can be used for further upgrading or for blending with other fuels.

However, a major drawback of distillation upgrading techniques is that at temperatures >100 °C the oil "ages" (thermal degradation and polymerization) [32]. The temperature can be lowered by vacuum distillation [31]. Distillates produced from pyrolysis oil by short-path vacuum distillation (previous work) and atmospheric fractional distillation were used as reference cases to the permeates produced via pervaporation.

1.1.2.2 Membrane separation

A small number of membrane separation studies have been performed to separate components from pyrolysis oil [19,33,34]. Nanofiltration and reverse osmosis membranes were tested to separate acetic acid from an artificial pyrolysis oil aqueous phase mixture [19]. To economically operate the pervaporation process with these nanofiltration and reverse osmosis membranes, high trans-membrane pressures and phenol resistant membrane materials were necessary to archive sufficient fluxes [19]. Other research showed a successful increase of sugars in the aqueous fraction of pyrolysis oil from green pinewood with reverse osmosis membranes [33]. The oil was pretreated with n-butane to remove phenolic components [33]. Membrane separation processes are promising for the removal of water and other components from the pyrolysis oil aqueous phase [34]. Based on this promising but limited number of studies, the pervaporation process was investigated in this work for upgrading pyrolysis oil at moderate temperatures (≤ 80 °C).

1.2 Pervaporation

Pervaporation (Figure 1.1) is a process to separate liquid/liquid mixtures through membranes by a difference in vapour pressure and concentration. It is a method that can

effectively remove water and other low molecular weight components from pyrolysis oil.

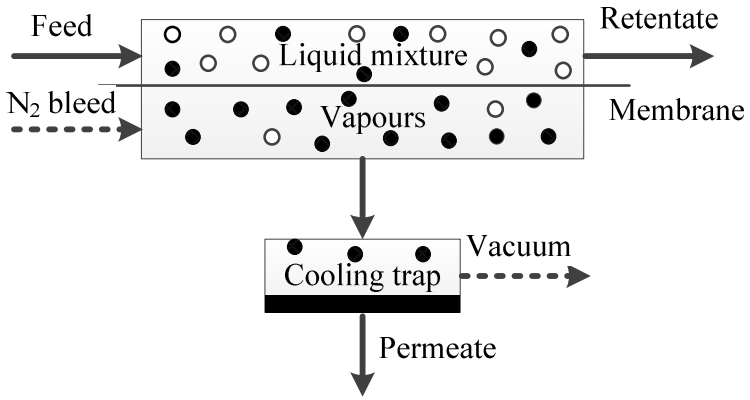

Figure 1.1: Schematic drawing of the pervaporation principle.

The target component diffuses into the membrane and evaporates on the permeate side where it is then condensed in a cold trap. In the following section, membrane types and materials, characterization of membrane parameters and effects on performance, pervaporation applications, and advantages are described.

1.2.1 Membrane types

Membranes can be macro-porous, micro-porous, or non-porous. Most commonly, non-porous membranes are used for pervaporation applications. Membranes can be separated into three main categories (organic membranes, inorganic membranes, and composite membranes) [35]. The organic membranes are polymeric membranes. Ceramic membranes are categorized as inorganic membranes. Composite membranes are also referred to as hybrid membranes and are a composite of organic and inorganic

materials [35]. The composite membranes used in this work are described in more detail in *Chapter 2*.

1.2.2 Membrane materials

The type of pervaporation membrane used is a function of the separation application. The most common materials for hydrophilic and organophilic membrane separation processes are shown in Figure 1.2. Synthetic polymers, e.g. polyacrylic acid (PAA) [36,37], polyvinyl alcohol (PVA) [37–39], and polyacrylonitrile (PAN) [40], are used in most commercial applications.

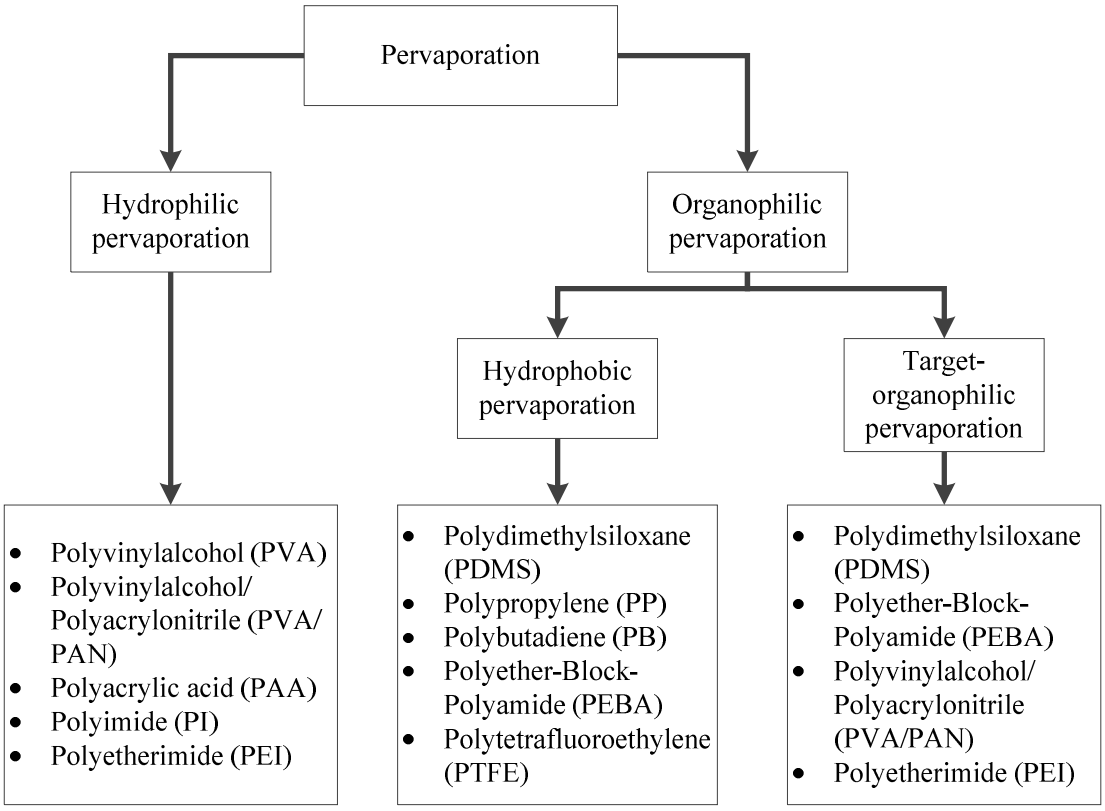

Figure 1.2: Commonly used pervaporation membrane materials [41].

1.2.3 Pervaporation mass transport models

The overall membrane flux in a pervaporation process is described with mass transport models, such as the pore-flow model for porous membranes and the solution-diffusion model for non-porous membranes [41–43].

1.2.3.1 Mass transport through the membrane

The pore-flow model describes the separation process with a pressure-driven convection flow through a porous membrane. The model considers three steps: liquid transport from the pore inlet to the liquid-vapour phase boundary; evaporation at the phase boundary; and vapour transport from the boundary to the pore outlet (Figure 1.3) [42]. Separation is achieved by different diffusion rates of the components through the membrane pores.

In the solution-diffusion model approach, the components in the feed dissolve into the membrane material and then diffuse through the membrane. This process follows a concentration gradient (Figure 1.3). The model considers three steps: sorption of the permeate from the feed to the membrane; diffusion of the permeate in the membrane; desorption of the permeate to the vapour phase on the downstream side of the membrane [42]. Separation is driven by the difference in partitioning behaviour of each component into the membrane material and the difference in diffusion rate within the membrane.

The membranes used for this research had a non-porous polyvinyl alcohol separation layer. Therefore, the solution-diffusion model was used to analyze permeate flux.

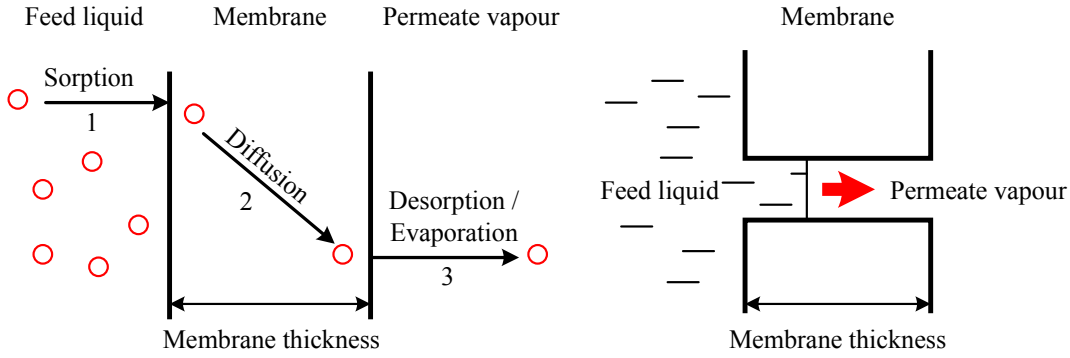

Figure 1.3: Schematic drawing of the solution-diffusion model (left) and the pore-flow model (right) [42].

1.2.3.2 Membrane flux

The permeate flux through the membrane involves the diffusion of a component from the liquid feed into and across the membrane. This process involves a phase change from the liquid state to the vapour state due to a driving force. In this case, the driving forces were partial pressure difference and concentration difference between the feed and the permeate. The overall membrane flux can be described by Eq. (1.1). The flux J is the flow rate of permeate Q which is passing through the membrane, per membrane area A.

$$J = \frac{Q}{A} \qquad \text{Eq. (1.1)}$$

1.2.4 Factors that influence pervaporation performance

Performance is driven by operating parameters such as feed temperature, permeate pressure, and feed composition as indicated above. Membrane swelling, concentration polarization, coupling effects of components, and membrane fouling also impact

performance, and an understanding of the influence of these effects on the membrane performance is critical.

1.2.4.1 Swelling of the membrane

Polymeric membranes generally swell when they are exposed to liquids. In pervaporation, the components of the feed solution partitioning into the membrane to cause the swelling. This phenomenon can change the permeability and selectivity of the membrane. A swollen membrane tends to have higher permeability and a lower selectivity [44]. The swelling effect on the membrane used in this work was tested and described in *Chapter 2*.

1.2.4.2 Concentration polarization

The term concentration polarization describes the composition difference between the membrane boundary layer and the bulk feed. The separation process leads to an accumulation of the retained species and a depletion of the permeable species in the membrane boundary layer [45]. This effect will result in an overall decrease in separation efficiency by decreasing the driving force of the permeable species across the membrane and increasing the driving force of the less permeable species [45]. Figure 1.4 shows the effect of concentration polarization in the boundary layer.

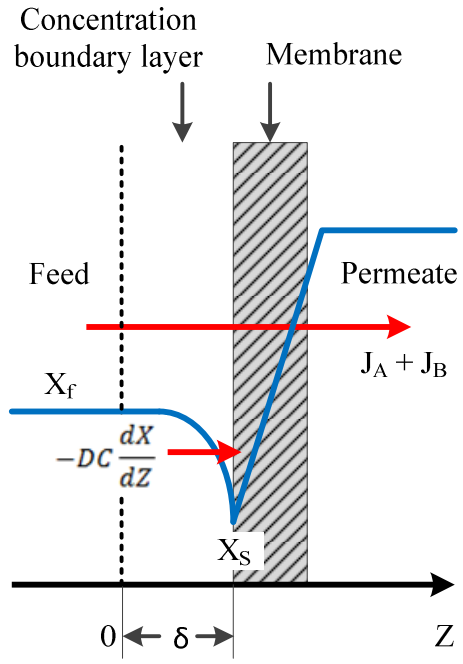

Figure 1.4: Schematic drawing of the boundary layer effect: concentration polarization [42].

The concentration of the target components across the membrane increased as the amount of the target components in the mixture increases relative to the decreasing amount of other components for which the membrane is less selective. Where X_f is the molar fraction of the target component in the feed, X_s is the molar fraction of the target component on the separation layer, J_A is the flux of membrane selective component out of the bulk and J_B the flux out through the boundary layer. Concentration polarization is more common in liquid feed separations because of the slower molecule transport in liquids compared to gases. The effect can be minimized by maximizing the temperature and mixing on the membrane surface [46]. The concentration polarization effect is negligible with small membrane fluxes and fast feed flow rates [42].

1.2.4.3 Coupling effect

The coupling effect describes the change of a component's partial flux in a binary system due to the coupling of fluxes from the other component. The flux for one component through the membrane is not independent and can change due to the diffusion of other components through the membrane [47]. This effect is difficult to measure, especially with pyrolysis oil as a feed solution due to its chemical complexity (approximately 300 main components). Indirect data was obtained by flux composition analysis by nuclear magnetic resonance (NMR) (*Chapter 2*).

1.2.4.4 Fouling

Membrane fouling is the major challenge for pervaporation processes [48–50]. It is caused by unintentional interactions between membrane material and components in the feed solution. As a result, the membrane surface is coated or blocked by adsorbed materials. Consequently, fouling results in a flux reduction and change in selectivity due to an additional barrier layer on the membrane. Foulants are classified into four different categories: particulates, organic, inorganic, and microbiological organisms [49]. In the case of pyrolysis oil, it contains char particles and polymeric components. The effect of fouling with pyrolysis oil on the membrane was investigated in a long-term study experiment described in *Chapter 2*.

1.2.5 Applications for pervaporation

Pervaporation has a variety of large-scale industrial applications [51]. The commercial applications can be divided into three major areas: dehydration of organic solvents (e.g. alcohols, ethers, esters, acids); removal of diluted organic compounds from water (e.g.

removal of volatile organic compounds, recovery of aroma, and biofuels from fermentation broth); separation of organic–organic mixtures (e.g. methyl tert-butyl ether (MTBE)/methanol, dimethyl carbonate (DMC)/methanol) [44,52–54].

1.2.6 Advantages of membrane technology and pervaporation

The main advantage of pervaporation compared to distillation is the cost savings [55]. In general, the membrane separation process requires less space compared to distillation. Pervaporation is a simple process and needs less maintenance compared to distillation columns. It is a practical and economic separation method, especially for smaller plants [55,56]. The overall economical balance benefits from the energy efficient and more environmentally friendly operating process conditions. Pervaporation can separate azeotropes and other difficult-to-separate mixtures [38,51,54,56].

1.3 Fuel cells

1.3.1 Proton exchange membrane fuel cell

A fuel cell is a device in which the chemical energy of a fuel is directly converted into electricity [57]. They are classified into low and high-temperature fuel cells; in this work, we focus on low-temperature cells.

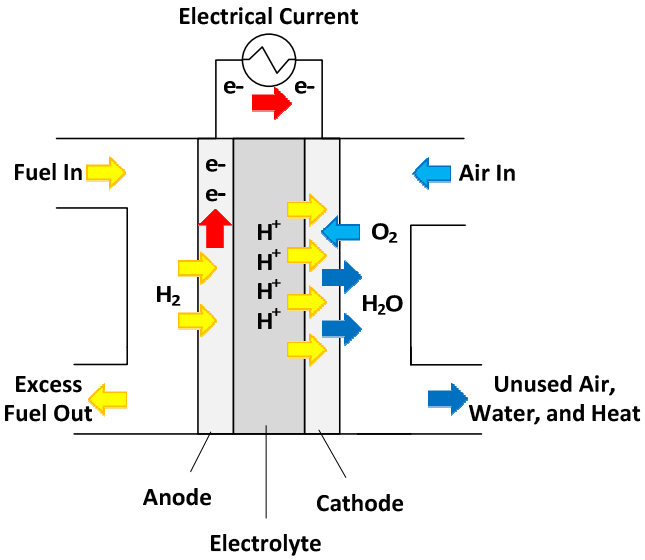

Figure 1.5: Schematic drawing of a PEM fuel cell.

There are three types of low-temperature liquid feed fuel cells depending on the type of ion exchange membrane separator: proton exchange (PEM) (Figure 1.5), cation (alkali metal) exchange (CEM), and anion (hydroxyl) exchange (AEM) [10]. The fuel and the oxidant are separated in the fuel cell by a solid polymer electrolyte consisting of a proton conductive Nafion™ membrane. A Pt-based catalyst on the anode causes the fuel to split into carbon dioxide, hydrogen ions (protons), and electrons. The protons cross through the Nafion membrane to the cathode and the electrons reach the cathode through an external circuit and thereby create an electrical current. On the cathode catalyst, the protons react with the provided oxygen (from air) into water. PEM fuel cells are low-temperature cells which normally operate best between 60 and 100 °C; the upper-temperature limit is governed by the stability of the Nafion membrane, which must remain hydrated with water. The low operating temperature and the fact that there is no liquid electrolyte, which could leak, makes this type of fuel cell suitable for

portable power application such as transportation, portable mobile devices such as laptops, as well as stationary applications for domestic power and heating applications [10,58–60].

Fuel cells have been identified as one of the most promising and efficient technologies to produce sustainable electrical energy by converting chemicals from renewable resources into electricity through oxidation [57,59,61,62]. Biofuels from renewable sources reduce greenhouse gases, reducing net CO_2 emissions compared to energy produced with fossil fuels [63]. The end products of complete oxidation of the fuel are water and carbon dioxide. If the fuel is from a renewable source, the released carbon dioxide is the same amount as the plant source required to grow, not considering emissions due to the biofuel production etc. [57,62].

Other advantages of PEM fuel cells compared to conventional energy production are the following. Fuel cells have higher theoretical conversion efficiencies than conventional thermo-mechanical systems for power production. Fuel cells convert chemical energy directly into electrical energy while thermal processes require additional steps and therefore energy losses occur. The theoretical electric efficiency for PEM fuel cells powered with ethanol is 97% [59]. Furthermore, PEM fuel cells operate quietly and at temperatures lower than 100 °C [57,59].

Conventional feedstocks for PEM fuel cells are hydrogen, or a water-based solution of methanol [10]. Cells are being developed to operate with ethanol, formic acid, ammonia, and borohydride [10,63–65]. Liquid fuels for PEM fuel cells have

advantages compared to hydrogen which has an extremely low volumetric energy density compared to liquid fuels at atmospheric pressure [10]. Therefore, high-pressure storage tanks are necessary to operate hydrogen fuel cells efficiently. The pressure in storage tanks for mobile applications is typically between 35 and 70 MPa. The energy density of pressurized hydrogen (70 MPa) is only 1300 Wh L^{-1} compared to the much higher energy densities of methanol 5897 Wh L^{-1}, and 6037 Wh L^{-1} for ethanol at atmospheric pressure [10]. Due to high storage hydrogen pressures and high flammability, transportation costs are very high [10]. Other advantages of liquid fuels are the existing infrastructure for transportation applications e.g. fuel for cars, buses, and air transport. Furthermore, liquids are easier to transport in road tankers due to safety restriction that apply to the transportation of flammable gasses; therefore, it is more cost effective to use liquids fuels [59,66]. While fuel cells represent an alternative to traditional fossil power sources the overall environmental sustainability of fuel cells is largely driven by the source of the fuel.

1.3.2 Direct methanol fuel cell (DMFC)

In general, methanol is produced from natural gas and is the most studied liquid fuel for PEM fuel cells [63]. The focus of this research is on methanol because its use in fuel cells is well developed, and analysis has shown that it is a major component of low boiling pyrolysis oil fractions. Pyrolysis oil from softwood contains approximately 2 to 5 mass% methanol [20,67,68]. Due to the high methanol crossover flux through the Nafion membrane, shown in Figure 1.6, the methanol is diluted with water before the

solution is fed to the fuel cell [10]. The water is also required in the reaction on the anode side (Eq. (1.2)).

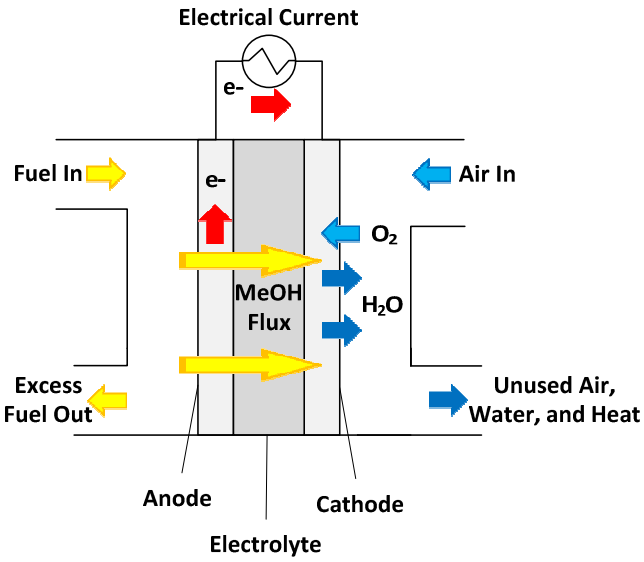

Figure 1.6: Schematic drawing of a DMFC showing methanol fuel crossover through the Nafion membrane.

A proton exchange membrane fuel cell fed directly with methanol is called a direct methanol fuel cell (DMFC). The energy conversion in a DMFC is possible through the methanol oxidation reaction in the presence of water to produce carbon dioxide and protons at the anode.

$$CH_3OH + H_2O \rightleftharpoons CO_2 + 6H^+ + 6e^- \qquad \text{Eq. (1.2)}$$

At the cathode, oxygen (from air) is reduced to water.

$$^3/_2\, O_2 + 6H^+ + 6e^- \rightleftharpoons 3H_2O \qquad \text{Eq. (1.3)}$$

The advantages for methanol as a direct fuel are the high energy density and relatively high energy conversion efficiency in DMFCs. These advantages promote DMFC

technology as a promising alternative power source for mobile applications [69]. Another advantage of DMFCs compared to hydrogen fuel cells is that they do not require a reformer. The liquid methanol feed results in a simpler design and increases the attractiveness of DMFCs for mobile applications. Furthermore, the present petrol station infrastructure can be used for methanol [60]. However, DMFC technology has some disadvantages to overcome such as the toxicity of methanol, low performance, poor durability, and catalyst poisoning by intermediates such as carbon monoxide [10,69,70]. Furthermore, expensive precious metal catalysts increase the cost for DMFCs [10,66].

Several different membrane types have been developed for the DMFCs. Each membrane has some advantages and disadvantages to overcome the thermal stability, durability, methanol crossover, and power density drawbacks of the DMFC technology. The crossover of methanol decreases with the thickness and equivalent weight of the membrane [71]. Currently, hydrocarbon and composite fluorinated membranes show high durability and low methanol crossover at maximal cost efficiency [71].

1.3.3 Other liquid PEM fuel cell fuels

Additionally to methanol, pyrolysis oil from softwood also contains ethanol, ethylene glycol, and formic acid. Ethanol [10,72,73], ethylene glycol [10,63,74], and formic acid [10,75,76] are used in direct liquid-fed fuel cells. Table 1.1 provides an overview of the thermodynamic features, the amount present in pyrolysis oil, and typical catalysts used for these and other fuels discussed in this work. Glycerol is a by-product in the

production of biodiesel and therefore a promising, readily available, low-cost PEM fuel cell fuel [77–79].

In this work, ethanol oxidation at Pt and PtRu catalyst was found to show slower kinetics and stoichiometries compared to methanol oxidation (*Chapter 3*) [80]. Ethylene glycol is a promising fuel due to its 10 theoretically available electrons [63]. Formic acid was not investigated in this particular research. In addition to these fuels found in pyrolysis oil, glycerol was also investigated.

Table 1.1: Thermodynamic features of DLFCs at 25 °C and 1 atm (n: number of electrons involved; E^0: cell voltage [10,63]; E_{sp}: theoretical specific energy [10,63]; η: theoretical energy conversion efficiency [10,63]; Globally Harmonised System (GHS) symbols; mass%: mass% of component in pyrolysis oil [81]; typical catalysts).

Type	Fuel/ oxidant	n	E^0 (V)	E_{sp} (Wh L^{-1})	η (%)	GHS	mass % (oil)	Catalyst
PEM	H_2(70 mPa) /O_2	2	1.23	1300	83.0		-	Pt, PtRu [82]
DMFC	CH_3OH/O_2	6	1.21	5897	96.7		0.4-2.4	Pt, PtRu [83]
DEFC	C_2H_5OH/O_2	12	1.15	6307	97.0		0.6-1.4	Pt, PtRu, PtSn, [59]
DEGFC	$C_2H_6O_2/O_2$	10	1.22	5800	99.0		0.7-2.0	Pt, PtSn [10]
DGFC	$C_3H_8O_3/O_2$	14	1.27	5965	95.1		-	Pt, Au [84]

1.3.4 Hydrogen production by electrolysis of methanol

Pure hydrogen can be produced by electrolysis of a methanol-water solution by applying DC voltage to the electrolysis cell [85–87]. The electrolysis cell set-up is equivalent to a DMFC set-up. The produced hydrogen can be used as a fuel in PEM fuel

cells. This method allows a renewable hydrogen production from the separated light end components of the pyrolysis oil enhancement (distillate/permeate).

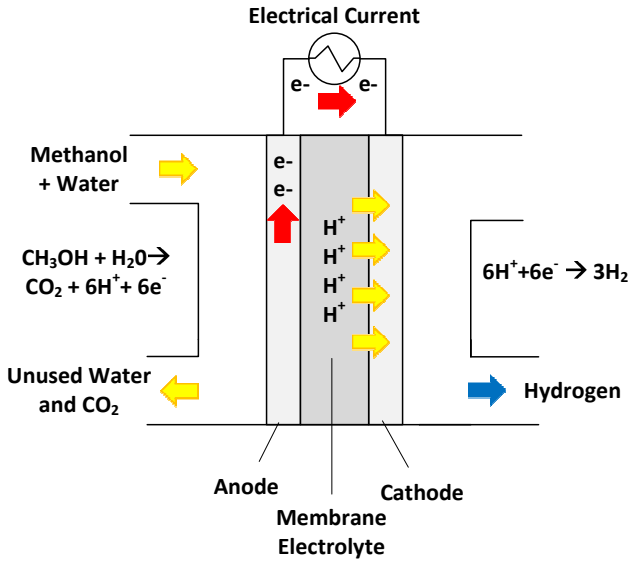

Figure 1.7: Schematic drawing of a methanol-water solution fed electrolysis cell.

Figure 1.7 shows a schematic drawing of a methanol water electrolysis cell set-up. The anode and cathode are separated by a membrane electrolyte, e.g. Nafion™. Typically, platinum-based precious metal catalysts are used for both anodes. With the applied DC power, methanol reacts with water on the anode side to carbon dioxide, protons, and electrons (Eq. (1.4)).

$$CH_3OH + H_2O \rightleftharpoons CO_2 + 6H^+ + 6e^- \qquad \text{Eq. (1.4)}$$

The produced carbon dioxide is exhausted with the unused water and methanol. The protons cross the membrane electrolyte to the cathode side, where they react with hydrogen and the electrons supplied from the anode side (Eq. (1.5)).

$$6H^+ + 6e^- \rightleftharpoons 3H_2 \qquad \text{Eq. (1.5)}$$

The overall aqueous methanol-fueled electrolysis cell reaction is shown in Eq. (1.6).

$$CH_3OH + H_2O \rightleftharpoons CO_2 + 3H_2 \qquad \text{Eq. (1.6)}$$

The main benefit of using an aqueous methanol solution as a feedstock is the low cost of the electrolysis process caused by a reduced electrical energy consumption of 0.03 V compared to 1.23 V of a state-of-the-art hydrogen production by electrolysis of water [85–87]. Alternatively, an aqueous glycerol solution could be oxidized in an electrolysis cell, with a required cell voltage of 0.22 V [88].

1.4 Research Objectives

The overall objective of this work was to enhance the quality of pyrolysis bark oil as a fuel and produce electric power or hydrogen from the produced waste stream in a fuel cell or an electrolysis cell.

The objective for *Chapter 2* was to enhance the heating value of the aqueous phase of bark pyrolysis oil by removing water via pervaporation. Additionally, to water, pyrolysis oil produced from wood biomass contains significant quantities of organic acids and alcohols [89,90]. Low boiling point compounds (e.g. methanol, acetic acid, and formic acid) are separated along with the water and could be used for other applications. A design of experiment study was carried out to determine optimal pervaporation conditions (temperature, feed flow rate, and membrane type) to enhance the heating value of the aqueous phase of the bark pyrolysis oil.

In *Chapter 3*, a novel approach was developed for screening catalysts for the oxidation of biofuels. Results from a multi-anode PEM electrolysis cell were modelled in order to characterize, evaluate, and quantify the performance of the various commercial catalysts. The method compares the kinetic parameters to determine the number of electrons (stoichiometry) that were involved in the oxidation process, providing information on which reactions were occurring on the catalyst surface.

The main objective in *Chapter 4* was to separate methanol and other value-added chemicals from pyrolysis oil by distillation. A short-path and a fractional distillation set-up were investigated. A secondary objective was to verify the possibility

to oxidize the separated components in an electrolysis cell. This value adding method converts the waste stream of the process into a valuable by-product to produce electric power or hydrogen.

The characterization method developed in *Chapter 3* was also used to gain information from catalyst screening (*Chapter 5*) carried out with various fuels in the multi-anode cell. The screening was carried out with methanol, ethanol, ethylene glycol, acetol and glycerol as fuels at a wide range of Pt-based and nano core-shell bi-metal catalysts.

1.5 References

[1] Meinshausen M, Meinshausen N, Hare W, Raper SCB, Frieler K, Knutti R, et al. Greenhouse-gas emission targets for limiting global warming to 2 degrees C. Nature 2009;458:1158–62. doi:10.1038/nature08017.

[2] Canada's Second Biennial Report on Climate Change. Government of Canada; 2016.

[3] European Commission. Communication from the Commission: Energy for the Future: Renewable Sources of Energy–White Paper for a Community Strategy and Action Plan. Brüssel: 1997.

[4] International Energy Agency. World Energy Outlook 2015. Executive Summary. Int Energy Agency Books Online 2015:1–9. doi:10.1787/weo-2005-en.

[5] Bridgwater A V. Renewable fuels and chemicals by thermal processing of biomass. Chem Eng J 2003;91:87–102. doi:10.1016/S1385-8947(02)00142-0.

[6] Branca C, Giudicianni P, Di Blasi C. GC/MS characterization of liquids generated from low-temperature pyrolysis of wood. Ind Eng Chem Res 2003;42:3190–202. doi:10.1021/ie030066d.

[7] Czernik S, Bridgwater A V. Overview of applications of biomass fast pyrolysis oil. Energy and Fuels 2004;18:590–8. doi:10.1021/ef034067u.

[8] Bridgwater A V. Review of fast pyrolysis of biomass and product upgrading. Biomass and Bioenergy 2012;38:68–94. doi:10.1016/j.biombioe.2011.01.048.

[9] Perkins G, Bhaskar T, Konarova M. Process development status of fast pyrolysis technologies for the manufacture of renewable transport fuels from biomass. Renew Sustain Energy Rev 2018;90:292–315. doi:10.1016/j.rser.2018.03.048.

[10] Soloveichik GL. Liquid fuel cells. Beilstein J Nanotechnol 2014;5:1399–418. doi:10.3762/bjnano.5.153.

[11] Guo M, Song W, Buhain J. Bioenergy and biofuels: History, status, and perspective. Renew Sustain Energy Rev 2015;42:712–25. doi:10.1016/j.rser.2014.10.013.

[12] Vamvuka D. Bio-oil, solid and gaseous biofuels from biomass pyrolysis processes-An overview. Int J Energy Res 2011;35:835–62. doi:10.1002/er.1804.

[13] Lehto J, Oasmaa A, Solantausta Y, Kytö M, Chiaramonti D. Fuel oil quality and combustion of fast pyrolysis bio-oils. 2013. doi:http://dx.doi.org/10.1016/j.apenergy.2013.11.040.

[14] Kersten S, Garcia-Perez M. Recent developments in fast pyrolysis of ligno-cellulosic materials. Curr Opin Biotechnol 2013;24:414–20. doi:10.1016/j.copbio.2013.04.003.

[15] Papari S. Pyrolysis: A Theoretical and Experimental Study on the Conversion of Softwood Sawmill residues to Biooil. Ind Eng Chem Res 2014:141229113832000. doi:10.1021/ie5039456.

[16] Zhang Q, Chang J, Wang T, Xu Y. Review of biomass pyrolysis oil properties

and upgrading research. Energy Convers Manag 2007;48:87–92. doi:10.1016/j.enconman.2006.05.010.

[17] Oasmaa A, van de Beld B, Saari P, Elliott DC, Solantausta Y. Norms, Standards, and Legislation for Fast Pyrolysis Bio-oils from Lignocellulosic Biomass. Energy & Fuels 2015;29:2471–84. doi:10.1021/acs.energyfuels.5b00026.

[18] Jacobson K, Maheria KC, Kumar Dalai A. Bio-oil valorization: A review. Renew Sustain Energy Rev 2013;23:91–106. doi:10.1016/j.rser.2013.02.036.

[19] Teella A, Huber GW, Ford DM. Separation of acetic acid from the aqueous fraction of fast pyrolysis bio-oils using nanofiltration and reverse osmosis membranes. J Memb Sci 2011;378:495–502. doi:10.1016/j.memsci.2011.05.036.

[20] Huber GW, Iborra S, Corma A. Synthesis of transportation fuels from biomass: Chemistry, catalysts, and engineering. Chem Rev 2006;106:4044–98. doi:10.1021/cr068360d.

[21] Huber GW, Corma A. Synergies between Bio- and Oil Refineries for the Production of Fuels from Biomass. Angew Chemie Int Ed 2007;46:7184–201. doi:10.1002/anie.200604504.

[22] Lehto J, Oasmaa A, Solantausta Y, Kytö M, Chiaramonti D. Review of fuel oil quality and combustion of fast pyrolysis bio-oils from lignocellulosic biomass. Appl Energy 2014;116:178–90. doi:10.1016/j.apenergy.2013.11.040.

[23] Mortensen PM, Grunwaldt JD, Jensen PA, Knudsen KG, Jensen AD. A review of

catalytic upgrading of bio-oil to engine fuels. Appl Catal A Gen 2011;407:1–19. doi:10.1016/j.apcata.2011.08.046.

[24] Butler E, Devlin G, Meier D, McDonnell K. A review of recent laboratory research and commercial developments in fast pyrolysis and upgrading. Renew Sustain Energy Rev 2011;15:4171–86. doi:10.1016/j.rser.2011.07.035.

[25] Krutof A, Hawboldt KA. Upgrading of biomass sourced pyrolysis oil review: focus on co-pyrolysis and vapour upgrading during pyrolysis. Biomass Convers Biorefinery 2018;8:775–87. doi:10.1007/s13399-018-0326-6.

[26] Gollakota ARK, Reddy M, Subramanyam MD, Kishore N. A review on the upgradation techniques of pyrolysis oil. Renew Sustain Energy Rev 2016;58:1543–68. doi:10.1016/j.rser.2015.12.180.

[27] Boucher E., Chaala, Roy C. Bio-oils obtained by vacuum pyrolysis of softwood bark as a liquid fuel for gas turbines. Biomass Bioenergy 2000;19:337–50. doi:10.1016/S0961-9534(00)00043-X.

[28] Capunitan JA, Capareda SC. Characterization and separation of corn stover bio-oil by fractional distillation. Fuel 2013;112:60–73. doi:10.1016/j.fuel.2013.04.079.

[29] Nam H, Choi J, Capareda SC. Comparative study of vacuum and fractional distillation using pyrolytic microalgae (Nannochloropsis oculata) bio-oil. ALGAL Res 2016;17:87–96. doi:10.1016/j.algal.2016.04.020.

[30] Zhang X, Yang G, Jiang H, Liu W, Ding H. Mass production of chemicals from biomass-derived oil by directly atmospheric distillation coupled with co-pyrolysis. 2013. doi:10.1038/srep01120.

[31] Rahman S, Helleur R, MacQuarrie S, Papari S, Hawboldt K. Upgrading and isolation of low molecular weight compounds from bark and softwood bio-oils through vacuum distillation. Sep Purif Technol 2018;194:123–9. doi:10.1016/j.seppur.2017.11.033.

[32] Alsbou E, Helleur B. Accelerated aging of bio-oil from fast pyrolysis of hardwood. Energy and Fuels 2014;28:3224–35. doi:10.1021/ef500399n.

[33] Barbary E, Abou-yousef H, Steele P. Increasing the efficiency of fast pyrolysis process through sugar yield maximization and separation from aqueous fraction bio-oil. Fuel Process Technol 2013;110:65–72. doi:10.1016/j.fuproc.2012.11.003.

[34] Kaombe DD, Hägg MB. Forward osmosis for the dewatering of pyrolysis oil aqueous phase. Sep Purif Technol 2014;138:92–7. doi:10.1016/j.seppur.2014.10.002.

[35] Wee S, Tye C, Bhatia S. Membrane separation process — Pervaporation through zeolite membrane. Sep Purif Technol 2008;63:500–16. doi:10.1016/j.seppur.2008.07.010.

[36] Wang L, Li J, Lin Y, Chen C. Separation of dimethyl carbonate/methanol

mixtures by pervaporation with poly (acrylic acid)/poly (vinyl alcohol) blend membranes. J Memb Sci 2007;305:238–46. doi:10.1016/j.memsci.2007.08.008.

[37] Amnuaypanich S, Naowanon T, Wongthep W, Phinyocheep P. Highly Water-Selective Mixed Matrix Membranes from Natural Rubber- blend -poly (acrylic acid) (NR- blend -PAA) Incorporated with Zeolite 4A for the Dehydration of Water – Ethanol Mixtures through Pervaporation. J Appl Polym Sci 2012;124:E319–29. doi:10.1002/app.

[38] Zhang S, Zou Y, Wei T, Mu C, Liu X, Tong Z. Pervaporation dehydration of binary and ternary mixtures of n-butyl acetate, n-butanol and water using PVA-CS blended membranes. Sep Purif Technol 2017;173:314–22. doi:10.1016/j.seppur.2016.09.047.

[39] Rhim J, Kim Y. Pervaporation Separation of MTBE – Methanol Mixtures Using Cross-linked PVA Membranes. J Appl Polym Sci 2000;75:1699–707.

[40] Tsai H, Chen W, Kuo C, Lee K, Lai J. Study on the pervaporation performance and long-term stability of aqueous iso -propanol solution through chitosan / polyacrylonitrile hollow fiber membrane. J Memb Sci 2008;309:146–55. doi:10.1016/j.memsci.2007.10.018.

[41] Lipnizki F, Hausmanns S, Ten P, Field RW. Organophilic pervaporation : prospects and performance. Chem Eng J 1999;73:113–29.

[42] Feng X, Huang RYM. Liquid Separation by Membrane Pervaporation : A

Review. Ind Eng Chem Res 1997;36:1048–66. doi:10.1021/ie960189g.

[43] Wijmans JG, Baker RW. The solution-diffusion model : a review. J Memb Sci 1995;107:1–21. doi:10.1016/0376-7388(95)00102-I.

[44] Feng X, Huang RYM. Liquid Separation by Membrane Pervaporation: A Review. Ind Eng Chem Res 1997;36:1048–66. doi:10.1021/ie960189g.

[45] Bhattacharya S, Hwang ST. Concentration polarization, separation factor, and Peclet number in membrane processes. J Memb Sci 1997;132:73–90. doi:10.1016/S0376-7388(97)00047-1.

[46] Wijmans JG, Athayde AL, Daniels R, Ly JH, Kamaruddin HD, Pinnau I. The role of boundary layers in the removal of volatile organic compounds from water by pervaporation. J Memb Sci 1996;109:135–46. doi:10.1016/0376-7388(95)00194-8.

[47] Heintz A, Stephan W. A generalized solution-diffusion model of the pervaporation process through composite membranes Part II. Concentration polarization, coupled diffusion and the influence of the porous support layer. J Memb Sci 1994;89:153–69. doi:10.1016/0376-7388(93)E0223-7.

[48] Guo W, Ngo HH, Li J. A mini-review on membrane fouling. Bioresour Technol 2012;122:27–34. doi:10.1016/j.biortech.2012.04.089.

[49] Liao Y, Bokhary A, Maleki E, Liao B. A review of membrane fouling and its control in algal-related membrane processes. Bioresour Technol 2018;264:343–

58. doi:10.1016/j.biortech.2018.06.102.

[50] Chen W, Qian C, Zhou KG, Yu HQ. Molecular Spectroscopic Characterization of Membrane Fouling: A Critical Review. Chem 2018;4:1492–509. doi:10.1016/j.chempr.2018.03.011.

[51] W.Kujawski. Application of Pervaporation and Vapour Permeation in Environmental Protection. Polish J Environ Stud 2000;9:13–26.

[52] Shao P, Huang RYM. Polymeric membrane pervaporation. J Memb Sci 2007;287:162–79. doi:10.1016/j.memsci.2006.10.043.

[53] Seader JD, Henley EJ, Roper DK. Separation Process Principles with Applications using Process Simulators. 3rd ed. Wiley; 2010.

[54] Murthy ZVP, Shah MK. Separation of isopropyl alcohol–toluene mixtures by pervaporation using poly(vinyl alcohol) membrane. Arab J Chem 2017;10:S56–61. doi:10.1016/j.arabjc.2012.07.008.

[55] Jonquières A, Clément R, Lochon P, Néel J, Dresch M, Chrétien B. Industrial state-of-the-art of pervaporation and vapour permeation in the western countries. J Memb Sci 2002;206:87–117.

[56] Smitha B, Suhanya D, Sridhar S, Ramakrishna M. Separation of organic-organic mixtures by pervaporation - A review. J Memb Sci 2004;241:1–21. doi:10.1016/j.memsci.2004.03.042.

[57] Boudghene Stambouli A, Traversa E. Fuel cells, an alternative to standard

sources of energy. Renew Sustain Energy Rev 2002;6:295–304. doi:10.1016/S1364-0321(01)00015-6.

[58] Kamarudin MZF, Kamarudin SK, Masdar MS, Daud WRW. Review: Direct ethanol fuel cells. Int J Hydrogen Energy 2013;38:9438–53. doi:10.1016/j.ijhydene.2012.07.059.

[59] Badwal SPS, Giddey S, Kulkarni A, Goel J, Basu S. Direct ethanol fuel cells for transport and stationary applications – A comprehensive review. Appl Energy 2015;145:80–103. doi:10.1016/j.apenergy.2015.02.002.

[60] Meyers JP, Newman J. Simulation of the Direct Methanol Fuel Cell. J Electrochem Soc 2002;149:A729. doi:10.1149/1.1473190.

[61] Xuan J, Leung MKH, Leung DYC, Ni M. A review of biomass-derived fuel processors for fuel cell systems. Renew Sustain Energy Rev 2009;13:1301–13. doi:10.1016/j.rser.2008.09.027.

[62] Gahleitner G. Hydrogen from renewable electricity: An international review of power-to-gas pilot plants for stationary applications. Int J Hydrogen Energy 2013;38:2039–61. doi:10.1016/j.ijhydene.2012.12.010.

[63] Demirci UB. Direct liquid-feed fuel cells: Thermodynamic and environmental concerns. J Power Sources 2007;169:239–46. doi:10.1016/j.jpowsour.2007.03.050.

[64] Rees N V, Compton RG. Carbon-free energy: A review of ammonia- and

hydrazine-based electrochemical fuel cells. Energy Environ Sci 2011;4:1255–60. doi:10.1039/c0ee00809e.

[65] Graś M, Sierczyńska A, Lota K, Acznik I, Lota G. The modification of anode material for direct borohydride fuel cell. Ionics (Kiel) 2016;22:2539–44. doi:10.1007/s11581-016-1892-x.

[66] Liu H, Song C, Zhang L, Zhang J, Wang H, Wilkinson DP. A review of anode catalysis in the direct methanol fuel cell. J Power Sources 2006;155:95–110. doi:10.1016/j.jpowsour.2006.01.030.

[67] Oasmaa A, Meier D. Norms and standards for fast pyrolysis liquids 1. Round robin test. J Anal Appl Pyrolysis 2005;73:323–34. doi:10.1016/j.jaap.2005.03.003.

[68] Oasmaa A, Fonts I, Pelaez-Samaniego MR, Garcia-Perez ME, Garcia-Perez M. Pyrolysis Oil Multiphase Behavior and Phase Stability: A Review. Energy and Fuels 2016;30:6179–200. doi:10.1021/acs.energyfuels.6b01287.

[69] Tiwari JN, Tiwari RN, Singh G, Kim KS. Recent progress in the development of anode and cathode catalysts for direct methanol fuel cells. Nano Energy 2013;2:553–78. doi:10.1016/j.nanoen.2013.06.009.

[70] An L, Zhao TS, Li YS. Carbon-neutral sustainable energy technology: Direct ethanol fuel cells. Renew Sustain Energy Rev 2015;50:1462–8. doi:10.1016/j.rser.2015.05.074.

[71] Neburchilov V, Martin J, Wang H, Zhang J. A review of polymer electrolyte membranes for direct methanol fuel cells. J Power Sources 2007;169:221–38. doi:10.1016/j.jpowsour.2007.03.044.

[72] Taneda K, Yamazaki Y. I-V characteristics of a direct type fuel cell using acetaldehyde as a fuel. J Power Sources 2006;157:177–80. doi:10.1016/j.jpowsour.2005.08.011.

[73] Antoniassi RM, Oliveira Neto A, Linardi M, Spinacé E V. The effect of acetaldehyde and acetic acid on the direct ethanol fuel cell performance using PtSnO2/C electrocatalysts. Int J Hydrogen Energy 2013;38:12069–77. doi:10.1016/j.ijhydene.2013.06.139.

[74] Schnaidt J, Heinen M, Jusys Z, Behm RJ. Electro-oxidation of ethylene glycol on a Pt-film electrode studied by combined in situ infrared spectroscopy and online mass spectrometry. J Phys Chem C 2012;116:2872–83. doi:10.1021/jp208162q.

[75] Yu X, Pickup PG. Recent advances in direct formic acid fuel cells (DFAFC). J Power Sources 2008;182:124–32. doi:10.1016/j.jpowsour.2008.03.075.

[76] Jeong KJ, Miesse CM, Choi JH, Lee J, Han J, Yoon SP, et al. Fuel crossover in direct formic acid fuel cells. J Power Sources 2007;168:119–25. doi:10.1016/j.jpowsour.2007.02.062.

[77] Simões M, Baranton S, Coutanceau C. Electrochemical Valorisation of Glycerol. ChemSusChem 2012;5:2106–24. doi:10.1002/cssc.201200335.

[78] Anitha M, Kamarudin SK, Kofli NT. The potential of glycerol as a value-added commodity. Chem Eng J 2016;295:119–30. doi:10.1016/j.cej.2016.03.012.

[79] Thanh LT, Okitsu K, Boi L Van, Maeda Y. Catalytic Technologies for Biodiesel Fuel Production and Utilization of Glycerol: A Review. Catalysts 2012;2:191–222. doi:10.3390/catal2010191.

[80] Brueckner TM, Pickup PG. Kinetics and Stoichiometry of Methanol and Ethanol Oxidation in Multi-Anode Proton Exchange Membrane Cells. J Electrochem Soc 2017;164:F1172–8. doi:10.1149/2.1181712jes.

[81] Diebold JP. A Review of the Chemical and Physical Mechanisms of the Storage Stability of Fast Pyrolysis Bio-Oils. 2000. doi:NREL/SR-570-27613.

[82] Ghenciu AF. Review of fuel processing catalysts for hydrogen production in PEM fuel cell systems. Curr Opin Solid State Mater Sci 2002;6:389–99. doi:10.1016/S1359-0286(02)00108-0.

[83] Joghee P, Malik JN, Pylypenko S, O'Hayre R. A review on direct methanol fuel cells – In the perspective of energy and sustainability. MRS Energy Sustain A Rev J 2015:1–31. doi:10.1557/mre.2015.4.

[84] Kwon Y, Schouten KJP, Koper MTM. Mechanism of the Catalytic Oxidation of Glycerol on Polycrystalline Gold and Platinum Electrodes. ChemCatChem 2011;3:1176–85. doi:10.1002/cctc.201100023.

[85] Take T, Tsurutani K, Umeda M. Hydrogen production by methanol-water

solution electrolysis. J Power Sources 2007;164:9–16. doi:10.1016/j.jpowsour.2006.10.011.

[86] Sasikumar G, Muthumeenal A, Pethaiah S, Nachiappan N, Nalaji R. Aqueous methanol electrolysis using proton conducting membrane for hydrogen production. Int J Hydrogen Energy 2008;33:5905–10. doi:10.1016/j.ijhydene.2008.07.013.

[87] Hu Z, Wu M, Wei Z, Song S, Shen PK. Pt-WC/C as a cathode electrocatalyst for hydrogen production by methanol electrolysis. J Power Sources 2007;166:458–61. doi:10.1016/j.jpowsour.2007.01.083.

[88] Marshall AT, Haverkamp RG. Production of hydrogen by the electrochemical reforming of glycerol-water solutions in a PEM electrolysis cell. Int J Hydrogen Energy 2008;33:4649–54. doi:10.1016/j.ijhydene.2008.05.029.

[89] Marsman JH, Wildschut J, Mahfud F, Heeres HJ. Identification of components in fast pyrolysis oil and upgraded products by comprehensive two-dimensional gas chromatography and flame ionisation detection. J Chromatogr A 2007;1150:21–7. doi:10.1016/j.chroma.2006.11.047.

[90] Rahman S, Helleur R, Macquarrie S, Papari S, Hawboldt K. Isolation of low MW compounds from bark and softwood bio-oil and quality improvement of the residual bio-oil by molecular distillation n.d.:1–15.

Chapter 2

Pyrolysis oil enhancement: A design of experiment study to remove water from bark pyrolysis oil by pervaporation to improve fuel quality

2 Pyrolysis oil enhancement: A design of experiment study to remove water from bark pyrolysis oil by pervaporation to improve fuel quality

2.1 Introduction

Renewable biofuels have the potential to reduce greenhouse gas emissions relative to fossil fuels, with second-generation biofuels preferred over first-generation biofuels for heat and power production [1,2]. Second generation fuels are produced from non-food materials such as energy crops on marginal land, municipal solid waste, and forestry and agricultural residues. These biomass resources can be converted to liquid, gaseous, and solid fuels via thermal, chemical, biological, and physical processes [3–5]. Fast pyrolysis of biomass is the thermochemical conversion of biomass to produce a liquid fuel, with solid and gaseous by-products [6–8]. The ratio of liquid:solid:gas is a function of process conditions [9]. Liquid fuels provide an energy-rich material that can be more easily transported from remote locations compared to the biomass feedstock.

In fast pyrolysis, the biomass is rapidly heated up to a range of 450 to 600 °C in the absence of oxygen, resulting in organic vapours (condensable and non-condensable gases) and char. The condensed vapours (pyrolysis oil) consist of over 300 main and 700 minor organic components [10–12] and are chemically distinct from petroleum oils because they contain little to no hydrocarbons [13].

The pyrolysis feedstock in this study was bark, a primary sawmill residue. Bark pyrolysis oil generally has high water content (30 to 70 mass%) [14–18] and therefore

has low heating values and flame temperatures [6,19,20], and often exists as two separate phases (an organic bottom phase and an aqueous top phase) [15,16,21]. The ASTM D7544-12 boiler fuel standard recommends a water content maximum of 30 mass%. In this study, the incombustible aqueous top phase was used (water content of 70.2 mass%). Therefore, the focus of this study was to decrease the water content to produce a standard boiler fuel.

Many upgrading methods, that can be applied during and/or after the pyrolysis process, have been investigated to improve the quality of pyrolysis oil [6,22]. In this work post-pyrolysis treatment of the oil was used to improve the oil quality. Chemical, physical, and catalytic processes can be used for post-pyrolysis upgrading. Chemical methods include esterification and hydrogenation [22], and solvent extraction processes [23,24]. Catalytic methods include cracking and hydrotreating [6,22,25]. Physical processes include emulsification [22,26], filtration [22], blending [27], and several distillation methods [14,28–31]. Many studies focus on distillation to separate the water and other low boiling point components from the pyrolysis oil [14,32]. However, distillation is energy intensive, due to the high temperatures required, and can lead to secondary cracking reactions [33]. Pervaporation can achieve similar separations at lower temperatures, which results in energy savings [34,35].

The focus of this chapter is the novel water removal through pervaporation, where the water permeates and evaporates across the membrane and is condensed to create a partial vacuum, maintaining a driving force for the permeation [36]. In addition to the concentration driving force between the liquid feed solution and the vapour

permeate, the diffusion rate determines permeation selectivity [37]. The advantages of pervaporation compared to conventional distillation processes are the better separation of azeotropic mixtures, and lower energy and building space requirements [38]. Unlike previous works where membranes have been used to separate value-added chemicals [39,40], here the objective was to enhance the bark oil quality and simultaneously identify essential value-added chemicals in the permeate for future applications. The effects of the factors temperature, feed flow rate, and membrane type, the interactions between factors, and their influence on oil quality were evaluated in a design of experiment (DoE) study. The oil quality was determined by the water separation yield, heating value, water content, dynamic viscosity, and total acid number.

2.2 Materials and methods

2.2.1 Bark pyrolysis oil

The pyrolysis bark oil used for this study was produced by ABRI-Tech Inc. in a one dry tonne/day auger reactor at 475 °C with steel shot as a heat carrier. A similar auger reactor built by ABRI-Tech Inc. is described in [18]. The feedstock was a mixture of spruce, pine, and fir softwood bark from the Groupe Crête division St-Faustin Inc. sawmill in Mont-Tremblant, Quebec, Canada.

2.2.2 Pervaporation experiments

Pervaporation (Figure 2.1) is a process to separate liquid/liquid mixtures through membranes at elevated temperatures. The target component permeates into the membrane and evaporates on the permeate side where it is condensed in a cooling trap.

A lab-scale pervaporation unit was custom made to treat the pyrolysis oil. The unit consists of two stainless steel parallel flow fields separated by a planar membrane (Figure 2.2).

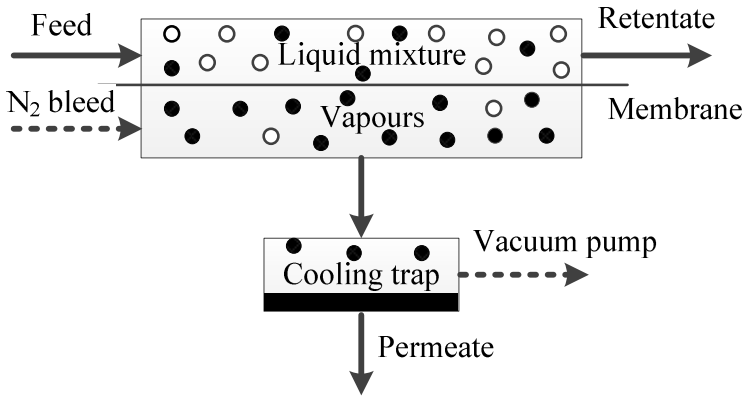

Figure 2.1: Schematic drawing of the pervaporation principle.

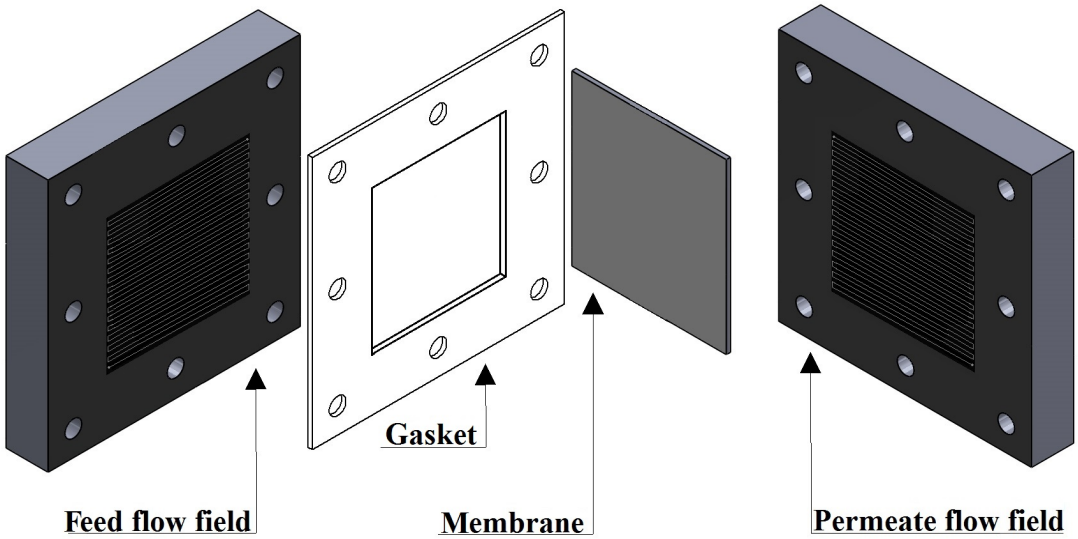

Figure 2.2: Lab-scale pervaporation unit, two heated stainless steel flow field plates separated by a membrane, sealed by a gasket.

The Pervap™ (DeltaMem AG) membranes employed are composite membranes consisting of a 0.5-5 μm thick polyvinyl alcohol (PVA) separation layer coated on a porous 70-100 μm thick polyacrylonitrile porous support layer on a 100-150 μm thick porous polyester mechanical support layer. The membranes differ in the extent of crosslinking of the PVA separation layer (Pervap 4155-30 < Pervap 4155-80 < Pervap 4101). Figure 2.3 shows a schematic membrane cross-section of the separation and the porous support layers.

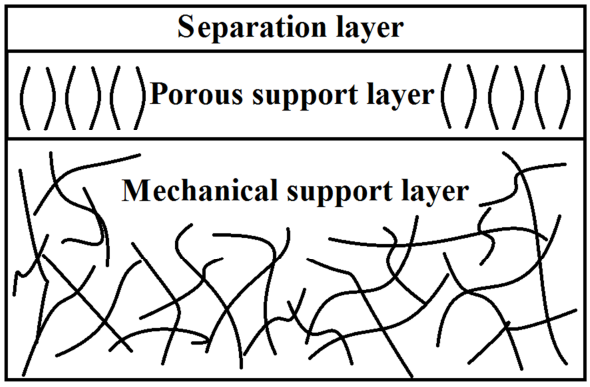

Figure 2.3: Schematic cross-section of a DeltaMem AG Pervap composite membrane.

The pyrolysis oil was fed into three parallel flow channels each 1.6 mm wide (Figure 2.2). The membrane area was 56.25 cm². The unit was operated at reduced pressure (60 cm Hg gauge; Welch WOB-L 2522 piston vacuum pump) with a 10 mL min^{-1} nitrogen (N_2) bleed stream. Preliminary experiments showed that these conditions produced the highest permeate flux. For each run, 50 ml of bark oil was pumped through the unit using a NE-300 New Era Pump Systems syringe pump. A Marinco cartridge heater and a Digi Sense temperature controller were used to heat the unit in all experiments. The permeate vapours were condensed in a trap cooled with an

ice + dry ice mixture. The cold trap was constructed from a 10 mL (± 0.05 mL) graduate cylinder, and the permeate volume was measured hourly.

2.2.3 Experimental design and statistical analysis

Design expert software (Version 9.0.6, State-Ease, Inc., Minneapolis, MN, USA) was used to analyze the significance and interactions between factors in a DoE study. A 2^3 factorial design, with two levels for each factor, was used in eight separate runs. The factors selected to study and optimize the pervaporation process were temperature (numeric), feed flow rate (numeric), and membrane type (categorical). The levels of the three factors were chosen based on preliminary screening results. Two temperatures (60 and 80 °C) and feed flow rates (0.1 and 0.2 mL min^{-1}) were employed as well as membranes with two different levels of crosslinking (Pervap 4155-30 < Pervap 4155-80). The yield, concentration, and composition of the permeate, as well as water content, dynamic viscosity, heating value, and total acid number of the retentate were analyzed as process responses. The permeate yield was calculated as Ep. (2.1).

$$Y_{Permeate}(vol\%) = \frac{\text{Permeate volume (mL)}}{\text{Start volume (mL)}} \times 100\% \quad (2.1)$$

The software was used to obtain the experimental matrix and perform the subsequent regression analysis and analysis of variance (ANOVA). The design matrix of the pervaporation runs is shown in Table 2.1.

Table 2.1: Experimental design matrix

Run	Variables (studied factors)		
	Membrane type -	Temperature °C	Feed flow rate mL min^{-1}
1	4155-30	80	0.1
2	4155-80	60	0.1
3	4155-30	60	0.2
4	4155-80	80	0.1
5	4155-80	80	0.2
6	4155-30	80	0.2
7	4155-80	60	0.2
8	4155-30	60	0.1

2.2.4 Characterization of the permeate and retentate

After each run, the permeate and retentate were collected in a sealed bottle and stored at 5 °C before analysis. The permeate was analyzed for chemical composition by proton nuclear magnetic resonance (NMR) spectroscopy with a Bruker AVANCE III 300 MHz NMR spectrophotometer. Fumaric acid was used as an internal standard to determine the concentrations of components that could be identified. The water content of the retentate was determined according to ASTM E203 as recommended in ASTM D7544-12 with a Mettler Toledo C20 Compact Karl Fischer Coulometer. Due to the higher water content in the retentate, samples were diluted with methanol (1:80 w/w). HPLC grade methanol was used because of its very low water content. The total acid number (TAN) of the retentate was determined according to ASTM D664. Each sample was dissolved in methanol and titrated potentiometrically with sodium hydroxide. A VWR B10P benchtop pH meter with a glass pH electrode was used to measure the change in potential. According to ASTM D445, a Brookefield DV-III Ultra Programmable Rheometer V 6.0 LV was used to measure the dynamic viscosity (v) at

40 °C. The sample was temperature controlled with a RM3 water circulator from LAUDA-Brinkmann Model S-1. The cylindrical sample cup was filled with 6.7 ml of sample and the spindle SC4-18/13RP was used for all analysis runs without the spindle guard leg. The rotational speed was increased from 10 rpm in increments of 10 rpm until torque readings exceeded 100%. The precision of the measurement is 1% at torque 100%. Therefore, the relative error is 1% at a torque of 100% and 10% at a torque of 10%. The higher heating value (HHV) was measured according to ASTM D240 with a Parr B41 calorimeter with a 1108 oxygen combustion bomb and a model 6775 digital thermometer. The bomb was pressurized with oxygen to 3 MPa for each run. The sample (0.5 g) was placed in a Parr gelatine capsule.

2.3 Results and discussion

The analysis of variance (ANOVA) results (*Appendix 2.7*) showed that no factor (temperature, membrane type, flow rate) was significant for the TAN response. A factor is significant if the p-value is lower than 0.05 and is insignificant if the value is greater than 0.1. However, the factors did impact HHV, viscosity, water content, and permeate yield. The membrane type was significant for viscosity only.

2.3.1 Design of experiments results

The retentate response values were water content, dynamic viscosity, HHV, and TAN, and the permeate yield (Table 2.2). All response values were measured as described in Chapter 2.2.4. The water content varied from 38.8 – 58.4 mass%, the dynamic viscosity varied between 2.35 – 8.54 mPa·s, the heating value varied between non-combustible to 12.7 MJ kg^{-1}, and the TAN varied from 42.5 to 50.5 mg NaOH/g oil.

Table 2.2: Response values of each DoE run

Run	Variables (studied factors)			Responses				
	Membrane type	Temp-erature	Feed flow rate	Permeate	Retentate			
				Yield	Water content	Dynamic viscosity	HHV	TAN
	-	°C	mL min^{-1}	mass%	mass%	mPa s^{-1} (40 °C)	MJ kg^{-1}	
1	4155-30	80	0.1	66	39.1	7.14	12.5	49.7
2	4155-80	60	0.1	60	40.3	6.02	12.0	50.5
3	4155-30	60	0.2	36	58.4	2.35	-	42.5
4	4155-80	80	0.1	62	38.8	8.54	12.7	47.7
5	4155-80	80	0.2	57	44.3	4.62	11.4	48.3
6	4155-30	80	0.2	56	48.7	3.66	10.4	44.8
7	4155-80	60	0.2	41	55.6	2.58	-	44.2
8	4155-30	60	0.1	59	43.7	5.08	11.47	47.2

In general, the water content decreases and therefore the HHV increases with higher temperatures and lower feed flow rates. Plotting the DoE analyses results gives an indication of trends and interaction between factors temperature and feed flow rate in Figure 2.4 for HHV, and Figure 2.5 for water content.

The final equations for the significant responses determined by the Design Expert software are shown in Table 2.3 and Table 2.5. In each equation T is the temperature in °C, U is the feed flow rate in mL min^{-1}, and A is the membrane type.

Table 2.3: Prediction equations with actual factors determined by the Design Expert software

HHV (MJ kg^{-1})	=	51.08	-	0.46	·	T	-	418.33	·	U	+	5.01	· T·U
Viscosity (Pervap 4155-30) (mPas)	=	2.71	+	0.10	·	T	-	33.93	·	U			
Viscosity (Pervap 4155-80) (mPas)	=	3.59	+	0.10	·	T	-	33.93	·	U			
Water content (mass%)	=	13.45	+	0.22	·	T	+	375.76	·	U	-	3.76	· T·U
Permeate yield (vol%)	=	97.30	-	0.27	·	T	-	560.00	·	U	+	5.75	· T·U
Permeate yield (mass%)	=	85.53	-	0.18	·	T	-	518.30	·	U	+	5.31	· T·U

The levels for the coded factors equations in Table 2.5 are shown in Table 2.4.

Table 2.4: Levels for the coded factor prediction equations

		Unit	-1	+1
Temperature	T	°C	60	80
Feed flow rate	U	mL min^{-1}	0.1	0.2
Membrane type	A	-	Pervap 4155-30	Pervap 4155-80

Table 2.5: Prediction equations with coded factors (factors normalized from -1 to 1) determined by the Design Expert software

HHV (MJ kg^{-1})	=	8.80	+	2.93	·	T	-	3.37	·	U	+	2.51 · T·U
Viscosity (mPas)	=	5.00	+	0.44	·	A	+	0.99	·	T	-	1.70 · U
Water content (mass%)	=	46.11	-	3.39	·	T	+	5.64	·	U	-	1.88 · T·U
Permeate yield (vol%)	=	55.13	+	5.98	·	T	-	7.88	·	U	+	2.88 · T·U
Permeate yield (mass%)	=	51.11	+	6.19	·	T	-	7.34	·	U	+	2.65 · T·U

The results indicate that the temperature (T), the feed flow rate (U), and the interaction between T and U were significant factors for all investigated responses, except for viscosity. The model equations are useful tool in assessing the impact of the factors on the performance of the lab scale pervaporation system in this work. Figure 2.4 shows the HHV and Figure 2.5 the water content as a function of temperature and flow rate.

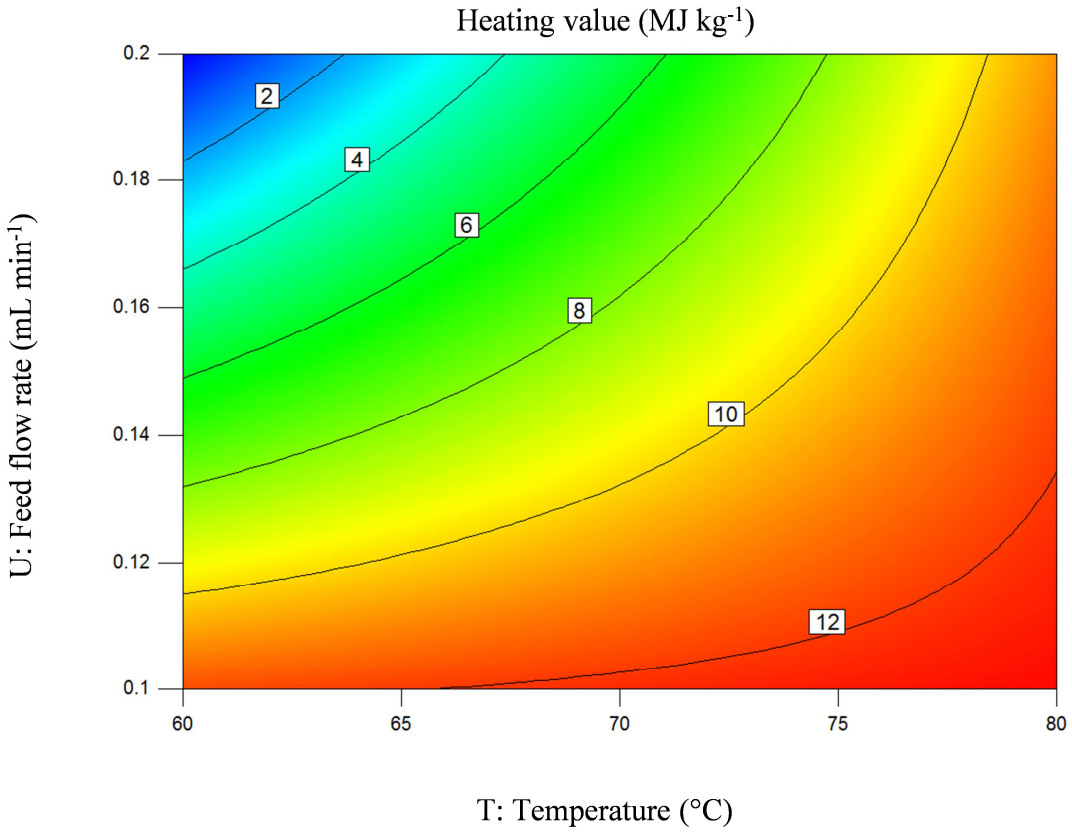

Figure 2.4: HHV as a function of flow rate and temperature.

Figure 2.4 shows that the highest heating value (> 12 MJ kg^{-1}) was reached with slow feed flow rates (< 0.12 mL min^{-1}) and high temperatures (> 70 °C).

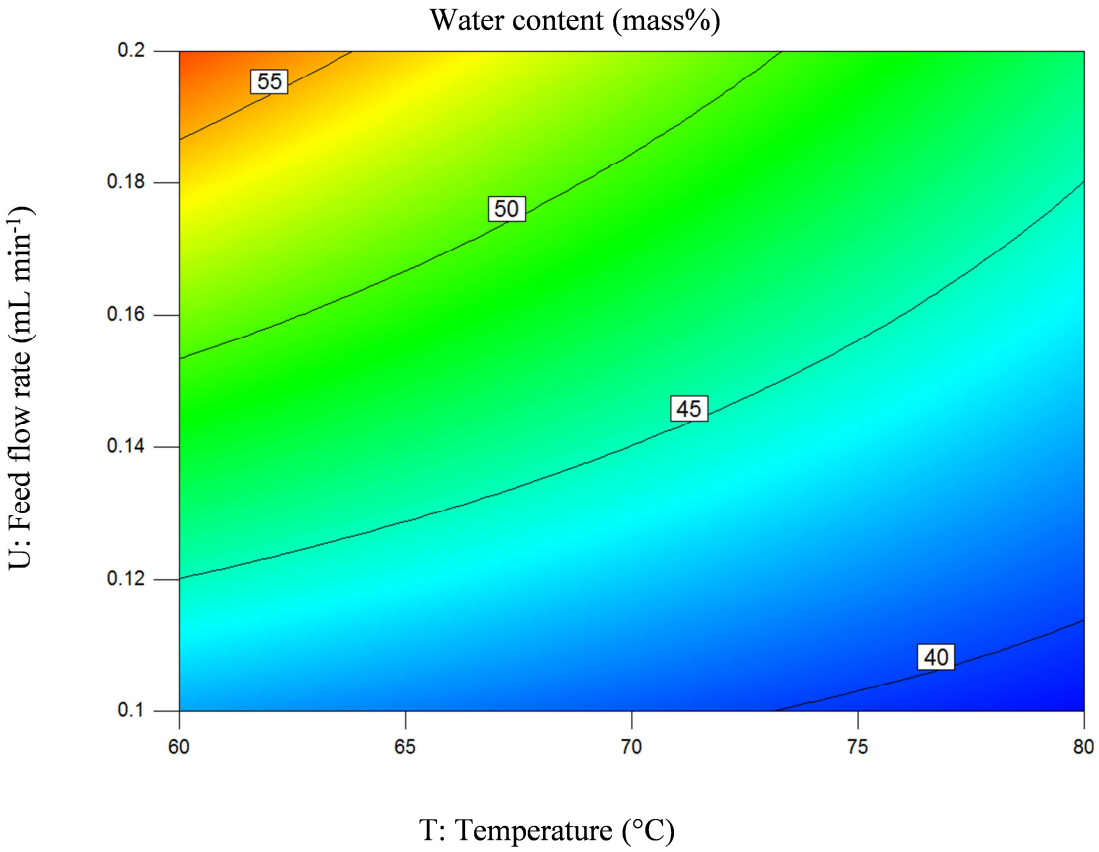

Figure 2.5: Water content as a function of flow rate and temperature.

Figure 2.5 shows that the lowest water content (< 40 mass%) was reached with a slow feed flow rate (0.1 mL min^{-1}) and high temperatures (> 75 °C). In addition to the statistical optimization approach, the retentate was analyzed for application as a fuel oil. Therefore, the retentate properties heating value, water content, dynamic viscosity, and total acid number were measured.

2.3.2 Retentate properties

The properties of the crude bark-oil and the retentate samples are compared with the specifications for ASTM D7544-12 standard in Table 2.6.

Table 2.6: Physical properties of the retentate

Run	Heating value (HHV) MJ kg^{-1}	Water content mass%	Dynamic viscosity mPa·s (40 °C)	Total acid number mg NaOH/ g bio-oil
ASTM D7544-12 standard	min. 15	max. 30	max. 125	/
Crude bark-oil	incomplete combustion	70.2	1.63	35.2
DoE 1	12.49	39.1	7.14	49.7
DoE 2	12.05	40.3	6.02	50.5
DoE 3	incomplete combustion	58.4	2.35	42.5
DoE 4	12.72	38.8	8.54	47.7
DoE 5	11.36	44.3	4.62	48.3
DoE 6	10.37	48.7	3.66	44.8
DoE 7	incomplete combustion	55.6	2.58	44.2
DoE 8	11.47	43.7	5.08	47.2

The grade G bio-oil described in the standard is intended for use in industrial burners and is not suitable for residential heaters, small commercial boilers, engines, or marine applications; grade D is for commercial/industrial burners requiring lower solids and ash content and suitable in residential heaters, engines, or marine applications modified to handle these types of fuel. For both grades, the standard recommends a maximum water content of 30 %. The bark-oil sample has a water content of 70.2 % which needs to be decreased greatly to meet the standard. The heating value of the crude aqueous bark-oil phase sample could not be determined because the high water content led to incomplete combustion. Pervaporation with both the Pervap 4155-30 and Pervap 4155-80 membranes lowered the water content and increased the heating value

of the retentate bark-oil, although none of the retentate samples reached the required ASTM D7544-12 value. In general, the higher temperature resulted in lower water content. The HHV could not be measured when the water content exceeded 55 mass%.

The dynamic viscosity of the aqueous phase bark oil was 1.63 mPa·s (at 40 °C) which is much lower than the maximum of 125 mPa·s required in ASTM D7544-12. All of the retentates met this viscosity standard.

The major components present in pyrolysis oils from forest residuals are water (20-30 mass%), lignin fragments (15-30 mass%), aldehydes (10-20 mass%), carboxylic acids (10-15 mass%), carbohydrates (5-10 mass%), phenols (2-5 mass%), furfurals (1-4 mass%), alcohols (2-5 mass%), and ketones (1-5 mass%) [41]. Due to the high acid content, pyrolysis oil is corrosive and can damage non-stainless steel equipment such as storage tanks and boilers [20]. The TAN of the crude aqueous phase bark-oil was 35.2 mg NaOH/g bio-oil. Although not covered by the standard, this is also an important characteristic of the oil. All retentates had higher TAN compared to the original aqueous phase of the bark oil. The retentate TAN correlates with the permeate yield; when the permeate yield is high, the retentate TAN is also high. Water is the main component removed from the retentate, which potentially concentrates low volatility organic acids, such as butyric, pentanoic, hexanoic, and glycolic acid in the retentate even though lighter organic acids are removed [41]. The permeate yield and TAN were higher at high temperatures and low flow rates.

The lowest water content in the retentate (38.8 mass%) occurred with the Pervap 4155-80 membrane at 80 °C and a feed flow rate of 0.1 mL min^{-1}. To meet the specifications in ASTM D7544-12 standard, a Pervap 4101 membrane designed for high water concentrations in the feed solution (>50 mass%) was operated at the optimum pervaporation conditions determined by the DoE. The PVA separation layer of the Pervap 4101 membrane is highly crosslinked. This follow-up experiment was carried out at 80 °C, with a feed flow rate of 0.1 mL min^{-1}, a nitrogen bleed stream of 10 mL min^{-1}, and a vacuum of 20 kPa (absolute). The results of this experiment are shown in Table 2.7 and compared to the ASTM 7544-12 pyrolysis oil standard.

Table 2.7: Results Pervap 4101 retentate compared to ASTM 7544-12 pyrolysis oil standard

Sample #	Heating value (HHV) MJ kg^{-1}	Water content mass%	Dynamic viscosity mPa·s (40 °C)	Total acid number (TAN) mg NaOH/ g bio-oil
ASTM D7544-12 standard	min. 15	max. 30	max. 125	/
Pervap 4101	16.07	21.42	13.98	84.9

The results with the Pervap 4101 membrane demonstrate that the bark oil aqueous phase can be upgraded by pervaporation to meet the ASTM D7544-12 standard. The advantage of pervaporation compared to distillation is that pervaporation can be a continuous operation process where the separation is based on a combination of heat and permeability mechanisms. Pervaporation can possible separate azeotrope mixtures. Contrarily distillation separation processes have a higher heat requirement and

can form hot spots in the distillation flask which lead to secondary cracking reactions in the pyrolysis oil.

In addition to improving the retentate quality, there are potential value-added products in the permeate. The pervaporation process separates fuel components from of the oil. This loss might lead to a HHV reduction, however, this selective removal of components is also an advantage compared to distillation techniques. The separated components increase the value of the separated water stream and make it useful for further applications. Therefore, the permeate fluxes and composition was analyzed. This was also in an effort to understand how compounds removed were impacting retentate quality.

2.3.3 Permeate properties

The permeate samples (Figure 2.6) were collected in glass vials and analyzed by NMR spectroscopy to obtain the concentrations of major components.

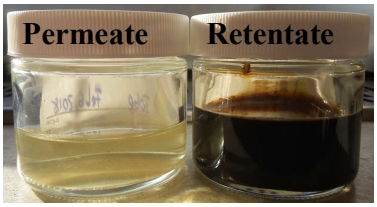

Figure 2.6: Permeate and retentate samples of DoE run 1 (Pervap 4155-30, 80 °C, 0.1 mL min^{-1}).

The average permeate fluxes through the membrane per run are shown in Table 2.8. The fluxes vary with temperature, membrane type, and feed flow rate in the range of 0.61 to 1.24 $Lm^{-2}h^{-1}$. With increasing feed flow rate (0.2 mL min^{-1}), the diffusion layer is

reduced (concentration polarization) and the overall flux increases. The Reynolds number was shown to be laminar for both feed flow rates (≤ 0.60).

Table 2.8: Permeate flux (L $m^{-2}h^{-1}$)

Membrane type -	Temperature (°C)	Feed flow rate (mL min^{-1})	Average flux (L $m^{-2}h^{-1}$)
Pervap 4155-30	80	0.1	0.68
Pervap 4155-80	60	0.1	0.63
Pervap 4155-30	60	0.2	0.72
Pervap 4155-80	80	0.1	0.70
Pervap 4155-80	80	0.2	1.24
Pervap 4155-30	80	0.2	1.21
Pervap 4155-80	60	0.2	0.86
Pervap 4155-30	60	0.1	0.61

Table 2.9 shows the concentrations of components in the permeate that have been identified by NMR.

Table 2.9: Chemical composition of the permeate

Concentration (M)	Boiling point (°C)	DoE run 1	DoE run 2	DoE run 3	DoE run 4	DoE run 5	DoE run 6	DoE run 7	DoE run 8
Acetic acid	118.1	0.59	0.53	0.49	0.75	0.52	0.53	0.43	0.51
Methanol	64.7	0.29	0.43	0.56	0.37	0.34	0.31	0.45	0.40
Hydroxyacetone	146.0	0.30	0.26	0.23	0.37	0.29	0.25	0.20	0.24
Formic acid	100.8	0.07	0.05	0.04	0.08	0.06	0.06	0.04	0.05
Furfural	161.7	0.01	0.02	0.02	0.02	0.01	0.01	0.02	0.02
Water content (mass%)		90.4	93.8	93.8	88.0	93.9	90.6	94.7	94.3

The permeate was primarily water (≥ 88 % by mass), with acetic acid, methanol, hydroxyacetone, formic acid, and furfural [14,42]. Unidentified components comprised ≤ 4.2 % by mass. Table 2.9 indicates that it was possible to simultaneously dehydrate the aqueous phase of pyrolysis bark oil and separate value-added chemicals (alcohols and acids). Removal of acids is important to the use of bark pyrolysis oils as an intermediate in the production of fuels and chemicals. The separated acetic acid would be a value-added by-product if it was separated from the permeate. The separated alcohols could be potentially used as solvents or fuels for fuel cell applications.

The three driving forces in membrane separation are differences in concentration, pressure, and temperature between the retentate and permeate side [43,44]. The separation principle for non-porous membranes is based on the solution desorption model where transport through the membrane is governed by a component's solubility and diffusivity [43–45]. In this experimental series, the pressure difference and concentration in the feed were kept constant for each run, and the temperature was varied from 60 to 80 °C. The higher temperature (80 °C) and slow feed flow rate (0.1 mL min^{-1}) in Run 4 resulted in the highest acetic acid concentration (0.75 M) in the permeate, while the lower temperature of (60 °C) and higher flow rate (0.2 mL min^{-1}) in Runs 3 and 7 gave the lowest values (0.49 and 0.43 M, respectively). In contrast, the highest methanol concentrations (0.56 M in Run 3 and 0.45 M in Run 7) were reached at 60 °C and 0.2 mL min^{-1}. The highest methanol concentration occurred with the thinner Pervap 4155-30 membrane.

The separated acetic and formic acid in the permeate did not lead to an expected TAN decrease in the retentate, on the contrary the TAN increased in all retentate samples to 42.5 - 50.5 mg NaOH/g bio-oil from 35.2 mg NaOH/g bio-oil in the crude bark-oil (Table 2.6). This is likely due to increased concentration of acids in the remaining retentate due to the water reduction from 70.2 mass% in the crude bark-oil to 38.8 - 58.4 mass% in the retentate.

In general, the higher temperature of 80 °C increased the flux of all components through the membrane. To investigate the correlations of the permeate composition, the flux for each identified component was calculated by Eq. (2.2).

$$J = \frac{C \cdot V}{t \cdot A} \left(\text{mol cm}^{-2} \cdot \text{s}\right) \tag{2.2}$$

Where the flux (J) depends on the concentration C (mol dm^{-3}) in the collected volume V (dm^3), t (s) is the time and A (cm^2) the membrane area. For example, Figure 2.7 shows the influence of the temperature and the flow rate on the acetic acid flux in the permeate. All identified components, except furfural, show the same flow rate and temperature dependence as the acetic acid flux.

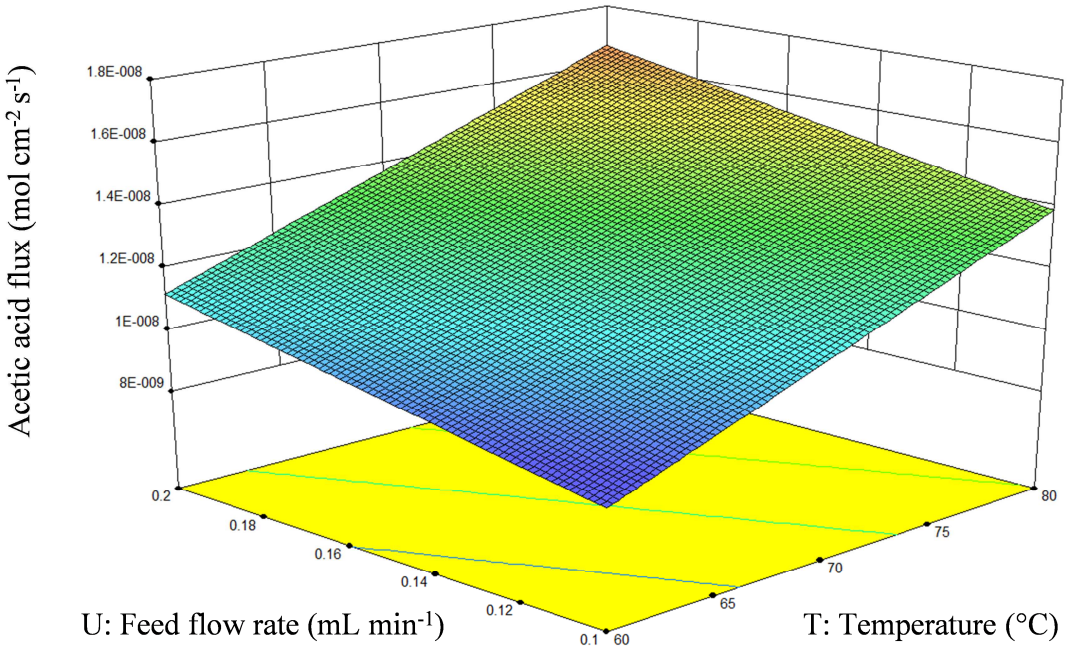

Figure 2.7: 3D response plot for the acetic acid flux (mol $cm^{-2}s^{-1}$) dependence on the flow rate and temperature.

The final predictive equations for the methanol, acetic acid, hydroxyacetone, and formic acid fluxes determined by the Design Expert software are shown in Table 2.10.

Table 2.10: Flux prediction equations in actual factors determined by the Design Expert software (mol $cm^{-2}s^{-1}$)

Water	=	1.9E-06	-	2.1E-08	.	T	-	1.1E-05	.	U	+	2.3E-07 . TU
Methanol	=	2.7E-09	+	4.2E-08	.	U						.
Acetic acid	=	-1.1E-08	+	2.7E-10	.	T	+	2.8E-08	.	U		.
Hydroxyacetone	=	-6.8E-09	+	1.6E-10	.	T	+	1.4E-08	.	U		.
Formic acid	=	6.3E-10	+	4.0E-12	.	T	-	1.5E-08	.	U	+	2.5E-10 . TU

No factor (temperature, membrane type, flow rate) was significant for the flux of furfural. These predictive equations can be used to screen process conditions which favour different components or groups of components in the permeate. The flux and

compositions are vital parameters in the membrane selection; however, the durability of membranes are essential in the long term use.

2.3.4 Membrane durability

The durability of a Pervap 4101 membrane was investigated by repeating pervaporation runs at 80 °C and a feed flow rate of 0.1 mL min^{-1}. The same membrane was used for >15 hours over several days. Between each run, a washing step was conducted with 15 ml of a methanol:water mixture (1:1 v:v) at 0.5 mL min^{-1} to remove pyrolysis oil residue on the membrane surface. The permeate flux results in Figure 2.8 show that the performance of the membrane remained stable within the experimental uncertainty.

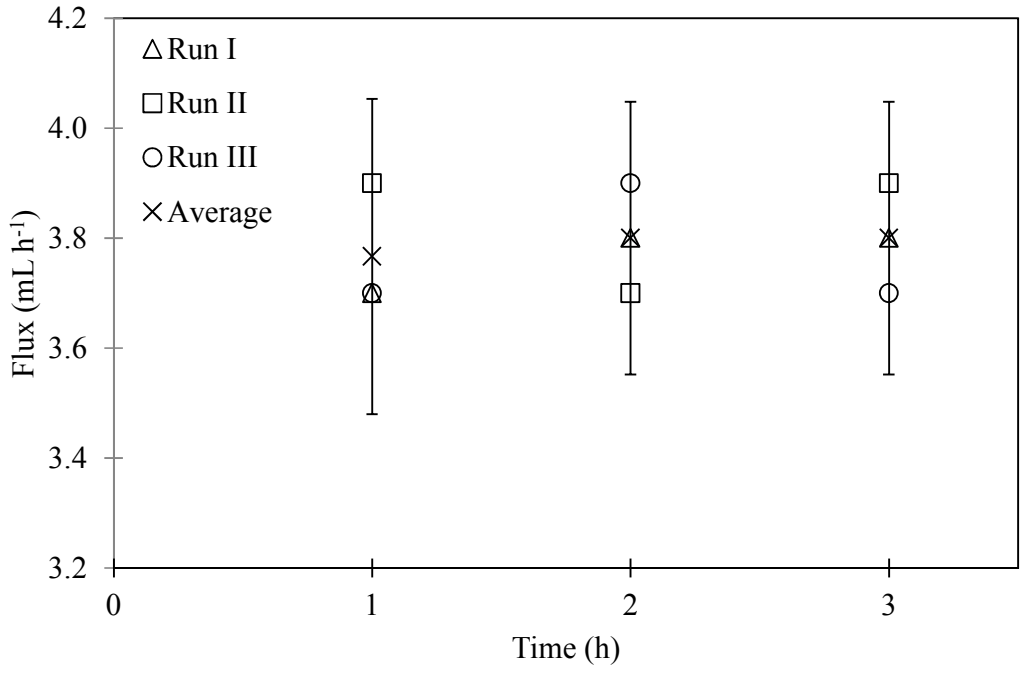

Figure 2.8: Permeate fluxes analyzed for a membrane stability test. The error bars indicate the 95% confidence interval.

Visual inspection, following a final wash with a 50:50 vol/vol mixture of methanol and water, showed no changes except some coloration of residue pyrolysis oil on the membrane surface. The used membrane showed the imprint of the flow channels from the pervaporation system. For a more accurate inspection scanning electron microscopy (SEM) images were carried out. Figure 2.9 shows the used Pervap 4101 membrane (left), the SEM picture of the new membrane surface (middle), and the membrane surface with pyrolysis oil residue after a run (right).

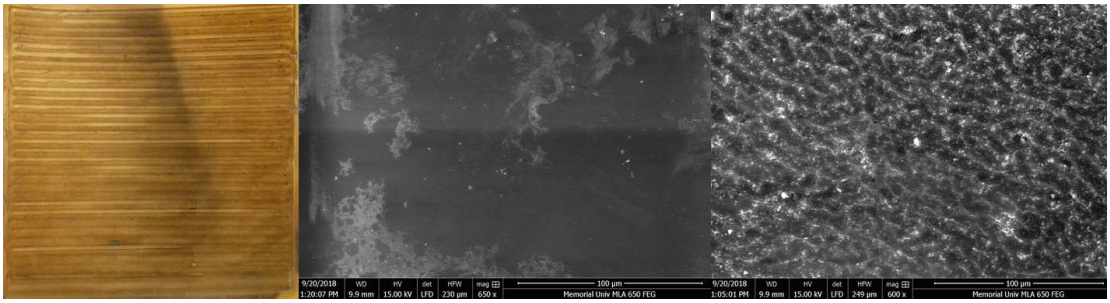

Figure 2.9: Used Pervap 4101 membrane (left), the SEM image of the new membrane surface (middle), and the SEM image of the membrane surface with tried pyrolysis oil residue after a run (right)

No evidence of any damage to the PVA layer was detected. However, the images show oil residues on the membrane surface, especially on the side of the channel walls. No membrane fouling due to the residue pyrolysis oil on the surface was detected during the run series.

To determine whether there were changes in membrane selectivity, the permeate composition was analyzed by NMR. Table 2.11 shows the concentrations of selected components of the permeate samples.

Table 2.11: Concentrations of selected permeate components from the membrane stability test

Concentration (M)	Run I	Run II	Run III
Methanol	0.082	0.362	0.143
Acetic acid	0.052	0.093	0.185
Hydroxyacetone	0.015	0.031	0.071
Formic acid	0.018	0.026	0.037

The concentrations of the investigated compounds in the permeate increased during repeated runs, except for a drop in methanol concentration in run 3 (the methanol concentration may contain a random residual amount from the washing procedure). The increased flux of small organic components might be due to membrane swelling of the PVA layer by the high water content in the washing solution and bark oil. However, the swelling impact was small and the concentrations in the permeate were smaller than for the less water selective, less crosslinked Pervap 4155 membranes (Table 2.9).

2.4 Conclusions

In this chapter, a series of lab-scale pervaporation experiments on the aqueous phase of a pyrolysis bark-oil were performed to determine the impact of temperature, membrane cross-linking, and feed flow rate. The results show that the temperature and feed flow rate were significant factors for the HHV, water content, and permeate yield models. All three investigated effects were significant for the viscosity model. None of the factors showed a significant influence on the TAN. The optimum values for Pervap 4155-30 and 80 membranes were as follows: a pervaporation temperature in the range of 80 °C, and a feed flow rate of 0.1 mL min^{-1}. The results demonstrate that it is possible to simultaneously dehydrate the aqueous phase of pyrolysis bark oil and separate

value-added chemicals (alcohols and acids). The main outcome of this work was to improve the unusable aqueous phase of a Canadian softwood bark pyrolysis oil into a useful low viscosity oil meeting the ASTM 7544-12 standard. The pervaporation process with the Pervap 4101 membrane lowered the water content from 70.2 to 21.42 mass% and consequently increased the heating value from < 10 MJ kg^{-1} to 16.07 MJ kg^{-1}. This novel upgrading of high water content, low-quality pyrolysis oil via pervaporation broadens the types of feedstock that can be used to produce pyrolysis oil for the ASTM 7544-12 standard. Simultaneously to oil enhancement, the permeate waste stream is potentially useful for several applications, since it contains chemicals, such as acetic and formic acid, methanol, hydroxyacetone, and furfural.

2.5 Acknowledgements

This work was supported by the Centre for Forest Science and Innovation (CFSI, NL Provincial Government), the Natural Sciences and Engineering Research Council of Canada (NSERC) (grant number 2017-04260) and Memorial University of Newfoundland (MUN). We would like to thank Dr. Celine Schneider who helped to identify the components by NMR.

2.6 References

[1] Vallejos ME, Kruyeniski J, Area MC. Second-generation bioethanol from industrial wood waste of South American species. Biofuel Res J 2017;15:654–67. doi:10.18331/BRJ2017.4.3.4.

[2] Sims REH, Mabee W, Saddler JN, Taylor M. An overview of second generation biofuel technologies. Bioresour Technol 2010;101:1570–80. doi:10.1016/j.biortech.2009.11.046.

[3] European Commission. Communication from the Commission: Energy for the Future: Renewable Sources of Energy–White Paper for a Community Strategy and Action Plan. Brüssel: 1997.

[4] International Energy Agency. World Energy Outlook 2015. Executive Summary. Int Energy Agency Books Online 2015:1–9. doi:10.1787/weo-2005-en.

[5] Bridgwater A V. Renewable fuels and chemicals by thermal processing of biomass. Chem Eng J 2003;91:87–102. doi:10.1016/S1385-8947(02)00142-0.

[6] Kersten S, Garcia-Perez M. Recent developments in fast pyrolysis of ligno-cellulosic materials. Curr Opin Biotechnol 2013;24:414–20. doi:10.1016/j.copbio.2013.04.003.

[7] Czernik S, Bridgwater A V. Overview of applications of biomass fast pyrolysis oil. Energy and Fuels 2004;18:590–8. doi:10.1021/ef034067u.

[8] Bridgwater A. Fast pyrolysis processes for biomass. Renew Sustain Energy Rev

2000;4:1–73. doi:10.1016/S1364-0321(99)00007-6.

[9] Oasmaa A, Fonts I, Pelaez-Samaniego MR, Garcia-Perez ME, Garcia-Perez M. Pyrolysis Oil Multiphase Behavior and Phase Stability: A Review. Energy and Fuels 2016;30:6179–200. doi:10.1021/acs.energyfuels.6b01287.

[10] Branca C, Giudicianni P, Di Blasi C. GC/MS characterization of liquids generated from low-temperature pyrolysis of wood. Ind Eng Chem Res 2003;42:3190–202. doi:10.1021/ie030066d.

[11] Zhang L, Liu R, Yin R, Mei Y. Upgrading of bio-oil from biomass fast pyrolysis in China: A review. Renew Sustain Energy Rev 2013;24:66–72. doi:10.1016/j.rser.2013.03.027.

[12] Stas M, Kubic D, Chudoba J, Posp M. Overview of Analytical Methods Used for Chemical Characterization of Pyrolysis Bio-oil. Energy & Fuels 2014;28:385–402. doi:10.1021/ef402047y.

[13] Elliott DC, Oasmaa A, Meier D, Preto F, Bridgwater A V. Results of the IEA Round Robin on Viscosity and Aging of Fast Pyrolysis Bio-oils : Long-Term Tests and Repeatability. Energy & Fuels 2012:7362–6. doi:10.1021/ef301607v.

[14] Rahman S, Helleur R, MacQuarrie S, Papari S, Hawboldt K. Upgrading and isolation of low molecular weight compounds from bark and softwood bio-oils through vacuum distillation. Sep Purif Technol 2018;194:123–9. doi:10.1016/j.seppur.2017.11.033.

[15] Ren X, Meng J, Chang J, Kelley SS, Jameel H, Park S. Effect of blending ratio of loblolly pine wood and bark on the properties of pyrolysis bio-oils. Fuel Process Technol 2017;167:43–9. doi:10.1016/j.fuproc.2017.06.025.

[16] Ren X, Gou J, Wang W, Li Q, Chang J, Li B. Optimization of Bark Fast Pyrolysis for the Production of Phenol-Rich Bio-oil. Bioresources 2013;8:6481–92.

[17] Ingram L, Mohan D, Bricka M, Steele P, Strobel D, Crocker D, et al. Pyrolysis of Wood and Bark in an Auger Reactor : Physical Properties and Chemical Analysis of the Produced Bio-oils 2008:614–25.

[18] Papari S, Hawboldt K, Helleur R. Production and Characterization of Pyrolysis Oil from Sawmill Residues in an Auger Reactor. Ind Eng Chem Res 2017;56:1920–5. doi:10.1021/acs.iecr.6b04405.

[19] Lehto J, Oasmaa A, Solantausta Y, Kytö M, Chiaramonti D. Fuel oil quality and combustion of fast pyrolysis bio-oils. 2013. doi:http://dx.doi.org/10.1016/j.apenergy.2013.11.040.

[20] Zhang Q, Chang J, Wang T, Xu Y. Review of biomass pyrolysis oil properties and upgrading research. Energy Convers Manag 2007;48:87–92. doi:10.1016/j.enconman.2006.05.010.

[21] Chaala A, Ba T, Garcia-perez M, Roy C. Colloidal Properties of Bio-oils Obtained by Vacuum Pyrolysis of Softwood Bark : Aging and Thermal Stability.

Energy & Fuels 2004;18:1535–42. doi:10.1021/ef030156v.

[22] Bridgwater A V. Review of fast pyrolysis of biomass and product upgrading. Biomass and Bioenergy 2012;38:68–94. doi:10.1016/j.biombioe.2011.01.048.

[23] Wei Y, Lei H, Wang L, Zhu L, Zhang X, Liu Y, et al. Liquid − Liquid Extraction of Biomass Pyrolysis Bio-oil. Energy & Fuels 2014;28:1207–12. doi:10.1021/ef402490s.

[24] Hu X, Mourant D, Gunawan R, Wu L, Wang Y, Lievens C, et al. RSC Advances Production of value-added chemicals from bio-oil via acid catalysis coupled with liquid – liquid extraction {. RSC Adv 2012;2:9366–70. doi:10.1039/c2ra21597g.

[25] Huber GW, Corma A. Synergies between Bio- and Oil Refineries for the Production of Fuels from Biomass. Angew Chemie Int Ed 2007;46:7184–201. doi:10.1002/anie.200604504.

[26] Jiang X, Ellis N. Upgrading Bio-oil through Emulsification with Biodiesel: Thermal Stability. Energy & Fuels 2010:2699–706. doi:10.1021/ef901517k.

[27] Krutof A, Hawboldt K. Blends of pyrolysis oil, petroleum, and other bio-based fuels: A review. Renew Sustain Energy Rev 2016;59:406–19. doi:10.1016/j.rser.2015.12.304.

[28] Capunitan JA, Capareda SC. Characterization and separation of corn stover bio-oil by fractional distillation. Fuel 2013;112:60–73. doi:10.1016/j.fuel.2013.04.079.

[29] Gorelova OM, Komarova LF. Fractional distillation of pyrolysis products of straight-run gasolines for production of feedstock for synthesis of petropolymeric resins. Chem Technol Fuels Oils 2015;51:17–25. doi:10.1007/s10553-015-0570-4.

[30] Pedersen TH, Jensen CU, Sandström L, Rosendahl LA. Full characterization of compounds obtained from fractional distillation and upgrading of a HTL biocrude. Appl Energy 2017;202:408–19. doi:10.1016/j.apenergy.2017.05.167.

[31] Nam H, Choi J, Capareda SC. Comparative study of vacuum and fractional distillation using pyrolytic microalgae (Nannochloropsis oculata) bio-oil. ALGAL Res 2016;17:87–96. doi:10.1016/j.algal.2016.04.020.

[32] Zhang X, Yang G, Jiang H, Liu W, Ding H. Mass production of chemicals from biomass-derived oil by directly atmospheric distillation coupled with co-pyrolysis. 2013. doi:10.1038/srep01120.

[33] Guo X, Wang S, Guo Z, Liu Q, Luo Z, Cen K. Pyrolysis characteristics of bio-oil fractions separated by molecular distillation. Appl Energy 2010;87:2892–8. doi:10.1016/j.apenergy.2009.10.004.

[34] Feng X, Huang R. Y. M. Liquid Separation by Membrane Pervaporation : A Review. Ind Eng Chem Res 1997;36:1048–66. doi:10.1021/ie960189g.

[35] Huang H, Ramaswamy S, Tschirner UW, Ramarao B V. A review of separation technologies in current and future biorefineries. Sep Purif Technol 2008;62:1–21.

doi:10.1016/j.seppur.2007.12.011.

[36] Boon J, Heuver H, Velterop F, Veen H Van, Groot A De. Pervaporation Membrane Module Design with Simulation. COMSOL Conf., 2016, p. 2–4.

[37] Abdallah H, El-Gendi A, El-Zanati E, Matsuura T. Pervaporation of methanol from methylacetate mixture using polyamide-6 membrane. Desalin Water Treat 2013;51:7807–14. doi:10.1080/19443994.2013.775077.

[38] Martin N, Chemtech S. Removal of Methanol by Pervaporation. Sulzer Tech Rev 2003:19–21.

[39] Teella A, Huber GW, Ford DM. Separation of acetic acid from the aqueous fraction of fast pyrolysis bio-oils using nanofiltration and reverse osmosis membranes. J Memb Sci 2011;378:495–502. doi:10.1016/j.memsci.2011.05.036.

[40] Barbary E, Abou-yousef H, Steele P. Increasing the efficiency of fast pyrolysis process through sugar yield maximization and separation from aqueous fraction bio-oil. Fuel Process Technol 2013;110:65–72. doi:10.1016/j.fuproc.2012.11.003.

[41] Basu P. Biomass Gasification, Pyrolysis and Torrefaction. 2nd ed. Elsevier; 2013.

[42] Marsman JH, Wildschut J, Mahfud F, Heeres HJ. Identification of components in fast pyrolysis oil and upgraded products by comprehensive two-dimensional gas chromatography and flame ionisation detection. J Chromatogr A 2007;1150:21–

7. doi:10.1016/j.chroma.2006.11.047.

[43] Jyoti G, Keshav A, Anandkumar J. Review on Pervaporation: Theory, Membrane Performance, and Application to Intensification of Esterification Reaction. J Eng (United States) 2015; doi:10.1155/2015/927068.

[44] Thiess H, Schmidt A, Strube J. Development of a scale-up tool for pervaporation processes. Membranes (Basel) 2018;8. doi:10.3390/membranes8010004.

[45] Langhagen U. Synthese und Charakterisierung von porengefüllten Kompositmembranen aus Kernspurmembranen. Universität Duisburg-Essen, 2008.

2.7 Appendix

Table 2.12: Analysis of variance table for all analyzed DOE responses.

Response	Source	Sum of squares	Mean square	df	F value	Prob > F	
HHV ($MJ\ kg^{-1}$)	Model	209.69	3	69.90	415.75	0.00002	significant
	T-Temperature	68.45	1	68.45	407.12	0.00004	
	U-Flow rate	90.99	1	90.99	541.22	0.00002	
	TU	50.25	1	50.25	298.90	0.00007	
	Residual	0.67	4	0.17			
	Cor Total	210.36	7				
TAN (mgNaOH/ g oil)	Model	41.10	3	10.27	2.29	0.261	not significant
	A-Membrane type	5.28	1	5.28	1.18	0.357	
	T-Temperature	4.65	1	4.65	1.04	0.383	
	U-Flow rate	29.26	1	29.26	6.53	0.084	
	Residual	13.44	4	4.48			
	Cor Total	54.54	7				
Dynamic viscosity (mPas)	Model	32.44	3	10.81	80.01	0.0005	significant
	A-Membrane type	1.56	1	1.56	11.53	0.0274	
	T-Temperature	7.86	1	7.86	58.17	0.0016	
	U-Flow rate	23.02	1	23.02	170.33	0.0002	
	Residual	0.54	4	0.14			
	Cor Total	32.98	7				
Water content (mass%)	Model	374.37	3	124.79	25.38	0.005	significant
	T-Temperature	91.76	1	91.76	18.66	0.012	
	U-Flow rate	254.37	1	254.37	51.73	0.002	
	TU	28.23	1	28.23	5.74	0.075	
	Residual	19.67	4	4.92			
	Cor Total	394.03	7				

Permeate yield (vol%)	Model	0.08	3	0.03	67.05	0.0007	significant
	T-Temperature	0.03	1	0.03	67.76	0.0012	
	U-Flow rate	0.05	1	0.05	117.70	0.0004	
	TU	0.01	1	0.01	15.69	0.0167	
	Residual	0.00	4	0.00			
	Cor Total	0.09	7				
Permeate yield (mass%)	Model	0.08	3	0.03	82.61	0.000	significant
	T-Temperature	0.03	1	0.03	95.69	0.001	
	U-Flow rate	0.04	1	0.04	134.55	0.000	
	TU	0.01	1	0.01	17.58	0.014	
	Residual	0.00	4	0.00			
	Cor Total	0.08	7				

Chapter 3

Kinetics and Stoichiometry of Methanol and Ethanol Oxidation in Multi-Anode Proton Exchange Membrane Cells

The principal author (Tobias M. Brueckner) contributed to all aspects of the project as the main researcher including: literature review, performing all of the experiments, collecting and analyzing the data, designing some of the experiments, presenting and discussing some of the data, writing partial first draft of section 3.2 and 3.31.

The corresponding author (Prof. Peter G. Pickup) was the principal investigator and developed the initial ideas for this research. He oversaw all aspects of the project, including supervision of the principal author (Tobias M. Brueckner), the design of experiments, data analysis; he produced and submitted the manuscript.

This chapter has been published as; Tobias M. Brueckner and Peter G. Pickup. Kinetics and Stoichiometry of Methanol and Ethanol Oxidation in Multi-Anode Proton Exchange Membrane Cells. Journal of The Electrochemical Society, 164 (12) F1172-F1178 (2017)

3 Kinetics and stoichiometry of methanol and ethanol oxidation in multi-anode proton exchange membrane cells

3.1 Introduction

Direct alcohol fuel cells are emerging technologies for power production from renewable fuels [1–5]. Direct methanol fuel cells (DMFC) with polymer electrolyte membranes (PEM) are already well developed and have achieved small scale commercialization [1,6,7]. Direct ethanol fuel cells (DEFC) are more attractive for sustainable energy production [8,9]. However, although there have been a number of demonstration projects [1,9], performances are not yet sufficient for commercialization [9]. Ethylene glycol [10,11] and glycerol [12] are also being studied for use in fuel cells, but present more complex problems. There are many challenges that are impeding the development of DAFC technology [1,6,9,13]. Relative to hydrogen PEMFCs, which already have relatively large markets, DAFCs suffer from much larger anode overpotentials, efficiency and power losses due to fuel crossover, and incomplete oxidation of the fuel. The primary requirement for commercialization of ethanol, ethylene glycol, and glycerol fuel cells is the development of anode catalysts that oxidize these fuels completely to carbon dioxide at low overpotentials [11,14–16]. Better anode catalysts are also required for widespread implementation of DMFC technology [17].

The importance of DAFC technology for a sustainable energy future based on clean and efficient use of renewable fuels has resulted in intensive studies of the

electrochemical oxidation of alcohols and the development of thousands of different anode catalysts. Generally, these have been evaluated at ambient temperatures in liquid electrolytes by cyclic voltammetry and in many cases by chronoamperometry. Products have been analyzed in some cases by techniques such as FTIR spectroscopy [15,18–20] and differential electrochemical mass spectroscopy (DEMS) [21–24]. However, the complexity and cost of testing in fuel cells have limited the implementation of new catalysts, and it is difficult to predict which will be most suitable for further development. A number of recent publications have highlighted the need for new experimental protocols and methods for comparing the activities of different catalysts in order to account for poisoning [25] and mass transport [26–28] effects, and differences in the average number of electrons transferred (n_{av}) due to differences in product distributions [26,27]. Accounting for differences in n_{av} is crucial for the oxidation of ethanol and higher alcohols because it plays a central role in determining the cell efficiency [29,30] and by-product emissions [8,31].

The purpose of the work described here was to explore the use of multi-anode PEM electrolysis cells for the evaluation and comparison of different catalysts for methanol and ethanol oxidation. The method employed is based on the crossover mode of operation of a PEM methanol electrolysis cell described by Ren et al. [32]. In this configuration (Figure 3.1), the fuel is delivered to the cathode and diffuses across the membrane to the anode, while the anode is flushed with N_2 to avoid interference from oxygen. Electrochemical reduction of hydronium ions at the cathode provides a stable reference potential (dynamic hydrogen electrode). The attraction of running the cell in

crossover mode is the well-defined mass-transport limitation provided by diffusion of the fuel through the membrane, which simplifies analysis of the electrochemical kinetics and can provide the stoichiometry (n_{av}) of the reaction. The goals of this work were to develop procedures for comparing the kinetics and stoichiometries of methanol and ethanol oxidation at different catalysts. This would be valuable for catalyst screening, developing steady state kinetic models for these reactions in fuel cells, and providing characteristic parameters that can be compared across research groups. Commercially available catalysts have been used to develop, validate, and benchmark the methodology.

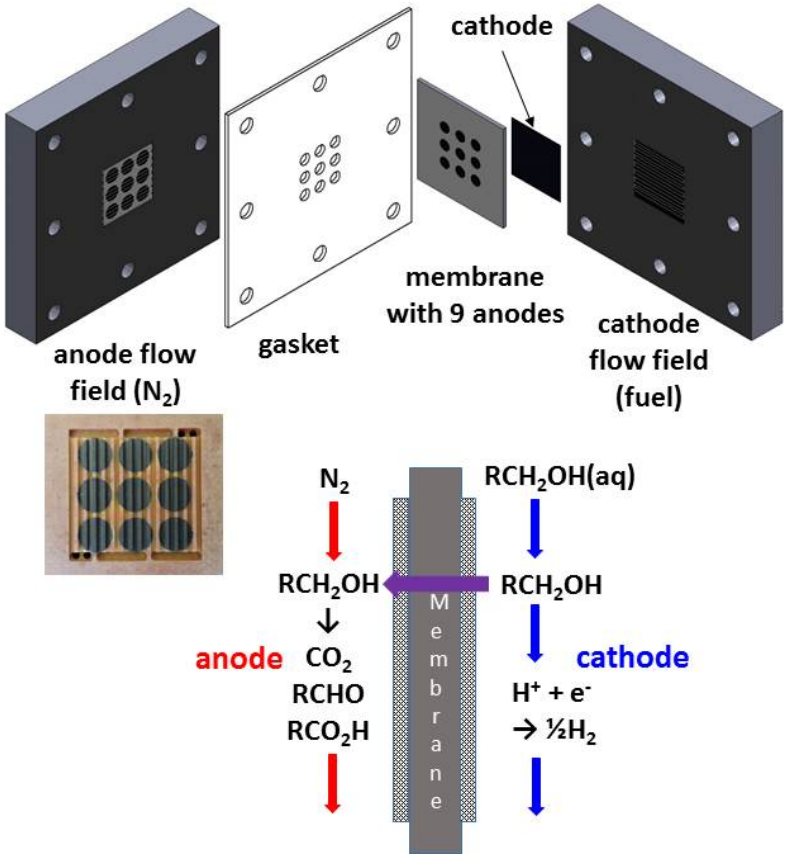

Figure 3.1: Schematic diagram of the nine anode cell (top) and crossover mode of operation (bottom). R=H or CH_3.

3.2 Experimental

3.2.1 Materials

The experiments were carried out with 99.8% methanol from ACP Chemical Inc., anhydrous ethanol (99.9%) from Commercial Alcohols Inc., and distilled and filtered deionized water. Nafion 115 and 117 membranes (DuPont) were cleaned at 80 °C in 3% H_2O_2 (aq) (EMD Millipore) and 1 M H_2SO_4 (aq) (Fisher Scientific), rinsed with deionized water, and stored in deionized water. Anodes consisted of the following

catalysts on Toray carbon paper: platinum black (Pt; 4.0 mg cm^{-2}); platinum ruthenium black (PtRu; 5.4 mg cm^{-2}); carbon supported Pt (Pt/C; various loadings; HiSPEC 13100, 70% Pt on a high surface area advanced carbon support; Alfa Aesar; Lot# M22A026); carbon supported PtRu (PtRu/C; 4.0 mg PtRu cm^{-2}; HiSPEC 12100, 50% Pt and 25% Ru on a high surface area advanced carbon support; Alfa Aesar; Lot# P17B047). The Pt black electrodes contained polytetrafluoroethylene as a binder, while the PtRu black anodes contained 15 mass% Nafion and the anodes prepared with supported catalysts contained 20% Nafion.

3.2.2 PEM cells

Cells with four (4E) or nine (9E) separate anodes, a single 5 cm^2 Pt black cathode and a Nafion proton conducting membrane electrolyte were used (Figure 3.1). Each cell was based on a commercial (ElectroChem Inc.) PEM fuel cell graphite plate flow field and hardware for the cathode side and a Lexan or Bakelite plate with a similar flow field for the anodes. The anode current collectors were graphite rods embedded in the Lexan or Bakelite plate. The anode catalyst area was 0.236 cm^2 (9E) or 0.385 cm^2 (4E) per anode. A cell with a single 5 cm^2 anode was used in one experiment to determine n_{av}, as previously described [33]. The applied potential was controlled with a MSTAT potentiostat from Arbin Instruments. The fuel was supplied by a NE-300 New Era Pump Systems syringe pump. A 60 W Watlow heat plate and a Digi Sense temperature controller were used to heat the cathode plate. The cell was preconditioned at 0.7 V for one hour at the operating temperature. Polarization curves were then obtained from 0.9 V to 0.0 V in 25 mV steps. Each potential was held for three minutes, with the

current recorded every second. The reported currents are averages over the final two minutes.

3.2.3 Operating mode

The cells were operated in crossover mode (Figure 3.1) with the liquid fuel solution pumped through the cathode flow field while the anode flow field was purged with 10 mL min^{-1} nitrogen (N_2) gas to prevent interference from oxygen. In this mode, the cathode approximates a dynamic hydrogen electrode, since the cathode reaction is $H^+ + e^- \rightarrow 0.5H_2$ [34]. Furthermore, the steady fuel flux through the membrane to the anode side simplifies modeling of the kinetic and mass transport processes. The cell was operated with 0.1 M and 1 M aqueous solutions of ethanol and methanol (in water with no electrolyte or buffer) at a flow rate of 0.5 mL min^{-1} and at temperatures of 50 and 80 °C.

Polarization curves for 1 M methanol and ethanol were corrected for the uncompensated resistance measured by impedance spectroscopy with a EG&G Model 273A potentiostat/galvanostat and EG&G Model 5210 Lock-in Amplifier operated with Power-Suite software. Since resistances did not vary significantly between electrodes, the same average values were applied to all electrodes in each cell. They were 0.44 Ω for the 9E cell and 0.61 Ω for the 4E cell at 50 °C.

3.3 Results and discussion

3.3.1 Methanol oxidation

Initially, a cell was operated with nine Pt black anodes in order to determine the reproducibility between electrodes and develop suitable kinetic analysis. Steady-state polarization curves for oxidation of 1 M methanol in crossover mode at nine equivalent electrodes are shown in Figure 3.2.

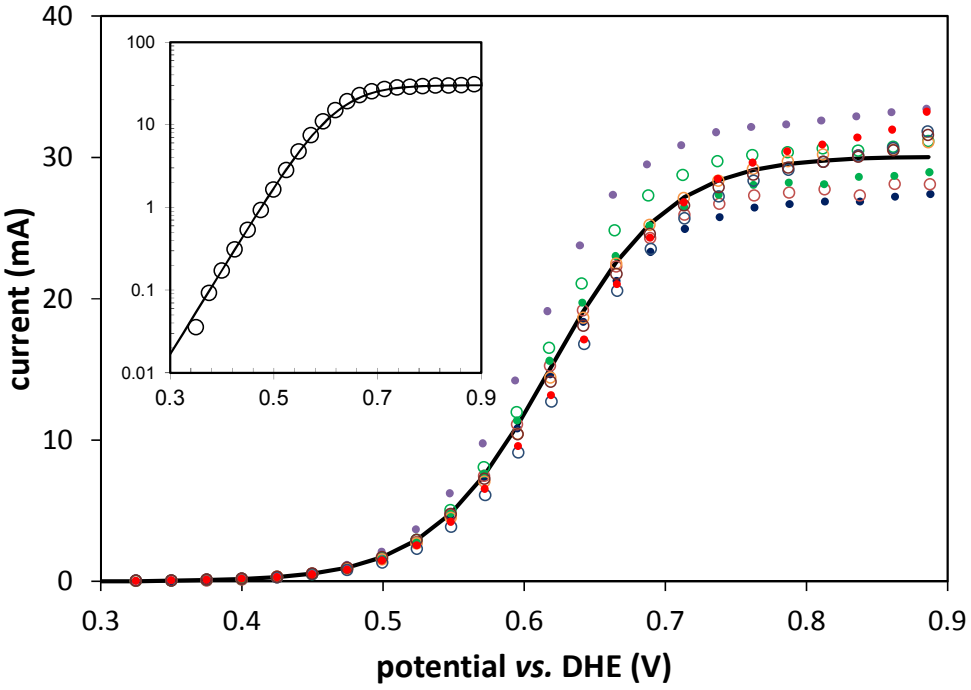

Figure 3.2: Polarization curves for the oxidation of 1.0 M methanol at 50 °C at nine equivalent Pt black anodes. The solid line is the best fit of the average current at each potential to Eq. (3.3). The inset shows a Tafel plot (log(current) vs. E) for the average current and the best fit.

The current rose to the same limiting current density (j_{lim}) at each electrode, within a standard deviation of ±6.6%, illustrating the well-defined diffusion of methanol

through the cathode and membrane to the anode. If the small effects of electro-osmotic drag [35] are neglected, j_{lim} is given by Eq. (3.1),

$$J_{lim} = n_{av} FmC \qquad \text{Eq. (3.1)}$$

Where m is the mass transport coefficient, F is the Faraday constant (96500 C mol^{-1}), and C is the concentration of methanol. Since m depends on the thicknesses of both the cathode and the membrane, and diffusion characteristics of methanol within both of these layers, an accurate value is not available. However, it has been shown previously that methanol is completely oxidized to CO_2 (n_{av} = 6) under these conditions [36], and so Eq. (3.1) can be used to determine m from j_{lim}. Average values of j_{lim} and m are listed in Table 3.1. The j_{lim} of 128 mA cm^{-2} is similar to the value of 91 mA cm^{-2} reported by Ren et al. [35] for similar conditions.

Although detailed models are available for analysis of the polarization curves in Figure 3.2 [37–39], a simpler, more generic model based on first-order kinetics is used here. Since the equilibrium potential was not controlled or known, the kinetic current (i_k) is written in terms of the standard rate constant (k^0) according to Eq. (3.2).

$$i_k = n_{av} FAk^0 C \cdot \exp[\alpha F \frac{E - E^0}{RT}] \qquad \text{Eq. (3.2)}$$

Where A is the electrode area, α is the electron transfer coefficient, and E^0 is the standard potential of 0.016 V for methanol oxidation. Assuming that the rate of the reverse reaction is negligible, the steady-state current density (j) as a function of potential is given by Eq. (3.3).

$$i_k = n_{av}FAk^0C\ (1 - \frac{j}{j_{lim}}) \cdot \exp[\alpha F \frac{E - E^0}{RT}] \qquad \text{Eq. (3.3)}$$

Table 3.1: Parameters from least squares fit of Eq. (3.3) to polarization curves at 50 °C for the oxidation of 1.0 M methanol at various electrodes.

Catalyst (cell)	Loading (mg cm^{-2})	j_{lim} (mA cm^{-2})	m x 10^3 (cm s^{-1})	Tafel slope (mV)	α	k^0 x 10^{10} (cm s^{-1})
Pt black (9E)	4.0	128±6	0.22±0.01	98±6	0.66±0.04	1.4±0.8
Pt black (4E)	4.0	158±8	0.27±0.01	81±5	0.79±0.05	0.27±0.26
PtRu black (4E)	5.47	145±1	0.251±0.002	96±11	0.67±0.08	150±100
70%Pt/C (9E)	1.0-3.25	110±15	0.19±0.03	105±9	0.61±0.06	6.5±3.2

Eq. (3.3) is a generic equation for steady-state mass transport, and is used as the Koutecky-Levich equation for extraction of kinetic data from rotating disk voltammetry [40]. Its validity for steady-state oxidation of methanol and ethanol at rotating electrodes coated with Pt and PtRu fuel cell catalysts has been demonstrated [26,27]. The best fit of Eq. (3.3) to the data in Figure 3.2 can be found by using the SOLVER function in an Excel spreadsheet to minimize the absolute deviations (least squares), or similar procedure, and is shown in Figure 3.2 for the average currents from the nine anodes. The inset in Figure 3.2 shows Tafel plots for the average currents and the best fit. Average parameters and standard deviations from the best fits to the nine data sets are shown in the first row of Table 3.1.

Polarization curves for the oxidation of 1 M methanol were also measured in a cell with four anodes (Figure 3.3), which were larger than those in the 9E cell. Two Pt

black and two PtRu black anodes were used. It can be seen that both the onset potential and half-wave potential were much lower at the PtRu black electrodes. However, the limiting currents were similar for Pt and PtRu. This provides compelling evidence that the current plateaus reached in both cases represent the rate of mass transport to the anodes, and that n_{av} = 6. Otherwise, the limiting currents would depend on the electrode material and potential.

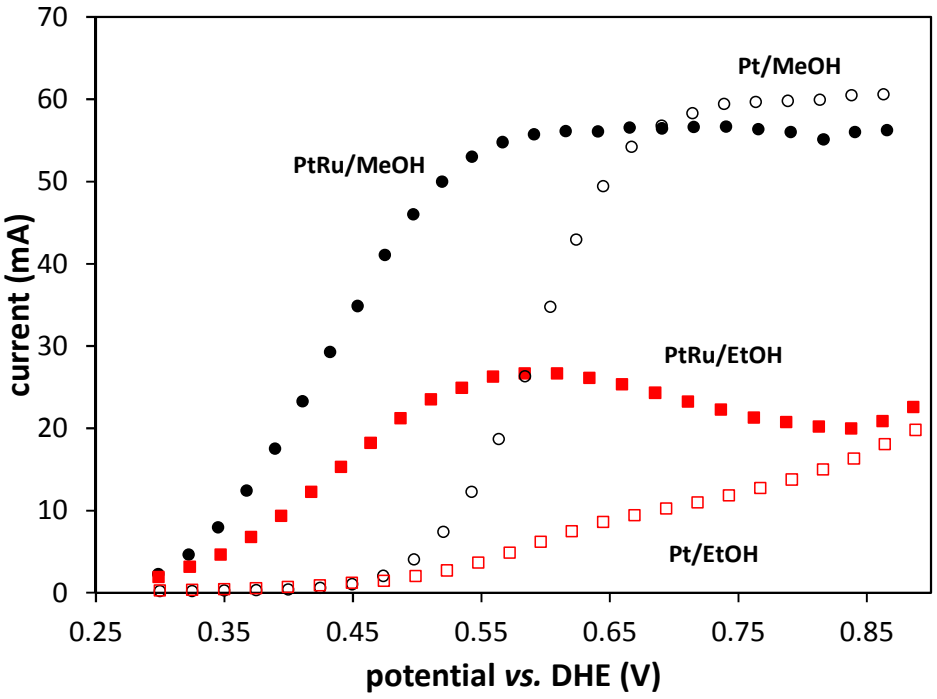

Figure 3.3: Comparison of polarization curves for 1.0 M methanol (●,○) and 1.0 M ethanol (■,□) solutions at Pt black (○,□) and Pt/Ru black (●,■) anodes in a 4E cell at 50 °C.

Kinetic and mass transport parameters obtained by fitting the methanol oxidation data in Figure 3.3 to Eq. (3.3) are presented in Table 3.1. For Pt black, the 4E cell gave somewhat higher mass transport limited current densities than the 9E cell, while the

Tafel slope and k^0 were lower. These differences are all statistically significant based on *t*-tests at 95% confidence. The difference in j_{lim} can be attributed to a difference in the compression of the membrane electrode assembly (MEA) [41], and/or a difference in the permeability of the cathode. Although the cells were both assembled with a torque of 2 Nm, differences in the gasket and MEA thickness can lead to differences in the compression of the cathode. The differences in the Tafel slopes and k^0 obtained for Pt black between the two cells are related, since a higher slope leads to a higher extrapolated current for determination of k^0. The differences between the two cells can be attributed to small differences in the background current at low overpotentials, and in establishing the zero faradaic current point [42]. The background current was not reproducible, and so could not be accurately corrected. Although variations in the background current should lead to random errors, and these can be seen to be very large for k^0 in Table 3.1, there does appear to be some bias. This illustrates the difficulties in obtaining meaningful kinetic parameters for fuel cell catalysts and the importance of testing multiple electrodes.

When the parameters for Pt and PtRu black in the 4E cell are compared (Table 3.1), only the difference in k^0 is statistically significant. The much earlier onset of methanol oxidation at the PtRu electrodes can therefore be attributed to the ca. 200 fold increase in k^0 relative to Pt black (based on the average k^0 for Pt black in the 4E and 9E cells). This is explained by the well-known bifunctional mechanism [43] in which the adsorbed CO intermediate in methanol oxidation is oxidized to CO_2 at sites adjacent to surface Ru-OH sites. These are formed at lower potentials than Pt-OH sites.

Polarization curves for the oxidation of 1 M methanol were also obtained for a series of anodes prepared with various loadings of a commercial carbon supported Pt catalyst (HiSPEC 13100, 70% Pt). Two anodes with each nominal loading were used in the 9E cell, with a Pt black electrode as a control. Figure 3.4 shows m and k^0 values obtained by fitting of Eq. (3.3) to each data set, as a function the nominal Pt loading. Although there is significant scatter in the data due to difficulty in controlling the loading and compression of each electrode, there was not a significant dependence of either parameter, or the Tafel slope (not shown), on the Pt loading. Consequently, average parameters for the 8 Pt/C anodes are reported in Table 3.1. It can be seen that the uncertainties were similar to those obtained for Pt and PtRu electrodes with constant loadings, again indicating a lack of loading dependence for the Pt/C anodes. Comparison of the data for Pt/C and Pt black in the 9E cell (Table 3.1) shows that the Tafel slopes were not significantly different, while k^0 was significantly higher for the Pt/C anodes (based on a t-test at 95% confidence). Clearly Pt/C was the better catalyst for methanol oxidation, even at a much lower Pt loading (1 mg cm^{-2} for Pt/C vs. 4 mg cm^{-2} for Pt black). The m-values obtained for the Pt/C anodes were lower and more variable than for the Pt black anodes. This was most likely due to uneven and variable compression of the cathode.

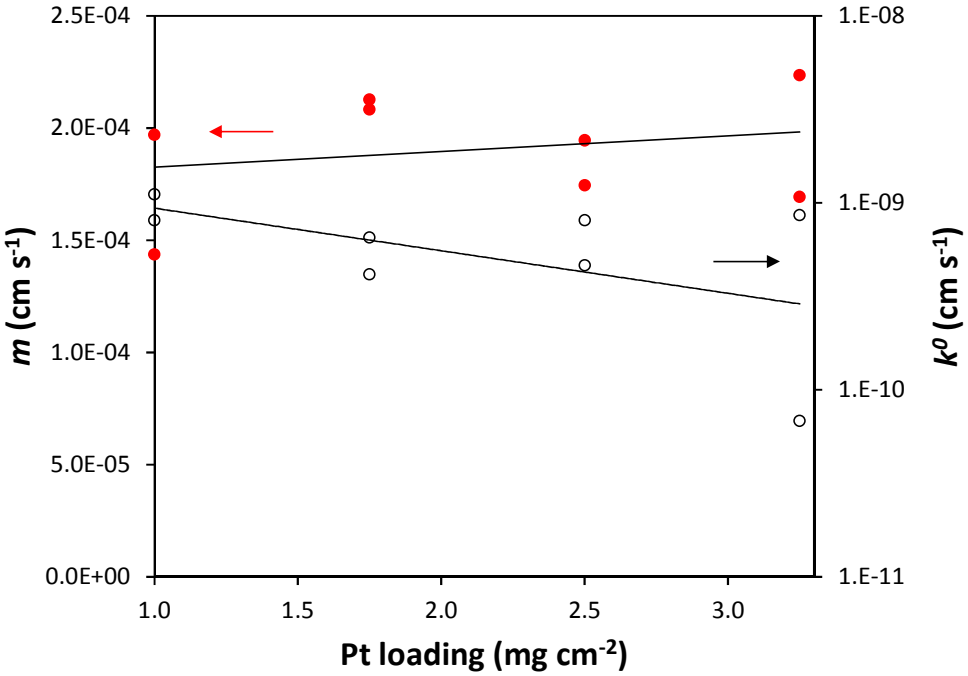

Figure 3.4: Mass transport coefficients (m,●) and standard rate constants (k^0,○), from Eq. (3.3), as a function of nominal catalyst loading for the oxidation of 1.0 M methanol at HiSPEC 13100 70% Pt/C electrodes in a 9E cell. Two electrodes with each nominal loading were used.

Overall, the Tafel slopes reported in Table 3.1 do not show any clear differences between the three catalyst types. The average slope of 95 mV is much lower than the value of 166 mV at 300 K calculated from first principles for methanol oxidation at Pt(111), with the first C-H bond breaking as the rate determining step [44]. Experimental Tafel slopes reported in the literature for a variety of electrode types and conditions cover a wide range that encompasses these two values [45]. Literature Tafel slopes for methanol oxidation at Pt black, PtRu black, Pt/C and PtRu/C range from 80–

195 mV [26,46–53], and do not show significant correlation with the temperature (22-80 °C), catalyst, or electrolyte ($HClO_4$, H_2SO_4, or Nafion [49–51]). The slopes reported in Table 3.1 are at the low end of this range, and this is most likely due to the correction for resistance and mass transport effects employed in the analysis.

Since Tafel slopes do not currently appear to be useful for discriminating between catalysts, k^0 is a crucial parameter. The data in Table 3.1 show that it qualitatively reflects the differences in activities of the Pt black, PtRu black, and 70% Pt/C catalysts. However, extrapolation of the kinetic current to E^0 can lead to large uncertainties and inaccuracies. Furthermore, there are only a few literature reports that provide data for comparison. Wang et al. reported an exchange current of 9.4 mA cm^{-2} for the oxidation of 1 M methanol at PtRu in a DMFC at 80 °C [54]. This corresponds to $k^0 \sim 5 \times 10^{-6}$ cm s^{-1} at 50 °C [54], which is much larger than the value of $(1.5 \pm 1.0) \times 10^{-8}$ cm s^{-1} for PtRu in Table 3.1. This can be attributed mainly to the much higher Tafel slope of 293 mV obtained for the DMFC [54]. Fitting parameters to a model for a DMFC provided $k^0 \sim 3 \times 10^{-5}$ cm s^{-1} at 50 °C for PtRu/C for an assumed Tafel slope of 118 mV [37]. However, this was based on fitting of polarization curves with only one data point in the Tafel region.

This brief survey of kinetic parameters for methanol oxidation highlights the need for a standardized methodology to provide characteristic parameters that can be compared across research groups. Steady-state measurements in a PEM electrolysis cell in crossover mode appear to be well suited for comparing the activities of DAFC

catalysts. This conjecture was explored further with ethanol as the fuel, which brings the added complication of variations in n_{av} with potential.

3.3.2 Ethanol oxidation

A comparison of ethanol polarization curves with methanol polarization curves is shown in Figure 3.3. It can be seen that the currents were much lower for ethanol at all potentials, with the difference more pronounced for Pt than PtRu. Inspection of the data in Figure 3.3 reveals that the half-wave potentials are similar for ethanol and methanol at ca. 0.44 V for PtRu and 0.61 V for Pt, indicating that the kinetics (i_k), are similar. Consequently, the main differences in the currents are due to differences in the mass transport coefficient (m) and stoichiometry (n_{av}). These are most obvious and illuminating in the mass transport region, above ca. 0.6 V for PtRu and ca. 0.7 V for Pt. Whereas methanol oxidation produced an almost constant current in this region, that was essentially the same for PtRu and Pt, the currents for ethanol oxidation varied significantly with potential, and were very different for PtRu vs. Pt. Since m cannot vary with potential or the electrode material, the variations in the ethanol oxidation current in the mass transport region indicate that n_{av} depends on the potential and the electrode material. This is consistent with numerous studies of product distributions for ethanol oxidation [15,16].

Quantitative analysis of the ethanol polarization curves in Figure 3.3 can be achieved by application of a Tafel analysis Eq. (3.2) at low potentials, where j is less than ca. 10% of j_{lim}, followed by application of Eq. (3.3) to determine how n_{av} varies with potential in the high potential region. Figure 3.5 shows Tafel plots of the low

potential data from Figure 3.3. Average values of $k^0 n_{av}$, the Tafel slope, and α for the two Pt and two PtRu electrodes are reported in Table 3.2. k^0 cannot be accurately determined here because n_{av} is unknown for the Tafel region.

Table 3.2: Parameters from Tafel analysis of polarization curves for the oxidation of 1.0 M ethanol at Pt black and PtRu black electrodes.

Catalyst (cell)	Loading (mg cm^{-2})	Tafel slope (mV decade^{-1})	α	$k^0 n_{av}$ (cm s^{-1})
Pt black (4E)	4.0	154±11	0.42±0.03	(9.5±7.1) x 10^{-8}
PtRu black (4E)	5.47	116±5	0.55±0.03	(3.6±0.9) x 10^{-7}

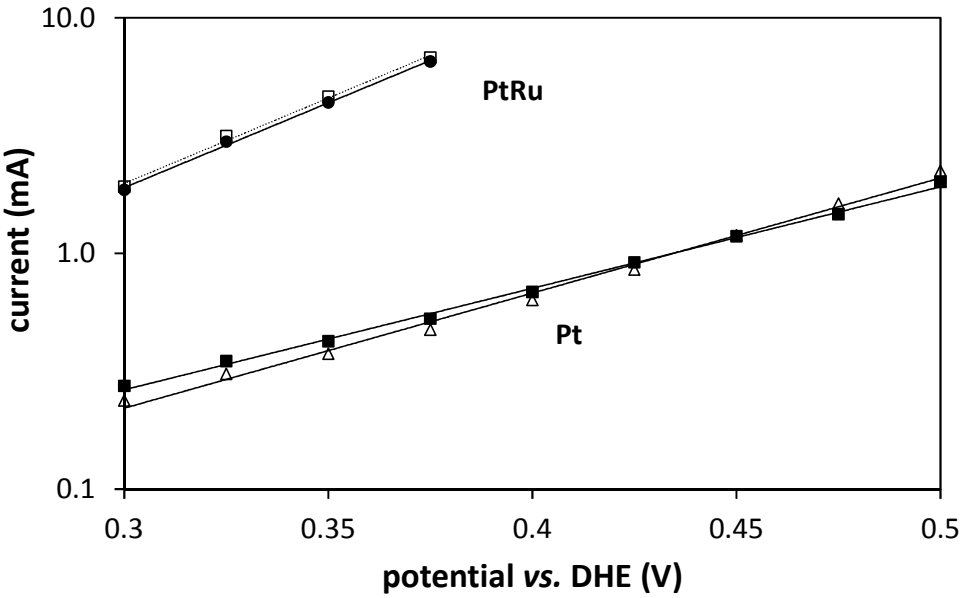

Figure 3.5: Tafel plots for the low potential data in Figure 3.3 for oxidation of 1.0 M ethanol at Pt (■,Δ) and PtRu black (●,□) anodes.

The $k^0 n_{av}$ and α values from the Tafel plots were subsequently used in Eq. (3.3) to calculate j_{lim} as a function of potential. Results are shown in Figure 3.6 for one of the

PtRu electrodes, where the measured current is compared with the calculated kinetic and mass transport limited currents. The variation of the calculated j_{lim} with potential is most likely due to changes in n_{av} although it could be an artifact caused by extreme deviation from the Tafel relationship at high potentials. Deviations from the low potential Tafel behaviour have generally been observed for ethanol oxidation, and it was shown in a rotating disc study that the mass transport limit could not be reached due to oxide formation on the Pt surface [27]. However, the very thick catalyst layers used here together with restriction of mass transport by the membrane and cathode have clearly allowed the mass transport limit to be reached for methanol oxidation in Figure 3.2 and Figure 3.3, with no effect of oxide formation over the potential range employed. It therefore does not appear to be reasonable to attribute the decreasing j_{lim} seen in Figure 3.6 to changes in the kinetic current.

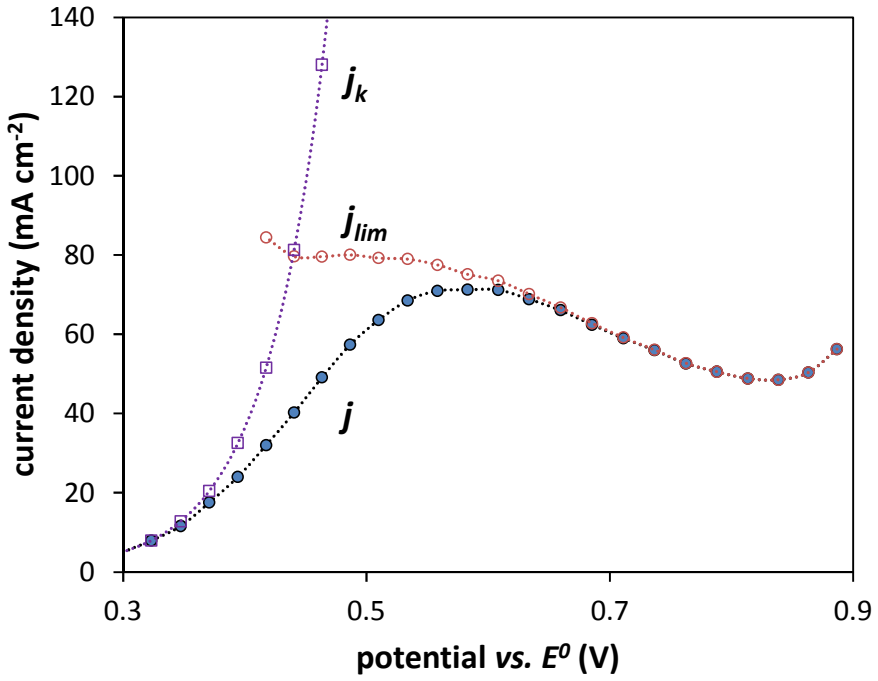

Figure 3.6: Experimental current densities (j) and calculated kinetic (j_k) and mass transport limited (j_{lim}) current densities for oxidation of 1.0 M ethanol at a PtRu black anode in a 4E cell at 50 °C.

In order to explore this interpretation further, and to quantify n_{av}, the flow rate (u) dependence of the ethanol oxidation current (i) was measured in a normal 5 cm^2 cell. This allows n_{av} to be determined with reasonable accuracy [55] by use of Eq. (3.4) [33]:

$$i = n_{av} F C_{in} u \left(1 - \exp\left(-\frac{I_{lim}}{n_{av} F C_{in} u}\right)\right) \qquad \text{Eq. (3.4)}$$

Where C_{in} is the concentration of ethanol entering the cell and j_{lim} is the current at high flow rates. The polarization curve and n_{av} vs. potential are shown in Figure 3.7. It can be seen that the polarization curve shows a similar decrease in the current at potentials above 0.55 V to that seen in Figure 3.3 for ethanol oxidation at PtRu, and that this can be attributed to the parallel decrease in n_{av} observed in Figure 3.7. The n_{av} values in

Figure 3.7 are close to the n_{av} of 3 previously determined for a Pt black electrode at 0.7 V under these conditions [33]. They indicate that the ethanol was oxidized primarily to acetaldehyde (n = 2) and acetic acid (n = 4), with little formation of CO_2 (n = 12), which is consistent with product yields at ≤ 50 °C measured by DEMS [56–58].

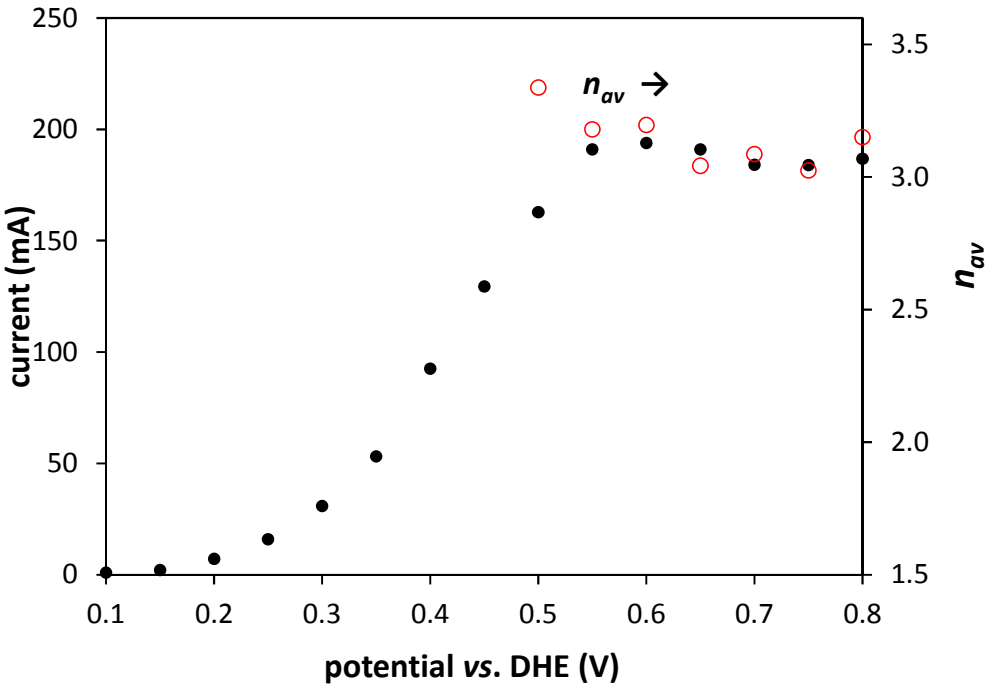

Figure 3.7: Polarization curve (•) and n_{av} (o) vs. potential for the oxidation of 1.0 M ethanol at a PtRu black anode in a 5 cm² cell at 50 °C.

The mass transport coefficient for ethanol in the 4E cell can be estimated from Eq. (3.1) by using the j_{lim} values in Figure 3.6 with the n_{av} values in Figure 3.7 at the same potentials. An average m of (2.0 ± 0.2) x 10^{-4} cm s^{-1} was obtained, which is somewhat lower than the value of (2.7 ± 0.1) x 10^{-4} cm s^{-1} obtained for methanol under the same conditions (Table 3.1). This is as expected based on the larger size of the

ethanol molecule. This value of m was then used with Eq. (3.1) and Eq. (3.3) to calculate n_{av} vs. potential from the data in Figure 3.3, for both the PtRu and Pt anodes. The results are shown in Figure 3.8. The values for PtRu are similar to those in Figure 3.7 for the 5 cm^2 cell because they were used for determining m. The Pt black anodes gave similar n_{av} values at high and low potentials, but significantly lower values at intermediate potentials. The higher n_{av} values at low potentials are consistent with the potential dependence of CO_2 formation reported in a DEMS study [57]. However, the very low values of n_{av} for the Pt anodes at intermediate potentials in Figure 3.8 (0.6 to 0.85 V) indicate that they are not accurate, and that these anodes were not operating under mass transport controlled conditions. The values below $n_{av} = 2$ are not possible because ethanol cannot be oxidized to a stable product by less than two electrons. Clearly, i_k deviated from the low potential Tafel relationship at potentials above 0.6 V (or lower) and accurate values of j_{lim} and n_{av} were not obtained from Eq. (3.3).

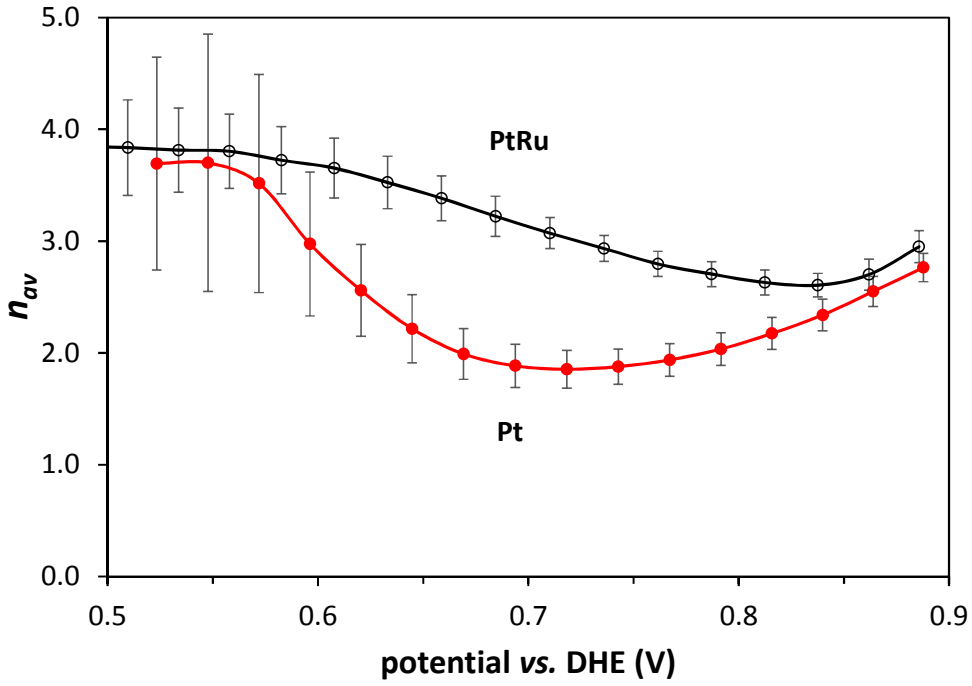

Figure 3.8: Apparent n_{av} from Eq. (3.1), vs. potential for the oxidation of 1.0 M ethanol at a Pt black (●) and PtRu black (○) anodes in a 4E cell at 50 °C. The error bars represent the standard deviations obtained from four measurements (two measurements on consecutive of each type).

3.3.3 0.1 M methanol and ethanol

Previous work in the 5 cm^2 cell has shown that the mass transport limit can be reached at Pt electrodes when 0.1 M ethanol is employed, and that n_{av} is increased by decreasing the ethanol concentration and increasing the temperature [33,55]. Consequently, further experiments were conducted with 0.1 M methanol (for calibration) and 0.1 M ethanol at 80 °C. In addition, a thicker membrane (Nafion 117 instead of Nafion 115) was employed to decrease the mass transport current relative to the kinetic current. A 9E cell was used to simultaneously collect polarization curves for three electrodes each of three

different types of anode: Pt/C, PtRu/C, and a 50:50 mixture by mass of these two catalysts (Figure 3.9).

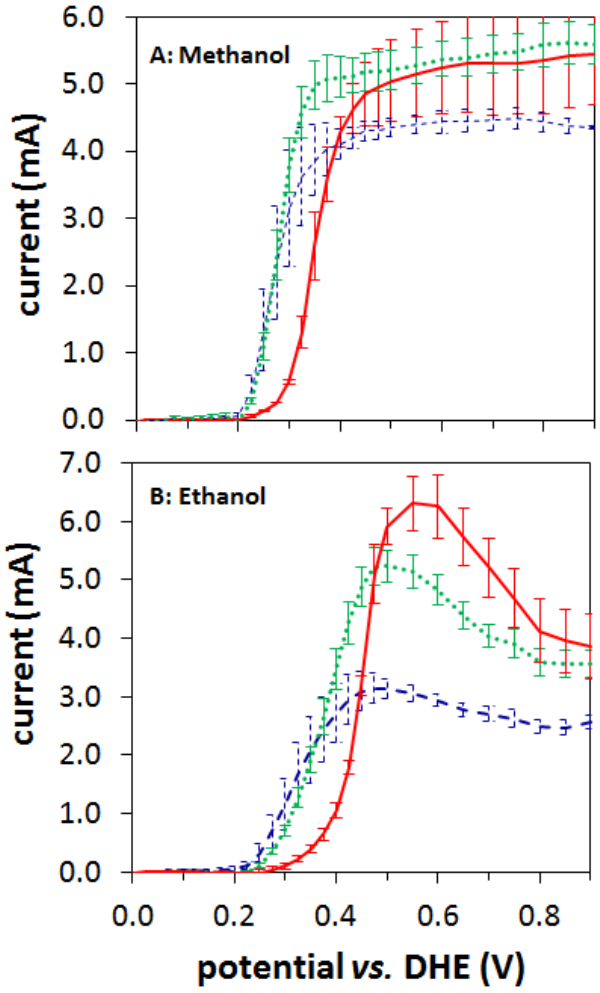

Figure 3.9: Polarization curves in a 9E cell for the oxidation of 0.1 M methanol (A) and 0.1 M ethanol (B) at 80 °C at three 70% Pt/C anodes (—), three 75% PtRu/C anodes (- - -) and three mixed Pt/C and PtRu/C anodes (····) (4.0 mg cm^{-2} of metal in all cases). Error bars are standard deviations for each set of 3 electrodes.

The data for methanol in Figure 3.9 shows a significant difference in the half-wave potential between the Pt/C and PtRu/C anodes, while the mixed anode shows

the same half-wave potential as PtRu/C. Although, the limiting current for PtRu/C appears to be lower than for the other two types of anode, the difference is only statistically significant (95% confidence *t*-test) relative to the mixed anodes. The low limiting current for PtRu/C implies that methanol oxidation did not proceed to completion at these anodes (i.e. $n_{av} < 6$). Consequently, the PtRu/C results were not used in the estimation of *m* for methanol for these conditions. Averaging the limiting currents for the Pt and mixed anodes gave $m = (4.0 \pm 0.4) \times 10^{-4}$ cm s^{-1} for the Nafion 117 membrane at 80 °C. If it is assumed that the ratio of *m* for methanol and ethanol is the same as for Nafion 115 at 50 °C, then *m* for ethanol with Nafion 117 at 80 °C can be estimated to be ca. 3.0×10^{-4} cm s^{-1}. This can then be used to estimate n_{av} vs. potential for ethanol oxidation from the data in Figure 3.9 B.

From a visual comparison of the data sets in Figure 3.9, it can be seen that the half-wave potentials showed a similar trend for methanol and ethanol, while the limiting current region showed a much stronger dependence on the catalyst for ethanol than for methanol. This indicates that n_{av} was influenced more by the catalyst, with Pt producing up to twice as many electrons as PtRu. This is in agreement with measurements of product distributions and ethanol consumption for these two catalysts under similar conditions in a 5 cm^2 cell [59]. It can also be seen from the data in Figure 3.9 B that the mixture of the two catalysts gave a similar half-wave potential to PtRu/C, while n_{av} values were closer to those for Pt/C. There was clearly a significant synergistic effect between the two catalysts, and this is being investigated in further work.

Quantitative analysis of the polarization curves in Figure 3.9 B to determine the potential dependent n_{av} values was conducted by fitting to Eq. (3.3), as described for Figure 3.6. Figure 3.10 shows the n_{av} vs. potential plots that were obtained for each type of anode. For comparison, n_{av} values obtained by measuring the amount of ethanol consumed in a 5 cm^2 cell are included [59]. These were measured with 0.1 M ethanol supplied to the anode and N_2 at the cathode and verified by simultaneously measuring the product distribution [59]. It can be seen that there is a remarkable agreement between the two data sets in Figure 3.10 for the PtRu/C anodes. However, the voltammograms in Figure 3.9 for the Pt/C anodes gave n_{av} values that were significantly higher than those from Ref. [59] at most potentials. This may have been due to the difference in the way in which the cells were operated, since the crossover mode employed here has been shown to produce higher yields of CO_2 [36] and higher n_{av} values [33] under the conditions employed here. For example, $n_{av} = 9.4 \pm 0.2$ was obtained in a crossover experiment at 0.7 V for 0.1 M ethanol at 80 °C [33]. This is higher than both values at 0.7 V for Pt/C in Figure 3.10.

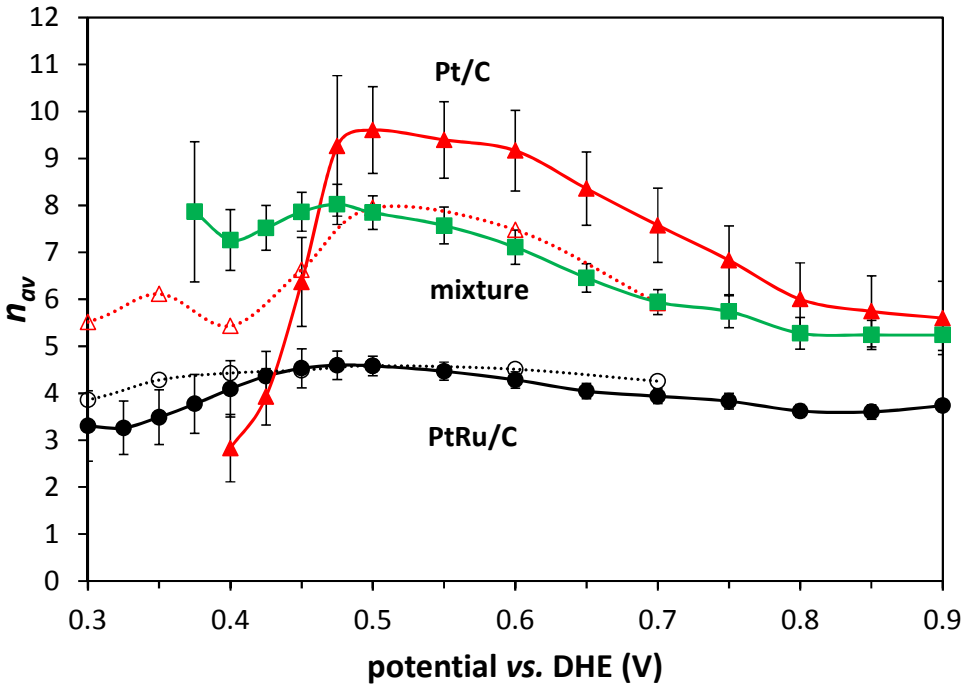

Figure 3.10: Apparent n_{av}, from Eq. (3.1), vs. potential for the oxidation of 0.1 M ethanol at a Pt/C (▲), PtRu/C (●), and Pt/C + PtRu/C (■) anodes in a 9E cell at 80 °C. The error bars represent the standard deviations obtained from measurements on three different electrodes of each type. The metal loading was 4.0 mg cm^{-2} for all anodes. Values for Pt/C (Δ) and PtRu/C(○) from Ref. [59] are included for comparison.

The data in Figure 3.10 show that polarization curves obtained in crossover mode can provide useful estimates of stoichiometries for the oxidation of ethanol if the mass transport limit can be reached. The data for PtRu/C indicates that a reasonable mass transport coefficient was estimated. This methodology, applied to a multi-anode cell, will allow rapid screening of new catalysts simultaneously for activity (current and power density) and faradaic (fuel) efficiency.

Both methanol and ethanol produce poisoning intermediates on the electrode surface. The most serious poisoning species is CO, which can be oxidized more easily

at PtRu than Pt, which largely explains the lower half-wave potentials for both methanol and ethanol at the PtRu anodes. One of the attractions of the methodology reported here (relative to cyclic voltammetry or chronoamperometry) is the use of steady-state conditions, where the coverage of poisoning intermediates reaches a steady-state.

3.4 Conclusions

Operation of fuel cell hardware in crossover mode can produce steady-state polarization curves with mass transport regions that provide stoichiometric information in addition to the kinetic data obtained at low potentials. Polarization curves for methanol oxidation were accurately modelled by a normal first-order electrochemical rate expression coupled with steady-state mass transport Eq. (3.3). However, the limiting current can vary from the value expected for complete oxidation to CO_2 (n = 6). Polarization curves for ethanol oxidation can also be modelled with a first order electrochemical rate expression, although the mass transport limited current varies with potential due to variation in the product distribution with potential [59], which causes the number of electrons transferred to vary. In the mass transport region, the current is proportional to n_{av} Eq. (3.1), while n_{av} can be estimated from Eq. (3.3) in the mixed kinetic-mass transport region. The accuracy of this methodology is good for ethanol oxidation at PtRu catalysts, but further assessment is required for Pt catalysts. Nevertheless, steady-state polarization curves obtained in crossover mode provide excellent data for the preliminary evaluation of catalysts for methanol and ethanol oxidation in PEMFC hardware, and kinetic data that is well suited for understanding the kinetics of these reactions in fuel cells.

3.5 Acknowledgements

This work was supported by the Natural Sciences and Engineering Research Council of Canada (grant #1957-2012) and Memorial University.

3.6 References

[1] Corti HR, Gonzalez ER. Direct Alcohol Fuel Cells. 2014.

[2] Braunchweig B, Hibbitts D, Neurock M, Wieckowski A. Electrocatalysis : A direct alcohol fuel cell and surface science perspective. Catal Today 2013;202:197–209. doi:10.1016/j.cattod.2012.08.013.

[3] Antolini E, Gonzalez ER. Alkaline direct alcohol fuel cells. J Power Sources 2010;195:3431–50. doi:10.1016/j.jpowsour.2009.11.145.

[4] Lerhun Â, Delime F, Lamy C, Lima A, Coutanceau C, Le J. Recent advances in the development of direct alcohol fuel cells (DAFC). J Power Sources 2002;105:283–96.

[5] Yu EH, Krewer U, Scott K. Principles and Materials Aspects of Direct Alkaline Alcohol. Energies 2010;3:1499–528. doi:10.3390/en3081499.

[6] Mehmood A, Scibioh MA, Prabhuram J, An M, Yong H. A review on durability issues and restoration techniques in long-term operations of direct methanol fuel cells. J Power Sources 2015;297:224–41. doi:10.1016/j.jpowsour.2015.07.094.

[7] Mallick RK, Thombre SB, Shrivastava NK. Vapor feed direct methanol fuel cells (DMFCs): A review. Renew Sustain Energy Rev 2016;56:51–74. doi:10.1016/j.rser.2015.11.039.

[8] Ramachandran S, Stimming U. Environmental Science Well to wheel analysis of low carbon alternatives for road traffic. Energy Environ Sci 2015;8:3313–24.

doi:10.1039/C5EE01512J.

[9] Badwal SPS, Giddey S, Kulkarni A, Goel J, Basu S. Direct ethanol fuel cells for transport and stationary applications – A comprehensive review. Appl Energy 2015;145:80–103. doi:10.1016/j.apenergy.2015.02.002.

[10] Serov A, Kwak C. Applied Catalysis B : Environmental Recent achievements in direct ethylene glycol fuel cells (DEGFC). "Applied Catal B, Environ 2010;97:1–12. doi:10.1016/j.apcatb.2010.04.011.

[11] An L, Chen R. Recent progress in alkaline direct ethylene glycol fuel cells for sustainable energy production. J Power Sources 2016;329:484–501. doi:10.1016/j.jpowsour.2016.08.105.

[12] Anitha M, Kamarudin SK, Kofli NT. The potential of glycerol as a value-added commodity. Chem Eng J 2016;295:119–30. doi:10.1016/j.cej.2016.03.012.

[13] Kumar P, Dutta K, Das S, Kundu PP. An overview of unsolved deficiencies of direct methanol fuel cell technology: factors and parameters affecting its widespread use. Int J Energy Res 2014;38:1367–90. doi:10.1002/er.

[14] Akhairi MAF, Kamarudin SK. Catalysts in direct ethanol fuel cell (DEFC): An overview. Int J Hydrogen Energy 2016;41:4214–28. doi:10.1016/j.ijhydene.2015.12.145.

[15] Wang Y, Zou S, Cai W-B. Recent Advances on Electro-Oxidation of Ethanol on Pt- and Pd-Based Catalysts: From Reaction Mechanisms to Catalytic Materials.

Catalysts 2015;5:1507–34. doi:10.3390/catal5031507.

[16] Friedl J, Stimming U. Model catalyst studies on hydrogen and ethanol oxidation for fuel cells. Electrochim Acta 2013;101:41–58. doi:10.1016/j.electacta.2012.12.130.

[17] Kakati N, Maiti J, Lee SH, Jee SH, Viswanathan B, Yoon YS. Anode Catalysts for Direct Methanol Fuel Cells in Acidic Media : Do We Have Any Alternative for Pt or Pt − Ru ? Chem Rev 2014;114:12397–429. doi:10.1021/cr400389f.

[18] Huang L, Sun JY, Cao SH, Zhan M, Ni ZR, Sun HJ, et al. Combined EC-NMR and in Situ FTIR Spectroscopic Studies of Glycerol Electrooxidation on Pt/C, PtRu/C, and PtRh/C. ACS Catal 2016;6:7686–95. doi:10.1021/acscatal.6b02097.

[19] Beden B, Morin M-C, Hahn F, Lamy C. “IN SITU” Analysis by infrared reflectance spectroscopy of the adsorbed species resulting from the electrosorption of ethanol on platinum in acid medium. J Electroanal Chem 1987;229:353–66.

[20] Iwasita T, Vielstich W. The electrochemical oxidation of ethanol on platinum. J Electroanal Chem 1988;257:319–24.

[21] Baltruschat H. Differential electrochemical mass spectrometry. J Am Soc Mass Spectrom 2004;15:1693–706. doi:10.1016/j.jasms.2004.09.011.

[22] Schnaidt J, Heinen M, Jusys Z, Behm RJ. Electro-oxidation of ethylene glycol on a Pt-film electrode studied by combined in situ infrared spectroscopy and online

mass spectrometry. J Phys Chem C 2012;116:2872–83. doi:10.1021/jp208162q.

[23] Kwon Y, Schouten KJP, Koper MTM. Mechanism of the Catalytic Oxidation of Glycerol on Polycrystalline Gold and Platinum Electrodes. ChemCatChem 2011;3:1176–85. doi:10.1002/cctc.201100023.

[24] Wang HS, Abruna HD. Electrocatalysis of Direct Alcohol Fuel Cells: Quantitative DEMS Studies. In: Bocarsly A, Mingos DMP, editors. Fuel Cells Hydrog. Storage, 2011, p. 141.

[25] Hernandez-Fernandez P, Lund PB, Kallesøe C, Clausen HF, Christensen LH. Supported Pt-based nanoparticulate catalysts for the electro-oxidation of methanol: An experimental protocol for quantifying its activity. Int J Hydrogen Energy 2015;40:284–91. doi:10.1016/j.ijhydene.2014.10.095.

[26] Sayadi A, Pickup PG. Evaluation of methanol oxidation catalysts by rotating disc voltammetry. Electrochim Acta 2016;199:12–7. doi:10.1016/j.electacta.2016.03.112.

[27] Sayadi A, Pickup PG. Evaluation of ethanol oxidation catalysts by rotating disc voltammetry. Electrochim Acta 2016;215:84–92. doi:10.1016/j.electacta.2016.08.097.

[28] Bach Delpeuch A, Jacquot M, Chatenet M, Cremers C. The influence of mass-transport conditions on the ethanol oxidation reaction (EOR) mechanism of Pt/C electrocatalysts. Phys Chem Chem Phys 2016;18:25169–75.

doi:10.1039/C6CP04294E.

[29] Vigier F, Coutanceau C, Perrard A, Belgsir EM, Lamy C. Development of anode catalysts for a direct ethanol fuel cell. J Appl Electrochem 2004;34:439–46. doi:10.1023/B:JACH.0000016629.98535.ad.

[30] An L, Zhao TS, Li YS. Carbon-neutral sustainable energy technology: Direct ethanol fuel cells. Renew Sustain Energy Rev 2015;50:1462–8. doi:10.1016/j.rser.2015.05.074.

[31] Abdelkareem MA, Masdar MS, Tsujiguchi T, Nakagawa N, Sayed ET, Barakat NAM. Elimination of toxic products formation in vapor-feed passive DMFC operated by absolute methanol using air cathode filter. Chem Eng J 2014;240:38–44. doi:10.1016/j.cej.2013.11.043.

[32] Ren X, Zawodzinski JTA, Uribe F, Dai H, Gottesfeld S. Proton Conducting Membrane Fuel Cells. In: Gottesfeld GHS, Landgrebe A, editors. Prot. Conduct. Membr. Fuel Cells. 1st ed., Pennington, NJ: The Electrochemical Society; 1995, p. 284.

[33] Majidi P, Pickup PG. Determination of the average number of electrons released during the oxidation of ethanol in a direct ethanol fuel cell. Electrochim Acta 2015;182:856–60. doi:10.1016/j.electacta.2015.09.168.

[34] Ren X, Springer TE, Gottesfeld S. Water and Methanol Uptakes in Nafion Membranes and Membrane Effects on Direct Methanol Cell Performance. J

Electrochem Soc 2000;147:92. doi:10.1149/1.1393161.

[35] Ren X, Springer TE, Zawodzinski T a, Gottesfeld S. Methanol Transport Through Nafion Membranes. Electro-osmotic Drag Effects on Potential Step Measurements. J Electrochem Soc 2000;147:466–74. doi:10.1149/1.1393219.

[36] James DD, Pickup PG. Measurement of carbon dioxide yields for ethanol oxidation by operation of a direct ethanol fuel cell in crossover mode. Electrochim Acta 2012;78:274–8. doi:10.1016/j.electacta.2012.05.120.

[37] Rosenthal NS, Vilekar SA, Datta R. A comprehensive yet comprehensible analytical model for the direct methanol fuel cell. J Power Sources 2012;206:129–43. doi:10.1016/j.jpowsour.2012.01.080.

[38] Bahrami H, Faghri A. Review and advances of direct methanol fuel cells: Part II: Modeling and numerical simulation. J Power Sources 2013;230:303–20. doi:10.1016/j.jpowsour.2012.12.009.

[39] Meyers JP, Newman J. Simulation of the Direct Methanol Fuel Cell: II. Modeling and Data Analysis of Transport and Kinetic Phenomenna. J Electrochem Soc 2002;149:A718. doi:10.1149/1.1473189.

[40] Bard JA, Faulkner RL. Electrochemical Methods Fundamentals and Applications. 2nd ed. New York: Wiley; 2001.

[41] Song C, Pickup PG. Effect of hot pressing on the performance of direct methanol fuel cells. J Appl Electrochem 2004;34:1065–70.

[42] Fletscher S. Tafel slopes from first principles. J Solid State Electrochem 2009;13:537–49.

[43] Lee MJ, Kang JS, Kang YS, Chung DY, Shin H, Ahn CY, et al. Understanding the Bifunctional Effect for Removal of CO Poisoning: Blend of a Platinum Nanocatalyst and Hydrous Ruthenium Oxide as a Model System. ACS Catal 2016;6:2398–407. doi:10.1021/acscatal.5b02580.

[44] Fang YH, Liu ZP. First principles Tafel kinetics of methanol oxidation on Pt(111). Surf Sci 2015;631:42–7. doi:10.1016/j.susc.2014.05.014.

[45] Cohen JL, Volpe DJ, Abruña HD. Electrochemical determination of activation energies for methanol oxidation on polycrystalline platinum in acidic and alkaline electrolytes. Phys Chem Chem Phys 2007;9:49–77. doi:10.1039/B612040G.

[46] Schmidt TJ, Gasteiger HA, Behm RJ. Methanol electrooxidation on a colloidal PtRu-alloy fuel-cell catalyst. Electrochem Commun 1999;1:1–4. doi:10.1016/S1388-2481(98)00004-6.

[47] Dubau L, Coutanceau C, Garnier E, Leger J-M, Lamy C. Electrooxidation of methanol at platinum -ruthenium electrocatalysts prepared from colloidal precursors. J Appl Electrochem 2003;33:419–29.

[48] Gojković SL, Vidaković TR, Durović DR. Kinetic study of methanol oxidation on carbon-supported PtRu electrocatalyst. Electrochim Acta 2003;48:3607–14.

doi:10.1016/S0013-4686(03)00481-X.

[49] Khazova OA, Mikhailova AA, Skundin AM, Tuseeva EK, Havránek A, Wippermann K. Kinetics of Methanol Oxidation on Supported and Unsupported Pt/Ru Catalysts Bonded to PEM. Fuel Cells 2002;2:99–108. doi:10.1002/fuce.200290008.

[50] Tapan NA, Mustain WE, Gurau B, Sandi G, Prakash J. Investigation of methanol oxidation electrokinetics on Pt using the asymmetric electrode technique. J New Mater Electrochem Syst 2004;7:281–6.

[51] Vidaković T, Christov M, Sundmacher K. Rate expression for electrochemical oxidation of methanol on a direct methanol fuel cell anode. J Electroanal Chem 2005;580:105–21. doi:10.1016/j.jelechem.2005.03.015.

[52] Gojković SL, Vidaković TR. Methanol oxidation on an ink type electrode using Pt supported on high area carbons. Electrochim Acta 2001;47:633–42. doi:10.1016/S0013-4686(01)00730-7.

[53] Roth C, Martz N, Hahn F, Léger J-M, Lamy C, Fuess H. Characterization of Differently Synthesized Pt-Ru Fuel Cell Catalysts by Cyclic Voltammetry, FTIR Spectroscopy, and in Single Cells. J Electrochem Soc 2002;149:E433. doi:10.1149/1.1511191.

[54] Wang ZH, Wang CY. Mathematical Modeling of Liquid-Feed Direct Methanol Fuel Cells. J Electrochem Soc 2003;150:A508. doi:10.1149/1.1559061.

[55] Altarawneh RM, Majidi P, Pickup PG. Determination of the efficiency of ethanol oxidation in a proton exchange membrane electrolysis cell. J Power Sources 2017;351:106–14. doi:10.1016/j.jpowsour.2017.03.084.

[56] Colmenares L, Wang H, Jusys Z, Jiang L, Yan S, Sun GQ, et al. Ethanol oxidation on novel, carbon supported Pt alloy catalysts-Model studies under defined diffusion conditions. Electrochim Acta 2006;52:221–33. doi:10.1016/j.electacta.2006.04.063.

[57] Sun S, Chojak Halseid M, Heinen M, Jusys Z, Behm RJ. Ethanol electrooxidation on a carbon-supported Pt catalyst at elevated temperature and pressure: A high-temperature/high-pressure DEMS study. J Electroanal Chem 2009;190:2–13. doi:10.1016/j.jpowsour.2009.01.073.

[58] Rao V, Cremers C, Stimming U, Cao L, Sun S, Yan S, et al. Electro-oxidation of Ethanol at Gas Diffusion Electrodes A DEMS Study. J Electrochem Soc 2007;154:B1138. doi:10.1149/1.2777108.

[59] Altarawneh RM, Pickup PG. Product Distributions and Efficiencies for Ethanol Oxidation in a Proton Exchange Membrane Electrolysis Cell. J Electrochem Soc 2017;164:F861–5. doi:10.1149/2.0051709jes.

Chapter 4

Production and electrolysis of methanol rich pyrolysis oil distillates and permeates

4 Production and electrolysis of methanol rich pyrolysis oil distillates and permeates

4.1 Introduction

Proton exchange membrane fuel cells (PEMFC) are important power production technologies for small-scale and mobile applications. Hydrogen fueled PEMFC are well developed and have achieved commercialization for fuel cell electric vehicles (FCEV) (vehicles, trains) and backup power systems. The hydrogen for those cells is produced by steam reforming of hydrocarbons (natural gas) or electrolysis of water [1]. Moreover, many studies investigate renewable hydrogen production with catalytic steam reforming [2–5]. Hydrogen can be produced by steam reforming of renewable fuels such as pyrolysis oils [6–10]. However, thermal decomposition (coking) and high water content lead to catalyst deactivation in the steam reforming process [6].

Water electrolysis is the decomposition of water into oxygen and hydrogen through application of an electric potential [1]. The electrolysis process has a standard cell potential of 1.23 V, to decompose water into oxygen and hydrogen [11,12]. To drive the reaction a higher potential of 1.48 V is experimentally required for hydrogen production through water electrolysis. The difference between the standard potential and the experimentally observed potential is called overpotential. The term overpotential describes any kind of potential loss in an electrochemical process. Hydrogen can also be produced renewably by electrolysis of alcohols such as ethanol and methanol, for example those produced from biomass waste products [13–16].

Methanol-water electrolysis produces H_2 and CO_2 as a by-product at much lower potentials than 1.48 V through the following reactions [11,17]:

$$CH_3OH + H_2O \rightarrow CO_2 + 6H^+ + 6e^- \quad \text{Eq. (4.1)}$$

$$6H^+ + 6e^- \rightarrow 3H_2 \quad \text{Eq. (4.2)}$$

The standard potential is 0.02 V, however, to produce hydrogen from methanol-water solution, a potential of ca. 0.2 V is typically required [17]. Catalytic steam reforming of methanol is an alternative way to produce hydrogen, however, this process requires high process temperatures (250 °C) whereas PEM electrolysis cells can be operated at moderate temperatures (< 100 °C) [11]. Methanol derived from a sustainable source (e.g. as a by-product from the pyrolysis oil enhancement described in *Chapter 2*) could be used as a feedstock for methanol-water electrolysis. These advantages of methanol-water electrolysis expand the utilization of pyrolysis oil for a hydrogen production.

In this study, an electrolysis cell was used to oxidize low boiling point components of pyrolysis oil such as methanol to produce hydrogen, as it has the potential to require less energy than steam reforming or water electrolysis. In addition, this process is a more sustainable/renewable approach to produce hydrogen if the required electric energy for the electrolysis process was produced by a renewable electricity production. Figure 4.1 illustrates the production of renewable hydrogen and value-added chemicals from a by-product stream which is itself derived from pyrolysis oil enhancement (low boiling point mixture, Figure 4.2) via electrolysis.

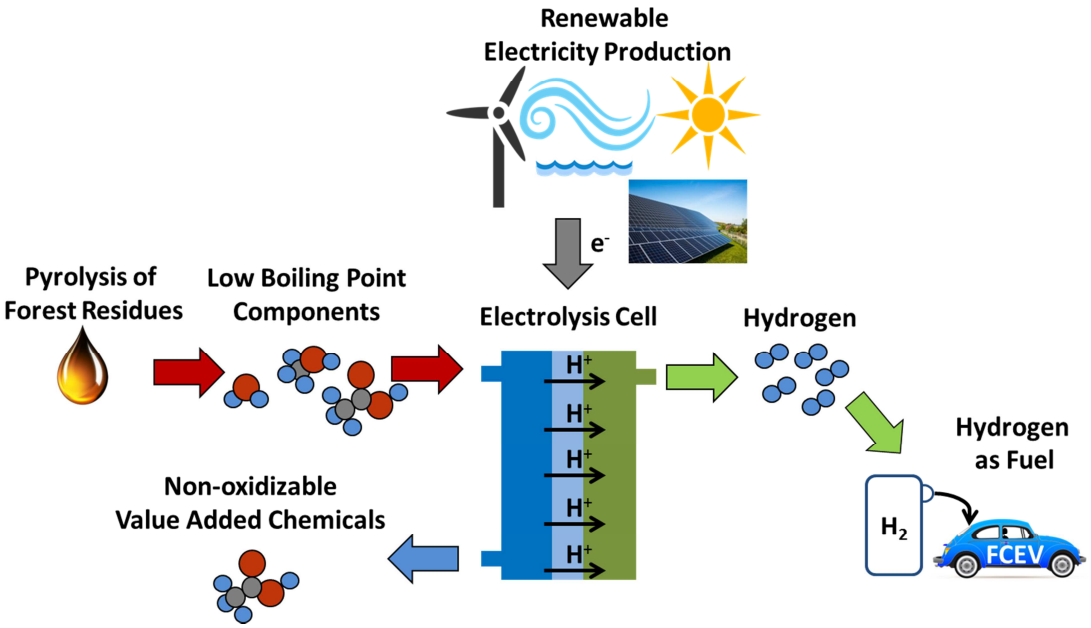

Figure 4.1: Schematic illustration of the sustainable/renewable hydrogen production process and value-added chemicals that are additionally produced from a pyrolysis oil low boiling point component mixture (Figure 4.2) via methanol-water solution electrolysis.

The low boiling point mixture (distillate/permeate) is a by-product of fractional distillation or pervaporation, which were used to enhance the fuel quality of the pyrolysis oil (Figure 4.2).

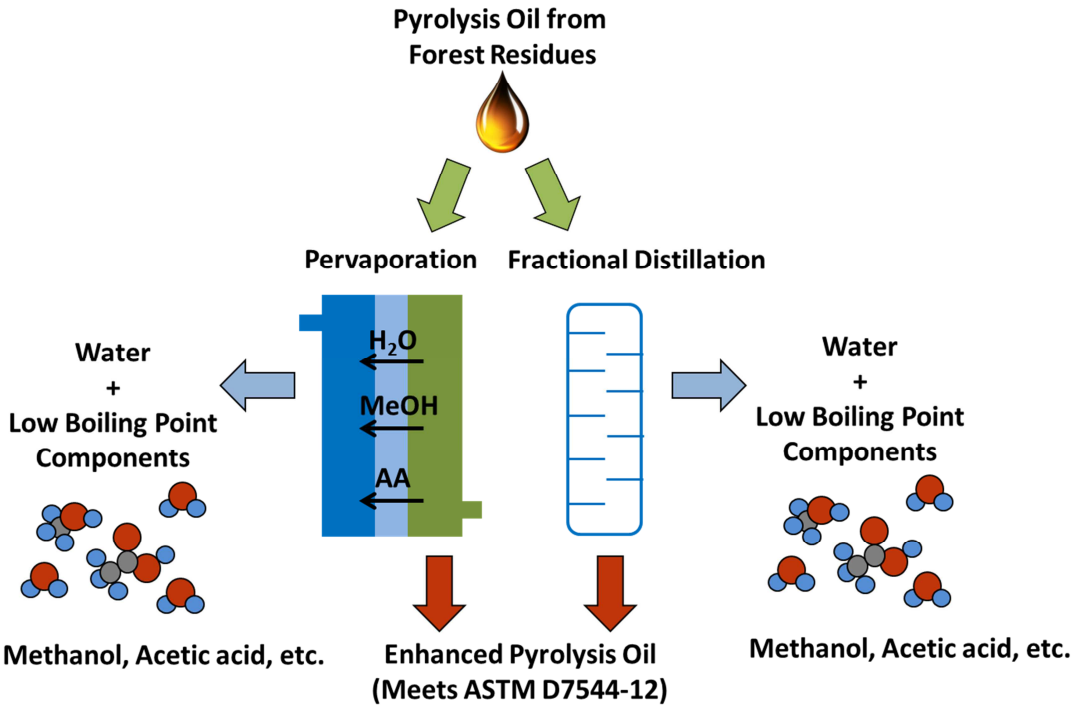

Figure 4.2: Schematic illustration of the pyrolysis oil enhancement via pervaporation/fractional distillation to meet ASTM D7544-12 standard requirements. Producing a valuable methanol rich low boiling point mixture as a by-product.

The goal of the enhancement method was to increase the heating value of the pyrolysis oil by lowering the water content, and to reduce the acid content by separation of small carboxylic acids. The enhanced oil met the ASTM D7544-12 requirements.

The ASTM D7544-12 standard describes two fuel oil grades for fast pyrolysis oil. Grade G for industrial burners and Grade D for the use in commercial/industrial burners which require a lower solids and ash content. Table 4.1 lists the requirements for pyrolysis liquid biofuels

Table 4.1: Detailed requirements for pyrolysis liquid biofuels [18].

Property	Grade G	Grade D
Gross heat of combustion, min MJ kg^{-1}	15	15
Water content, max mass%	30	30
Pyrolysis Solids Content, max mass%	2.5	0.25
Kinematic Viscosity at 40°C, max mm^2 s^{-1}	125	125
Density at 20°C, kg dm^{-3}	1.1-1.3	1.1-1.3
Sulfur Content, max mass%	0.05	0.05
Ash Content, max mass%	0.25	0.15
pH	Report	Report
Flash Point, min °C	45	45
Pour Point, max °C	-9	-9

Fast pyrolysis is a pyrolysis process optimized for the highest oil yield from biomass feedstock. In fast pyrolysis, the biomass is rapidly heated to between 450 °C and 550 °C in the absence of oxygen, resulting in organic vapours (condensable and non-condensable gases) and char. The condensed vapours (pyrolysis oil) consist of over 300 main and 700 minor organic components [19–21] that are chemically distinct from petroleum oils because they contain little to no hydrocarbons [22]. Pyrolysis oil contains a mixture of organic acids, esters, alcohols, ketones, aldehydes, phenols (guaiacols and syringol), alkenes, furans, sugars, miscellaneous oxygenates, and inorganic metals [23–25]. Pyrolysis oil from a softwood feedstock typically forms a homogenous oil which contains 15 to 35 mass% water [26]. In contrast to softwood oil, softwood bark oil contains more water (30-70 mass%) resulting in two distinct liquid phases. The bark oil top aqueous phase which is limited in use, but rich in low boiling point components such as water, methanol, acetic acid, formic acid, acetol, and acrolein, was used to enhance it to oil which meets the ASTM D7544-12 standard.

The initial purpose of the work described here was to explore the use of separated low boiling point components from softwood and bark pyrolysis oil as a fuel in an electrolysis cell (route 1, Figure 4.3).

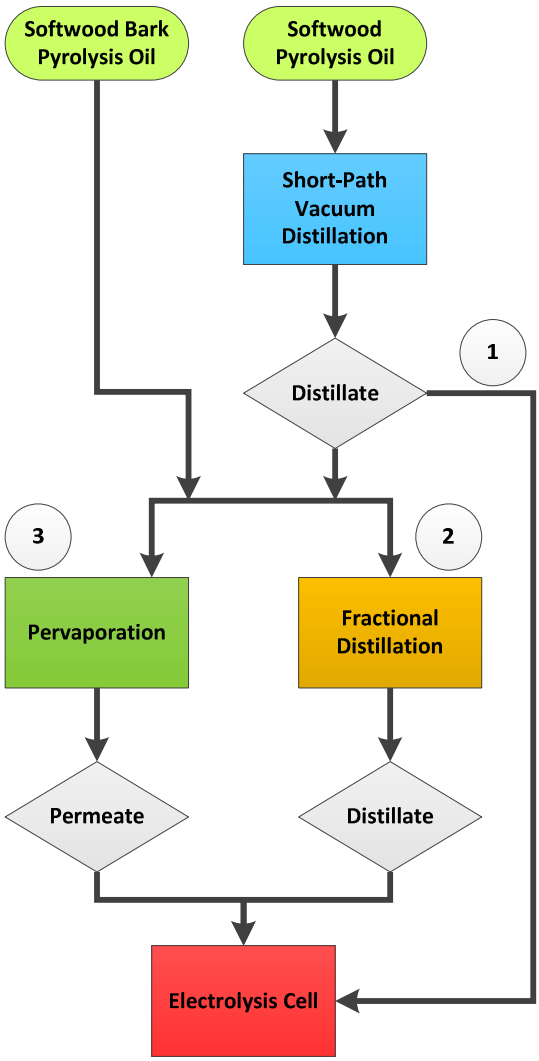

Figure 4.3: Flowchart for upgrading pyrolysis oils by several distillation and pervaporation techniques and use of distillates/permeates in an electrolysis cell for hydrogen production. Route 1 short-path vacuum distillation (softwood oil), route 2 fractional distillation (softwood distillate, bark oil), and route 3 pervaporation (softwood distillate, bark oil).

The low boiling point mixture was a by-product in the pyrolysis oil enhancement by distillation or pervaporation to meet ASTM D7544-12 requirements. The composition of the distillates was determined by proton nuclear magnetic resonance (NMR). Components with a content higher than 0.5 mass% were identified by NMR. The influence of the identified components on the electrolysis cell performance was investigated with artificial mixtures. Preliminary experiments with commercially available Pt-based catalysts showed a strong efficiency loss due to catalyst poisoning by some of the components of the pyrolysis oil distillate (e.g. acrolein). Due to this challenge, the purpose shifted to a broader view of adding value to the pyrolysis oils, through a production of value-added chemicals (e.g. acetic acid, methanol) and simultaneous enhancement of the oil quality.

The focus of this work was on the fractional distillation (route 2, Figure 4.3) and pervaporation enhancement (route 3, Figure 4.3) to separate low boiling point components from pyrolysis oil. The main advantages of this process are the enhancement of the pyrolysis oil (distillation/pervaporation residue) by increasing the heating value through lowering the water content, separation of acids, and the simultaneous use of the separated aqueous phase (distillation head/permeate) for value-added chemicals or rather as fuel for a renewable hydrogen production via electrolysis.

4.2 Materials and methods

4.2.1 Materials

The experiments were carried out with 99.8% methanol from ACP Chemical Inc., acetic acid from Caledon Laboratory Chemicals, acetol (90%, containing ≤500 ppm sodium carbonate as stabilizer) from Sigma-Aldrich Co., acrolein (90%, containing hydroquinone as stabilizer) from Sigma-Aldrich Co., methylglyoxal from Sigma-Aldrich Co. (~40% in water), sodium bisulfite from ACP Chemical Inc., sodium hydroxide from ACP Chemical Inc., and distilled and filtered deionized water. Industrial grade nitrogen (NI-K, 99.998%) from Air Liquide was used in all electrolysis experiments. Nafion™ 115 and 117 membranes (DuPont) were cleaned at 80 °C in 3% H_2O_2 (aq) (EMD Millipore) and 1 M H_2SO_4 (aq) (Fisher Scientific), then rinsed with deionized water, and stored in deionized water. Anodes consisted of the following catalysts on Toray carbon paper: platinum black (Pt black; 4.0 mg cm^{-2}); platinum-ruthenium black (PtRu black; 5.4 mg cm^{-2}); carbon supported Pt (70%Pt/C; 4.0 mg cm^{-2}, HiSPEC 13100, 70% Pt on a high surface area advanced carbon support; Alfa Aesar; Lot# M22A026); carbon-supported PtRu (75%PtRu/C; 4.0 mg cm^{-2}; HiSPEC 12100, 50% Pt and 25% Ru on a high surface area advanced carbon support; Alfa Aesar; Lot# P17B047). The Pt black electrodes contained polytetrafluoroethylene as a binder, while the PtRu black anodes contained 15 mass% Nafion and the anodes prepared with supported catalysts contained 20% Nafion. The preparation of the electrodes is described in *Chapter 3* and *Chapter 5*.

4.2.2 Pyrolysis oils

Two different pyrolysis oils were used in this study. Both oils were produced in a 2-4 kg h^{-1} feed rate auger reactor at 475 °C with steel shot as a heat carrier described in [27]. The softwood pyrolysis oil feedstock was softwood shavings from a local sawmill in Newfoundland, Canada. The same softwood pyrolysis oil was characterized by GC-FID and can be found in [28].

The feedstock for the bark pyrolysis oil was a mixture of spruce, pine, and fir softwood bark from the Groupe Crête division St-Faustin Inc. sawmill in Mont-Tremblant, Quebec, Canada. The bark pyrolysis oil formed two phases, an aqueous top and a heavy bottom phase. The aqueous top phase of the bark pyrolysis oil was used to in this work. The bark pyrolysis oil was the same as described in *Chapter 2*. The GC-FID composition analysis of a similar bark oil [28] can be seen in *Appendix 4.7.1*.

4.2.3 Separation techniques

4.2.3.1 Short-path vacuum distillation

The work in this chapter started with the continuation of a small-scale short-path vacuum distillation experiment described in [28]. All short-path distillation experiments were carried out by Shofiur Md. Rahman and Brittany Traverse. This by Shofiur Md. Rahman developed technique was used for the separation of low boiling point components [28]. The small-scale set-up allowed distillation of 25 g softwood pyrolysis oil at 80 °C under vacuum (10 kPa) conditions. Each batch distillation was operated for

1 h and produced ca. 5 g of distillate. The distillation was repeated until 100 mL of the low boiling point distillate was collected. The mixture contained a number of C1 to C3 components, including methanol, acetic, and formic acid.

4.2.3.2 Fractional distillation

In addition to the small short-path vacuum distillation, a larger scale fractional distillation set-up was used to produce higher volume distillate fractions. The apparatus for fractional distillation at atmospheric pressure is shown schematically in Figure 4.4.

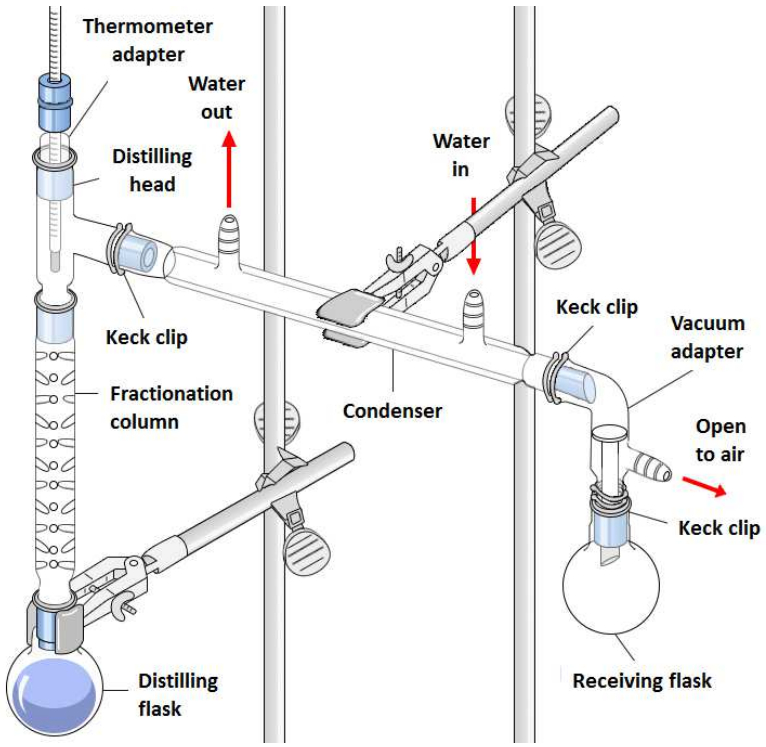

Figure 4.4: Fractional distillation set-up [29].

A 500 mL distillation flask, and 50 cm Vigreux fractionation column were used. The temperature was monitored in the head and in the boiling liquid. The liquid in the distillation flask was heated to 100 °C ± 2 °C using a jacket heater, the vapour

temperature in the head was 98 °C ± 2 °C. Fractions of 10 mL each were collected in glass vials. For each distillation run, 250 mL of the bark pyrolysis oil aqueous phase was placed in the distillation flask with boiling chips to prevent bumping. The objective was to collect a methanol-rich fraction. Therefore, 10 mL fractions were collected in 3 min to 5 min at a constant distillation temperature of 100 °C. After 100 mL (10 fractions) of distillate was collected the distillation was discontinued (approximately after 30 min).

4.2.3.3 Pervaporation

All permeate samples (except Nafion 112 permeate (*Section 4.3.1.6*) and Nafion 211 permeate (*Section 4.3.2.1*)) used in this section were produced with the method described in *Chapter 2*. The Nafion 112 and Nafion 211 permeates were produced with a smaller unit (12.25 cm²) without vacuum on the permeate side. The Nafion 112 pervaporation was operated for 3 h at 60 °C, at a feed flow rate of 0.3 mL min cm^{-1}, and a nitrogen bleed stream of 30 mL min^{-1}. Under these conditions, 2.8 g permeate were collected from 20 mL bark pyrolysis oil aqueous phase. The Nafion 112 membrane was hydrated in distilled water for 24 h prior to the experiment. The Nafion 211 pervaporation was operated for 7 h at 60 °C, at a feed flow rate of 0.1 mL min^{-1}, and a nitrogen bleed stream of 30 mL min^{-1}. Under these conditions, 6 mL permeate were collected from 20 mL bark pyrolysis oil aqueous phase. The difference of those Nafion membranes is described by the number. The first two numbers describe the molecular weight divided through 100, the third number describes the thickness in “mil” (1 mil = 2.54×10^{-6} m). Both Nafion membranes have the same chemical structure, but

different physical properties. The Nafion 211 is 25.4 micrometres thick and has a basis weight of 50 g m^{-2}, the Nafion 112 is 50.8 micrometres thick and has a basis weight of 100 g m^{-2}. Various membranes were used and are listed in Table 4.2.

Table 4.2: Investigated pervaporation membranes.

Membrane name	Company	Membrane type
Nafion 112	DuPont	Sulfonated tetrafluoroethylene based fluoropolymer-copolymer
Nafion 211	DuPont	Sulfonated tetrafluoroethylene based fluoropolymer-copolymer
Pervap 4155-30	DeltaMem	Composite membrane with a less crosslinked PVA separation layer
Pervap 4101	DeltaMem	Composite membrane with a higher crosslinked PVA separation layer

The second pervaporation experiments for the permeate performance comparison results described in *Section 4.3.2.1* were carried out with the larger pervaporation unit (56.25 cm²) described in *Chapter 2*. The process operating conditions are listed in Table 4.3. For both experiments, the vacuum and the nitrogen bleed stream flow rate were kept constant.

Table 4.3: Process parameters for the membrane comparison pervaporation experiments.

Process parameter	Unit	Permeate Pervap 4155-30	Permeate Pervap 4101
Temperature	°C	60	80
Feed flow rate	mL min^{-1}	0.2	0.1
Bleed stream flow rate (N_2)	mL min^{-1}	10	10
Vacuum	mmHg	66	66

4.2.4 Analysis of permeate and distillate fractions

After each experiment, the permeate or distillate fractions were collected in a sealed bottle and stored at approximately 5 °C before analysis. The samples were analyzed for chemical composition by proton nuclear magnetic resonance (NMR) spectroscopy with a Bruker AVANCE III 300 MHz NMR spectrometer. Fumaric acid was used as an internal standard to determine the concentrations of identified components.

4.2.5 Electrolysis cell

All electrochemical experiments in this Chapter were carried out with the multi-anode electrolysis cell described in *Chapter 3* [30]. Anodes were prepared with Pt, 70%Pt/C, PtRu, and 75%PtRu/C catalysts, described as reference catalysts in *Chapter 3*. The cell was operated at 80 °C. Steady-state polarization curves (current density (mA cm^{-2}) vs. cell potential (V) were obtained from 0.9 V to 0 V in 25 mV or 50 mV steps. Each potential was held for three or one minute, with the current recorded every second. The reported currents are averages over the final minute or final 50 s. Polarization curves were obtained in either anode polarization and crossover mode.

Initially, the electrolysis cell was operated in crossover mode, in which fuel flows through the cathode chamber and diffuses through the membrane to be oxidized at the anode, to provide controlled mass transport conditions. The diffusion rate through the membrane will be different for the various components of the distillate/permeate. Larger components cannot diffuse through the membrane as readily and should therefore show a lower poisoning effect on the catalyst performance. In anode polarization mode, the fuel only diffuses through the carbon fibre paper of the anode

and thus the direct effect of the impurity components on the anode catalyst performance can be studied. Currents are higher in anode polarization mode, because the diffusion through the membrane is not a limiting factor. In both modes, the fuel was supplied at a flow rate of 0.5 mL min^{-1} while nitrogen was fed at 30 mL min^{-1} to the opposite chamber to avoid interference from oxygen. In both modes, the cathode approximates a dynamic hydrogen electrode [31].

A new, faster sample testing method for the electrolysis cell was developed to screen the performances of small samples of distillates and permeates. Recording a polarization curve requires a relatively large volume of samples (10 mL to 60 mL) due to the long running time of 2 h required for conditioning of the cell and collection of steady-state data. Therefore, a constant potential injection method was developed. The cell was preconditioned in anode polarization mode with 1 M methanol solution at 0.1 mL min^{-1} and 0.5 V for 10 min. The fuel pump was then stopped and the flow field was rapidly flushed with 2 mL of water followed by the injection of the sample (1 mL) at a flow rate of 0.1 mL min^{-1}. The experiment was stopped after a total of 20 min. The shape of the current versus time curve indicates how the catalyst was affected by poisoning species in the oil fraction.

4.2.6 Experimental approach

The focus of this work was to enhance the pyrolysis oil quality by separating low boiling point components and subsequently use the separated components as a fuel in an electrolysis cell for renewable hydrogen production. The following separation and

electrolysis experiments were carried out with two different pyrolysis oils (softwood and bark) and artificial pyrolysis oil mixtures (Figure 4.5).

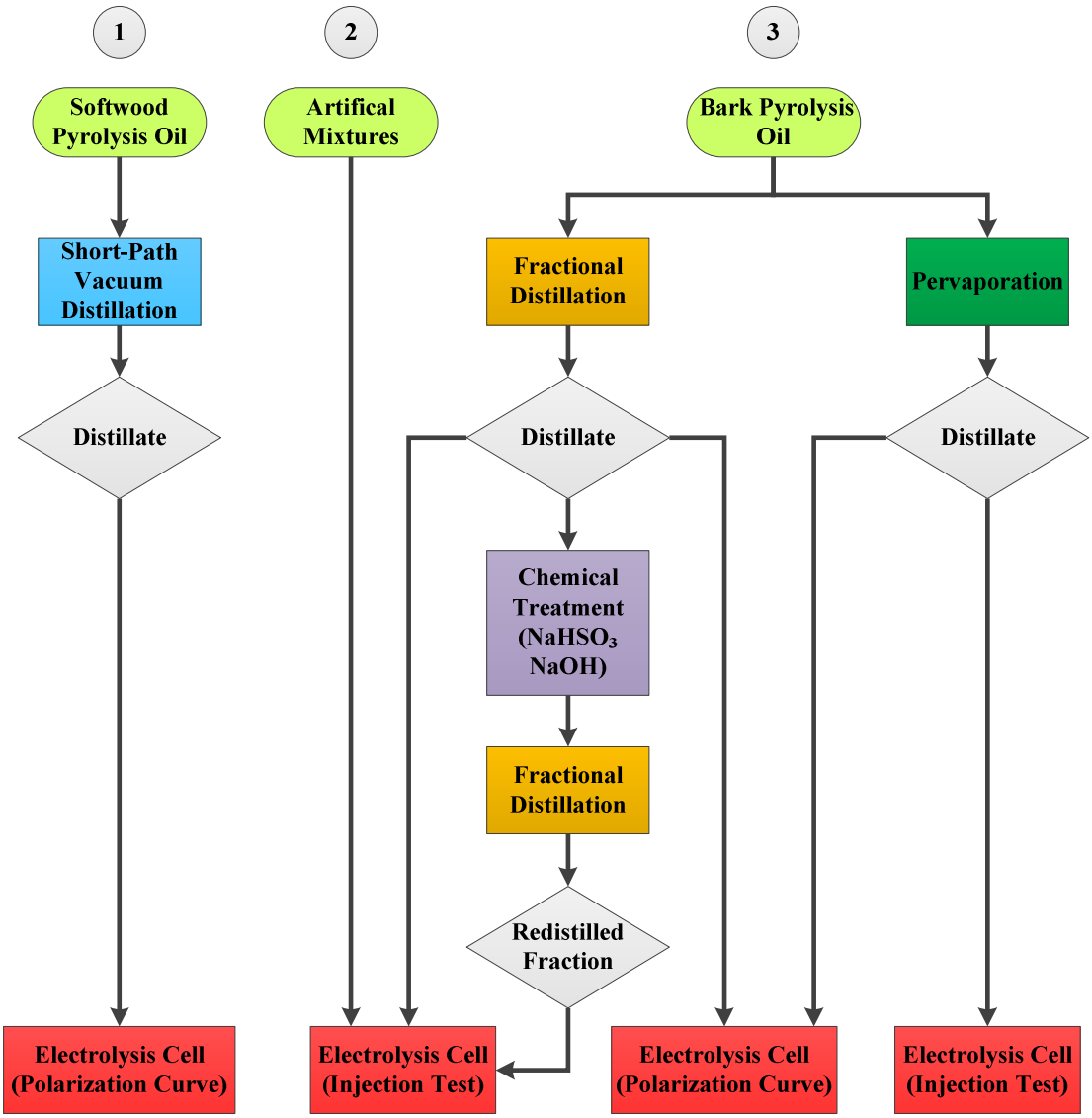

Figure 4.5: Flowchart of the experimental approach within the order of use of the different pyrolysis oils and separation techniques to separate low boiling point components for the use in an electrolysis cell.

Initial experiments were carried out with softwood pyrolysis oil distillate from a short-path vacuum distillation (Route 1 in Figure 4.5, *Section 4.2.3.1*). The distillation experiments of softwood pyrolysis oil showed the potential of separating low boiling point components at small volume rates. However, the use of the distillate in the electrolysis cell (*Section 4.3.1.3*) was not feasible due to low methanol and high acid content, as well as the presence of other impurities such as acrolein which decreased the performance (*Section 4.3.1.2*). High methanol and low impurities content (e.g. acetic acid) are preferable to increase hydrogen production rates.

Artificial mixtures were used to investigate the poisoning of Pt black and PtRu black catalysts by individual components identified in the distillate (Route 2 in Figure 4.5, *Section 4.3.1.4)*. Acrolein showed a significant poisoning effect on the catalyst, decreasing cell performance. Following the experiments with softwood pyrolysis oil and artificial mixtures, experiments were carried out with a bark pyrolysis oil aqueous phase (Route 3 in Figure 4.5). The aqueous phase bark oil has a different chemical composition and higher water content (70.2 mass%) compared to the single-phase softwood oil. The aqueous phase was used as a feedstock for the pervaporation and fractional distillation experiments (Figure 4.5).

To reduce the acid content of the bark pyrolysis oil distillate, a sample was neutralized with sodium hydroxide (NaOH). Additionally, acrolein, which cause severe poisoning, was partially removed by reaction with sodium bisulfite ($NaHSO_3$). After the neutralization and the acrolein elimination, the sample was then redistilled by fractional distillation to increase the methanol content and separate sodium

1-hydroxy-2-propene-1-sulfonate formed after $NaHSO_3$ addition (Figure 4.5) (*Section 4.3.1.5*). The performance of the purified and redistilled fraction in the electrolysis cell was evaluated via the injection method (*Section 4.3.1.6*).

In addition to the enhancement of pyrolysis oil through distillation, pervaporation was investigated to remove water and other low boiling-point components (permeate). Four different membranes were compared and the performance of the bark pyrolysis oil permeates in the electrolysis cell was then evaluated and compared to literature values for a hydrogen production via electrolysis of waste newspaper (*Section 4.3.2.1*). For optimum pervaporation conditions, the upgraded pyrolysis oil (retentate) met the requirements of ASTM D7544-12 standard.

4.3 Results and discussion

4.3.1 Distillation results

4.3.1.1 Short-path distillate composition (softwood pyrolysis oil)

The composition of the short-path distillate was determined in this work by NMR, and by GC-MS and GC-FID in a previous work [28]. The major compounds in the softwood pyrolysis oil distillate sample qualified and quantified by NMR are summarized in Table 4.4. The 1H NMR spectrum for the short-path distillate sample can be seen in *Appendix 4.7.3*.

Table 4.4: Chemical composition of components identified in the short-path softwood distillate (100 mL combined distillate from multiple distillations) determined by NMR.

Component	Short-path softwood distillate (M)
Methanol	0.53
Acetic acid	1.88
Acrolein	0.03
Acetol	0.40
Formic acid	0.17
Furfural	0.03
Glycolaldehyde	0.03
Isoeugenol	0.01

In addition to water, the main components in the distillate were acetic acid, methanol, acetol, and formic acid. Furthermore, the distillate contained small concentrations of components such as acrolein, furfural, glycolaldehyde, and isoeugenol. The full GC-MS analysis of the original softwood pyrolysis oil and the short-path distillate can be seen in *Appendix 4.7.1* [28]. The GC-MS spectra indicate that the separation yield for methanol and acrolein from the pyrolysis oil was 100% since there was no peak detected in the residual bio-oil [28]. However, only 40% of the acetic acid and 25% of the acetol were separated from the pyrolysis oil via short-path distillation at 80 °C under vacuum conditions. To increase the methanol content for the electrolysis experiments the short-path distillate (Table 4.4) was redistilled in the fractional distillation set-up described in *Section* 4.2.3.2. 30 mL short-path softwood distillate were distilled at 100 °C. Three fractions were collected in 90 min, the first fraction (6 mL) was collected after 35 min and used for the electrolysis experiment. The methanol content of the

redistilled fraction one increased from 0.53 M to 2.02 M. Other relevant composition changes can be seen in Table 4.5. The 1H NMR spectrum for the by fractional distillation redistilled F1 (short-path distillate) sample can be seen in *Appendix 4.7.3*.

Table 4.5: Chemical composition of the redistilled first fraction of the short-path softwood distillate by fractional distillation determined by NMR.

Component	Short-path softwood distillate (M)	Redistilled F1 (short-path softwood distillate) (fractional distillation) (M)
Methanol	0.53	2.02
Acetic acid	1.88	0.55
Acrolein	0.03	0.13
Acetol	0.40	0.17
Formic acid	0.17	0.06
Furfural	0.03	0.14
Glycolaldehyde	0.03	0.01
Isoeugenol	0.01	0.05

Polarization curves recorded for the redistilled F1 short-path softwood distillate are shown in Figure 4.8 and Figure 4.9 in *Section 4.3.1.4* to investigate its electrolysis cell fuel qualities. However, due to the low performance of the redistilled short-path softwood sample, the influence of each identified main component in the short-path distillate and acrolein were investigated via artificial mixture polarization curve experiments in *Section 4.3.1.4*. Furthermore, the aqueous phase of a bark pyrolysis oil was investigated to see if the different composition of the bark oil improves the electrolysis cell experiments.

4.3.1.2 Fractional distillation distillate composition (bark pyrolysis oil)

The compositions of the fractions from fractional distillation of the bark pyrolysis oil were determined by NMR and can be found in *Appendix 4.7.2*, Table 4.11. It was possible to separate low boiling point alcohols, acids, ketones, and aldehydes from the crude aqueous layer of the bark pyrolysis oil. Figure 4.6 shows how the concentration of each component varied over the distilled fractions. As indicated in the methods section, each fraction represents 10 mL of the total 100 mL of distillate taken over the length of the distillation (30 min). In a previous study, other components in distillates from a similar bark pyrolysis oil, identified by GC-MS, were methylglyoxal, 2,3 butanedione, diethyl ether [28].

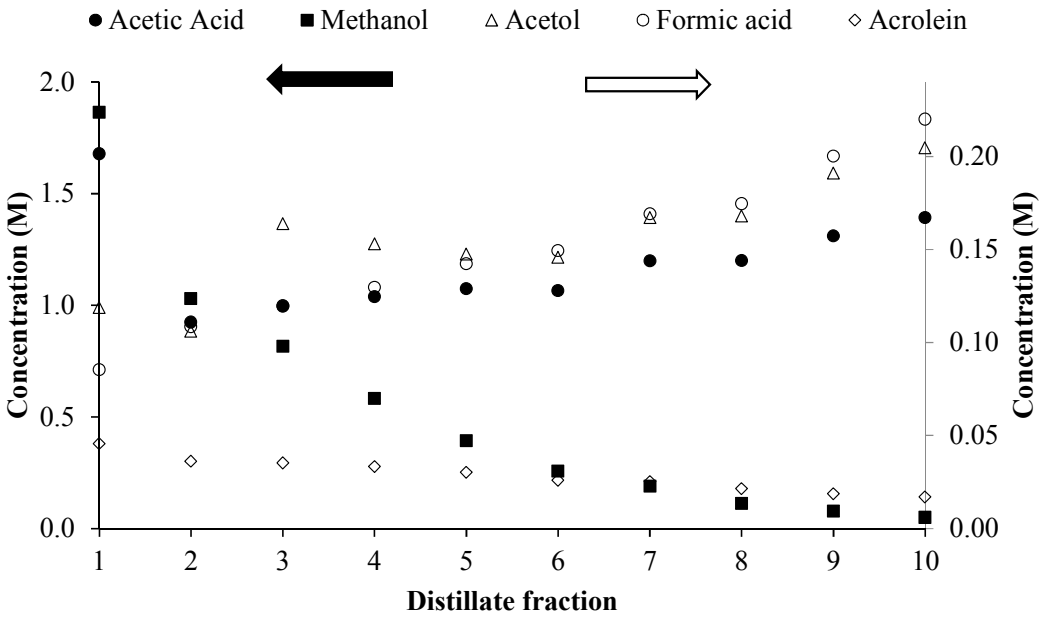

Figure 4.6: Concentrations of selected bark pyrolysis oil distillate components plotted vs. fraction number (10 mL samples). The concentrations for the filled data points can be seen on the left and for the unfilled data points on the right.

The distillate also contains minor concentrations of glycolaldehyde, isoeugenol, and furfural. Since the fractional distillation was carried out at 100 °C at 1 atm the distillate should only contain components with a boiling point of approximately 100 °C. However, against expectations, high boiling point glycolaldehyde, furfural and isoeugenol were identified in the distillate. Glycolaldehyde has a boiling point of 131 °C, furfural 162 °C, and isoeugenol of 266 °C. The possibility of distilling such high boiling point components at lower temperatures must be related to the non-ideal behaviour of the mixture due to the high polarity molecular bonding with water of these components [32]. The high water content of the bark pyrolysis oil (70 mass%) leads to partitioning of polar components from the heavy oil phase into the aqueous phase. Other studies showed that water was able to extract 63% glycolaldehyde, 88% acetic acid, 95% acetol, 74% furfural, and 32% furanone from pyrolysis oil into the aqueous extract phase [32].

The water content was ≥83 mass% for all distillate fractions. The concentration of methanol decreased from fraction 1 (1.86 M) to fraction 10 (0.05 M), while the formic acid (0.09 to 0.22 M) and acetol (0.12 to 0.20 M) concentrations increased. Acetic acid had a high concentration in fraction 1 (1.68 M). It slightly dropped in fraction 2 (0.92 M) and then increased steadily until fraction 10 (1.39 M). The acrolein concentrations are low (≤ 0.05 M) and decreased slightly with increasing fraction number from 0.05 M (fraction 1) to 0.02 M (fraction 10). The concentration changes for the minor components (glycolaldehyde, furfural, and isoeugenol) can be seen in Table 4.11 in *Appendix 4.7.2*. The methanol content decreased quickly over the collected

fractions to 0.05 M in fraction 10 (Figure 4.6); therefore, fraction 1 and 2 were used for electrolysis cell experiments because of their high methanol content (both over 1 M).

4.3.1.3 Polarization curves of distillate fractions

To analyze the performance and long-term effects of the separated distillates in an electrolysis cell, steady-state polarization curves were recorded for 70%Pt/C and 75%PtRu/C catalysts, in anode polarization mode at 80 °C. In anode polarization mode, the tested sample was fed into the anode side and nitrogen was fed through the cathode chamber. Therefore, the sample only had to diffuse through the carbon fibre paper of the anode and can demonstrate its direct effect on the catalyst. The mode is explained in more detail in *Section 4.2.5*. The tested distillate was the first fraction (10 mL) separated by fractional distillation of bark pyrolysis oil (aqueous phase) at 100 °C and 1 atm. The polarization curves for the distillate with a methanol content of 1.84 M were compared to 1 M methanol reference polarization curves (Figure 4.7). The plot shows the average polarization curves recorded for three individual anodes of the same catalyst. The composition of the components identified in the distillate fraction is listed in Table 4.6. The 1H NMR spectrum for the bark distillate sample can be seen in *Appendix 4.7.3*.

Table 4.6: Chemical composition of components identified in the first bark oil distillate fraction determined by NMR.

Component	Bark distillate (fractional distillation) (M)
Methanol	1.84
Acetic acid	1.56
Acrolein	0.04
Acetol	0.09
Formic acid	0.08

Furfural	0.04
Glycolaldehyde	0.01
Isoeugenol	0.01

The results in Figure 4.7 indicate that it was possible to oxidize the distillate fraction at a 70%Pt/C and 75%PtRu/C catalyst with an onset potential of 0.5 V. However, the comparison of the 1 M MeOH polarization curve to the distillate polarization curve showed that the current density was four times higher for 1 M methanol (440 mA cm^{-2} 70%Pt/C, and 425 mA cm^{-2} for 75%PtRu/C) than for the distillate fraction (128 mA cm^{-2} 70%Pt/C, and 137 mA cm^{-2} for 75%PtRu/C) at 0.9 V. The reduced current density recorded for the distillate was due to high concentrations of impurities other than methanol in the sample (Table 4.6). 75%PtRu/C catalyst showed a slightly higher tolerance to the impurities in the distillate compared to 70%Pt/C. However, it is necessary to purify the distillate fraction further to increase the electrolysis cell performance.

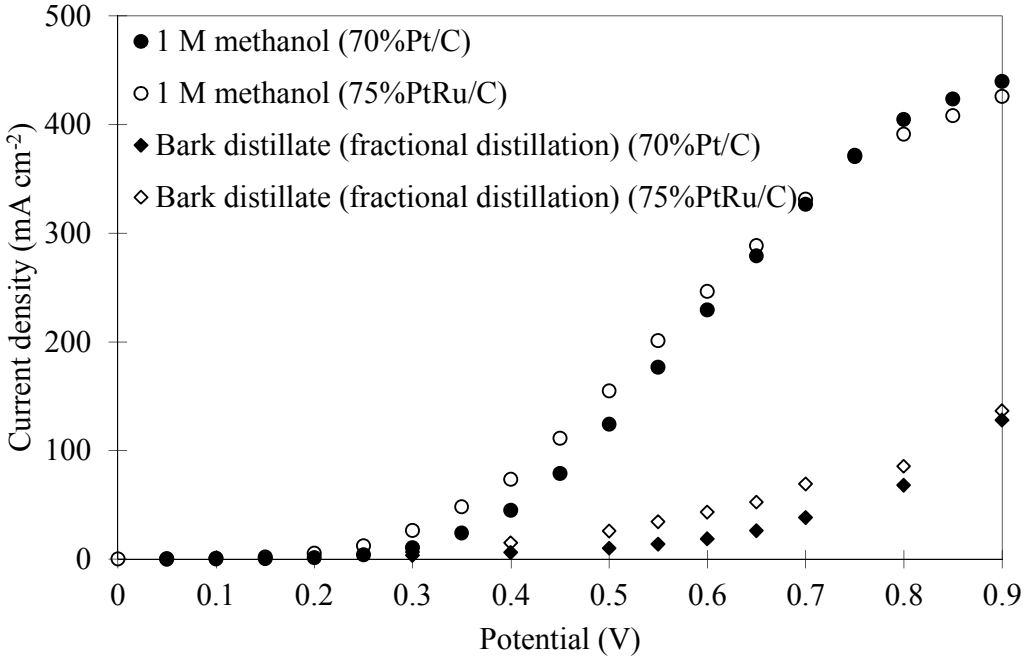

Figure 4.7: Average bark distillate and 1 M methanol reference polarization curve at 70%Pt/C and 75%PtRu/C in anode polarization mode at 80 °C.

To improve the performance of the distillate in the electrolysis cell the influence of each component must be investigated. In the following, the catalyst performance of artificial mixtures of each component identified in the distillate mixed with 1 M methanol was individually analyzed in the electrolysis cell.

4.3.1.4 Polarization curves of artificial mixtures

In addition to methanol and formic acid, which can be easily oxidized in an electrolysis cell to produce H_2, the aqueous distillates contained acetic acid, acetol, acrolein, and many other minor components as impurities that cannot be oxidized at low potentials (Table 4.4). Due to the lack of data on the influence of these impurities on methanol electrolysis, or direct methanol fuel cells (DMFC), their effects on electrolysis cell

performance were tested by adding them individually to a 1 M methanol solution. Polarization curves were recorded in crossover mode at 80 °C to evaluate the impact of each impurity on the performances of Pt black and PtRu black anodes. In crossover mode, the sample was fed into the cathode chamber (0.5 mL min^{-1}) and had to diffuse through the membrane to be oxidized at the anode. The anode chamber was fed with nitrogen (30 mL min^{-1}). This mode provides a controlled mass transport which depends on the diffusion rate of each component through the membrane and carbon fibre paper of the electrode. The crossover mode is explained in more detail in *Section 4.2.5.* Furthermore, a polarization curve for the redistilled short-path softwood distillate (composition in Table 4.5, 1H NMR spectrum in *Appendix 4.7.3*) was recorded to investigate its electrolysis cell fuel qualities.

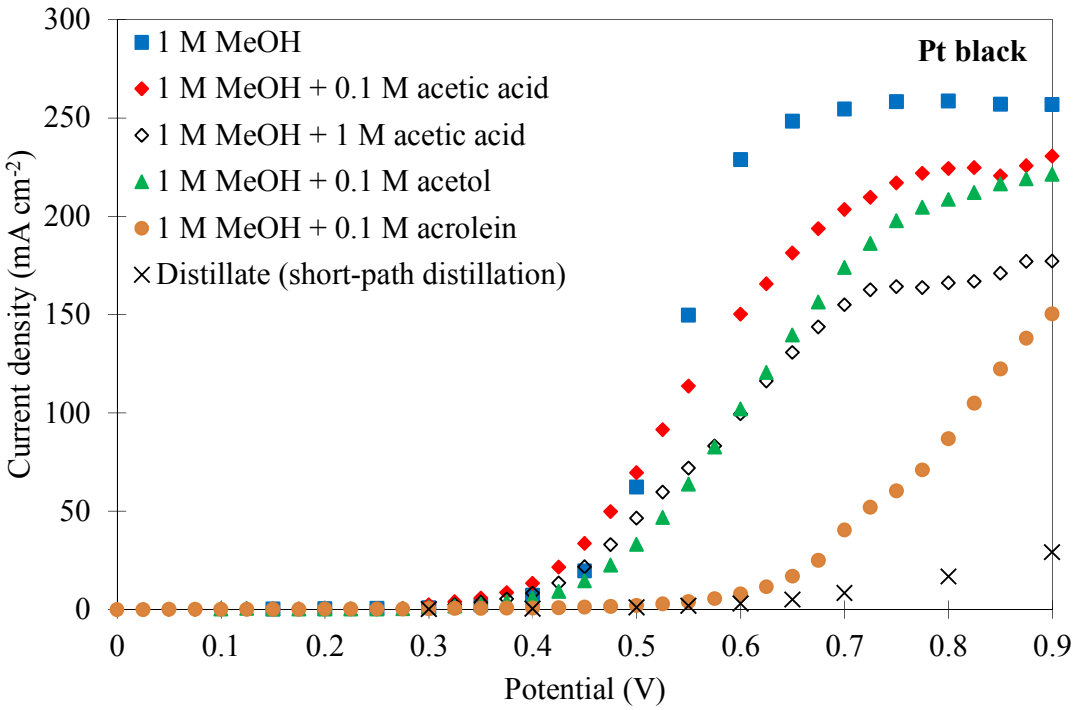

Figure 4.8: Impurity influence on methanol polarization curves at Pt black anodes in an electrolysis cell at 80 °C in crossover mode.

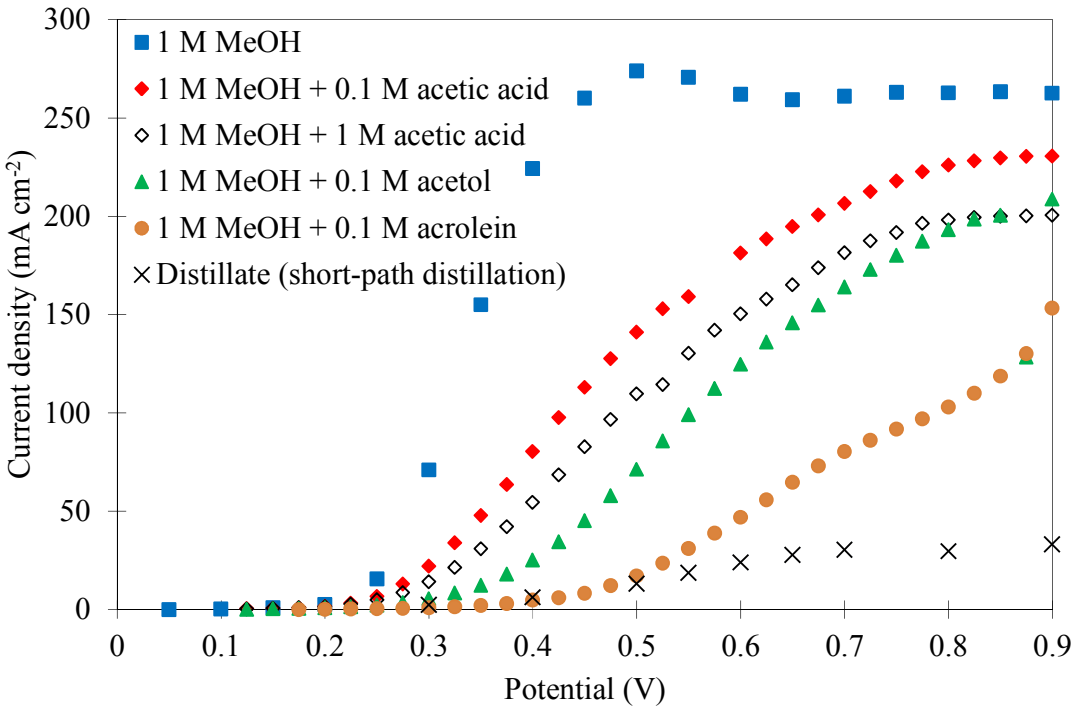

Figure 4.9: Impurity influence on methanol polarization curves at PtRu black anodes in an electrolysis cell at 80 °C in crossover mode.

Figure 4.8 and Figure 4.9 show the results with a 1 M methanol reference polarization curve. The results indicate that the impurities influence the electrolysis cell performance by lowering the limiting current and shifting the half wave potential to higher potentials. Pt black is more tolerant to acetic acid than PtRu black. Acetol showed a significant effect at Pt black and PtRu black. Acrolein showed a major influence on the cell performance by poisoning the catalyst. The influences of acrolein and the softwood distillate on the electrolysis cell performance are especially unfavourable. The distillate sample showed poorer performance compared to the individual compounds due to the presence of impurities other than those that were tested. Further processing of the

softwood distillate is clearly required before it will be of significant value for electrolysis or use in a fuel cell.

4.3.1.5 Processing of the bark distillate to decrease impurity levels

As seen in the previous section in Figure 4.8 and Figure 4.9, acrolein and acetic acid have a significant effect on the electrolysis cell performance and should be avoided. Acrolein is highly toxic with permissible Exposure Level (PEL) of 0.25 mg m^{-3}. It is a chemical formed by reaction of formaldehyde with acetaldehyde in the pyrolysis process. Acrolein can form acetals and alkoxypropionaldehydes in contact with alcohols and 3-hydroxypropionaldehyde in contact with water [33,34]. To overcome impurity issues in the distillate fractions, an upgrading process with sodium bisulfite ($NaHSO_3$) and sodium hydroxide (NaOH) was developed (Figure 4.10). $NaHSO_3$ reacts with acrolein to form sodium 1-hydroxy-2-propene-1-sulfonate (Eq. (4.3)) and NaOH reacts with acids in a neutralization reaction. The solid sodium 1-hydroxy-2-propene-1-sulfonate salt can be separated via an additional fractional distillation step.

$$NaHSO_3 + C_3H_4O \leftrightarrow C_3H_5NaO_4S \qquad \text{Eq. (4.3)}$$

The first four fractions (50 mL) of a fractional bark pyrolysis oil distillation were combined and treated with 9 g solid $NaHSO_3$ powder, which was slowly added under stirring over 5 min, to eliminate the acrolein. Additionally, 15 mL of 5 M NaOH was added to neutralize the acids. The pH was measured to be 6 with pH measuring strips after the treatment. A fractional distillation followed the chemical treatment to separate sodium 1-hydroxy-2-propene-1-sulfonate and the acid salts from the treated sample

(Figure 4.10). The remaining liquid in the distillation flask contained white solid precipitate (sodium 1-hydroxy-2-propene-1-sulfonate, sodium acetate, etc.). The distillation head was collected into two 20 mL fractions. The first fraction from the distillation ("redistilled F1 ($NaHSO_3$, NaOH)") was used to measure its electrolysis performance via the injection method.

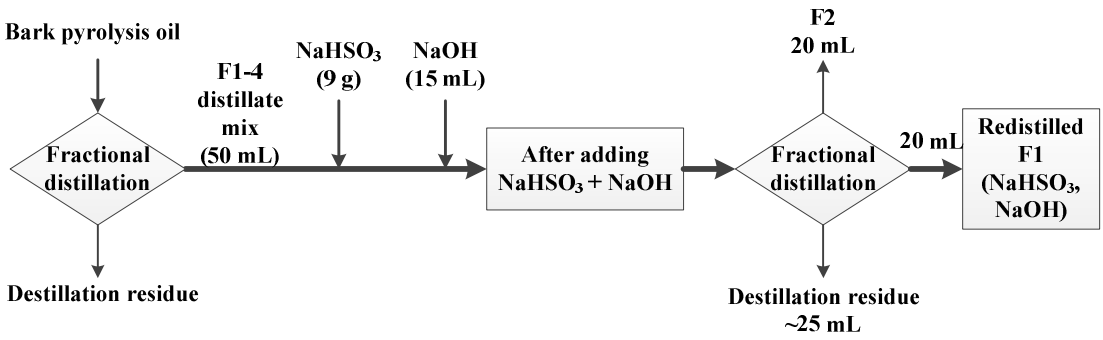

Figure 4.10: Flowchart for the chemical treatment with $NaHSO_3$ and NaOH and redistillation of the bark pyrolysis distillate to produce the "Redistilled F1 ($NaHSO_3$, NaOH)" sample.

The chemical composition changes during the upgrading process (Figure 4.10), are shown in Table 4.7. The methanol content was increased (1.19 to 1.96 M), and the acids were decreased (acetic acid 1.20 to 0.11 M, formic acid 0.12 to 0.00 M). Acrolein, however, was eliminated by the $NaHSO_3$ but reformed in an equilibrium reaction during the fractional distillation step to separate sodium 1-hydroxy-2-propene-1-sulfonate, performed at high temperatures (100 °C). The acetol content was reduced from 0.15 to 0.07 M in the sample.

Table 4.7: Chemical composition of components identified in the original, $NaHSO_3$ + NaOH treated, and redistilled first fraction determined by NMR

Component	F1-4 distillate mix (M)	After adding $NaHSO_3$ + NaOH to the F1-4 distillate mix (M)	Redistilled F1 ($NaHSO_3$, NaOH) (fractional distillation) (M)
Methanol	1.19	0.69	1.96
Acetic acid	1.20	0.59	0.11
Acrolein	0.04	0.00	0.03
Acetol	0.15	0.14	0.07
Formic acid	0.12	0.00	0.00
Furfural	0.04	not identified	0.03
Glycolaldehyde	0.03	not identified	0.02
Isoeugenol	0.01	not identified	0.02

4.3.1.6 Evaluation of purified bark distillate samples

In order to rapidly screen pyrolysis oil distillates and permeates in the electrolysis cell, small volume samples (1 mL) were injected into the anode flow field of an electrolysis cell in anode polarization mode. The cell was preconditioned with 1 M methanol for 10 min followed by flushing of the flow channels with water (2 mL) to remove residual methanol before injecting the sample.

A water background curve (grey dotted line) (Figure 4.11 and Figure 4.12), was recorded by injecting water instead of a sample. The results displays how long it takes to flush/oxidize the methanol that remains in the preconditioned cell. The result in Figure 4.11 shows that after flushing the cell (600 s), there was still residue methanol in the anode catalyst layer. All remaining methanol was entirely consumed after 950 s.

This information was useful to confirm that the current increase after flushing was due to the injected sample and not due to residue methanol.

Artificial mixtures of 1 M methanol with various acetic acid and acetol concentrations were used to characterize the injection method at commercial 70%Pt/C, 75%PtRu/C, and Pt/C mixed with PtRu/C (1:1) catalysts. The results for the 75%PtRu/C and the 1:1 mixture of both catalysts can be seen in *Appendix 4.7.5*. Figure 4.11 shows that the current versus time results for the oxidation of artificial mixtures results at the 70%Pt/C anodes at a constant potential of 0.5 V. For example, the 1 M MeOH + 0.1 M acetic acid curve shows the average current of two individual 70%Pt/C anodes. The experiment was carried out with two anodes of the same catalyst in order to determine the reproducibility between injection runs. The reproducibility plot for the artificial mixture of 1 M methanol with 0.1 M acetic acid at 70%Pt/C, 75%PtRu/C, and Pt/C mixed with PtRu/C (1:1) anodes can be seen in *Appendix 4.7.4*. The first 600 s represents the stable preconditioned current (ca. 35 to 40 mA) of 1 M methanol, which demonstrates adequate recovery from previous runs. At 600 s, flushing of the cell with water caused the current to drop. This was due to the displacement of the oxidizable 1 M methanol in the flow channels with water. At ca. 670 s, the current increased as the sample entered the flow field and reached its maximum value at approximately 800 s. The maximum current value following injection of the sample differs from the preconditioning current prior to water injection due to the influence of the single impurity component (e.g. 0.1 M acetic acid) on the catalyst's performance.

The acetic acid results at 70%Pt/C anodes indicated that the electrolysis cell performance decreased with increasing acetic acid concentration from 0.1 to 1 M. The maximum current at 800 s for the artificial mixture with 0.1 M acetic acid was 32 mA (vs. 39 mA for 1 M MeOH, 18% current reduction) and 23 mA (vs. 34 mA for 1 M MeOH, 32% current reduction) for 1 M acetic acid. Moreover, the acetic acid displayed a slight long-term poisoning effect that decreased the current from the maximum of 32 to 31 mA at 1200 s (0.1 M acetic acid) and from 23 to 21 mA (1 M acetic acid).

The injection results of the artificial mixture with 0.1 M acetol (Figure 4.11) at 70%Pt/C anodes showed that the maximum current was 25 mA (vs. 35 mA for 1 M MeOH, 29% current reduction) at 800 s and had a stronger long-term poisoning effect compared to 0.1 M acetic acid which was reduced to 21 mA at 1200 s. These results demonstrate that the injections of artificial impurity samples based on 1 M MeOH were useful for a rapid assessment of the effects of impurities on the catalyst's performance.

The injection results for the 75%PtRu/C and the Pt/C PtRu/C mix (1:1) anodes in *Appendix 4.7.5* showed no significant difference compared to the 70%Pt/C results in Figure 4.11.

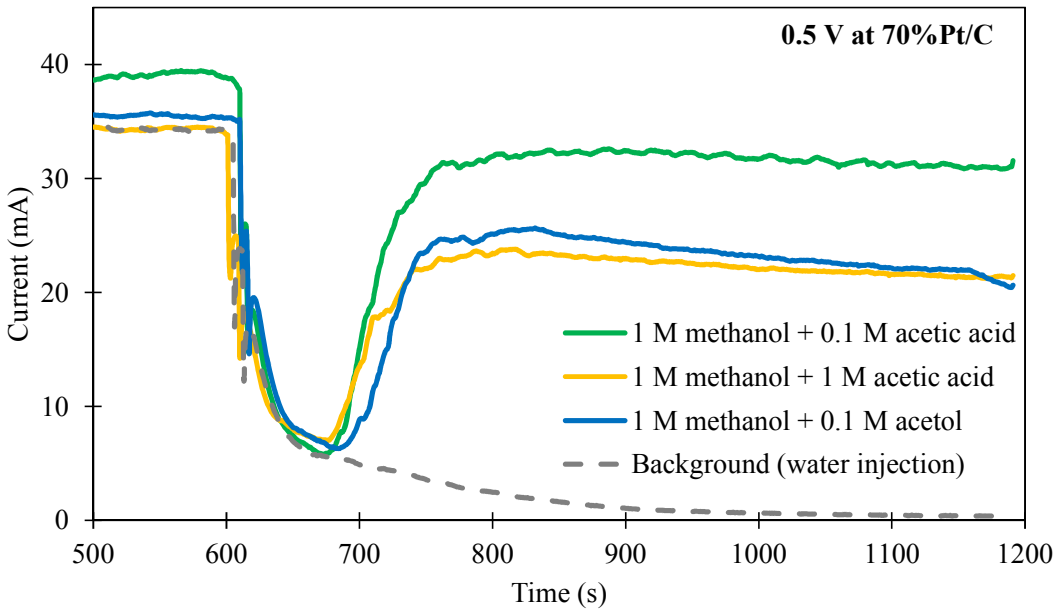

Figure 4.11: Current vs. time results of 1 M MeOH (0 to 600 s) at 70%Pt/C electrodes in an electrolysis cell operated at a constant potential of 0.5 V in anode polarization mode at 80 °C. The samples (1 M MeOH + impurity component) were injected after being flushed with water at 600 s.

Following the validation test with the artificial mixtures, crude and redistilled bark pyrolysis oil distillates (*Section 4.3.1.5*) and permeate samples listed in Table 4.8 and were tested with the injection method. Figure 4.12 shows the poisoning effect of the distillate and permeate samples at the 70%Pt/C catalyst. The polarization curves of the distillate and permeate samples at 75%PtRu/C, and Pt/C mixed with PtRu/C (1:1) catalysts are reported in *Appendix 4.7.5*.The chemical composition of the components identified in the samples is listed in Table 4.8. The 1H NMR spectra of the investigated samples can be seen in *Appendix 4.7.3*.

Table 4.8: Chemical composition of components identified in the distillate fractions and permeate determined by NMR

Component	F1 (fractional distillation) (bark pyrolysis oil) (M)	Redistilled F1 ($NaHSO_3$, NaOH) (fractional distillation) (M)	Permeate pervaporation (Nafion 112) (M)	Methanol reference sample (M)
Methanol	1.86	1.96	0.32	0.30
Acetic acid	1.68	0.11	0.59	-
Acrolein	0.05	0.03	0.01	-
Acetol	0.12	0.07	0.15	-
Formic acid	0.09	0.00	0.12	-
Furfural	0.04	0.03	0.01	-
Glycolaldehyde	0.02	0.02	0.03	-
Isoeugenol	0.01	0.02	0.005	-

The injection results of fraction F1 (Figure 4.12) showed a maximum current of 13 mA at 680 s (vs. 28 mA for 1 M MeOH, 54% current reduction) followed by a rapid decay. The sample showed a strong long-term poisoning effect, with a current reduction to 2 mA at 1200 s at the 70%Pt/C catalyst, due to the high acrolein content in the sample (0.05 M). Acrolein is a major catalyst poisoning component and must be fully removed to obtain optimum performance in an electrolysis cell.

To overcome the catalyst poisoning effect of acrolein, a first distilled bark pyrolysis oil fraction was treated with $NaHSO_3$ and NaOH (*Section 4.3.1.5*). The results for the redistilled first fraction ($NaHSO_3$, NaOH) in Figure 4.12 reached a maximum current of 15 mA at 680 s (vs. 32 mA for 1 M MeOH, 53% current reduction) which was slowly reduced to a negligibly small current compared to the previously untreated F1 sample, at 950 s. The redistilled sample showed a small performance improvement;

however, the acrolein content of 0.03 M in the redistilled sample still resulted in a significant long-term poisoning effect at the 70%Pt/C catalyst.

In comparison to the distillate samples, a permeate sample produced with a Nafion 112 membrane pervaporation of bark pyrolysis oil aqueous phase was injected. The chemical composition of identified components in the permeate sample are shown in (Table 4.8). The injection results in Figure 4.12 indicated a current reduction from 31 mA for 1 M MeOH to a maximum of 10 mA (ca. 750 s) for the injected permeate. The sample injection resulted in a long-term poisoning at the 70%Pt/C catalyst with a continuous current reduction of ca.4 mA at 1000 s. However, the overall performance of this sample showed that the reduced acrolein and acetic acid content helped to reduce the long-term catalyst poisoning compared to the other tested distillation samples. For a better comparison of the Nafion 112 permeate performance, a reference methanol sample with a similar concentration of 0.3 M was injected. The methanol sample reached a constant current of 17 mA after 800 s at 70%Pt/C.

The injection results for the 75%PtRu/C and the Pt/C PtRu/C mix (1:1) anodes in *Appendix 4.7.5* were similar compared to the 70%Pt/C results in Figure 4.12. 75%PtRu/C showed a reduced long-term poisoning effect of F1 (fractional distillation), with a current reduction from 19 mA at 700°s to 5 mA at 1200 s.

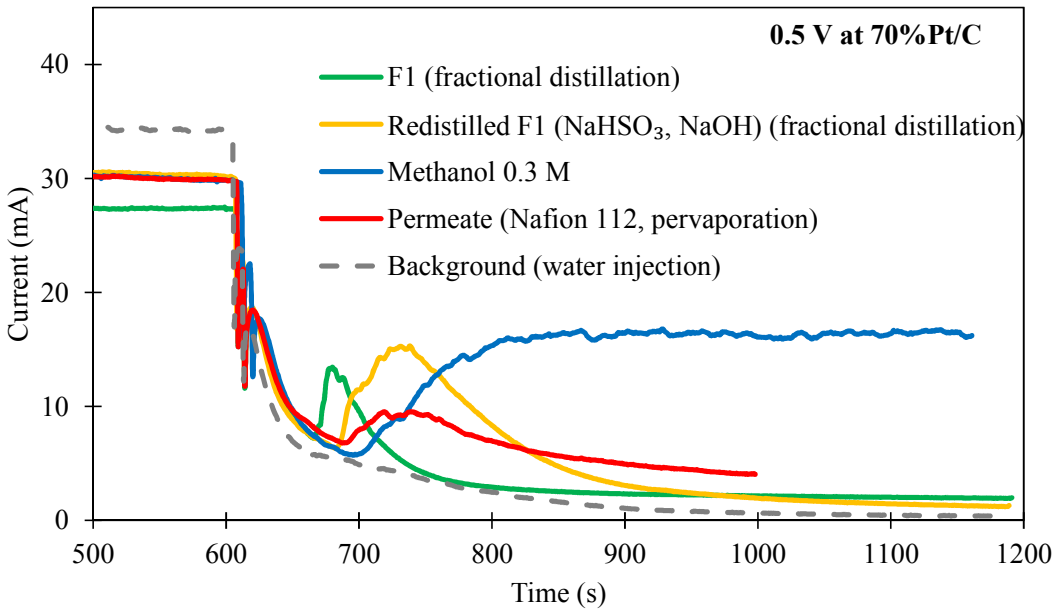

Figure 4.12: Current vs. time results of 1 M MeOH (0 to 600 s) at 70%Pt/C electrodes in an electrolysis cell operated at a constant potential of 0.5 V in anode polarization mode at 80 °C. Distillate and permeate samples were injected after being flushed with water at 600 s.

4.3.2 Pervaporation results

Instead of separating the low boiling point fractions via fractional distillation, this section focuses on pervaporation as a pyrolysis oil enhancement method. Pervaporation is a membrane separation technique in which substances permeate through a non-porous membrane and then evaporate on the other side (*Chapter 1* in *Section 1.2*). This technique allows separating of one or more components from a liquid feed into a vapour stream on the other side of the membrane. The vapour stream can be condensed (permeate). In this study, the permeate contained mainly water and some low boiling point components such as methanol, acetic acid, etc.. Polarization curves for electrolysis of two permeates were recorded at 70%Pt/C catalysts in anode polarization mode at

80 °C. Three different membranes were compared to separate water and low boiling point components (permeate) from the bark pyrolysis oil aqueous phase.

4.3.2.1 Permeate performance comparison in an electrolysis cell

A comparison between electrocatalytic oxidation performances of permeates in the electrolysis cell was carried out at 70%Pt/C , 75%PtRu/C, and Pt/C PtRu/C mix (1:1) anodes. The polarization curves for all permeates at 75%PtRu/C, and Pt/C mixed with PtRu/C (1:1) catalysts are reported in *Appendix 4.7.6.*The permeates were produced by the pervaporation of a bark pyrolysis oil aqueous phase. The pervaporation was conducted with commercially available membranes: a proton-conductive polymer fuel cell membrane (Nafion 211) and two commercially available polyvinyl alcohol (Pervap™) polymeric membranes. Nafion membranes are the most commonly used membranes for PEMFC. They are not typically utilized as pervaporation membranes, however due to their availability in the research lab, pervaporation with Nafion membranes was investigated.

DeltaMem's Pervap™ membranes were developed for dehydration and methanol removal and are based on a polyvinyl alcohol (PVA) separation layer. The difference between the two Pervap™ membranes used in this study was the degree of crosslinking in the polyvinyl alcohol (PVA) separation layer. The permeates obtained with a less crosslinked PVA separation layer membrane (Pervap 4155-30) and a highly crosslinked PVA layer (Pervap 4101) membrane were compared. The pervaporation process conditions for each pervaporation experiment are shown in Table 4.3 in *Section 4.2.3.3*. The chemical compositions of the permeates were determined by NMR (Table

4.9). The water selectivity increased with increased crosslinking of the PVA separation layer. The permeate separated via the highly crosslinked Pervap 4101 membrane showed significantly lower concentrations of organic components (e.g. methanol, acetic acid, and formic acid) compared to the permeate of the less crosslinked Pervap 4155-30 membrane. The 1H NMR spectra of the investigated permeate samples can be seen in *Appendix 4.7.3*. Further results on pervaporation experiments are described in *Chapter 2*.

Table 4.9: Chemical composition of components identified in the permeates determined by NMR

Component	Permeate Pervap 4155-30 (M)	Permeate Pervap 4101 (M)	Permeate Nafion 211 (M)
Methanol	0.54	0.14	0.62
Acetic acid	0.47	0.08	1.05
Acrolein	0.02	-	0.02
Acetol	0.21	0.04	0.18
Formic acid	0.04	0.02	0.14
Furfural	0.02	-	0.02
Glycolaldehyde	0.03	0.01	0.03
Isoeugenol	0.004	-	0.004

The permeates' electrochemical performance was investigated in the electrolysis cell. The permeate samples were tested as they were collected (crude permeate concentrations in Table 4.9) as well as with the addition of methanol to adjust the concentration of methanol to 1 M for the permeates separated with the Pervap membranes. A 1 M methanol polarization curve was plotted as a reference curve in Figure 4.13.

The results in Figure 4.13 indicate a poor performance of the crude Pervap 4155-30 permeate (red solid line) due to the high impurity content (acetic acid 0.47 M, acrolein 0.02 M, and acetol 0.21 M). The Pervap 4155-30 permeate with added methanol demonstrates a marginal current increase at potentials higher than 0.7 V (red dashed line). The Nafion 211 permeate resulted in an improved electrolysis cell performance compared to the Pervap 4155-30 permeate due to a slightly higher methanol content (0.62 M compared to 0.54 M) and an increased formic acid content (0.14 M compared to 0.04 M). Formic acid can easily be oxidized and therefore increased the current density of the tested Nafion 211 permeate sample.

The Pervap 4101 membrane with a higher crosslinked PVA separation layer was more selective for water than the Pervap 4155-30 membrane. Therefore, the Pervap 4101 permeate water content was higher (≥ 98 mass% compared to 91 mass% of the Pervap 4155-30 permeate) with less organic impurities (Table 4.9). This overall poor electrolysis cell performance of the Pervap 4101 permeate (blue solid line), with a current density of less than 100 mA cm^{-2} at 0.9 V, was a reflection of the low content of oxidizable components (methanol content of 0.14 M) relative to the 1 M methanol reference curve (Figure 4.13).

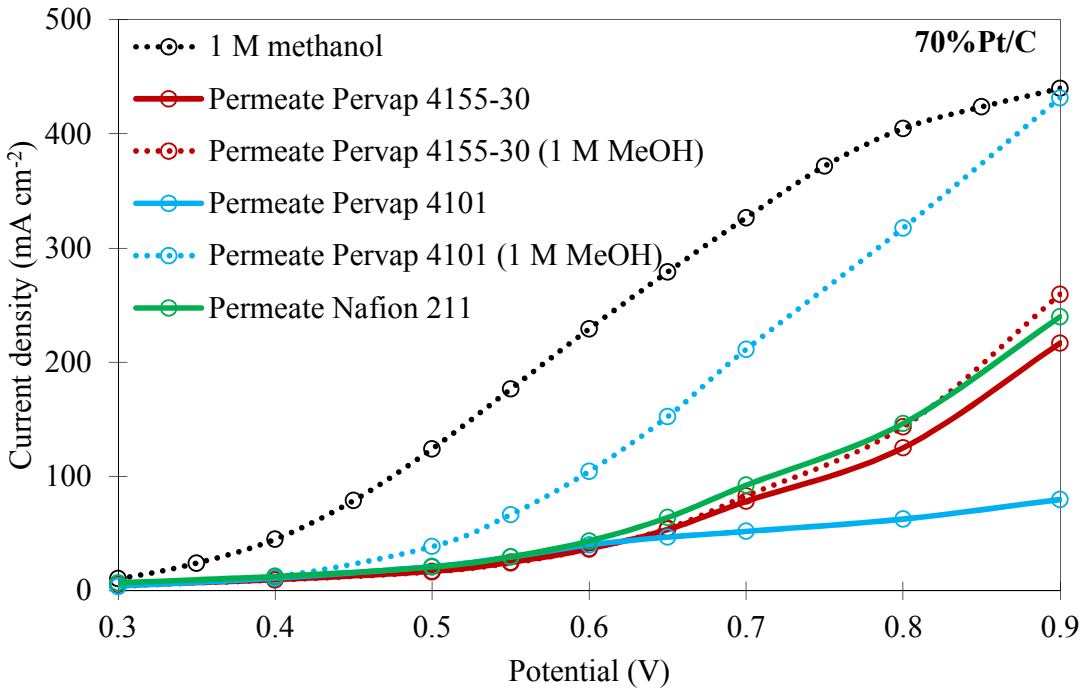

Figure 4.13: Polarization curves of crude Nafion 211, Pervap 4155-30, and Pervap 4101 permeate samples and samples with an adjusted methanol content to 1 M at 70%Pt/C in anode polarization mode at 80 °C.

When the methanol content was spiked to 1 M in the Pervap 4101 permeate (blue dashed line) there was a significant current increase for potentials above 0.4 V compared to the crude Pervap 4101 permeate (blue solid line). Compared to the 1 M methanol reference polarization curve the half wave potential shifted from 0.6 to 0.7 V. The decreased impurity content and the lack of acrolein increased the permeate performance in the electrolysis cell compared to the Pervap 4155-30 sample.

For the 75%PtRu/C and the Pt/C PtRu/C mix (1:1) anodes the results were similar, but PtRu had a reduced tolerance level for the impurities. Therefore, the current

densities for 75%PtRu/C were lower compared to 70%Pt/C. The mixed catalyst followed the PtRu trend with slightly increased current densities.

The results were compared to Hibino et al. who used waste newspaper as a feedstock for a sustainable hydrogen production via electrolysis [13]. This process was used as a reference case since it was a direct electrolysis process of a waste stream. Hibino's method involved making a paste of waste newspaper with phosphoric acid (H_3PO_4) [13]. This paste was then directly deposited on the anode. Hibino's oxidation results in a batch electrolysis cell at Pt/C showed a current density of 100 mA cm^{-2} at 0.8 V and 100 °C [13]. The Nafion 211 permeate reported here (Figure 4.13) produced a higher current density than Hibino's sample, of 146 mA cm^{-2} at 80 °C and 0.8 V. The oxidized Pervap 4155-30 permeate showed a slightly higher current density than Hibino's of 125 mA cm^{-2} at 80 °C and 0.8 V. The crude 4101 permeate resulted in a lower current density of 63 mA cm^{-2} at 0.8 V. Overall, the oxidation process of the "waste" low boiling point mixture from the pyrolysis oil enhancement resulted in higher current densities at a reduced temperature of 80 °C compared to [13]. Additionally, the oxidation of permeates preserves non-oxidizable value-added chemicals (acetic acid, acetol etc.) in the electrolysis cell outlet.

4.4 Summary

Fractional distillation and pervaporation processes have been investigated as methods to separate low boiling point components including water from softwood and bark pyrolysis oil to both meet ASTM D7544-12 standard requirements and produce a value-added by-product. The low boiling point distillate/permeates were used as a fuel

in an electrolysis cell to produce renewable hydrogen, and preserve non-oxidizable value-added chemicals. The separation of water and low boiling point components from the bark pyrolysis oil aqueous phase was monitored through NMR analysis of the permeates and distillates. Aside from water, the main identified low boiling point components were acetic acid, methanol, acetol, and formic acid. Furthermore, the mixtures contained minor components such as acrolein, glycolaldehyde, isoeugenol, and furfural.

Analysis of distillate factions demonstrated that the concentrations of low boiling point (<100 °C) methanol (1.86 to 0.05 M) and acrolein (0.05 to 0.02 M) decreased with increasing fraction numbers (1 to 10). On the other hand, the higher boiling point (>100 °C) formic acid (0.09 to 0.22 M), and acetol (0.12 to 0.20 M) concentrations increased with fraction number. The acetic acid concentration changed from 1.68 M in fraction 1 to a minimum of 0.92 M in fraction 2, and then increases steadily until fraction 10 (1.39 M).

Polarization curves for the separate low boiling point distillates show that it is possible to oxidize the mixture in an electrolysis cell. However, the current densities are lower than expected based on the methanol content. The onset potential was shifted from 0.3 V for the 1 M methanol reference curve to 0.5 V for the distillate sample (1.84 M MeOH). The oxidation of the distillate sample at 70%Pt/C and 75%PtRu/C displays little difference between the catalysts. This was reflected in the similar current densities of 128 mA cm^{-2} for 70%Pt/C and 137 mA cm^{-2} for 75%PtRu/C at 0.9 V. The

limited performance of the distillate sample in the electrolysis cell was due to the direct influence/poisoning of impurities on the catalyst in anode polarization mode.

To analyze catalyst poisoning effects of the impurities, steady-state polarization curves were recorded with artificial mixtures. All impurities (acetic acid, acetol, and acrolein added to 1 M MeOH) influence the electrolysis cell performance at Pt black by lowering the limiting current below 225 mA cm^{-2} and shifting the half wave potential to potentials above 0.55 V. Acrolein shows a major poisoning effect on the electrolysis cell performance and needs to be entirely removed from the electrolysis cell feed. Therefore, a treatment with sodium bisulfite to eliminate acrolein was investigated.

The treatment to eliminate acrolein with sodium bisulfite, as well as the treatment with sodium hydroxide to reduce the acid content, was followed by an additional fractional distillation step and showed no significant current density improvement. Even though acrolein was eliminated, it reformed in an equilibrium reaction at elevated temperatures when distilling (100 °C, atmospheric pressure). To quickly investigate the sample's performance in the electrolysis cell an injection method requiring a small sample volume was developed.

The developed injection method proved to be a quick screening tool to characterize the effect of impurities on electrolysis cell performance with a small sample volume. At 0.5 V the validation with single impurities added to 1 M methanol solution showed a current reducing effect of acetic acid (0.1 M and 1 M) and acetol (0.1 M) at 70%Pt/C. The first distillate fraction of a bark pyrolysis oil showed a current

drop from 13 mA to ca. 5 mA 200 s after the injecting due to significant poisoning effects. The redistilled sample treated with $NaHSO_3$ and NaOH still showed poisoning of 70%Pt/C 300 s after the injection. The impurities in the permeate (Nafion 112 pervaporation) showed a strong poisoning effect as well. The injection method proved to be a quick analysis method requiring only a small volume (1 mL) sample, to investigate the poisoning effects on the catalysts.

Additionally to fractional distillation, a pervaporation separation method was used to separate water and other low boiling point components from the bark oil aqueous phase. A Nafion fuel cell membrane and two pervaporation membranes (Pervap 4155-30 and Pervap 4101) were investigated. To compare differences in permeates produced with those membranes, steady-state polarization curves were recorded for the permeate samples in an electrolysis cell operated in anode polarization mode at 80 °C. The results indicate the possibility of oxidizing the permeate samples at a 70%Pt/C catalyst. The onset potential was at 0.5 V for all samples. The Nafion 211 permeate with a methanol content of 0.62 M resulted in a current density of 146 mA cm^{-2} at 0.8 V. The 4155-30 permeate showed a current density of 125 mA cm^{-2} for a methanol content of 0.54 M (vs. 144 mA cm^{-2}, with MeOH content adjusted to 1 M) at 0.8 V. The water-rich (≥ 98 mass%) 4101 permeate with a lower organic impurity content results in a lower current density of 63 mA cm^{-2} (0.14 M methanol, 0.8 V) and shows a significant current density increase to 317 mA cm^{-2} (0.8 V) for the same permeate sample with a methanol content adjusted to 1 M. The results indicate a good oxidization performance of the studied components in the electrolysis cell for

renewable hydrogen production at low potentials (<0.9 V). Comparing these values to the literature shows that our process, results in higher current densities at a reduced temperature of 80 °C. Hibino's results at Pt/C in a batch electrolysis cell shows a current density of 100 mA cm^{-2} at 0.8 V and 100 °C [13].

Overall, it was possible to enhance the pyrolysis oil to ASTM D7544-12 standard conditions with the Pervap 4101 membrane (80 °C, 0.1 mL min^{-1}) and oxidize the separated water and low boiling point component permeate mixture successfully at low potentials (<0.9 V) in an electrolysis cell to produce hydrogen (current density >400 mA cm^{-2} at 0.9 V, Permeate Pervap 4101, MeOH added to 1 M). The remaining value-added components which were not oxidizing to hydrogen at low potentials (acetic acid, acetol, e.g.) can be separated and sold individually for other applications.

4.5 Acknowledgements

This work was supported by the Centre for Forest Science and Innovation (CFSI, NL Provincial Government), the Natural Sciences and Engineering Research Council of Canada (NSERC) (grant number 2017-04260) and Memorial University of Newfoundland (MUN). We would like to thank Dr. Celine Schneider who helped to identify the components by NMR, Shofiur Md. Rahman and Brittany Traverse who carried out the short-path distillations and Mareike Serra for her help during her bachelor thesis.

4.6 References

[1] Abbas HF, Wan Daud WMA. Hydrogen production by methane decomposition: A review. Int J Hydrogen Energy 2010;35:1160–90. doi:10.1016/j.ijhydene.2009.11.036.

[2] Chen G, Tao J, Liu C, Yan B, Li W, Li X. Hydrogen production via acetic acid steam reforming: A critical review on catalysts. Renew Sustain Energy Rev 2017;79:1091–8. doi:10.1016/j.rser.2017.05.107.

[3] Bimbela F, Ábrego J, Puerta R, García L, Arauzo J. Catalytic steam reforming of the aqueous fraction of bio-oil using Ni-Ce/Mg-Al catalysts. Appl Catal B Environ 2017;209:346–57. doi:10.1016/j.apcatb.2017.03.009.

[4] Medrano JA, Oliva M, Ruiz J, García L, Arauzo J. Hydrogen from aqueous fraction of biomass pyrolysis liquids by catalytic steam reforming in fluidized bed. Energy 2011;36:2215–24. doi:10.1016/j.energy.2010.03.059.

[5] Wang D, Czernik S, Montané D, Mann M, Chornet E. Biomass to Hydrogen via Fast Pyrolysis and Catalytic Steam Reforming of the Pyrolysis Oil or Its Fractions. Ind Eng Chem Res 1997;36:1507–18. doi:10.1021/ie960396g.

[6] Ayalur Chattanathan S, Adhikari S, Abdoulmoumine N. A review on current status of hydrogen production from bio-oil. Renew Sustain Energy Rev 2012;16:2366–72. doi:10.1016/j.rser.2012.01.051.

[7] Garcia L, French R, Czernik S, Chornet E. Catalytic steam reforming of bio-oils

for the production of hydrogen: Effects of catalyst composition. Appl Catal A Gen 2000;201:225–39. doi:10.1016/S0926-860X(00)00440-3.

[8] Parthasarathy P, Narayanan KS. Hydrogen production from steam gasification of biomass: Influence of process parameters on hydrogen yield - A review. Renew Energy 2014;66:570–9. doi:10.1016/j.renene.2013.12.025.

[9] Wang D, Czernik S, Chornet E. Production of hydrogen from biomass by catalytic steam reforming of fast pyrolysis oils. Energy and Fuels 1998;12:19–24. doi:10.1021/ef970102j.

[10] Xie H, Yu Q, Wang K, Shi X, Li X. Thermodynamic Analysis of Hydrogen Production from Model Compounds of Bio-oil Through Steam Reforming. Environ Prog Sustain Energy 2014;33:1008–16. doi:10.1002/ep.

[11] Take T, Tsurutani K, Umeda M. Hydrogen production by methanol-water solution electrolysis. J Power Sources 2007;164:9–16. doi:10.1016/j.jpowsour.2006.10.011.

[12] Buttler A, Spliethoff H. Current status of water electrolysis for energy storage, grid balancing and sector coupling via power-to-gas and power-to-liquids: A review. Renew Sustain Energy Rev 2018;82:2440–54. doi:10.1016/j.rser.2017.09.003.

[13] Hibino T, Kobayashi K, Ito M, Nagao M, Fukui M, Teranishi S. Direct electrolysis of waste newspaper for sustainable hydrogen production: an oxygen-

functionalized porous carbon anode. Appl Catal B Environ 2018;231:191–9. doi:10.1016/j.apcatb.2018.03.021.

[14] Hibino T, Kobayashi K, Ito M, Ma Q, Nagao M, Fukui M, et al. Efficient Hydrogen Production by Direct Electrolysis of Waste Biomass at Intermediate Temperatures. ACS Sustain Chem Eng 2018;6:9360–8. doi:10.1021/acssuschemeng.8b01701.

[15] You B, Sun Y. Innovative Strategies for Electrocatalytic Water Splitting. Acc Chem Res 2018;51:1571–80. doi:10.1021/acs.accounts.8b00002.

[16] Lu L, Ren ZJ. Microbial electrolysis cells for waste biorefinery: A state of the art review. Bioresour Technol 2016;215:254–64. doi:10.1016/j.biortech.2016.03.034.

[17] Ju HK, Giddey S, Badwal SPS. The role of nanosized SnO2 in Pt-based electrocatalysts for hydrogen production in methanol assisted water electrolysis. Electrochim Acta 2017;229:39–47. doi:10.1016/j.electacta.2017.01.106.

[18] ASTM International. ASTM D7544 Standard Specification for Pyrolysis Liquid Biofuel. 2012. doi:10.1520/D7544-12.2.

[19] Branca C, Giudicianni P, Di Blasi C. GC/MS characterization of liquids generated from low-temperature pyrolysis of wood. Ind Eng Chem Res 2003;42:3190–202. doi:10.1021/ie030066d.

[20] Zhang L, Liu R, Yin R, Mei Y. Upgrading of bio-oil from biomass fast pyrolysis

in China: A review. Renew Sustain Energy Rev 2013;24:66–72. doi:10.1016/j.rser.2013.03.027.

[21] Stas M, Kubic D, Chudoba J, Posp M. Overview of Analytical Methods Used for Chemical Characterization of Pyrolysis Bio-oil. Energy & Fuels 2014;28:385–402. doi:10.1021/ef402047y.

[22] Elliott DC, Oasmaa A, Meier D, Preto F, Bridgwater A V. Results of the IEA Round Robin on Viscosity and Aging of Fast Pyrolysis Bio-oils : Long-Term Tests and Repeatability. Energy & Fuels 2012:7362–6. doi:10.1021/ef301607v.

[23] Krutof A, Hawboldt K. Blends of pyrolysis oil, petroleum, and other bio-based fuels: A review. Renew Sustain Energy Rev 2016;59:406–19. doi:10.1016/j.rser.2015.12.304.

[24] Balat M, Balat M, Kirtay E, Balat H. Main routes for the thermo-conversion of biomass into fuels and chemicals. Part 1: Pyrolysis systems. Energy Convers Manag 2009;50:3147–57. doi:10.1016/j.enconman.2009.08.014.

[25] Lehto J, Oasmaa A, Solantausta Y, Kytö M, Chiaramonti D. Fuel oil quality and combustion of fast pyrolysis bio-oils. 2013. doi:http://dx.doi.org/10.1016/j.apenergy.2013.11.040.

[26] Oasmaa A, Fonts I, Pelaez-Samaniego MR, Garcia-Perez ME, Garcia-Perez M. Pyrolysis Oil Multiphase Behavior and Phase Stability: A Review. Energy and Fuels 2016;30:6179–200. doi:10.1021/acs.energyfuels.6b01287.

[27] Papari S, Hawboldt K, Helleur R. Production and Characterization of Pyrolysis Oil from Sawmill Residues in an Auger Reactor. Ind Eng Chem Res 2017;56:1920–5. doi:10.1021/acs.iecr.6b04405.

[28] Rahman S, Helleur R, MacQuarrie S, Papari S, Hawboldt K. Upgrading and isolation of low molecular weight compounds from bark and softwood bio-oils through vacuum distillation. Sep Purif Technol 2018;194:123–9. doi:10.1016/j.seppur.2017.11.033.

[29] TutorVista. Fractional Distillation 2017. source: http://chemistry.tutorvista.com/inorganic-chemistry/fractional-distillation.html (accessed September 25, 2017).

[30] Brueckner TM, Pickup PG. Kinetics and Stoichiometry of Methanol and Ethanol Oxidation in Multi-Anode Proton Exchange Membrane Cells. J Electrochem Soc 2017;164:1172–8. doi:10.1149/2.1181712jes.

[31] Majidi P, Altarawneh RM, Ryan NDW, Pickup PG. Determination of the efficiency of methanol oxidation in a direct methanol fuel cell. Electrochim Acta 2016;199:210–7. doi:10.1016/j.electacta.2016.03.147.

[32] Vitasari CR, Meindersma GW, De Haan AB. Laboratory scale conceptual process development for the isolation of renewable glycolaldehyde from pyrolysis oil to produce fermentation feedstock. Green Chem 2012;14:321–5. doi:10.1039/c1gc16200d.

[33] Diebold JP. A Review of the Chemical and Physical Mechanisms of the Storage Stability of Fast Pyrolysis Bio-Oils. 2000. doi:NREL/SR-570-27613.

[34] Diebold JP. A Review of the Toxicity of Biomass Pyrolysis Liquids Formed at Low Temperatures. 1997. doi:NREL/TP-430-22739.

4.7 Appendix

4.7.1 Pyrolysis oils composition [28]

The following GC-FID composition analysis, carried out with a different batch of bark pyrolysis oil made using the same wood feedstock and pyrolysis reactor, is reproduced from [28] to provide analytical information on the type of bark oil employed in this work. A short-path vacuum distillation was employed to separate a light molecular weight distillate fraction from bark pyrolysis oil.

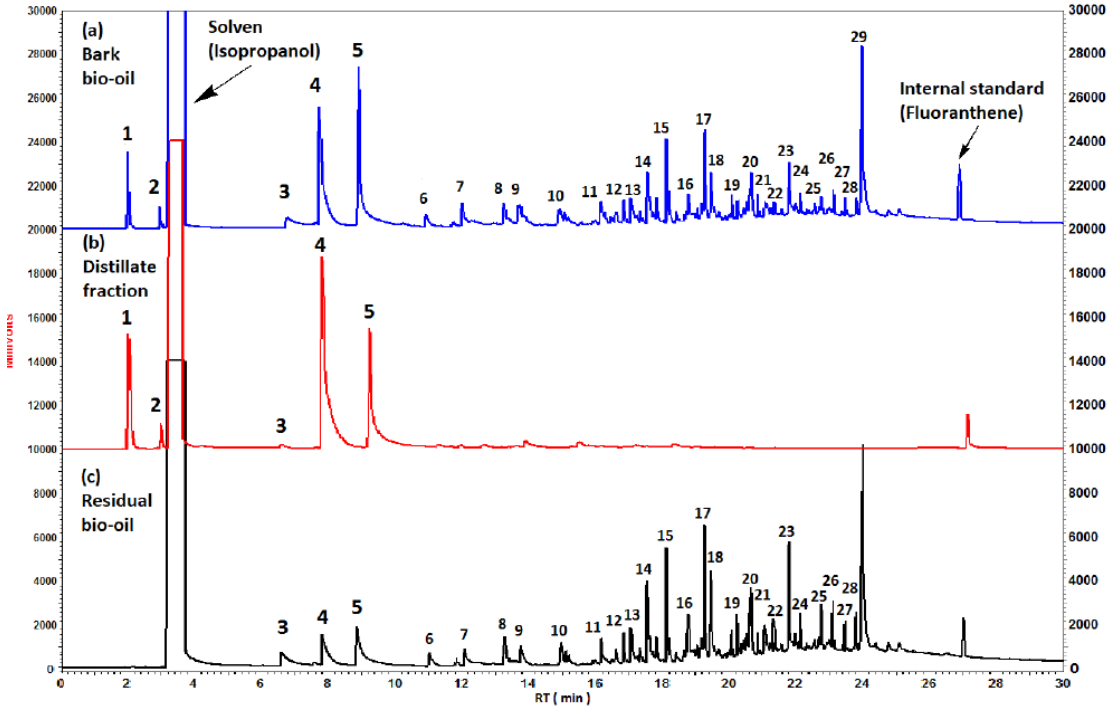

Figure 4.14: GC-FID chromatograms for (a) bark bio-oil, (b) distillate fraction, and (c) residual bark bio-oil after 1 h at 100 ºC [28].

Table 4.10: Identification of significant compounds present in shavings and bark bio-oil samples by GC-MS [28].

Peak #	RT (min)	Compound	Peak #	RT (min)	Compound
1	2.02	Methanol	16	18.18	Guaiacol
2	2.79	Acrolein	17	18.80	3-Hydroxymethylfurfural
3	6.65	Glycolaldehyde	18	19.26	4-Methyl-guaiacol
4	8.15	Acetic acid	19	19.47	4-Ethyl-guaiacol
5	8.90	Acetol	20	20.10	4-Vinylguaiacol
6	11.98	Furfural	21	20.86	Eugenol
7	12.35	2-Furfuryl alcohol	22	21.13	4-Propyl-guaiacol
8	13.26	2,3-Butanedione	23	21.18	Syringol
9	13.71	2-Acetylfuran	24	22.13	4-Methyl-syringol
10	15.19	3-Methyl-2,5-furandione	25	22.77	Vanillin
11	16.14	5-Methyl-2-furaldehyde	26	23.12	4-Ethylsyringol
12	16.56	3-Methyl-2,5-furandione	27	23.48	4-Allylsyringol
13	16.88	5-Methyl-2-furaldehyde	28	23.83	Syringaldehyde
14	17.03	5-Methyl-2,5-furandione	29	24.01	Levoglucosan
15	17.56	(5H)-Furan-2-one			

4.7.2 Distillate composition (fractional distillation, bark pyrolysis oil)

Table 4.11: Chemical composition of components identified in the distillate fractions determined by NMR

Component	F1 (M)	F2 (M)	F3 (M)	F4 (M)	F5 (M)	F6 (M)	F7 (M)	F8 (M)	F9 (M)	F10 (M)
Methanol	1.86	1.03	0.82	0.58	0.39	0.26	0.19	0.11	0.08	0.05
Acetic acid	1.68	0.93	1.00	1.04	1.07	1.07	1.20	1.20	1.31	1.39
Acrolein	0.05	0.04	0.04	0.03	0.03	0.03	0.03	0.02	0.02	0.02
Acetol	0.12	0.11	0.16	0.15	0.15	0.15	0.17	0.17	0.19	0.21
Formic acid	0.09	0.11	0.12	0.13	0.14	0.15	0.17	0.18	0.20	0.22
Furfural	0.00	0.04	0.04	0.03	0.03	0.03	0.03	0.02	0.02	0.02
Glycolaldehyde	0.02	0.022	0.03	0.04	0.04	0.04	0.04	0.04	0.05	0.05
Isoeugenol	0.01	0.010	0.02	0.01	0.01	0.01	0.01	0.01	0.01	0.01
Water content (mass%)		83.6				87.3				85.4

4.7.3 1H NMR spectra

Table 4.12: Identified components in the distillates and permeates samples by 1H NMR.

Peak #	Shift (ppm)	H's	Compound
1	9.38	1	Acrolein
2	8.12	1	Formic acid
3	7.79	1	Furfural
4	6.70	2	Fumaric acid (internal standard)
5	4.73		D_2O (solvent peak)
6	4.26	2	Acetol
7	3.74	3	Isoeugenol
8	3.36	2	Glycolaldehyde
9	3.24	3	Methanol
10	1.97	3	Acetic acid

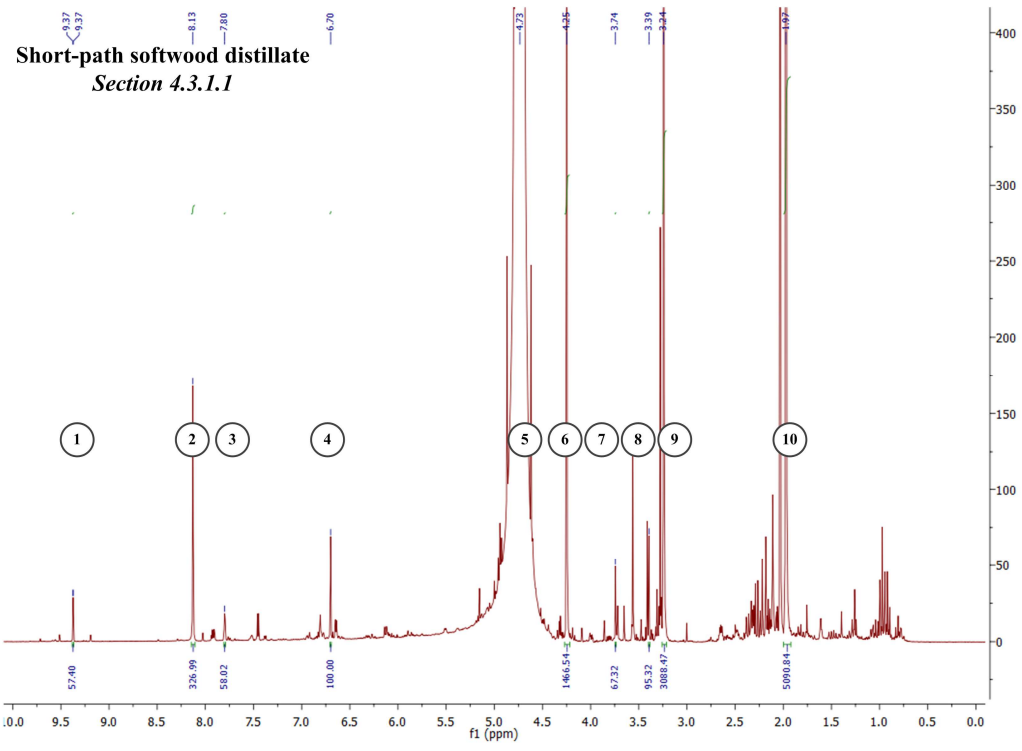

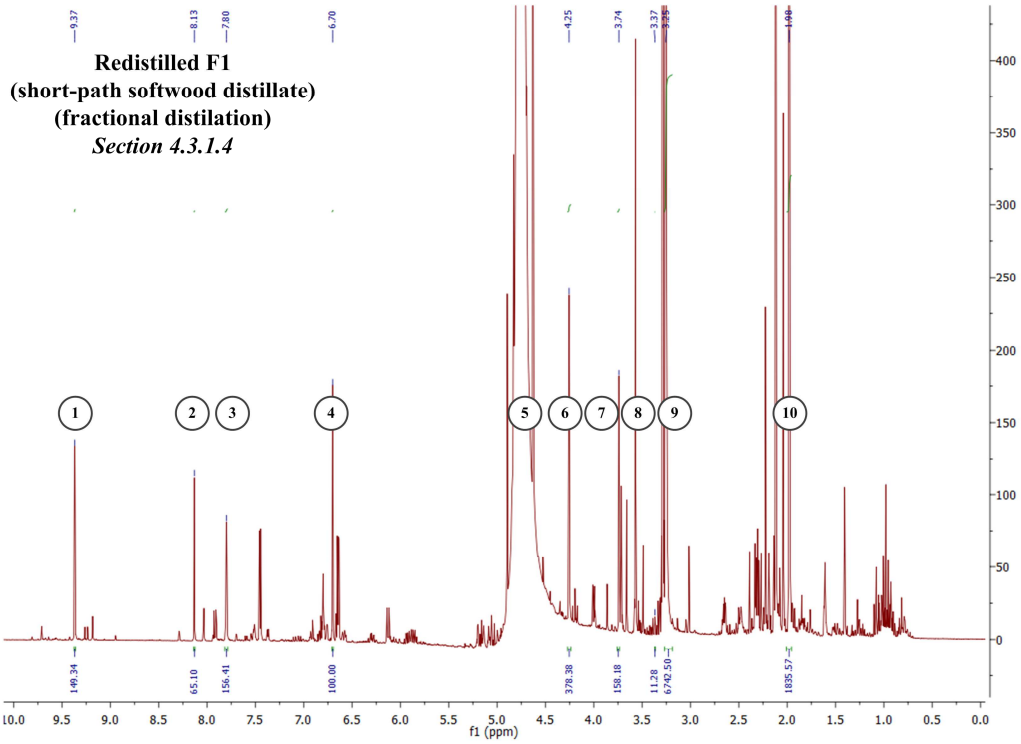
Redistilled F1
(short-path softwood distillate)
(fractional distilation)
Section 4.3.1.4
1
2
3
4
5
6
7
8
9
10
f1 (ppm)

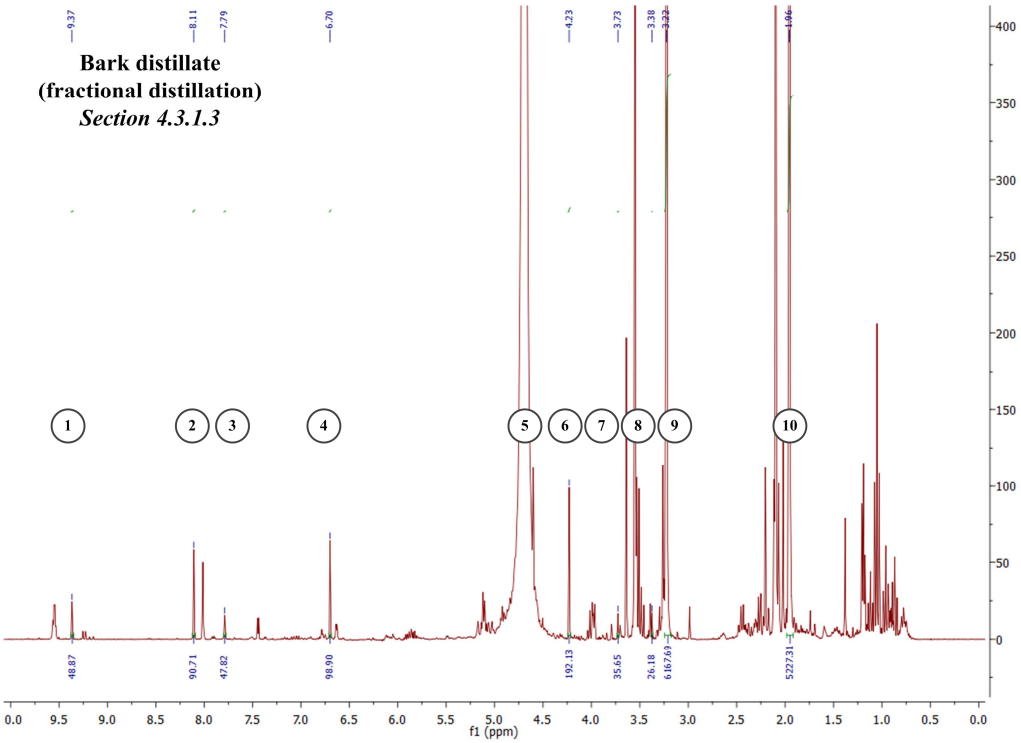
Bark distillate
(fractional distillation)
Section 4.3.1.3
1
2
3
4
5
6
7
8
9
10
f1 (ppm)

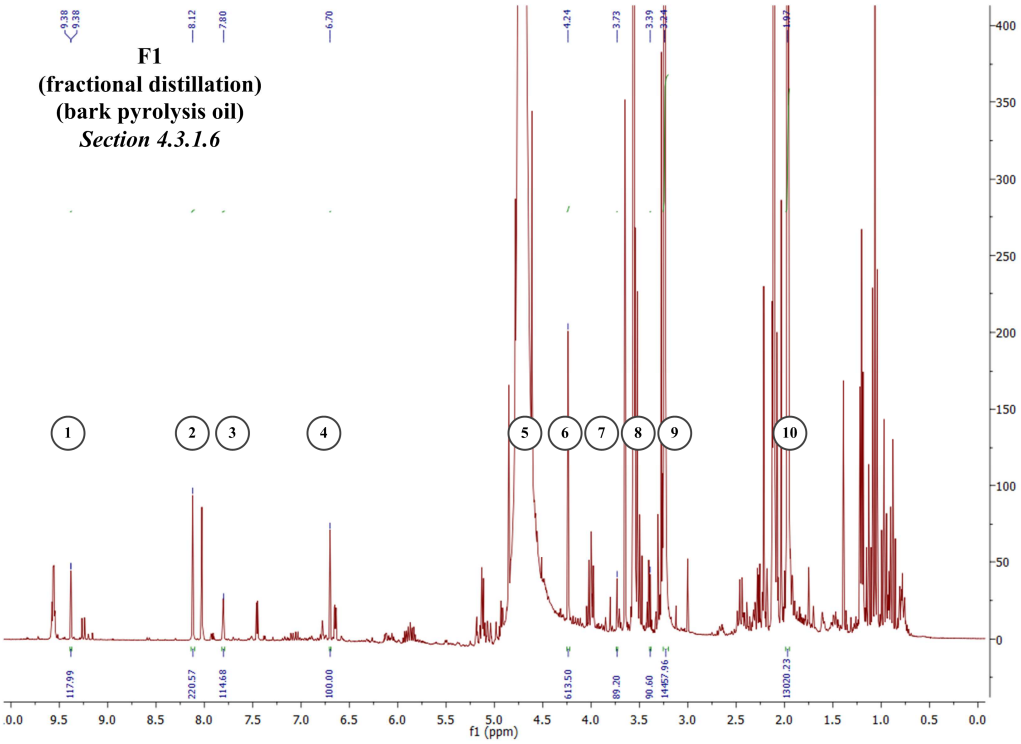
F1
(fractional distillation)
(bark pyrolysis oil)
Section 4.3.1.6
1
2
3
4
5
6
7
8
9
10
f1 (ppm)

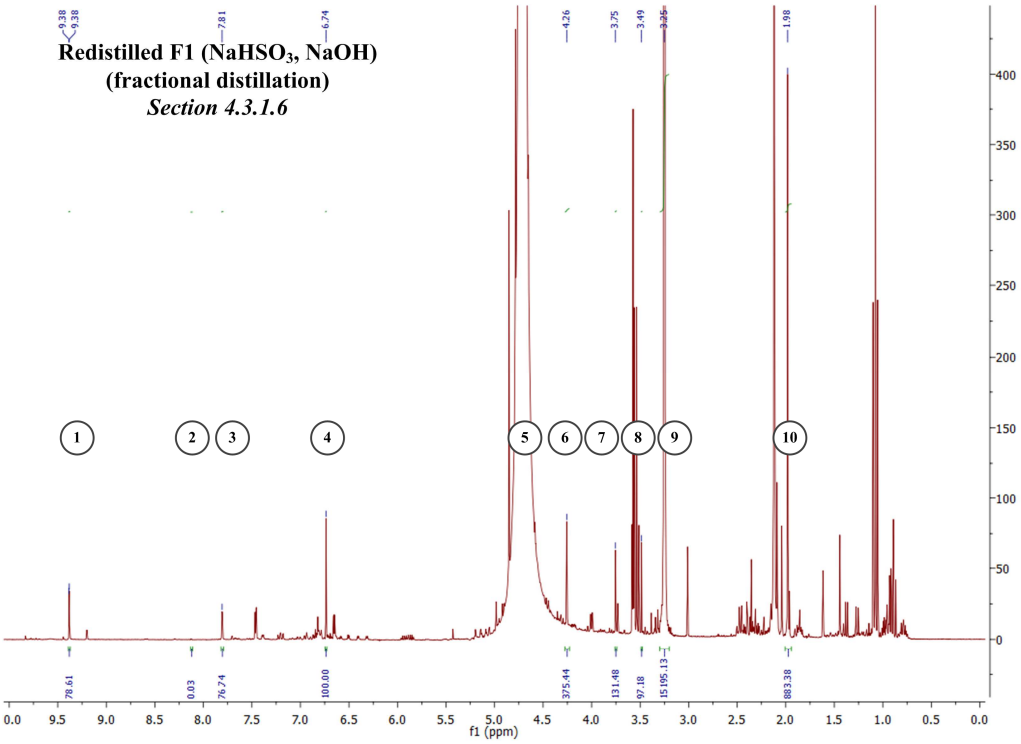
Redistilled F1 (NaHSO3, NaOH)
(fractional distillation)
Section 4.3.1.6
1
2
3
4
5
6
7
8
9
10
f1 (ppm)

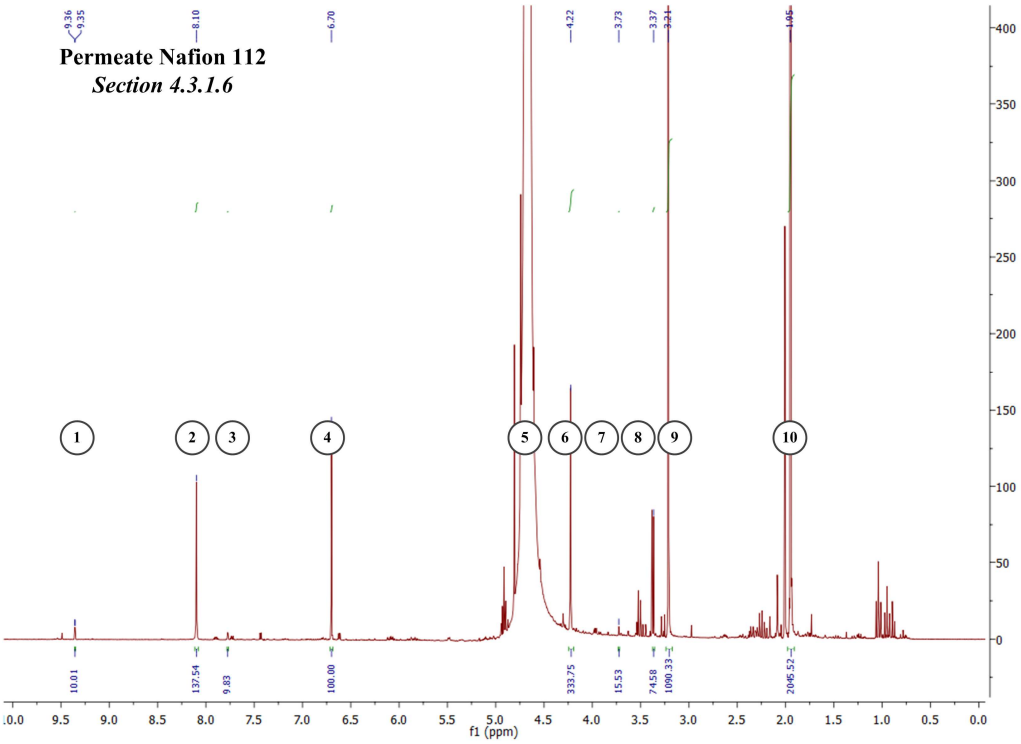
Permeate Nafion 112
Section 4.3.1.6
1
2
3
4
5
6
7
8
9
10
f1 (ppm)

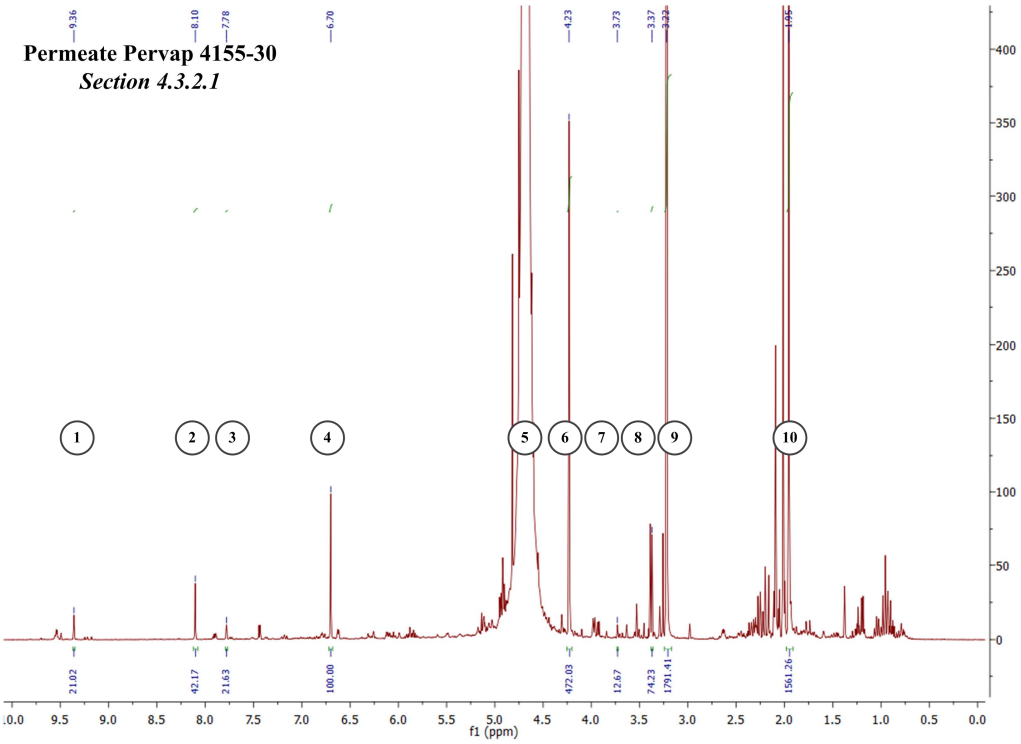
Permeate Pervap 4155-30
Section 4.3.2.1
1
2
3
4
5
6
7
8
9
10
f1 (ppm)

Permeate Pervap 4101
Section 4.3.2.1

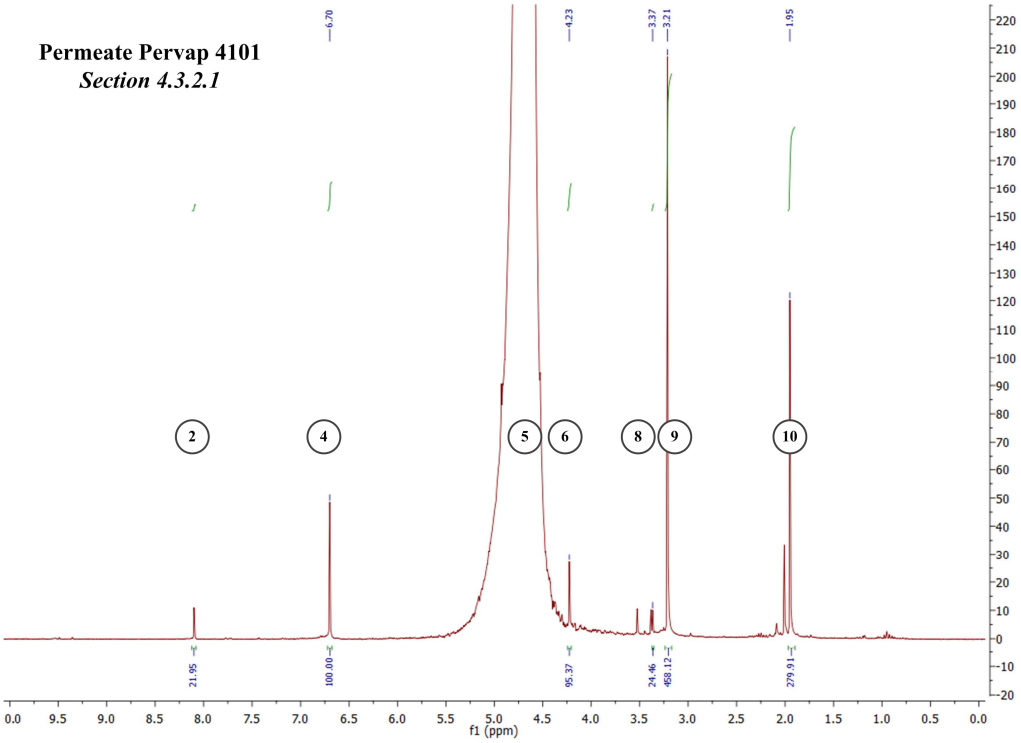

Permeate Nafion 211
Section 4.3.2.1

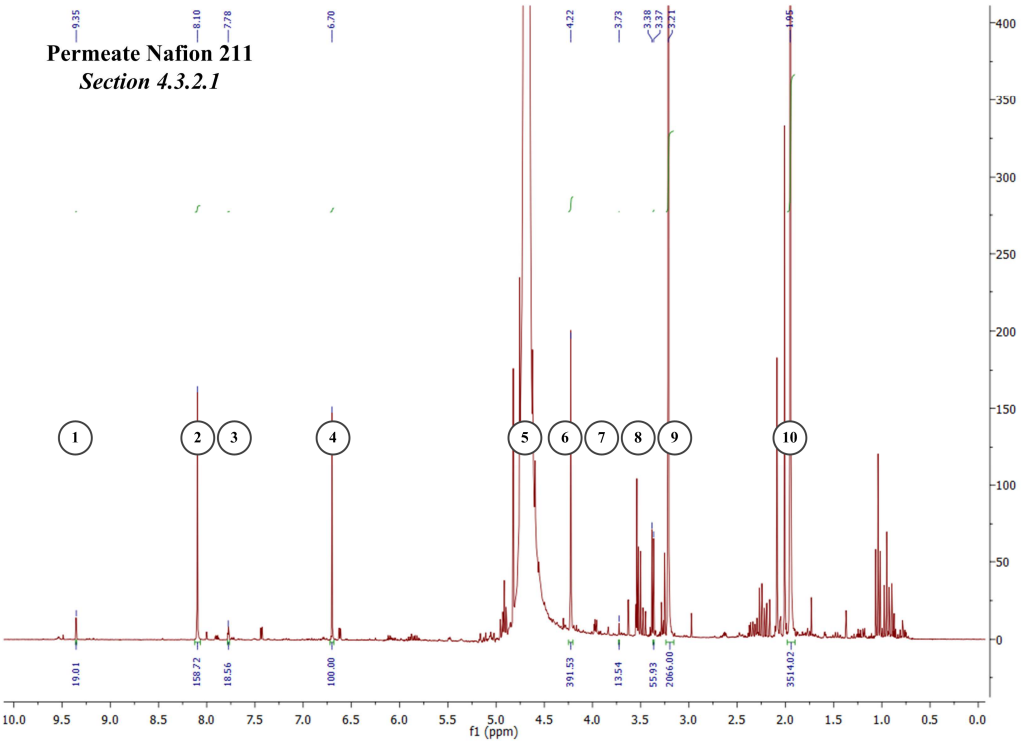

4.7.4 Reproducibility curves for the injection experiments

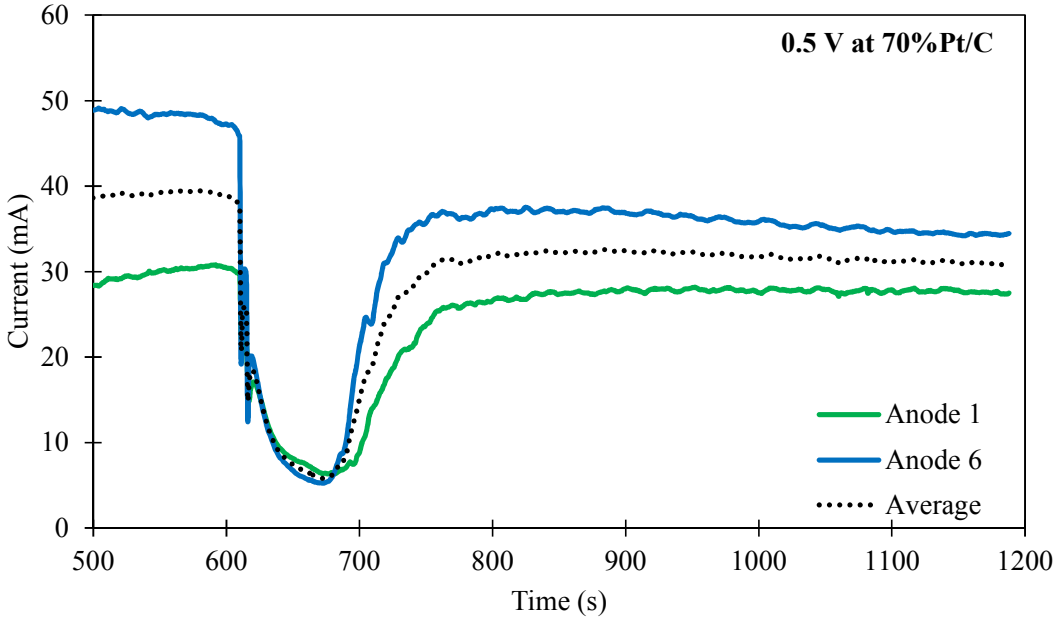

Figure 4.15: Current vs. time injection results of 1 M methanol + 0.1 M acetic acid at two 70%Pt/C anodes at 80 °C, 0.5 V in anode polarization mode.

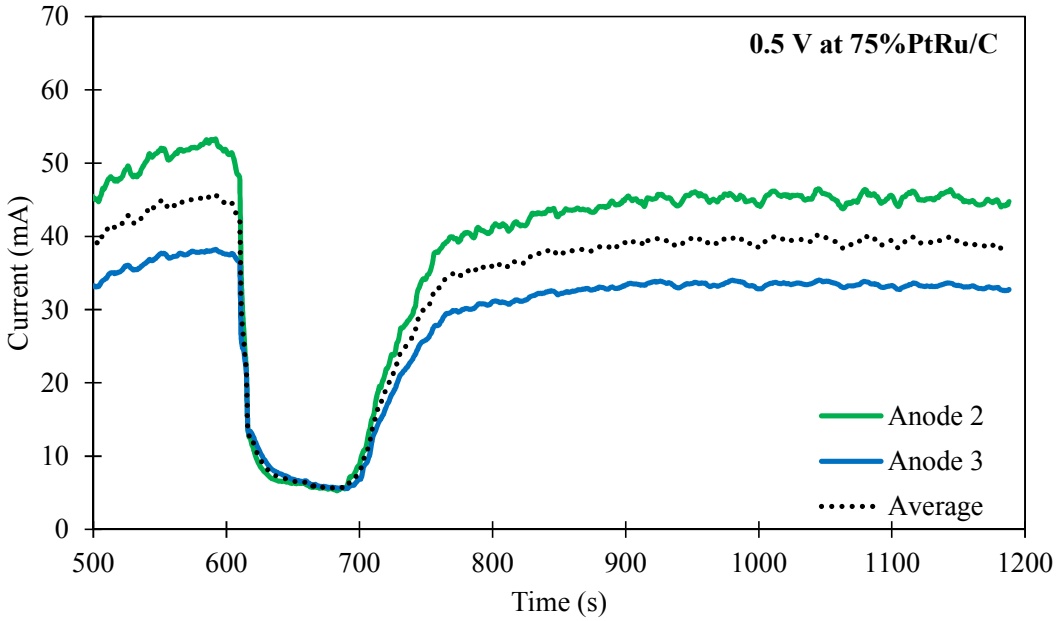

Figure 4.16: Current vs. time injection results of 1 M methanol + 0.1 M acetic acid at two 75%PtRu/C anodes at 80 °C, 0.5 V in anode polarization mode.

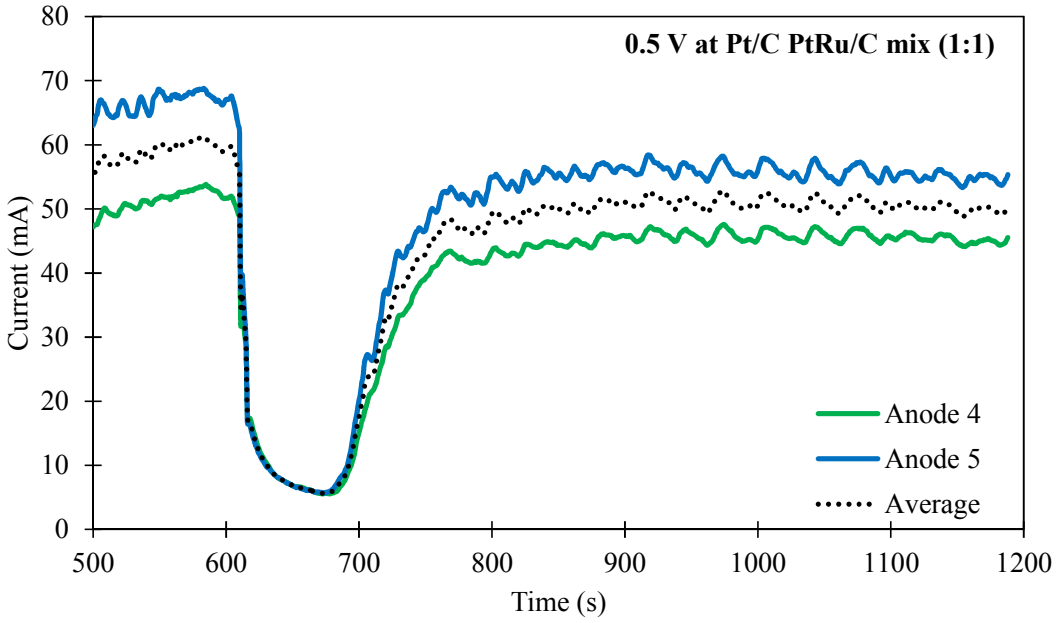

Figure 4.17: Current vs. time injection results of 1 M methanol + 0.1 M acetic acid at two Pt/C PtRu/C mix (1:1) anodes at 80 °C, 0.5 V in anode polarization mode.

4.7.5 Injection experiments 75%PtRu/C and Pt/C PtRu/C mix (1:1) plots

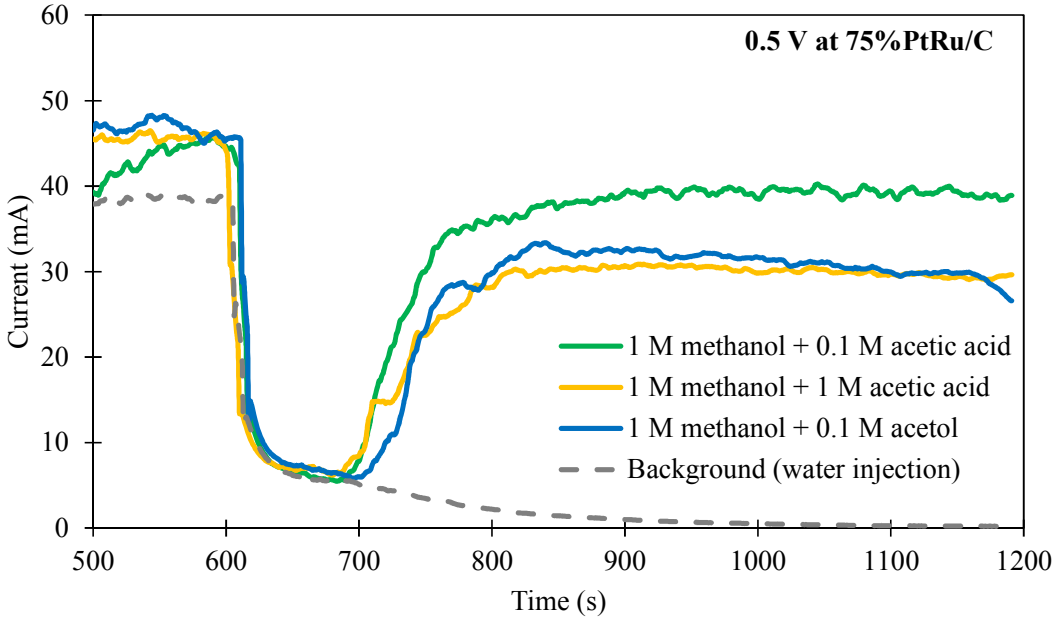

Figure 4.18: Current vs. time results of 1 M MeOH (0 to 600 s) at 75%PtRu/C electrodes in an electrolysis cell operated at a constant potential of 0.5 V in anode polarization mode at 80 °C. The samples (1 M MeOH + impurity component) were injected after being flushed with water at 600 s.

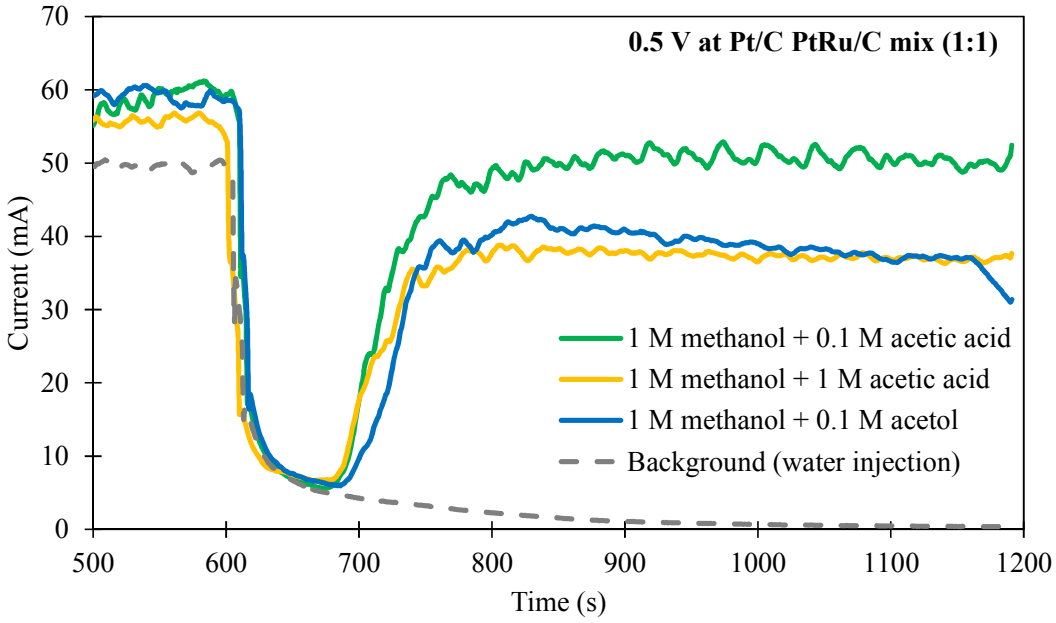

Figure 4.19: Current vs. time results of 1 M MeOH (0 to 600 s) at Pt/C PtRu/C mix (1:1) electrodes in an electrolysis cell operated at a constant potential of 0.5 V in anode polarization mode at 80 °C. The samples (1 M MeOH + impurity component) were injected after being flushed with water at 600 s.

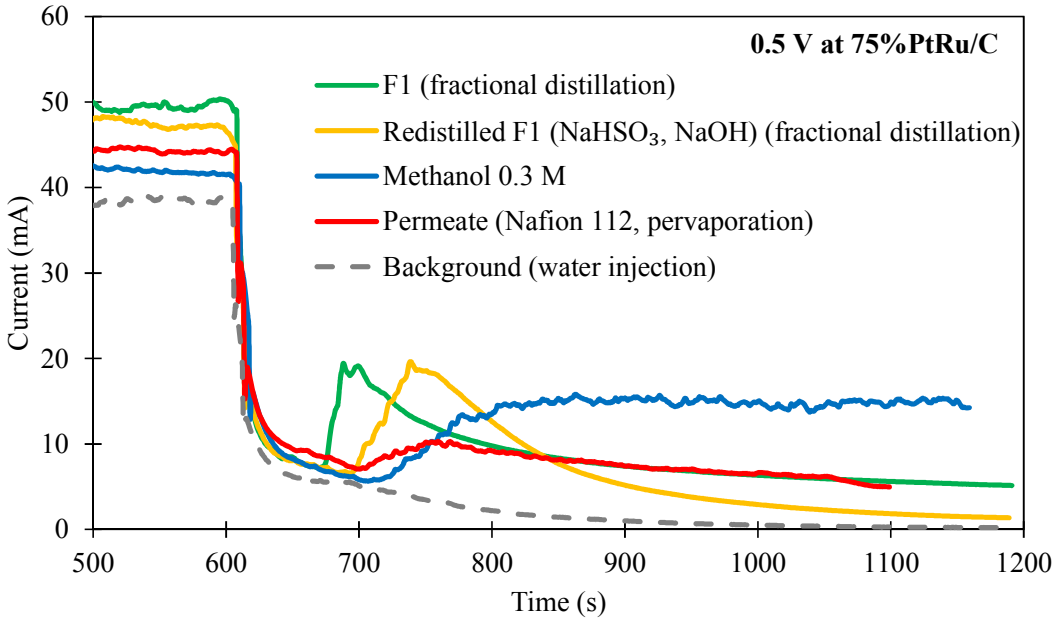

Figure 4.20: Current vs. time results of 1 M MeOH (0 to 600 s) at 75%PtRu/C electrodes in an electrolysis cell operated at a constant potential of 0.5 V in anode polarization mode at 80 °C. Distillate and permeate samples were injected after being flushed with water at 600 s.

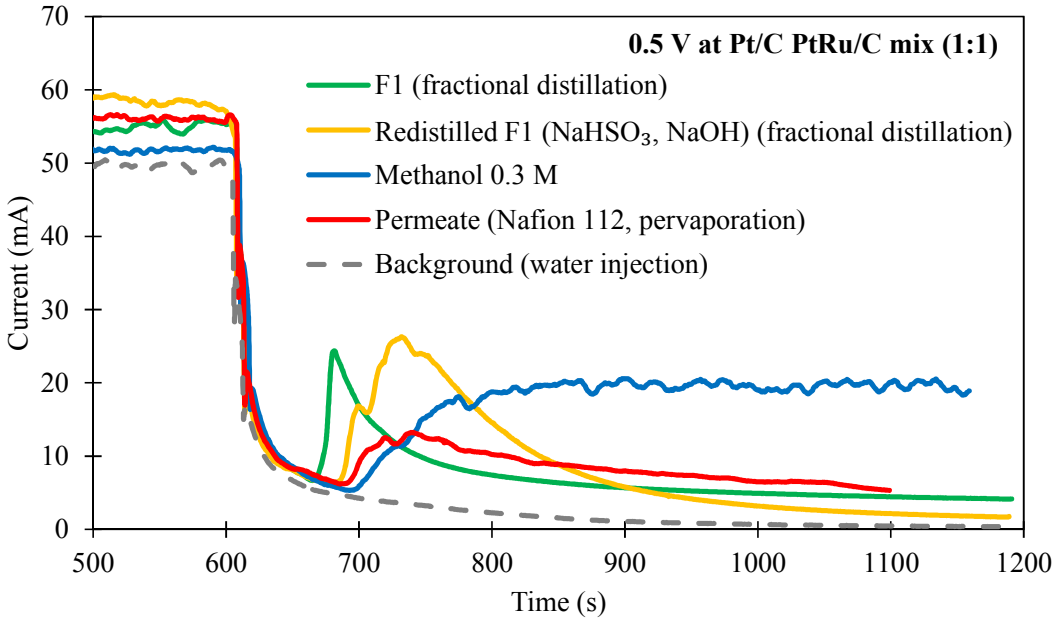

Figure 4.21: Current vs. time results of 1 M MeOH (0 to 600 s) at Pt/C PtRu/C mix (1:1) electrodes in an electrolysis cell operated at a constant potential of 0.5 V in anode polarization mode at 80 °C. Distillate and permeate samples were injected after being flushed with water at 600 s.

4.7.6 Permeate performance comparison in an electrolysis cell

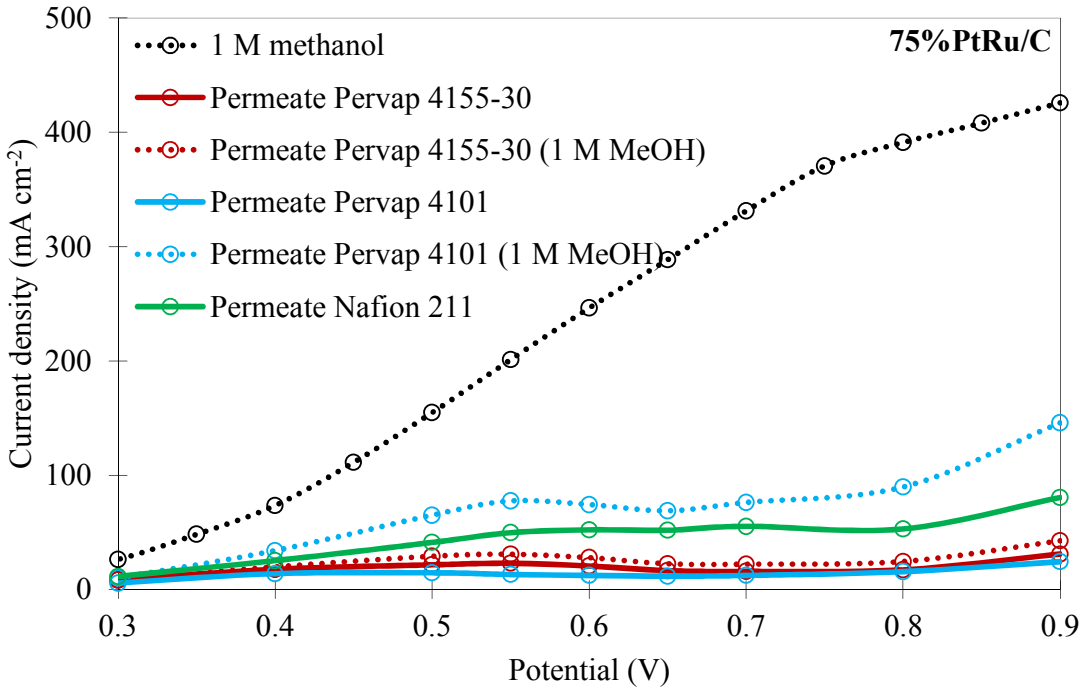

Figure 4.22: Polarization curves of crude Nafion 211, Pervap 4155-30, and Pervap 4101 permeate samples and samples with an adjusted methanol content to 1 M at 75%PtRu/C in anode polarization mode at 80 °C.

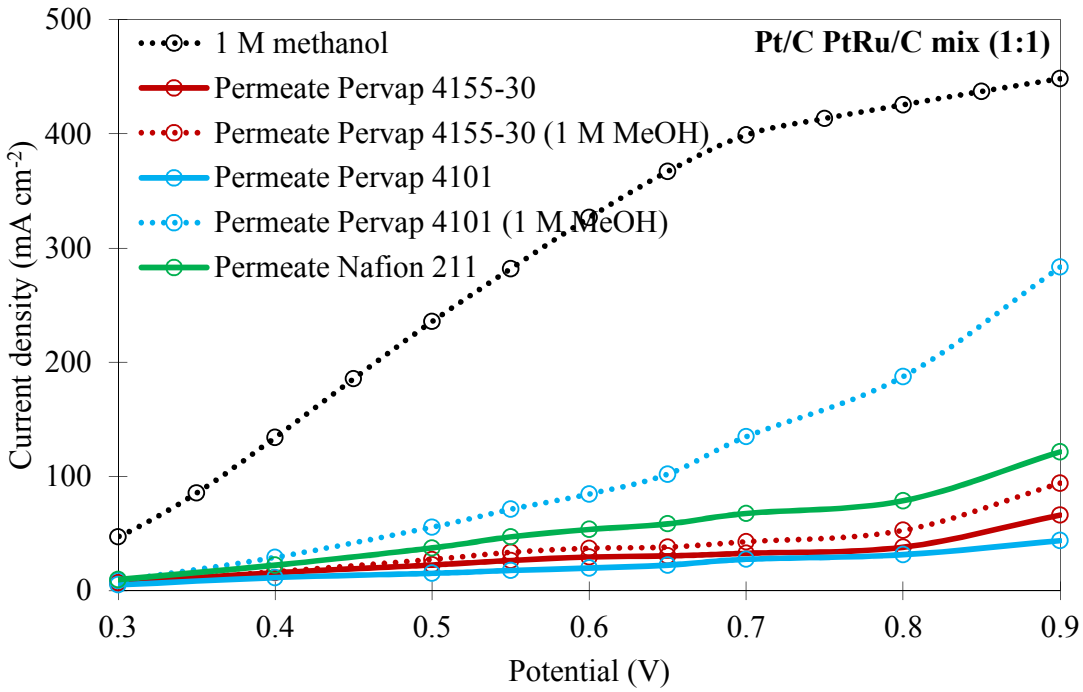

Figure 4.23: Polarization curves of crude Nafion 211, Pervap 4155-30, and Pervap 4101 permeate samples and samples with an adjusted methanol content to 1 M at Pt/C PtRu/C mix (1:1) in anode polarization mode at 80 °C.

Chapter 5

Catalyst screening for the electrochemical oxidation of bio-fuels

Some of the data for the Pt/Ru-Sn oxide/C catalysts in this chapter have been published in Binyu Chen, Tobias M. Brueckner, Rakan M. Altarawneh, and Peter G. Pickup. Composition Dependence of Ethanol Oxidation at Ruthenium Tin Oxide/Carbon Supported Platinum Catalysts. Journal of The Electrochemical Society, 165 (15) J3019-J3025 (2018).

The principal author (Binyu Chen) synthesized and characterized the Pt/Ru-Sn oxide/C catalysts.

The co-author (Tobias M. Brueckner) performed all of the experiments with the multi-anode cell, collecting and analyzing the data, designing of the experiments, presenting and discussing the data.

5 Catalyst screening for the electrochemical oxidation of bio-fuels

5.1 Introduction

Canada has committed to reduce its greenhouse gas (GHG) emissions 30% below the 2005 levels by 2030, under the Paris Agreement [1]. The transportation sector is Canada's second largest GHG contributor due to Canada's enormous landmass and vast distances between metropolitan and low population density areas [1]. Fuel cells have been identified as one of the most promising and efficient technologies to produce sustainable electrical energy by converting chemicals from renewable resources into electricity through oxidation [2–5]. Besides transportation applications, fuel cells can be used for stationary domestic power, heating applications, and portable applications such as laptops [3].

Proton exchange membrane fuel cells (PEMFC) are hydrogen (H_2) powered and can play a key role in reducing GHG, particularly the carbon dioxide (CO_2) emissions in transportation vehicles. However, the CO_2 reduction benefit of fuel cells strongly depends on the H_2 production method. Unlike the fossil fuel-based H_2, the CO_2 emissions of biomass-based H_2 are potentially zero because the released CO_2 was previously absorbed by the growing plant from the environment through photosynthesis [6–8]. One way to produce biomass-based H_2 is through electrolysis of renewably produced alcohols [9–11]. Another possibility is to skip the H_2 production and use the renewable alcohols directly as a water-based solution in PEMFCs to produce electricity [12–14]. Both methods allow a CO_2 neutral electricity production. In addition to the commonly studied direct liquid PEMFC fuels, such as methanol [14–16], and ethanol

[3,17,18], this research also focuses on by-product alcohols from biodiesel production (ethylene glycol, and glycerol) [19] and acetol which was a main component in pyrolysis oil enhancement by-product (*Chapter 4*).

Platinum (Pt) supported on high surface area active carbon is typically used as the anode catalyst in PEMFCs. However, the use of Pt significantly increases the manufacturing cost of the fuel cell. To decrease the required amount of expensive Pt, single-, double-, multiple metals, and carbon supported catalysts must be developed [20]. Furthermore, high catalyst activity and reliability against impurities have to be ensured to increase the catalyst performance [12].

The understanding of catalysts is extended in this study, to expand the catalyst knowledge and guide the selection of catalysts for various applications as well as the development of new catalysts. A multi-anode cell was utilized to simultaneously test multiple anode catalysts under the same conditions for an efficient screening process. This method allowed efficient testing of a large number of catalysts prepared by Prof. Dr. Pickup's research group, including a wide range of Pt-based catalysts and nano core-shell bi-metal catalysts. The objective was to find an optimized catalyst with high activities at low potentials and a high selectivity for the complete oxidation to CO_2 at higher potentials for each investigated fuel. The screening was carried out with 0.1 M methanol, ethanol, and ethylene glycol solutions, and with 1 M methanol, ethanol, ethylene glycol, glycerol, and acetol solutions in crossover mode at 80 °C. Ultimately, this will guide the selection of the best catalyst for each fuel in electrolysis or direct liquid fuel cells.

5.2 Materials and methods

5.2.1 Materials

The electrolysis experiments were carried out with methanol (99.8%) from ACP Chemical Inc., anhydrous ethanol (99.9%) from Commercial Alcohols Inc., acetol (90%, containing ≤500 ppm sodium carbonate as stabilizer) from Sigma-Aldrich Co., ethylene glycol from ACP Chemical Inc., 1-propanol from J.T.Barker, glycerol from Fisher Scientific, hydrogen peroxide (30%) from Merck KGaA, sulfuric acid from Fisher Scientific, and distilled and filtered deionized water. Industrial grade nitrogen (NI-K, 99.998%) from Air Liquide was used in all electrolysis experiments. All chemicals were used as received. Nafion 115 and 117 membranes (DuPont) were cleaned at 80 °C in 3% hydrogen peroxide (aq) and 1 M sulfuric acid (aq), rinsed with deionized water and stored in deionized water.

5.2.2 Catalyst preparation

Anodes consisted of commercial catalysts listed in Table 5.1 and Pt-based catalyst prepared by various researchers in Prof. Dr. Pickup's lab. The commercial catalysts were used as references materials for comparison with the homemade catalysts.

Table 5.1: Commercial fuel cell catalysts used as benchmarks catalysts.

Catalyst	Description
70%Pt/C	HiSPEC 13100, 70% Pt; Alfa Aesar, Lot# M22A026
75%PtRu/C	HiSPEC 12100, 50% Pt, 25% Ru, Alfa Aesar, Lot# P17B047
20%Pt/C	20% Pt on Vulcan 72, Etek
PtRu black	1:1 atomic ratio, Johnson-Matthey
Pt black	Engelhard Industries

The homemade catalysts were various mixtures of platinum (Pt), ruthenium (Ru), tin (Sn), lead (Pb), and rhodium (Rh) supported on Vulcan XC 72. A selection of the best-performing catalysts are described in Table 5.2. Other investigated homemade catalysts and additional information on all of the catalysts, electrodes and membranes are listed in Table 5.4 (*Appendix 5.7.1*).

Table 5.2: Descriptions and sources of selected homemade catalysts.

Catalyst	Description	Atomic ratio of metals	Person/ Reference
$Pt/RuSnO_2/C$	Pt nanoparticle catalysts supported on carbon black coated with Ru and Sn oxides		B. Chen [21]
$Pt/RhSnO_2/C$	Pt nanoparticle catalysts supported on carbon black coated with Rh and Sn oxides		E. Wheeler
Pt_2Ru	Pt nanoparticle Ru alloy catalyst prepared by the citrate method	2:1	[22]
$Ru_{54}@Pt_{46}$	$Ru_{core}@Pt_{shell}$ nanoparticle	54:46	E. N. El Sawey [23]
$Rh_{54}@Pt_{46}$	$Rh_{core}@Pt_{shell}$ nanoparticle	54:46	E. N. El Sawey [24]
$Rh_{46}@Pt_{54}$	$Rh_{core}@Pt_{shell}$ nanoparticle	46:54	E. N. El Sawey [24]
$Rh_{40}@Pt_{60}$	$Rh_{core}@Pt_{shell}$ nanoparticle	40:60	E. N. El Sawey [24]

All electrodes were prepared using non-wet-proofed carbon fibre paper (TGP-H-090 from Toray Industries Inc.) or wet-proofed carbon fibre paper (TGP-H-090) with 10 wt% polytetrafluoroethylene (PTFE) from Toray Industries Inc.. Both carbon fibre papers had a thickness of 0.276 mm. A catalyst ink was prepared by first dispersing the catalyst in 5% Nafion® solution (Aldrich) at a catalyst to Nafion mass ratio of 5:1 and subsequently adding 1-propanol (J.T.Barker) at a volume ratio of Nafion solution to 1-propanol of 2:1. The resulting mixture was sonicated for 3 hours and evenly spread on carbon fibre paper with a spatula. The 1-propanol was added to the ink to decrease viscosity and evaporated when the electrodes were dried at room temperature overnight. Further details are provided in *Appendix 5.7.1*.

5.2.3 Electrochemical measurements

All electrochemical measurements in this chapter were carried out with the multi-anode electrolysis cell illustrated in Figure 5.1. The cell is further described in *Chapter 4* [25].

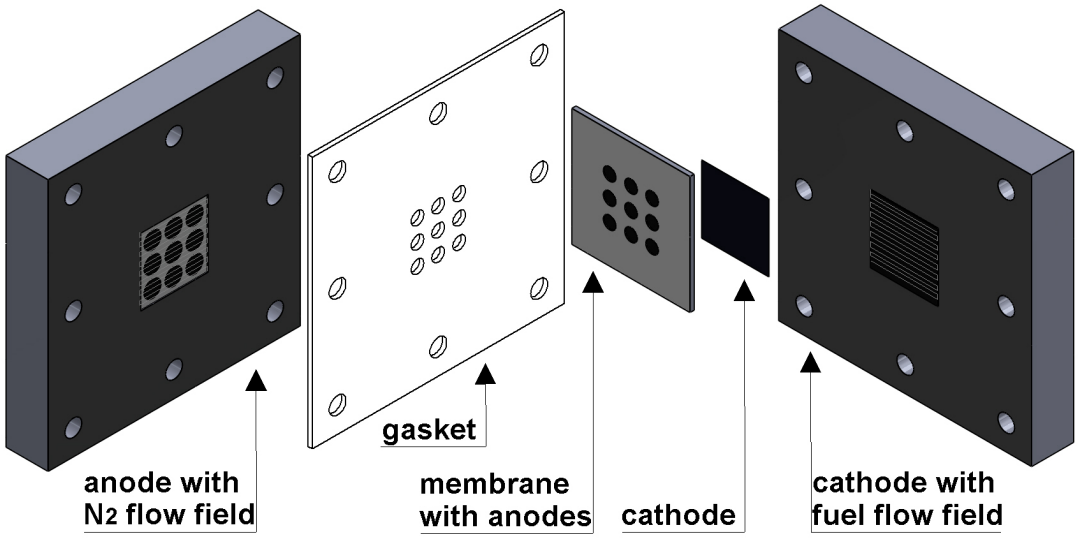

Figure 5.1: Schematic diagram of the nine anode cell set-up.

A multi-anode cell with nine separate anodes and a single 5 cm² Pt black cathode with a Nafion proton conducting membrane electrolyte was used. The cell was based on a commercial (ElectroChem Inc.) PEMFC graphite plate flow field and hardware for the cathode side, and a Bakelite plate with a similar flow field for the anodes. The anode current collectors were graphite rods embedded in the Bakelite plate. The anode catalyst area was 0.236 cm² per anode. The applied potential was controlled with a MSTAT potentiostat from Arbin Instruments. The fuel was supplied by an NE-300 New Era Pump Systems syringe pump. A 60 W Watlow heat plate and a Digi Sense temperature controller were used to heat the cathode plate. The cell was preconditioned with the fuel to test at 0.7 V for one hour at the operating temperature of 80 °C. Polarization curves were then obtained from 0.9 V to 0.0 V in 25 mV or 50 mV increments. Each potential step was held for three minutes, with the current recorded every second. The reported currents are averaged over the final two minutes.

5.2.4 Operating mode

The multi-anode cell was operated as an electrolysis cell to avoid interference from oxygen. In this so-called crossover mode, the liquid fuel solution was pumped through the cathode flow field at 0.5 mL min^{-1} while the anode flow field was purged with 30 mL min^{-1} nitrogen (N_2) gas. In this mode, the cathode approximates a dynamic hydrogen electrode, since the cathode reaction is [26]:

$$H^+ + e^- \rightarrow 0.5H_2 \qquad \text{Eq. (5.1)}$$

5.2.5 Catalyst performance characterization

The catalyst performance in the polarization curves was characterized by the onset potential, which is the potential when the current starts to rise. The onset potential depends strongly on the reaction kinetics of the fuel with the catalyst.

The half wave potential, which is an important value to determine the fuel cell performance, was also used to characterize the cell performance. The half wave potential was determined as 50% of maximal current (j_{max}) or limiting current (j_{lim}). If the catalyst performance did not reach a limiting current at high potentials (0.8 V to 0.9 V), 50% of the inflection point was used as the half-wave potential. For consistency, the current at 0.45 V was used to compare all investigated catalysts.

The potentials below the half-wave potential are regarded as low potentials. The catalyst performance in this region is important because fuel cells and electrolysis cells are more efficient at low anode potentials. An efficient catalyst produces high currents at low potentials. The term high potential is used for potentials above the half-wave

potential including the limiting current region. Changes of the current above the half-wave potential are primarily due to changes in the average number of electrons transferred (stoichiometry).

The cell was operated in crossover mode since previous research showed that it was more informative to compare catalyst activities under these controlled mass transport conditions as described in *Chapter 3* [25]. The current density in the mass transport region (j_{lim}) provides stoichiometric information for the preliminary evaluation of catalysts. In this region, the current is proportional to the average number of electrons (n_{av}) transferred per molecule of fuel (Eq. (5.2)). The n_{av} values obtained through this method are plotted on a secondary axis for all polarization curves in this chapter.

$$j_{lim} = n_{av} \cdot F \cdot m \cdot C \qquad \text{Eq. (5.2)}$$

Where F is the Faraday constant (96500 C mol^{-1}), m is the mass transport coefficient, and C is the concentration of each fuel used for the catalyst screening. m depends on the thicknesses of both the cathode and the membrane, and diffusion characteristics of each fuel used within both layers. Eq. (5.2), with n_{av} = 6, was used to determine m-values for methanol from the limiting currents at the Pt/C and PtRu/C commercial catalysts [25]. Literature data shows that m is a factor of 1.3 lower for ethanol [25,27] and 1.8 lower for ethylene glycol [27], compared to methanol. Since no mass transport coefficient could be found for glycerol, the limiting current at PtRu black was assigned to the lowest possible n_{av} value of two.

Table 5.3: *m*-values used to analyze catalyst performances.

Fuel	*C* (M)	*m* x 10^3 (cm s^{-1})	Temperature (°C)
Methanol	1.0	0.43	80
Methanol	0.1	0.36 ± 0.04	80
Ethanol	1.0	0.33	80
Ethanol	0.1	0.27 ± 0.02	80
Ethylene glycol	1.0	0.24	80
Ethylene glycol	0.1	0.19	80
Glycerol	1.0	0.10	80

5.3 Results and discussion

5.3.1 Methanol

5.3.1.1 Methanol (1 M) catalyst screening

Initially, the catalyst screening was carried out with well-studied methanol as the fuel [15], in order to determine the performance of the investigated homemade catalysts, and create a reference point for other less-studied fuels. The best commercial catalysts oxidize methanol almost exclusively to CO_2 (n_{av} ~ 6) under the conditions employed here, and so provide a benchmark for assessing the accuracy of n_{av} values obtained for other catalysts. The catalytic oxidation mechanism of methanol at Pt-based catalysts in acidic media is shown in Figure 5.2.

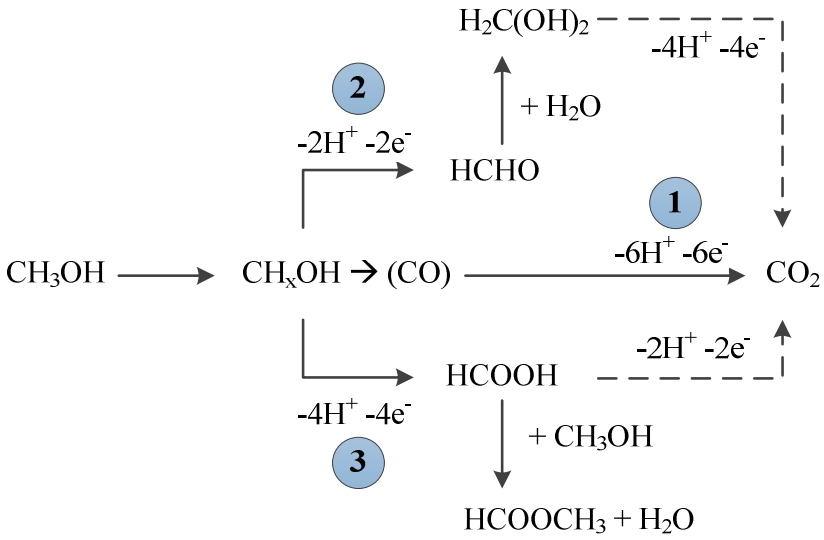

Figure 5.2: Methanol oxidation mechanism pathways to CO_2 at Pt-based catalysts [20].

Carbon monoxide (CO) is formed during the methanol oxidation reaction. The CO is strongly adsorbed onto the Pt catalyst which results in blocking active surface area, causing a performance reduction of the direct methanol fuel cell (DMFC). Methanol oxidation to CO_2 has three established pathways [20]. The first pathway is the complete oxidation of methanol to CO_2 by delivering 6 electrons (path 1, Figure 5.2). The second path forms formaldehyde (HCHO) (path 2, Figure 5.2), and the third formic acid (HCOOH) (path 3, Figure 5.2) as intermediate products towards the formation of CO_2. Pathways two and three also deliver 6 electrons in total for complete oxidation to CO_2.

Steady-state polarization curves for oxidation of 1 M methanol in crossover mode with commercial catalysts (PtRu black, 75%PtRu/C, 70%Pt/C, 20%Pt/C, and Pt black) are shown in Figure 5.3. For these commercial catalysts, the current rose to the

same limiting current density (j_{lim}) of 250 mA cm^{-2} at 0.9 V for the PtRu black, 75%PtRu/C, and 70%Pt/C anodes, within a standard deviation of ± 4.6%, illustrating the well-defined diffusion of methanol through the cathode and membrane to the anode. The average number of electrons (n_{av}) method developed as per *Chapter 3*, the limiting current of 250 mA cm^{-2} correlates to an n_{av} of 6 electrons. The Pt black and 20%Pt/C anodes did not reach the same limiting current as the other investigated catalysts , and the secondary y-axis in Figure 5.3 suggests that n_{av} did not reach 6. However, the current at high potentials may have been limited in part by the electron transfer kinetics [25], and so further experiments would be needed to identify the cause of the apparently low n_{av} values for these catalysts.

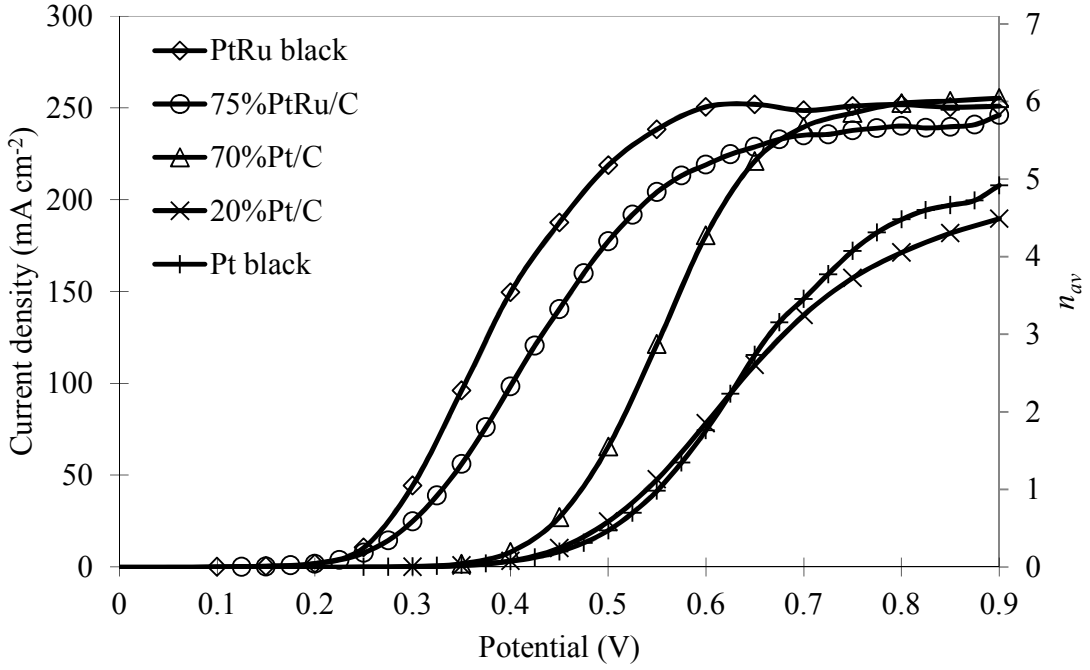

Figure 5.3: Polarization curves for the oxidation of 1 M methanol (0.5 mL min^{-1}) at commercial PtRu black, 75%PtRu/C, 70%Pt/C, 20%Pt/C, and Pt black anodes at 80 °C in crossover mode.

Amongst the commercial catalysts, PtRu black showed the lowest half-wave potential (0.4 V) and the best overall methanol oxidation performance. Alloyed Ru shows a unique activating effect for CO oxidation at low potentials. Both PtRu alloy catalysts showed a greater tolerance against CO poisoning compared to the single metal 70%Pt/C, Pt 20%/C, and Pt black catalysts.

Polarization curves for the oxidation of 1 M methanol were also recorded for the homemade catalysts. For clarity, only the three best-performing catalysts ($Pt/RuSnO_2/C$, $Pt/RhSnO_2/C$, and Pt_2Ru) are shown in Figure 5.4 in comparison to the commercial

PtRu black, and 70%Pt/C catalysts. Data for all of the homemade catalysts is summarized in Figure 5.6.

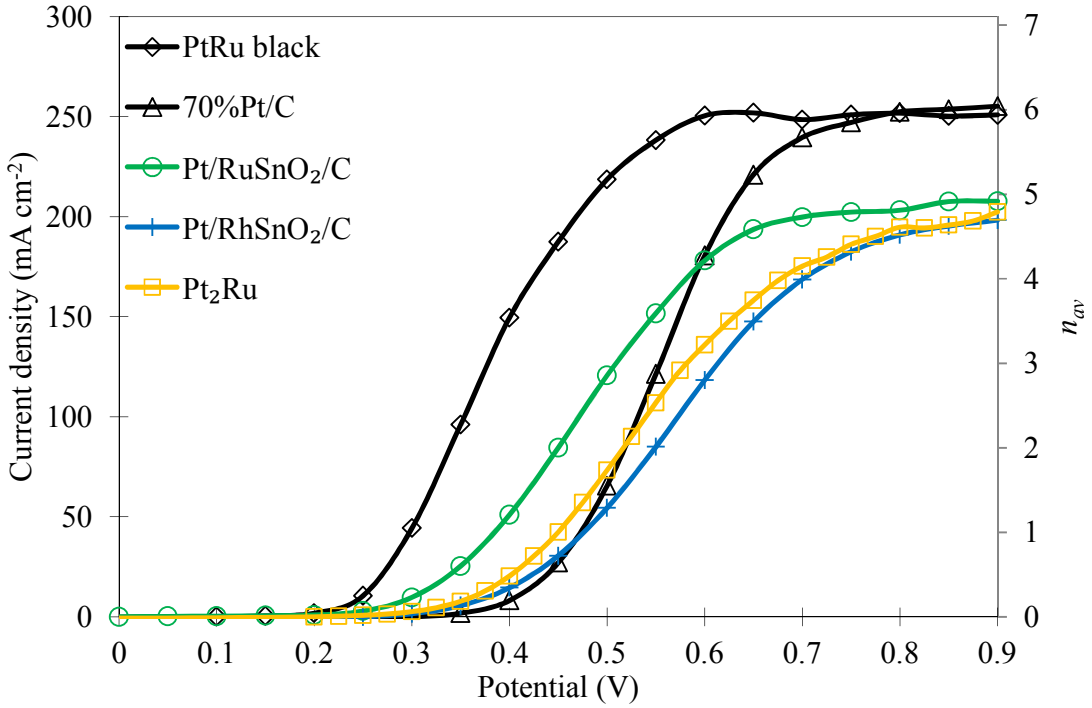

Figure 5.4: Polarization curves for the oxidation of 1 M methanol (0.5 mL min^{-1}) at PtRu black, 70%Pt/C, Pt/$RuSnO_2$/C, Pt/$RhSnO_2$/C, and Pt_2Ru anodes at 80 °C in crossover mode.

The current densities of the Pt/$RuSnO_2$/C, Pt/$RhSnO_2$/C, and Pt_2Ru anodes in Figure 5.4 were lower than for the commercial PtRu black anode at all potentials, but higher compared to those at the 70%Pt/C anode at low potentials. The lower performance of the homemade catalysts compared to the commercial PtRu alloy catalyst was due to weaker activation effects of Ru and Sn oxides compared to Ru alloys. The reduced performance of Pt_2Ru can be attributed to an incomplete alloying process or limited reactive Pt molecules on the catalyst surface. At high potentials (0.65 V to

0.9 V) the current density was controlled by the mass flow through the Nafion membrane which formed a limiting current between 180 mA cm^{-2} and 200 mA cm^{-2} for the homemade catalysts compared to 250 mA cm^{-2} for the two commercial catalysts. These lower limiting currents correspond to an apparent n_{av} of 4.5 to 5 compared to n_{av} of 6 for the commercial catalysts. However, it is more likely that the higher carbon contents of the homemade catalysts (ca. 70% by mass) created an additional mass transport barrier within the anodes, and that *m* was lower than for the PtRu black (no carbon) and 70% Pt/C (30% carbon) anodes. The low density of carbon relative to Pt results in volumetric ratios of C:Pt that are much higher than the mass ratios. Support for this interpretation is provided by the similarity of the currents at high potentials for the homemade catalysts in Figure 5.4 with those for the 20% Pt/C commercial catalyst in Figure 5.3. Consequently, 20%Pt/C commercial catalyst provides a more suitable benchmark for assessing the homemade catalyst.

The main benefits of the homemade catalysts were a lower onset potential of 0.25 V for $Pt/RuSnO_2/C$, and 0.3 V for $Pt/RhSnO_2/C$ and Pt_2Ru compared to 0.35 V for the 70%Pt/C catalyst. Furthermore, the homemade catalysts showed increased current densities at low potentials (0.25 V to 0.55 V) due to faster electron transfer kinetics. $RuSnO_2$ showed the most beneficial effect on the 1 M methanol oxidation performance at low potentials.

Figure 5.5 shows the polarization curve results for $Ru_{54}@Pt_{46}$, and Rh@Pt nano core-shell catalysts with different shell loadings, compared to the 20%Pt/C commercial catalyst.

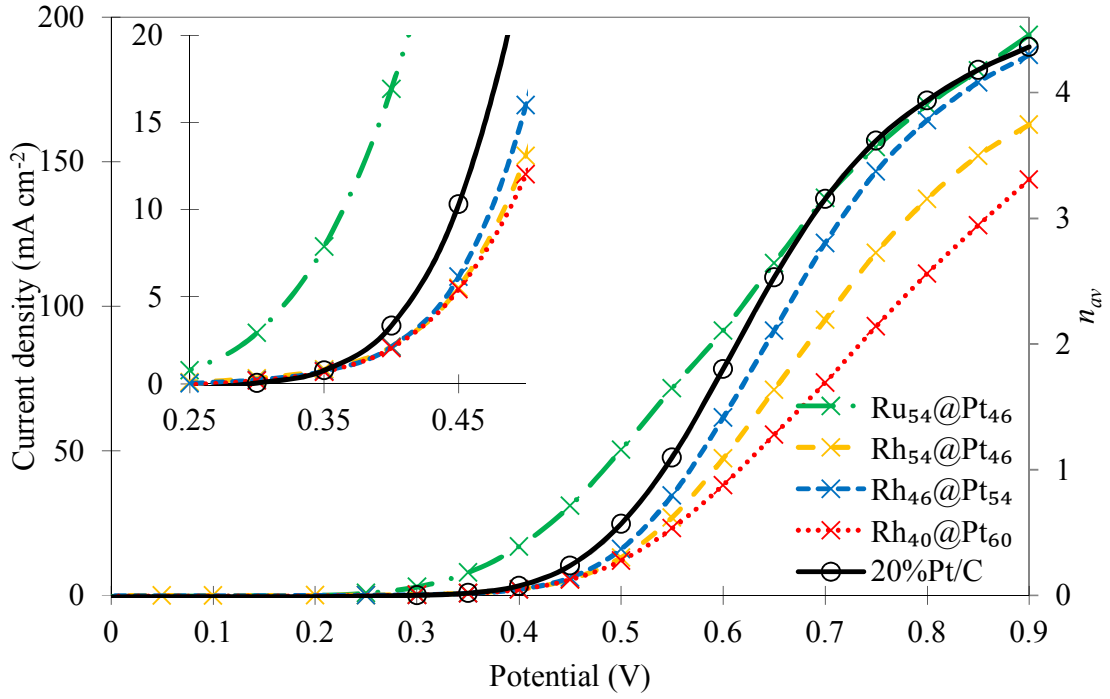

Figure 5.5: Polarization curves for the oxidation of 1 M methanol (0.5 mL min^{-1}) at $Ru_{54}@Pt_{46}$, $Rh_{54}@Pt_{46}$, $Rh_{46}@Pt_{54}$, $Rh_{40}@Pt_{60}$ nano core-shell catalysts, and 20%Pt/C anodes at 80 °C in crossover mode.

The current at the $Ru_{54}@Pt_{46}$ anode in Figure 5.5 showed an increased performance at low potentials compared to the 20%Pt/C anode (0.25 V to 0.65 V). At higher potentials 0.65 V to 0.9 V, the $Ru_{54}@Pt_{46}$ catalyst showed the same current densities compared to the commercial 20%Pt/C. The better performance of the $Ru_{54}@Pt_{46}$ catalyst compared to the 20%Pt/C catalyst at low potentials can be attributed to the electronic effect of the Ru core which weakens the adsorption of CO [23].

The Rh@Pt anodes in Figure 5.5 resulted in a lower performance compared to the 20%Pt/C catalyst. $Rh_{46}@Pt_{54}$ showed the best performance of all Rh@Pt nano core-shell catalysts for the oxidation of 1 M methanol. The current density of $Rh_{46}@Pt_{54}$

was slightly lower compared to the current density of 20%Pt/C. $Rh_{54}@Pt_{46}$ showed a further decreased performance followed by the $Rh_{40}@Pt_{60}$ catalyst with the highest Pt loading. The Rh core showed a negative effect on the 1 M methanol oxidation performance.

Figure 5.6 illustrates the results of all investigated anode catalysts for the oxidation of 1 M methanol in the multi-anode fuel cell. The data indicates that the screening method was useful to see significant performance differences of catalysts made in different batches or with different synthesis methods. Each bar represents the average current densities of up to three anodes of a catalyst at 0.45 V and 0.9 V. The error bars represent the standard deviations.

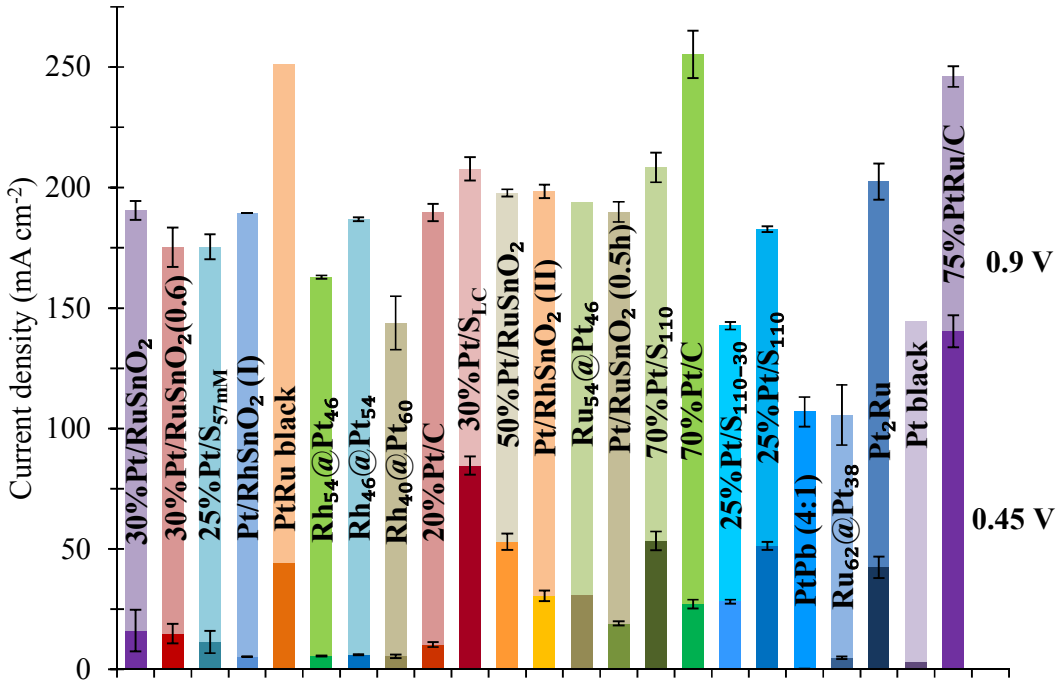

Figure 5.6: Current density bar plot of the investigated anode catalysts for the oxidation of 1 M methanol in the multi-anode cell at 80 °C in crossover mode.

5.3.1.2 Methanol (0.1 M) catalyst screening

Previous work in a different, 5 cm² cell has shown that higher n_{av} values can be reached at Pt electrodes by decreasing fuel concentration [28,29]. Further experiments were conducted with 0.1 M methanol (for calibration), followed by 0.1 M ethanol and ethylene glycol.

Steady-state polarization curves for the oxidation of 0.1 M methanol in crossover mode with commercial catalysts (75%PtRu/C, 70%Pt/C, and 20%Pt/C) are shown in Figure 5.7. 75%PtRu/C and 70%Pt/C reached a limiting current of ca. 20 mA cm^{-2}, which correlates to 6 transferred electrons at ca. 0.45 V. 20%Pt/C rose to a maximum current density of ca. 20 mA cm^{-2} at 0.9 V which correlates to 6 transferred

electrons as well. The plotted error bars in Figure 5.7 represent the standard deviation and demonstrate the accuracy of the 0.1 M n_{av} data. The comparison to the 1 M methanol data shows that the mass transport coefficient depends on the concentration, therefore *m* is decreasing slightly. The 1 M methanol *m*-value (0.43 x 10^{-3} cm s^{-1}) is within the standard deviation of the 0.1 M methanol value (0.36 ± 0.04 x 10^{-3} cm s^{-1}).

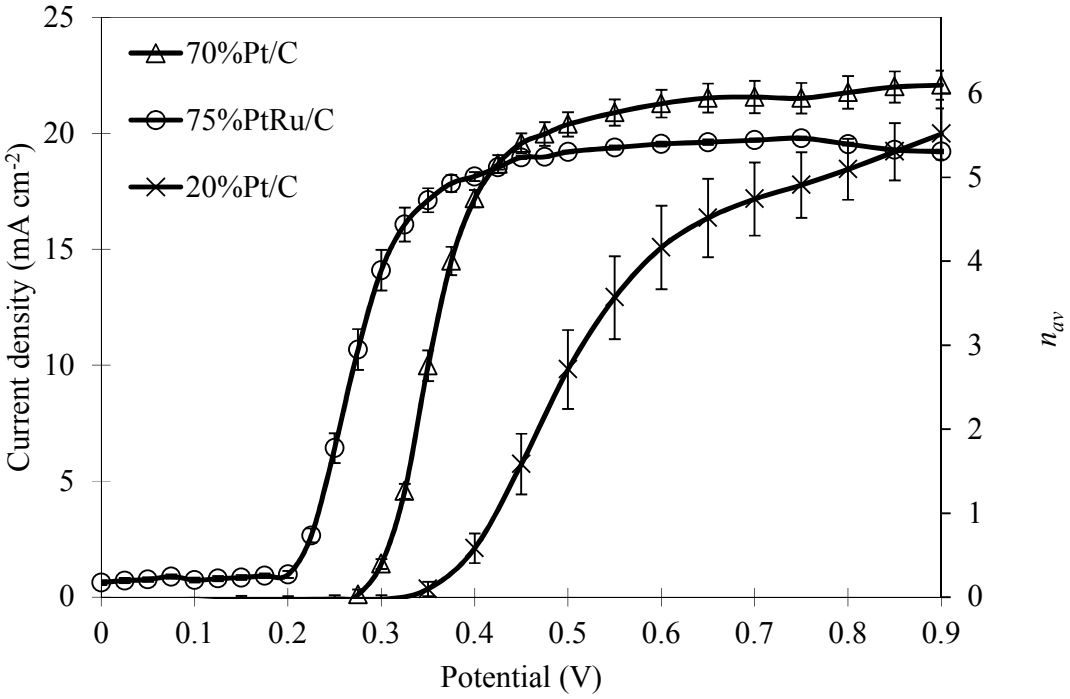

Figure 5.7: Polarization curves for the oxidation of 0.1 M methanol (0.5 mL min^{-1}) at commercial 70%Pt/C, 75%PtRu/C, and 20%Pt/C anodes at 80 °C in crossover mode.

Amongst the commercial catalysts, 75%PtRu/C showed the lowest half-wave potential (0.25 V) whereas 70%Pt/C showed slightly higher current densities at higher potentials. Alloyed Ru shows a unique activating effect for CO oxidation of 0.1 M methanol at low potentials.

Polarization curves for the oxidation of 0.1 M methanol were also recorded for the homemade catalysts. For clarity, only the two best-performing catalysts ($Pt/RuSnO_2/C$ and $Pt/RhSnO_2/C$) are shown in Figure 5.8 in comparison to the commercial 75%PtRu/C, and 70%Pt/C catalysts. Data for all homemade catalysts are summarized in Figure 5.10.

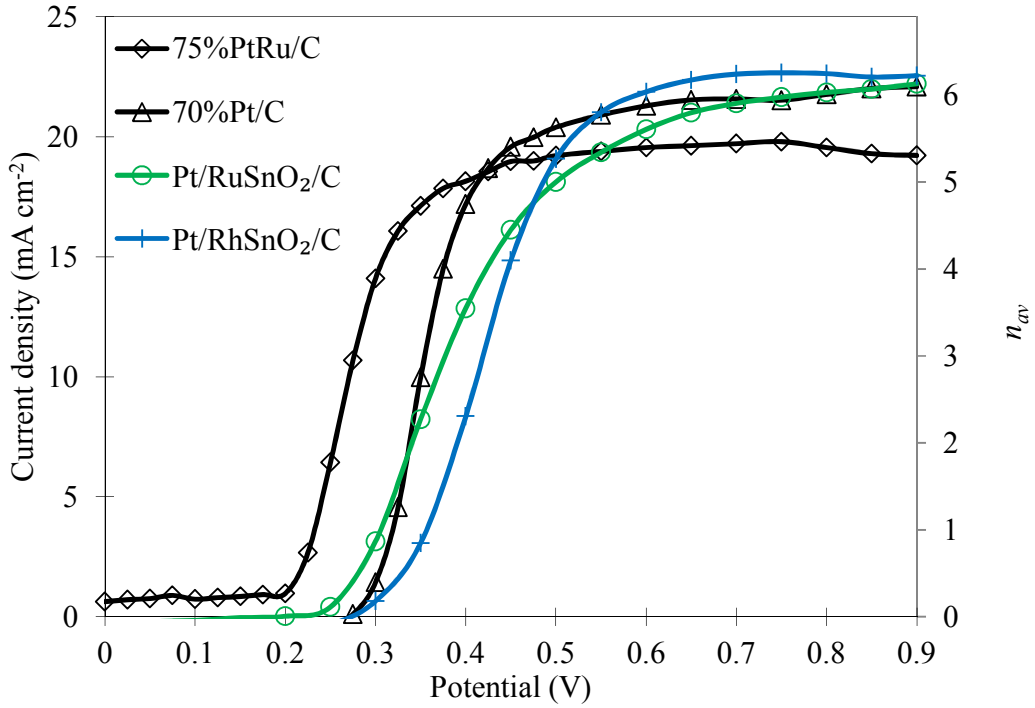

Figure 5.8: Polarization curves for the oxidation of 0.1 M methanol (0.5 mL min^{-1}) at 75%PtRu/C, 70%Pt/C, $Pt/RuSnO_2/C$, and $Pt/RhSnO_2/C$ anodes at 80 °C in crossover mode.

Both $Pt/RuSnO_2/C$ and $Pt/RhSnO_2/C$ anodes reached the limiting current of ca. 20 mA cm^{-2}. $Pt/RuSnO_2/C$ showed a slightly lower onset potential, but an increased half-wave potential compared to 70%Pt/C (0.4 V vs. 0.35 V). Similar to the oxidation of

1 M methanol results, $RuSnO_2$ showed the most beneficial effect at low potentials on the oxidation of 0.1 M methanol as well.

Figure 5.9 shows the polarization curve results for $Ru_{54}@Pt_{46}$, and Rh@Pt nano core-shell catalysts with different shell loadings, compared to 20%Pt/C commercial catalyst.

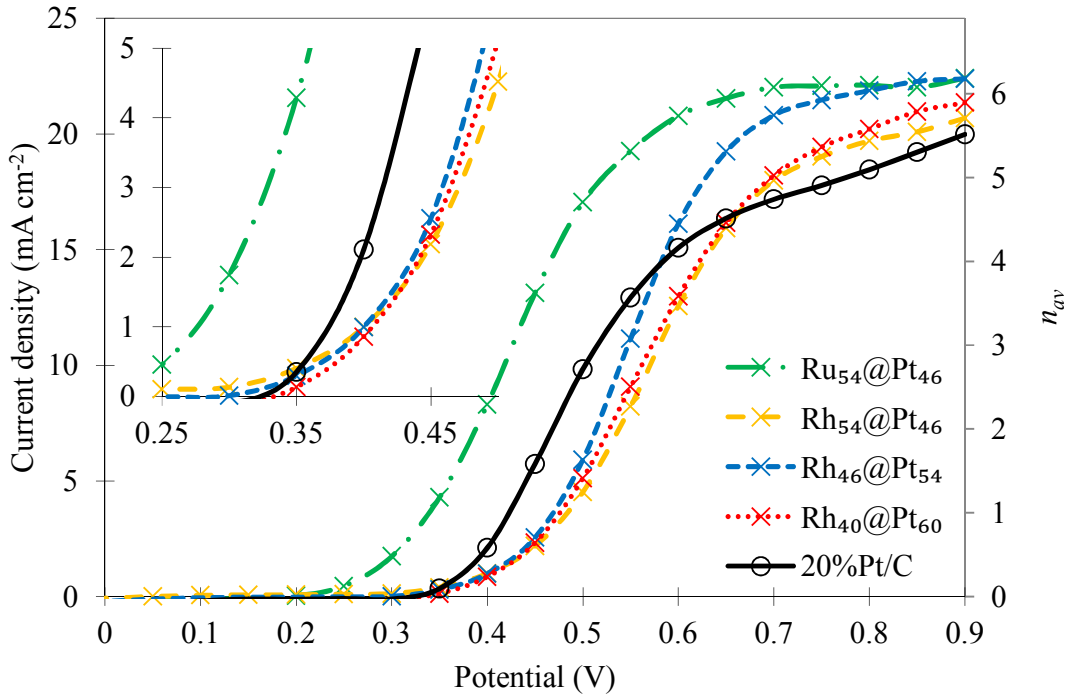

Figure 5.9: Polarization curves for the oxidation of 0.1 M methanol (0.5 mL min^{-1}) at $Ru_{54}@Pt_{46}$, $Rh_{54}@Pt_{46}$, $Rh_{46}@Pt_{54}$, $Rh_{40}@Pt_{60}$ nano core-shell catalysts, and 20%Pt/C anodes at 80 °C in crossover mode.

For all nano core-shell catalysts, the current rose to the same limiting current density of 20 mA cm^{-2} within a standard deviation of ± 0.8% at 0.9 V. $Ru_{54}@Pt_{46}$ showed a significant lower onset potential of 0.2 V compared to 0.35 V for 20%Pt/C and all Rh@Pt catalysts. The better performance of the $Ru_{54}@Pt_{46}$ catalyst can be

attributed to the electronic effect of the Ru core which weakens the adsorption of CO [23]. The Rh core showed a negative effect on the 0.1 M methanol oxidation performance with an increased onset and half wave potential compared to the commercial 20%Pt/C catalyst.

Figure 5.10 illustrates the results of all investigated anode catalysts for the oxidation of 0.1 M methanol in the multi-anode fuel cell. The data indicates that the screening method was useful to see significant performance differences of catalysts made in different batches or with different synthesis methods. Each bar represents the average current densities of up to three anodes of a catalyst at 0.45 V and 0.9 V. The error bars represent the standard deviations.

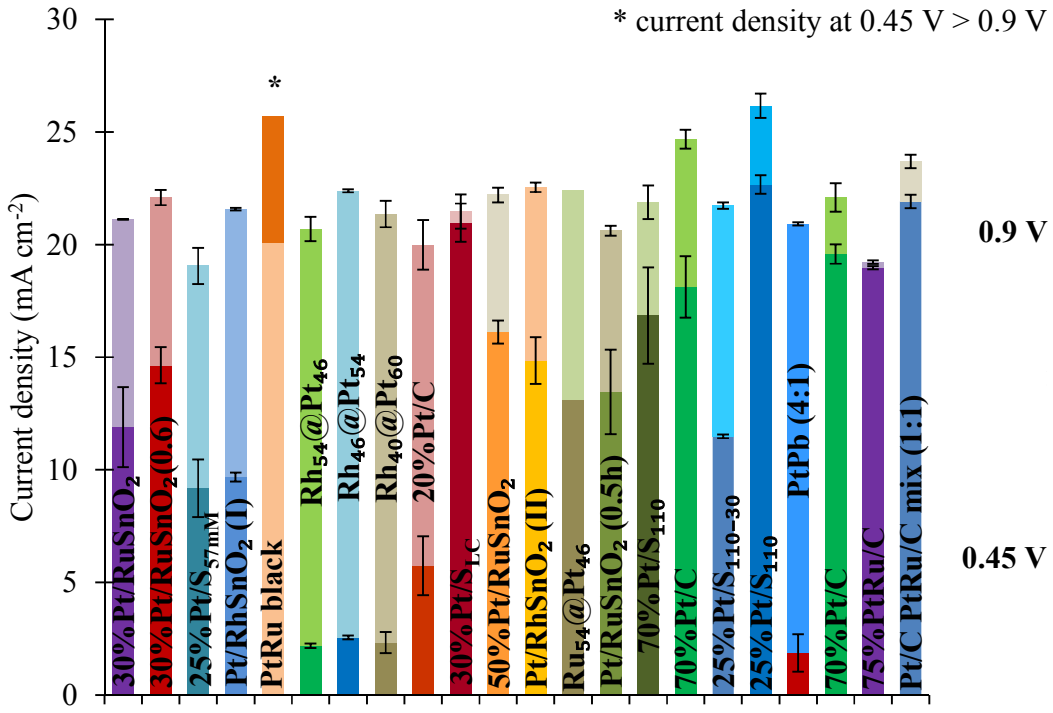

Figure 5.10: Current density bar plot of the investigated anode catalysts for the oxidation of 0.1 M methanol in the multi-anode cell at 80 °C in crossover mode.

5.3.2 Ethanol

5.3.2.1 Ethanol (1 M) catalyst screening

In addition to methanol, polarization curves were also recorded for 1 M ethanol solution on commercial and homemade catalysts. The catalytic oxidation mechanism of ethanol at Pt-based catalysts in acidic media is shown in Figure 5.11.

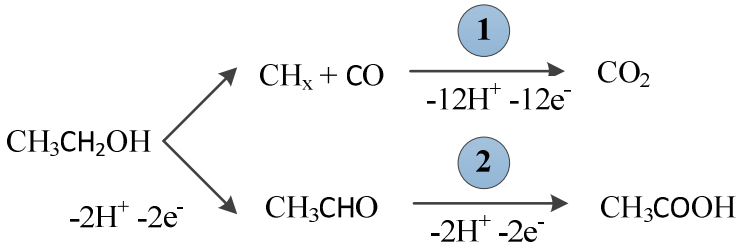

Figure 5.11: Ethanol oxidation mechanism pathways to CO_2 at Pt-based catalysts [30].

The catalytic oxidation mechanism of ethanol has two established pathways [30]. The first pathway is the complete oxidation of ethanol to CO_2 via intermediate products by delivering 12 electrons (path 1, Figure 5.11). The second pathway (path 2, Figure 5.11) is a partial oxidation to acetaldehyde (CH_3CHO) by delivering 2 electrons, which can further be oxidized to acetic acid (CH_3COOH) by delivering 2 electrons. The second pathway delivers a total of 4 electrons without breaking the C-C bond [30].

Steady-state polarization curves for oxidation of 1 M ethanol in crossover mode with commercial catalysts (PtRu black, 75%PtRu/C, 70%Pt/C, 20%Pt/C, and Pt black) are shown in Figure 5.12. For the commercial PtRu alloy catalysts, the current rose to a maximum at 0.6 V ± 0.5 V and then decreased at higher potentials. The PtRu black catalyst showed a greater tolerance against the CO poisoning at low potentials between

0.15 V and 0.45 V, whereas 75%PtRu/C reached a higher maximum current density of 107 mA cm^{-2} (vs. 93 mA cm^{-2} for PtRu black) at 0.6 V. Applying the average number of electrons (n_{av}) method, the maximum current density of 107 mA cm^{-2} correlates to an n_{av} of ca. 3.5 electrons. 70%Pt/C showed a weaker performance at low potentials but resulted in a similar high current density of 106 mA cm^{-2} (ca. 3.5 electrons) at a potential of 0.85 V compared to the PtRu alloy catalysts. The incomplete ethanol oxidation process to CO_2 with an n_{av} of ca. 3.5 resulted in the formation of acetaldehyde and acetic acid as the main oxidation products. Pt black and 20%Pt/C anodes did not result in high currents at high potentials. The current densities of the incomplete oxidation corresponded to the transfer of ca. 2 electrons with acetaldehyde as the primary intermediate product.

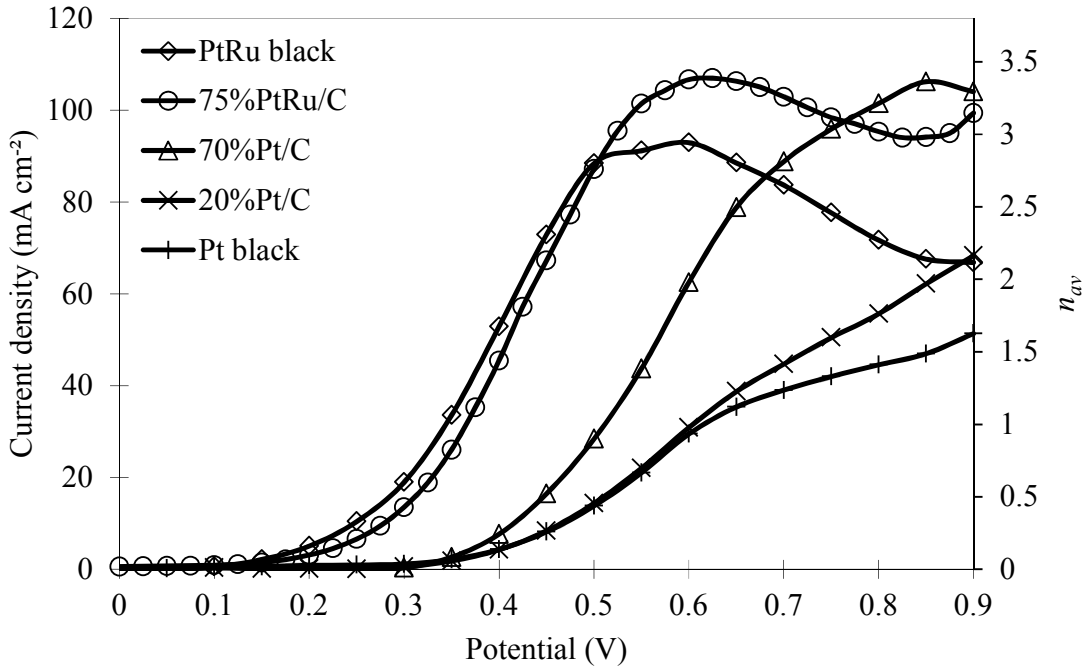

Figure 5.12: Polarization curves for the oxidation of 1 M ethanol (0.5 mL min^{-1}) at commercial PtRu black, 75%PtRu/C, 70%Pt/C, 20%Pt/C, and Pt black anodes at 80 °C in crossover mode.

Amongst the commercial catalysts, 75%PtRu/C showed a half-wave potential of 0.4 V and the best overall ethanol oxidation performance. Alloyed Ru shows a significant activating effect at low potentials and showed a higher tolerance against CO poisoning compared to the single metal 70%Pt/C, Pt 20%/C, and Pt black catalysts.

Polarization curves for the oxidation of 1 M ethanol were also recorded for the homemade catalysts. For clarity, only the three best-performing catalysts (Pt/$RuSnO_2$/C, Pt/$RhSnO_2$/C, and Pt_2Ru) are shown in Figure 5.13 in comparison to the commercial 75%PtRu/C, and 70%Pt/C catalysts. Data for all of the homemade catalysts is summarized in Figure 5.15.

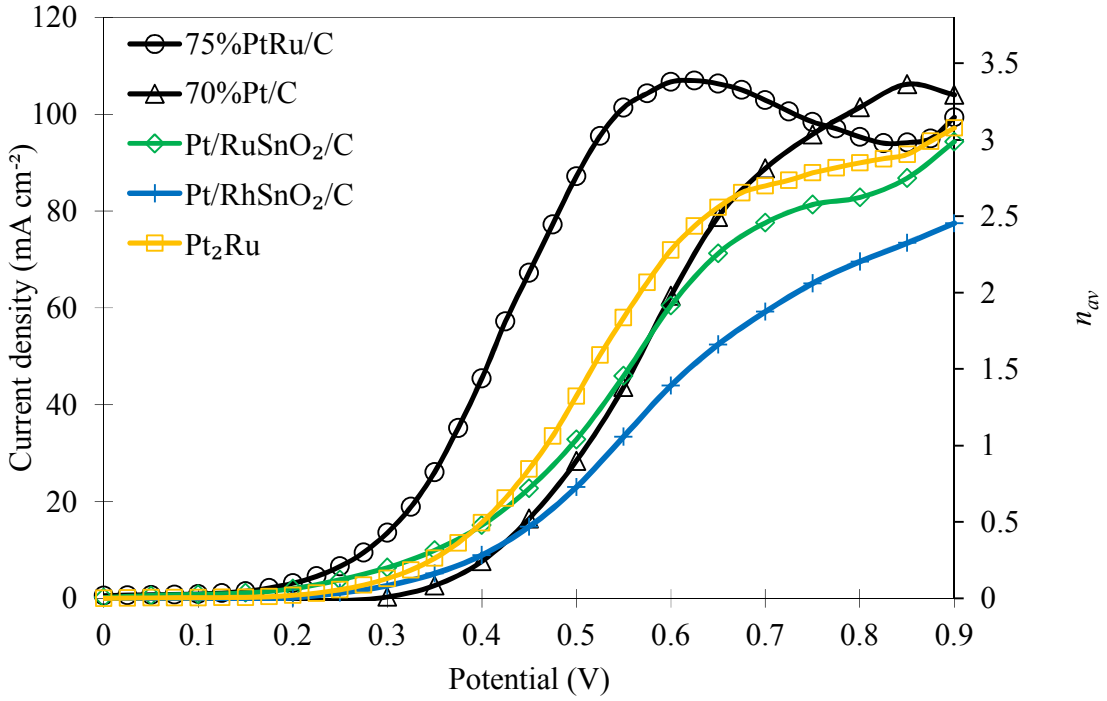

Figure 5.13: Polarization curves for the oxidation of 1 M ethanol (0.5 mL min^{-1}) at 75%PtRu/C, 70%Pt/C, Pt/$RuSnO_2$/C, Pt/$RhSnO_2$/C and Pt_2Ru anodes at 80 °C in crossover mode.

The current densities of the Pt/$RuSnO_2$/C, Pt/$RhSnO_2$/C, and Pt_2Ru anodes in Figure 5.13 were lower than for the commercial 75%PtRu/C anode at all potentials. Pt_2Ru reached similar currents at potentials above 0.85 V compared to PtRu alloy catalyst. In comparison to the 70%Pt/C catalyst, all homemade catalysts showed a significant improvement at low potentials. The lower performance of the homemade catalysts compared to the commercial PtRu alloy catalyst was due to weaker activation effects of Ru and Sn oxides compared to Ru alloys. None of the catalysts reached a limiting current for the oxidation of ethanol; therefore, the incomplete oxidation with an n_{av} of < 3.5 resulted in the formation of acetaldehyde and acetic acid as the main

oxidation products instead of CO_2. The onset potential occurred at a significantly lower potential (ca. 0.15 V) for all homemade catalysts relative to the commercial 70%Pt/C catalyst (ca. 0.3 V), while the 70%Pt/C catalyst provided higher currents at high potentials. The main benefits of the homemade catalysts were lower onset potentials of ca. 0.15 V compared to 0.3 V for the 70%Pt/C catalyst. Furthermore, the homemade catalysts showed increased current densities at low potentials (0.2 V up to 0.6 V) due to faster electron transfer kinetics. The most active Pt_2Ru outperformed $Pt/RuSnO_2/C$ and $Pt/RhSnO_2/C$, in comparison to the methanol oxidation performance and showed the most beneficial effect on the 1 M ethanol oxidation performance at low potentials.

Figure 5.14 shows the polarization curve results for $Ru_{54}@Pt_{46}$, and Rh@Pt with different shell loadings, compared to the 20%Pt/C commercial catalyst.

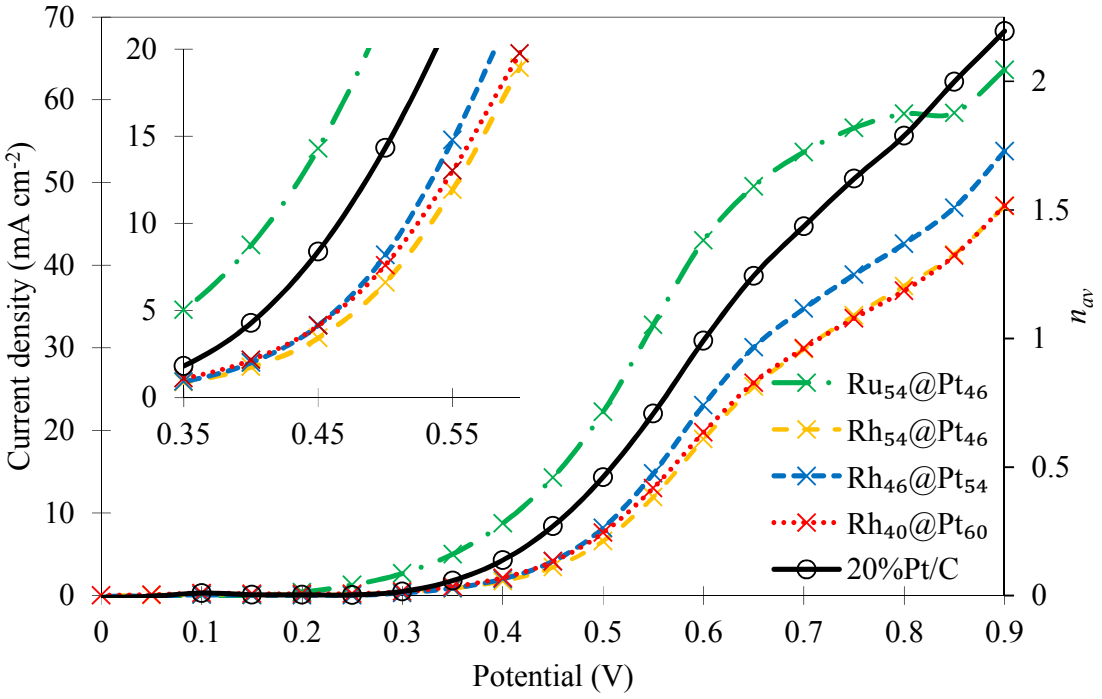

Figure 5.14: Polarization curves for the oxidation of 1 M ethanol (0.5 mL min^{-1}) at $Ru_{54}@Pt_{46}$, $Rh_{54}@Pt_{46}$, $Rh_{46}@Pt_{54}$, $Rh_{40}@Pt_{60}$ and 20%Pt/C anodes at 80 °C in crossover mode.

The $Ru_{54}@Pt_{46}$ nano core-shell catalyst outperforms the commercial 20%Pt/C catalyst, with a lower onset potential and higher current densities over a potential range from 0.2 V to 0.8 V (Figure 5.14). At higher potentials, the $Ru_{54}@Pt_{46}$ catalyst showed slightly lower current densities compared to the commercial 20%Pt/C catalyst. The increased ethanol oxidation performance of the $Ru_{54}@Pt_{46}$ catalyst compared to the 20%Pt/C catalyst is strongly due to the electronic effect of the Ru core [23].

The Rh@Pt anodes in Figure 5.14 resulted in a decreased performance compared to the 20%Pt/C catalyst. The most active $Rh_{46}@Pt_{54}$ showed the best performance of all Rh@Pt nano core-shell catalysts for the oxidation of 1 M ethanol. In comparison to the

1 M methanol oxidation $Rh_{54}@Pt_{46}$ and $Rh_{40}@Pt_{60}$ showed no performance difference in the oxidation of 1 M ethanol. The Rh core showed a negative effect on the 1 M ethanol oxidation performance an increased half-wave potential compared to the commercial 20%Pt/C catalyst.

Figure 5.15 illustrates the results of all investigated anode catalysts for the oxidation of 1 M ethanol in the multi-anode fuel cell. The data indicates that the screening method was useful to see significant performance differences of catalysts made in different batches or with different synthesis methods. Each bar represents the average current densities of up to three anodes of a catalyst at 0.45 V and 0.9 V. The error bars represent the standard deviations.

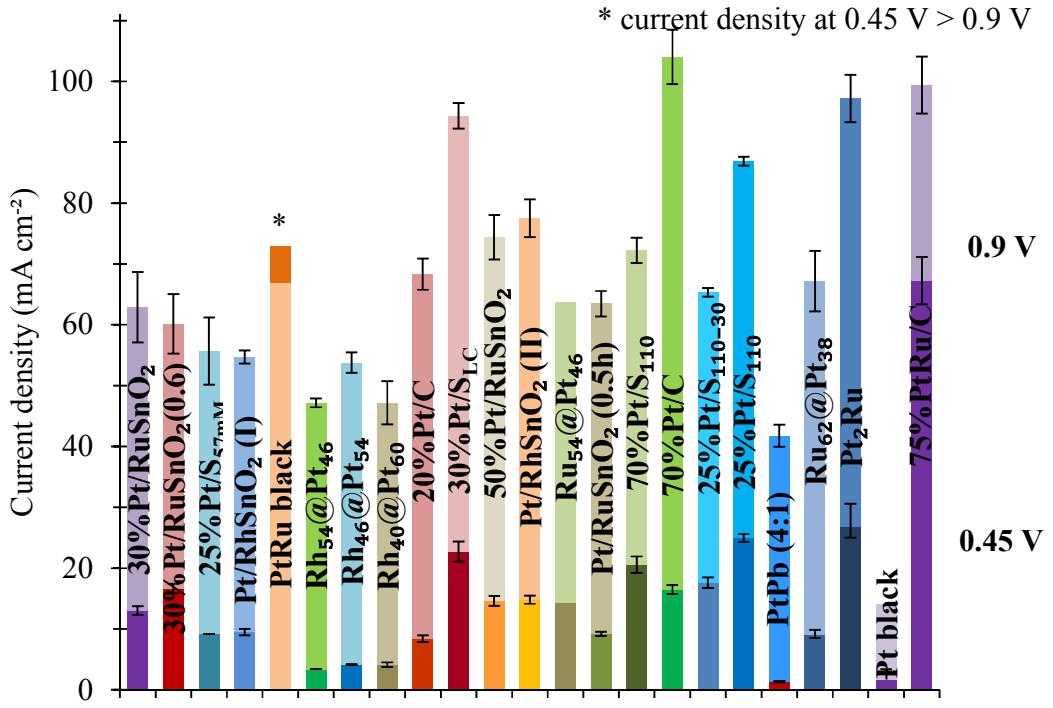

Figure 5.15: Current density bar plot of the investigated anode catalysts for the oxidation of 1 M ethanol in the multi-anode cell at 80 °C in crossover mode.

5.3.2.2 Ethanol (0.1 M) catalyst screening

In addition to the catalyst screening with 0.1 M methanol, polarization curves were also recorded for 0.1 M ethanol solution on commercial and homemade catalysts to analyze their performances at low fuel concentrations.

Steady-state polarization curves for the oxidation of 0.1 M ethanol in crossover mode with commercial catalysts (PtRu black, 75%PtRu/C, 70%Pt/C, and 20%Pt/C) are shown in Figure 5.16.

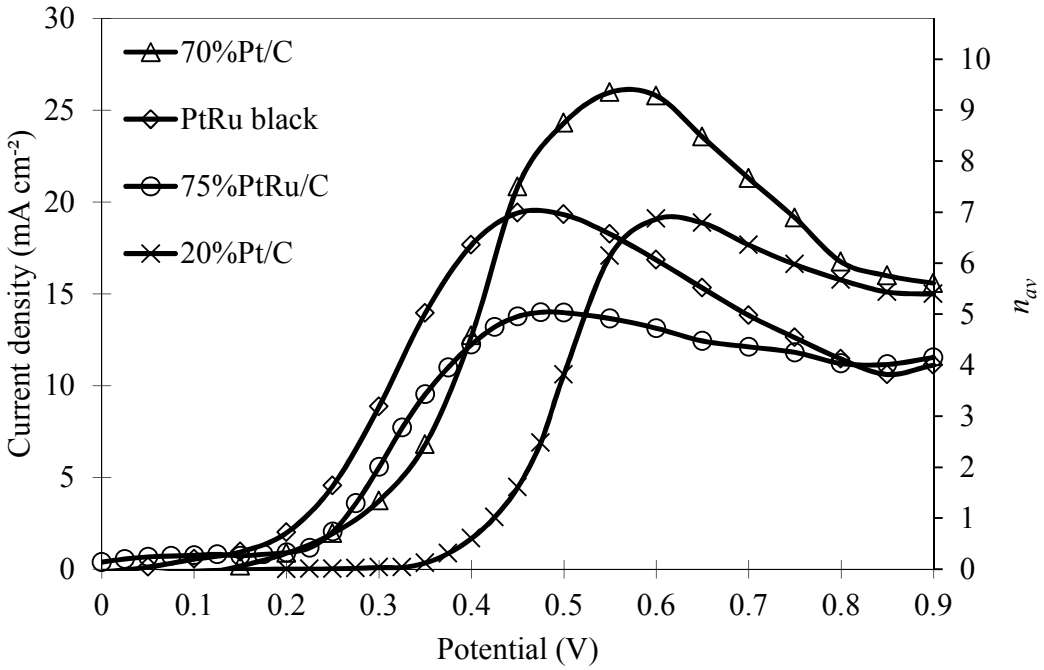

Figure 5.16: Polarization curves for the oxidation of 0.1 M ethanol (0.5 mL min^{-1}) at commercial PtRu black, 75%PtRu/C, 70%Pt/C, and 20%Pt/C anodes at 80 °C in crossover mode.

As for the 0.1 M methanol (Figure 5.7), the PtRu alloy catalysts had the lowest onset potentials and half-wave potentials for the oxidation of 0.1 M ethanol, while 70%Pt/C catalyst produced much higher currents at high potentials. The maximum current density at the 70%Pt/C anodes of 26 mA cm^{-2} (0.55 V) correlates to ca. 9 transferred electrons. 20%Pt/C showed the lowest catalyst activation at low potentials and rose to a maximum current density of ca. 20 mA cm^{-2} at 0.6 V which correlates to ca. 7 transferred electrons.

Polarization curves for the oxidation of 0.1 M ethanol were also recorded for the homemade catalysts. For clarity, only the two best-performing catalysts (Pt/$RuSnO_2$/C

and Pt/$RhSnO_2$/C) are shown in Figure 5.17 in comparison to the commercial PtRu black and 70%Pt/C catalysts. Data for all of the homemade catalysts is summarized in Figure 5.19.

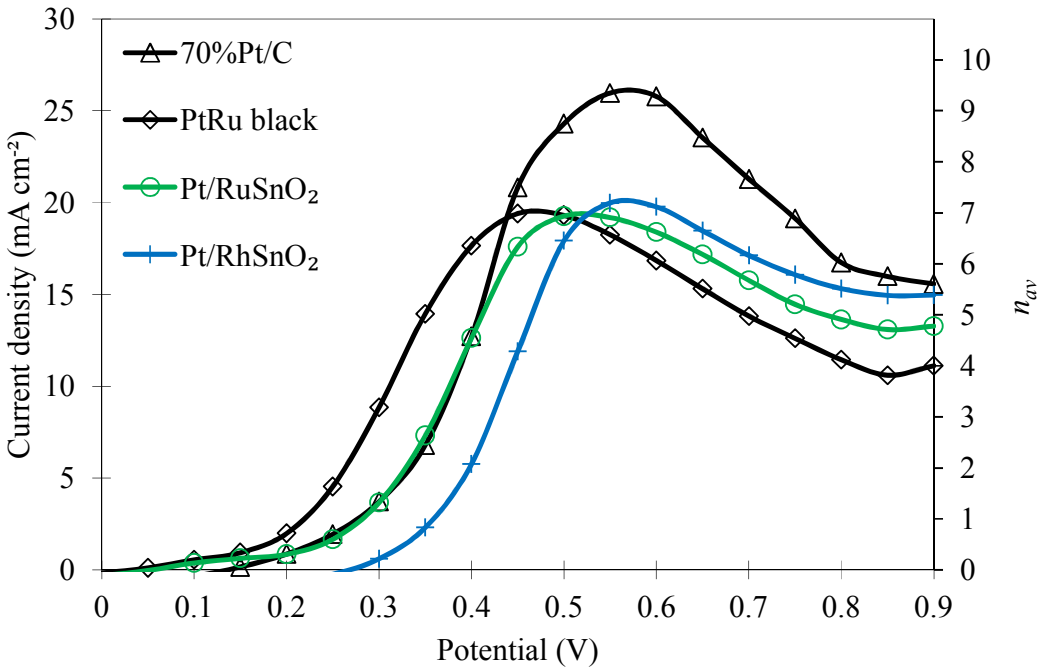

Figure 5.17: Polarization curves for the oxidation of 0.1 M ethanol (0.5 mL min^{-1}) at 70%Pt/C, PtRu black, Pt/$RuSnO_2$/C, and Pt/$RhSnO_2$/C anodes at 80 °C in crossover mode.

Both Pt/$RuSnO_2$/C, and Pt/$RhSnO_2$/C anodes reached a similar maximum current of ca. 20 mA cm^{-2} as PtRu black. Pt/$RuSnO_2$/C showed a slightly lower onset potential, compared to 70%Pt/C (0.05 V vs. 0.15 V). The performance of the homemade catalyst did not show any significant improvement on the oxidation of 0.1 M ethanol compared to the commercial catalysts. However, this was achieved with carbon supported catalysts with a reduced metal loading compared to the commercial catalysts.

Figure 5.18 shows the polarization curve results for $Ru_{54}@Pt_{46}$, and Rh@Pt nano core-shell catalysts with different shell loadings, compared to 20%Pt/C commercial catalyst.

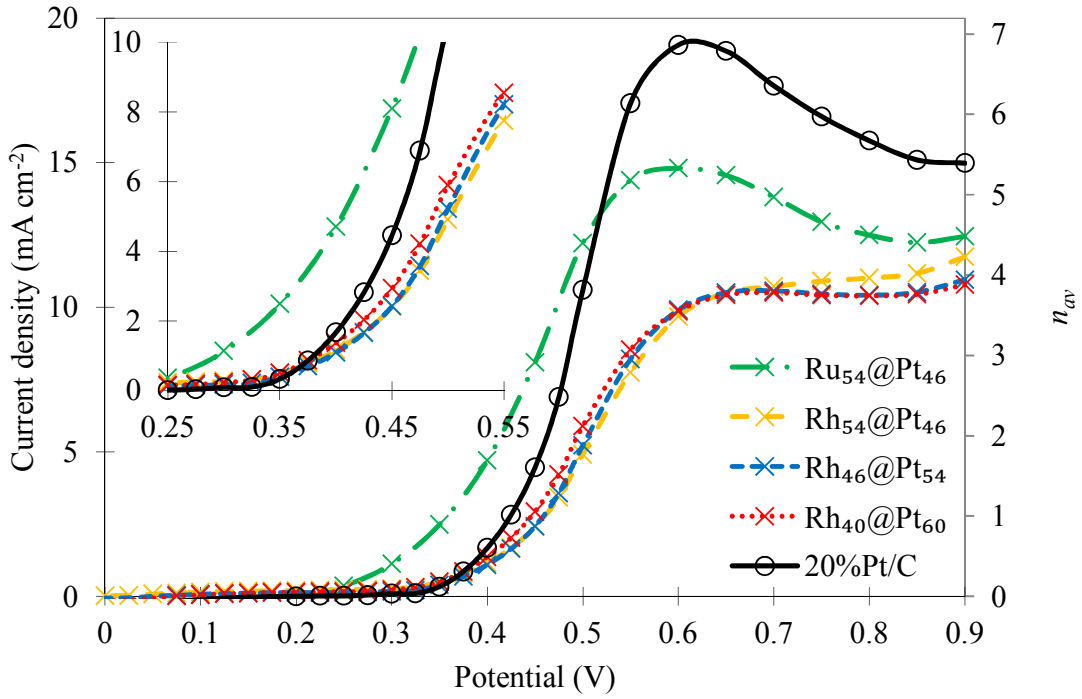

Figure 5.18: Polarization curves for the oxidation of 0.1 M ethanol (0.5 mL min^{-1}) at $Ru_{54}@Pt_{46}$, $Rh_{54}@Pt_{46}$, $Rh_{46}@Pt_{54}$, $Rh_{40}@Pt_{60}$ and 20%Pt/C anodes at 80 °C in crossover mode.

For all nano core-shell catalysts, the current rose to a limiting current density of 11.5 mA cm^{-2} within a standard deviation of ± 0.8% at 0.9 V. $Ru_{54}@Pt_{46}$ showed a significant lower onset potential of 0.25 V compared to 0.35 V for 20%Pt/C and all Rh@Pt catalysts. Similar to the 0.1 M methanol results (Figure 5.9), the Ru core increased the catalyst performance by the electronic effect of Ru which weakens the adsorption of CO [23]. The Rh core showed a negative effect on the 0.1 M ethanol

oxidation performance with an increased half-wave potential compared to the commercial 20%Pt/C catalyst.

Figure 5.19 illustrates the results of all investigated anode catalysts for the oxidation of 0.1 M ethanol in the multi-anode fuel cell. The data indicates that the screening method was useful to see significant performance differences of catalysts made in different batches or with different synthesis methods. Each bar represents the average current densities of up to three anodes of a catalyst at 0.45 V and 0.9 V. The error bars represent the standard deviations.

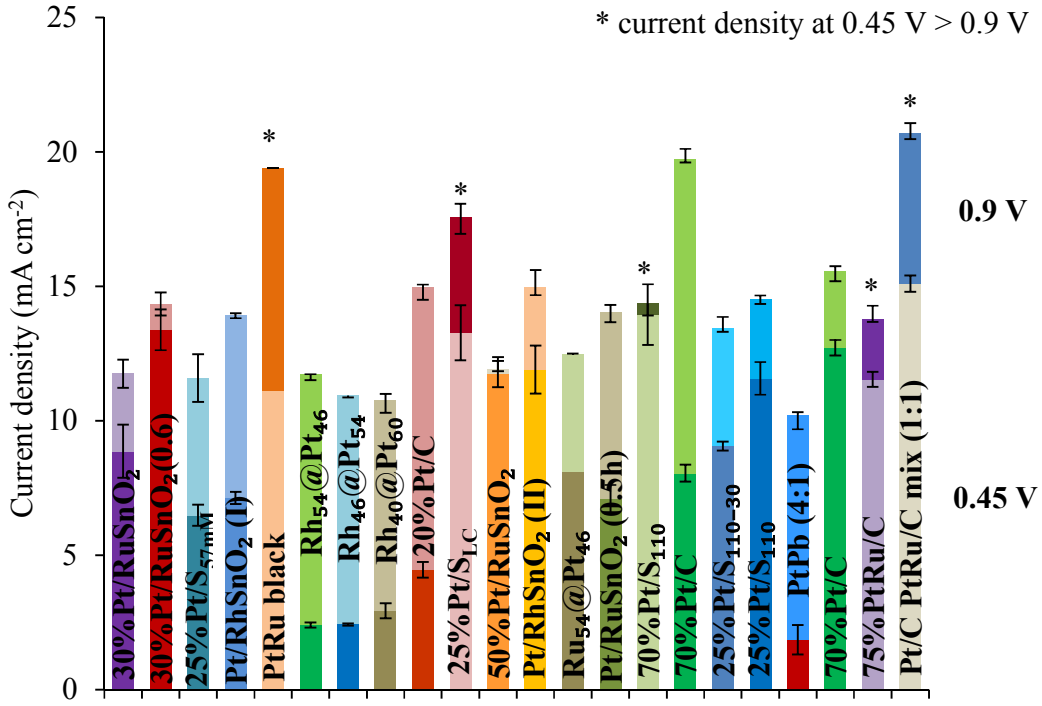

Figure 5.19: Current density bar plot of the investigated anode catalysts for the oxidation of 0.1 M ethanol in the multi-anode cell at 80 °C in crossover mode.

5.3.3 Ethylene glycol

5.3.3.1 Ethylene glycol (1 M) catalyst screening

In addition to methanol and ethanol, polarization curves were also recorded for 1 M ethylene glycol solution on commercial and homemade catalysts. The catalytic oxidation mechanism of ethylene glycol ($C_2H_6O_2$) is shown in Figure 5.20.

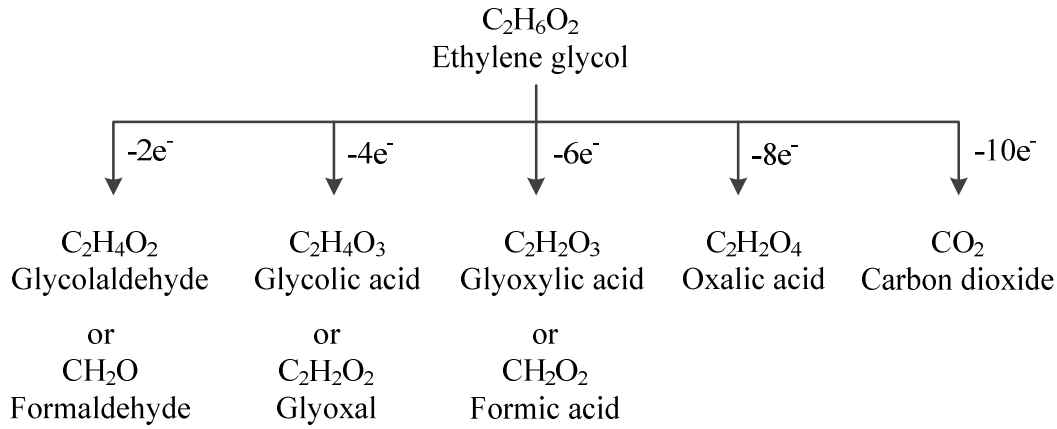

Figure 5.20: Electrocatalytic oxidation of ethylene glycol [31].

The complete oxidation of ethylene glycol to CO_2 delivers 10 electrons. However, the oxidation of ethylene glycol has several intermediate oxidation products, which produces different numbers of electrons. The developed n_{av} method will give valuable insight into the oxidation products of ethylene glycol.

Polarization curves for oxidation of 1 M ethylene glycol in crossover mode with commercial catalysts (PtRu black, 70%Pt/C, and 20%Pt/C) are shown in Figure 5.21. For 70%Pt/C and PtRu black, the current rose to limiting current densities (j_{lim}) of 80 mA cm^{-2} and ca. 40 mA cm^{-2}, respectively. Applying the average number of

electrons (n_{av}) method developed in *Chapter 3*, the limiting current for 70%Pt/C correlates to an n_{av} of 3.5 electrons and ca. 2 transferred electrons for PtRu black. 20%Pt/C anodes reached a maximum current density of 70 mA cm^{-2} which corresponded to the transfer of 3 electrons. All tested catalysts resulted in incomplete oxidation with glycolaldehyde, glycolic acid, formaldehyde, and glyoxal as possible intermediate products.

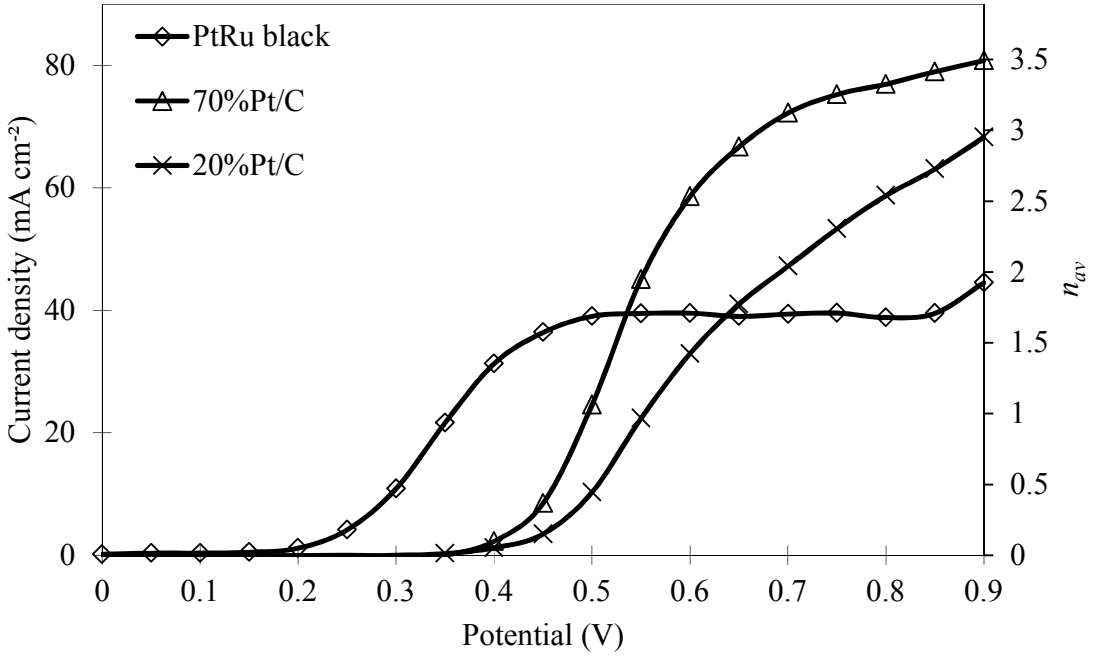

Figure 5.21: Polarization curves for the oxidation of 1 M ethylene glycol (0.5 mL min^{-1}) at commercial PtRu black, 70%Pt/C, and 20%Pt/C anodes at 80 °C in crossover mode.

Amongst the commercial catalysts, PtRu black showed the lowest half-wave potential (0.35 V) whereas 70%Pt/C showed the highest current densities above 0.5 V (ca. 80 mA cm^{-2} at 0.9 V). Alloyed Ru shows a unique activating effect for CO oxidation at low potentials. However, the oxidation was limited by the diffusion of

ethylene glycol through the Nafion membrane at potentials above 0.4 V. 20%Pt/C showed a similar performance to 70%Pt/C with significantly lower current densities. The maximal current density was ca. 70 mA cm^{-2} at 0.9 V.

The polarization curves for the three best-performing homemade catalysts ($Pt/RuSnO_2/C$, $Pt/RhSnO_2/C$, and $Ru_{54}@Pt_{46}$) are shown in Figure 5.22 in comparison to the commercial PtRu black, and 70%Pt/C catalysts, for the oxidation of 1 M ethylene glycol. Data for all of the homemade catalysts is summarized in Figure 5.24.

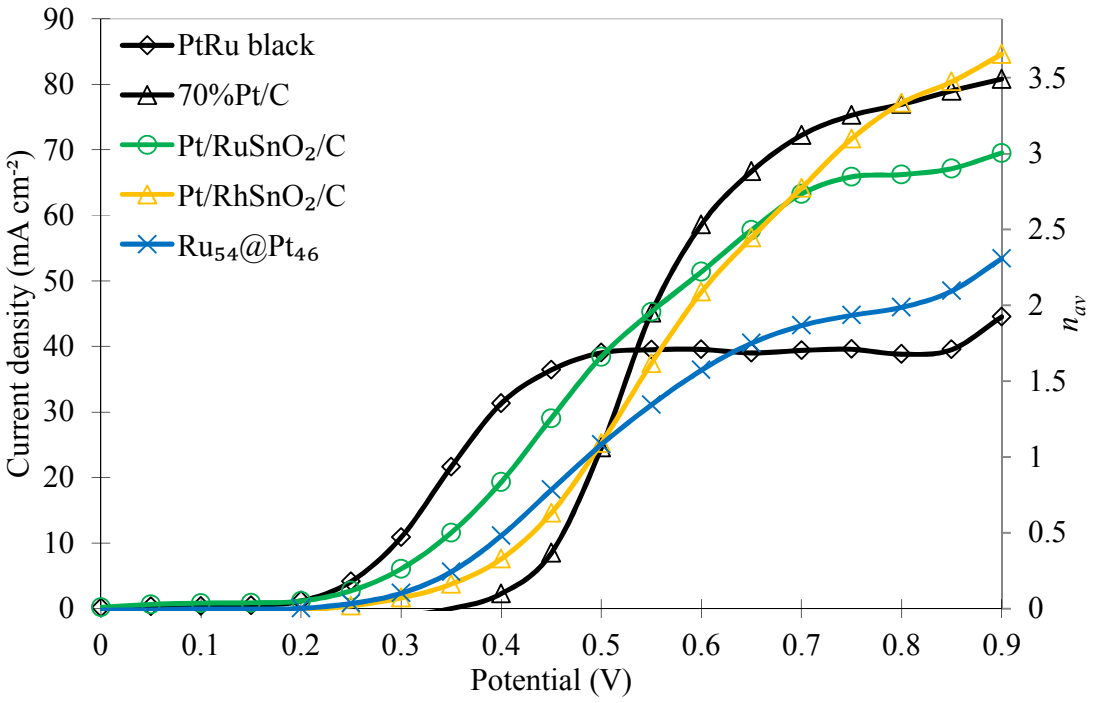

Figure 5.22: Polarization curves for the oxidation of 1 M ethylene glycol (0.5 mL min^{-1}) at PtRu black, 70%Pt/C, $Pt/RuSnO_2/C$, $Pt/RhSnO_2/C$, and $Ru_{54}@Pt_{46}$ anodes at 80 °C in crossover mode.

The homemade catalyst ($Pt/RuSnO_2/C$, $Pt/RhSnO_2/C$, and $Ru_{54}@Pt_{46}$) showed increased current densities at potentials up to 0.55 V compared to commercial 70%Pt/C

catalyst. The most active Pt/$RuSnO_2$/C homemade catalyst at low potentials showed a significant current density increase of factor eight compared to the commercial 70%Pt/C (19.3 mA cm^{-2} vs. 2.3 mA cm^{-2}) at 0.4 V. The potential range of 0.2 V to 0.4 V is the most relevant potential to operate direct liquid fuel cells. In contrast to 1 M methanol (Figure 5.4) and 1 M ethanol (Figure 5.13), Pt/$RhSnO_2$/C resulted in the highest current density of 85 mA cm^{-2} at a potential of 0.9 V. $RhSnO_2$ shows a positive effect on the ethylene glycol oxidation performance at high potentials.

The current of the Ru_{54}@Pt_{46} core-shell anode (Figure 5.22) was higher compared to that at the 70%Pt/C anode at potentials until 0.5 V, and higher compared to the PtRu black current densities above 0.65 V. The Ru_{54}@Pt_{46} core-shell nanoparticle catalyst shows a positive effect on the ethylene glycol oxidation performance at low potentials, but performs poorly at higher potentials due to inhibited electronic effects of the Ru core by the Pt shell.

Figure 5.23 shows the polarization curve results for Ru_{54}@Pt_{46}, and Rh@Pt nano core-shell catalysts with different shell loadings, compared to the 20%Pt/C commercial catalyst.

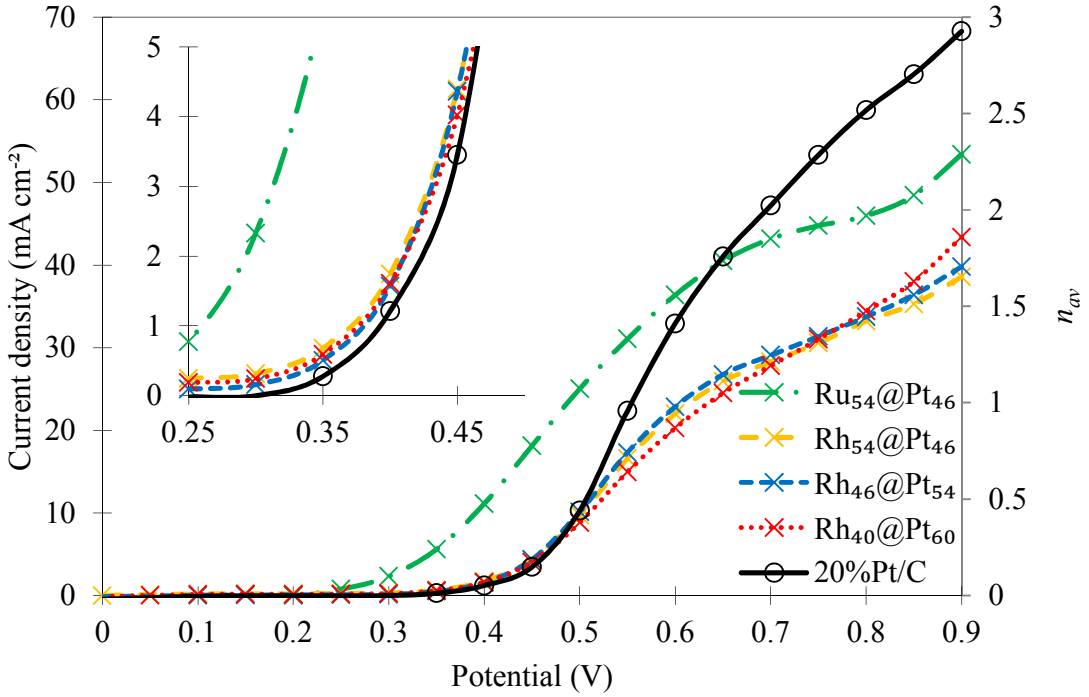

Figure 5.23: Polarization curves for the oxidation of 1 M ethylene glycol (0.5 mL min^{-1}) at $Ru_{54}@Pt_{46}$, $Rh_{54}@Pt_{46}$, $Rh_{46}@Pt_{54}$, $Rh_{40}@Pt_{60}$ and 20%Pt/C anodes at 80 °C in crossover mode.

The current at the $Ru_{54}@Pt_{46}$ anodes in Figure 5.23 showed an increased performance compared to the 20%Pt/C anode (up to 0.65 V). At higher potentials, the current density reached a plateau (45 mA cm^{-2}) at a lower performance than the commercial 20%Pt/C. The better performance of the $Ru_{54}@Pt_{46}$ catalyst at low potentials can be attributed to the electronic effect of the Ru core which weakens the adsorption of CO [23].

The Rh@Pt anodes in Figure 5.23 showed the same performance as the commercial 20%Pt/C catalyst at low potentials up to 0.5 V whereas at higher potentials the current densities were reduced. The different Pt shell loading showed no

significance in the catalyst activity. The Rh core showed a negative effect on the 1 M ethylene glycol oxidation performance.

Figure 5.24 illustrates the results of all investigated anode catalysts for the oxidation of 1 M ethylene glycol in the multi-anode fuel cell. The data indicates that the screening method was useful to see significant performance differences of catalysts made in different batches or with different synthesis methods. Each bar represents the average current densities of up to three anodes of a catalyst at 0.45 V and 0.9 V. The error bars represent the standard deviations.

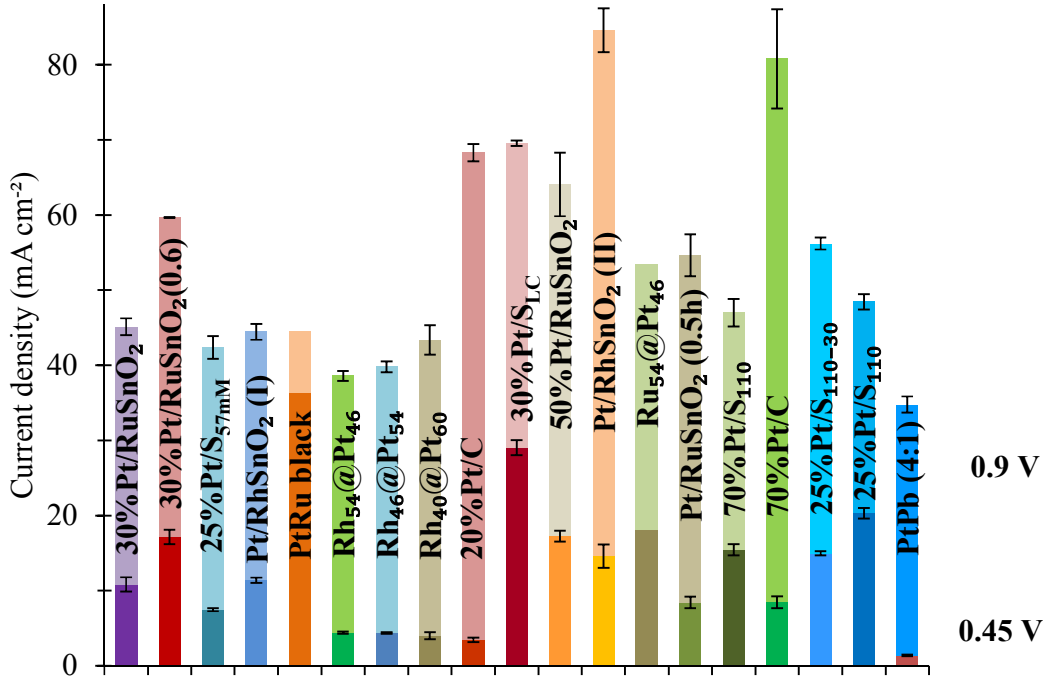

Figure 5.24: Current density bar plot of the investigated anode catalysts for the oxidation of 1 M ethylene glycol in the multi-anode cell at 80 °C in crossover mode.

5.3.3.2 Ethylene glycol (0.1 M) catalyst screening

In addition to the catalyst screening with 0.1 M methanol and ethanol, polarization curves were also recorded for 0.1 M ethylene glycol solution on commercial and homemade catalysts to analyze the catalyst performance at low fuel concentrations.

Polarization curves for the oxidation of 0.1 M ethylene glycol in crossover mode with commercial catalysts (PtRu black, and 20%Pt/C) are shown in Figure 5.25.

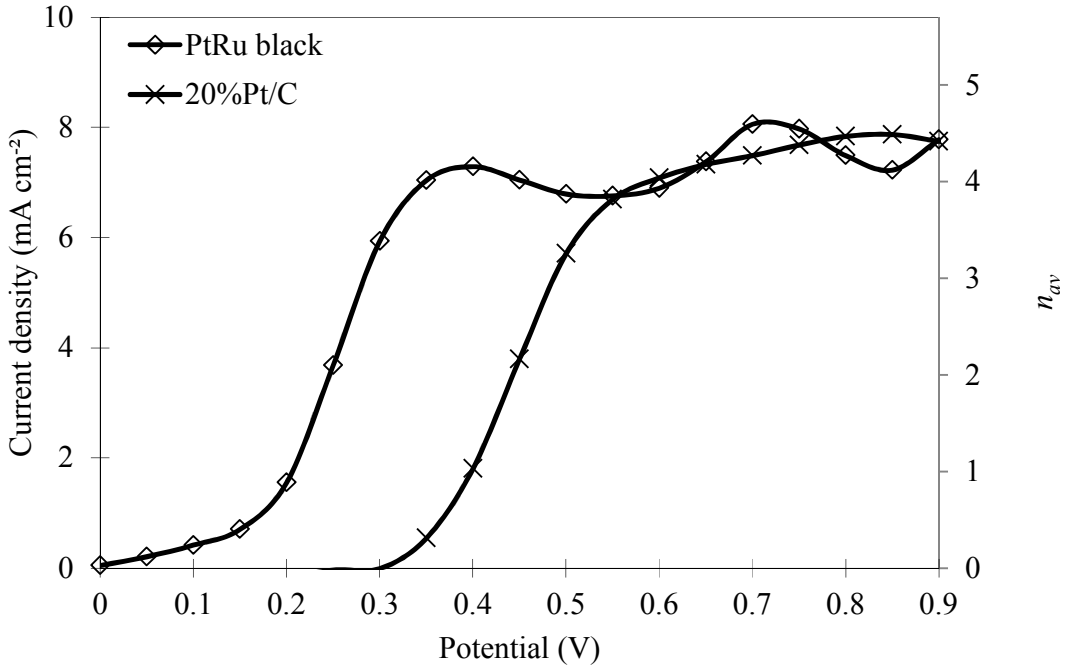

Figure 5.25: Polarization curves for the oxidation of 0.1 M ethylene glycol (0.5 mL min^{-1}) at commercial PtRu black, and 20%Pt/C anodes at 80 °C in crossover mode.

As for the 0.1 M methanol (Figure 5.7), and 0.1 M ethanol (Figure 5.16), the PtRu black catalyst had the lowest onset potential (0.05 V) and half-wave potential (0.25 V) for the oxidation of 0.1 M ethylene glycol. PtRu black and 20%Pt/C both rose

to a limiting current density of ca. 7.5 mA cm^{-2} which correlates ca. 4 transferred electrons. The transferred electrons resulted in glycolaldehyde (2 e^-) and glycolic acid (4 e^-) as oxidation products (Figure 5.20).

Polarization curves for the oxidation of 0.1 M ethylene glycol were also recorded for the homemade catalysts. For clarity, only the two best-performing catalysts ($Pt/RuSnO_2/C$, and $Pt/RhSnO_2/C$) are shown in Figure 5.26 in comparison to the commercial PtRu black, and 20%Pt/C catalysts. Data for all of the homemade catalysts is summarized in Figure 5.28.

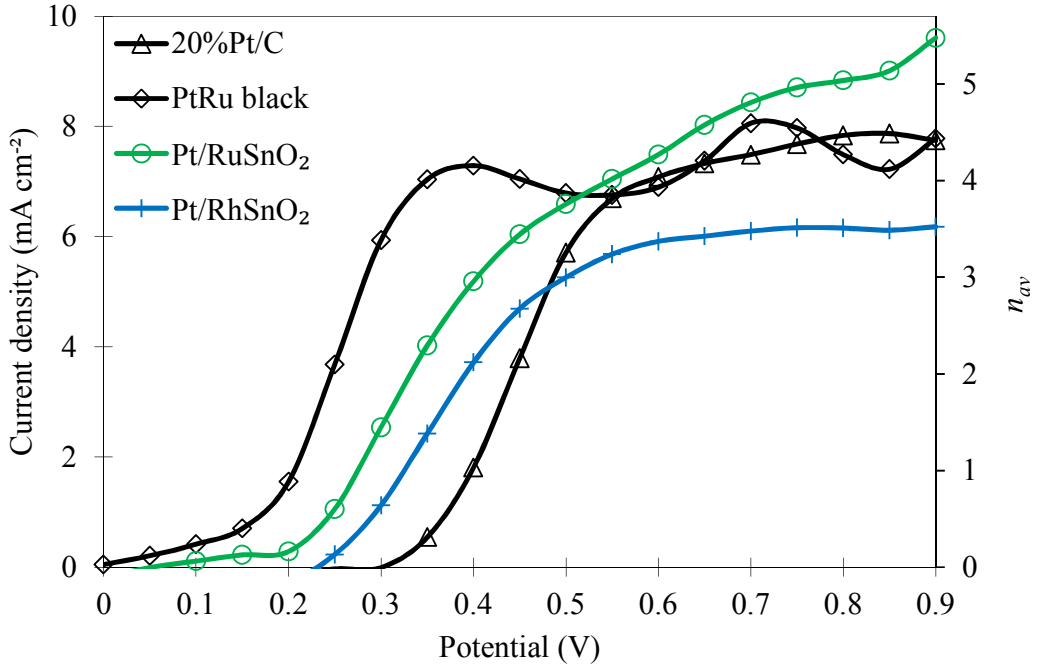

Figure 5.26: Polarization curves for the oxidation of 0.1 M ethylene glycol (0.5 mL min^{-1}) at 20%Pt/C, PtRu black, $Pt/RuSnO_2/C$, and $Pt/RhSnO_2/C$ anodes at 80 °C in crossover mode.

Both Pt/$RuSnO_2$/C, and Pt/$RhSnO_2$/C anodes showed a lower onset potential compared to 20%Pt/C (0.2 V or 0.25 V vs. 0.3 V). However, the current density of the Pt/$RhSnO_2$/C anodes (6 mA cm^{-2}) was lower than the commercial catalysts. Pt/$RuSnO_2$/C showed a slightly higher current density of ca. 9 mA cm^{-2} at high potentials which correlates to a production of glycolic acid (4 e^-) as an oxidation product.

Figure 5.27 shows the polarization curve results for Rh@Pt nano core-shell catalysts with different shell loadings, compared to 20%Pt/C commercial catalyst.

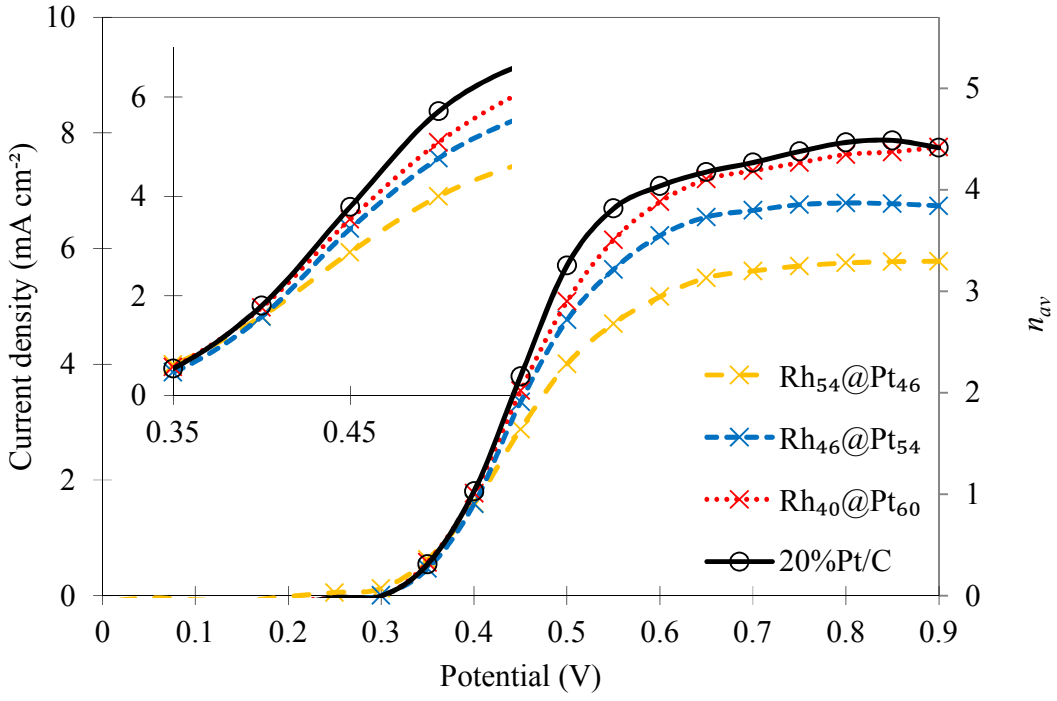

Figure 5.27: Polarization curves for the oxidation of 0.1 M ethylene glycol (0.5 mL min^{-1}) at Rh_{54}@Pt_{46}, Rh_{46}@Pt_{54}, Rh_{40}@Pt_{60} and 20%Pt/C anodes at 80 °C in crossover mode.

All Rh@Pt nano core-shell catalysts rose to a limiting current at higher potentials. $Rh_{40}@Pt_{60}$ showed a similar performance at all potentials to 20%Pt/C. The nano core-shell catalyst showed no performance increase in the oxidation of 0.1 M ethylene glycol compared to the commercial catalyst.

Figure 5.28 illustrates the results of all investigated anode catalysts for the oxidation of 0.1 M ethylene glycol in the multi-anode fuel cell. The data indicates that the screening method was useful to see significant performance differences of catalysts made in different batches or with different synthesis methods. Each bar represents the average current densities of up to three anodes of a catalyst at 0.45 V and 0.9 V. The error bars represent the standard deviations.

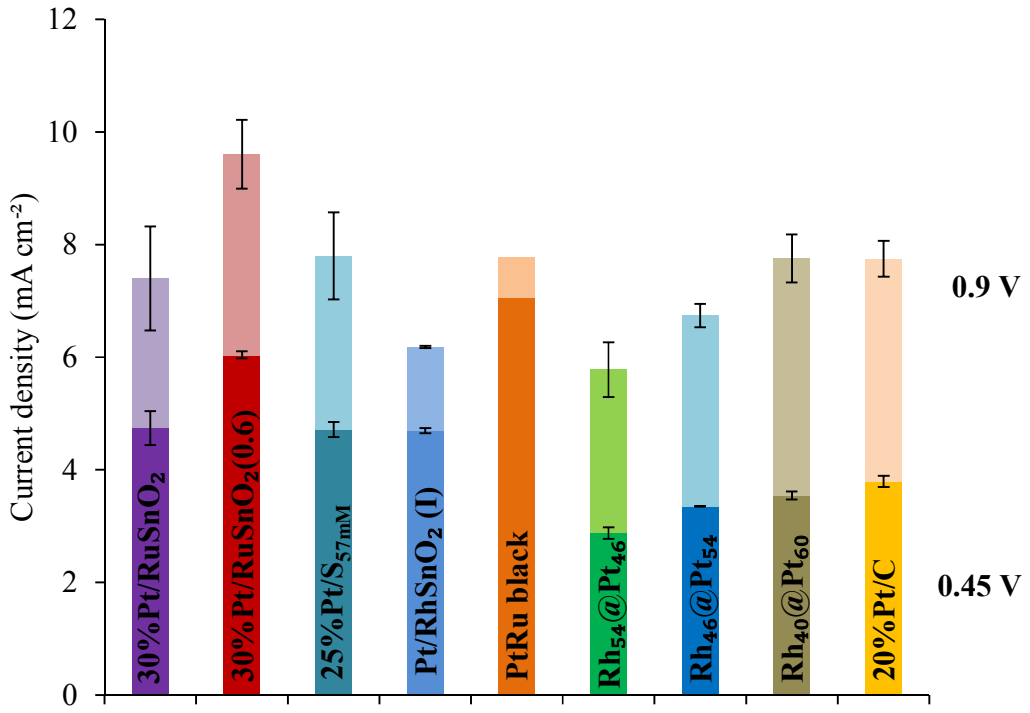

Figure 5.28: Current density bar plot of the investigated anode catalysts for the oxidation of 0.1 M ethylene glycol in the multi-anode cell at 80 °C in crossover mode.

5.3.4 Glycerol

5.3.4.1 Glycerol (1 M) catalyst screening

In addition to methanol, ethanol, and ethylene glycol, polarization curves were also recorded for 1 M glycerol solution on commercial and homemade catalysts. The catalytic oxidation mechanism of glycerol is shown in Figure 5.29.

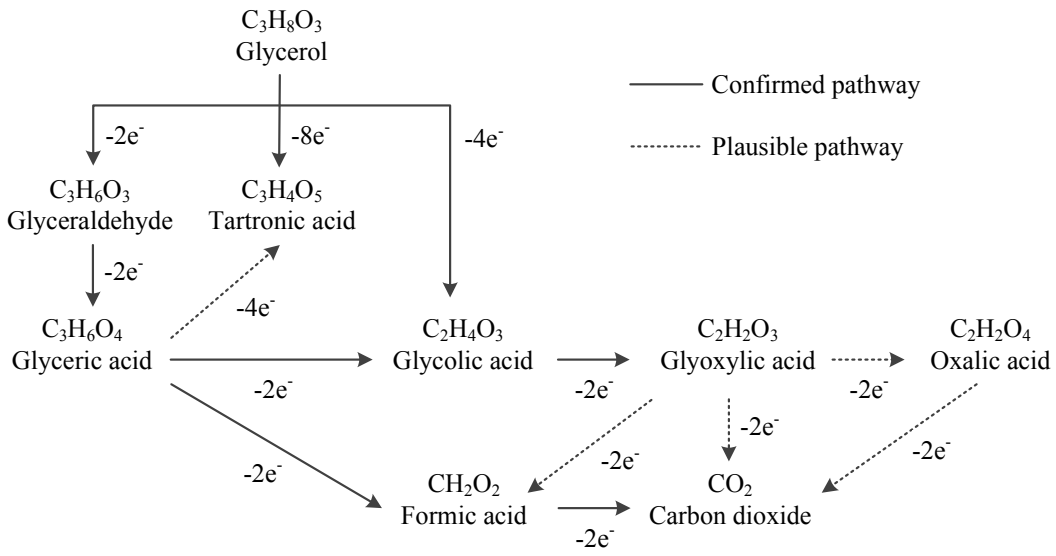

Figure 5.29: Glycerol electrooxidation mechanism pathways to CO_2 at Pt-based catalysts [32].

Steady-state polarization curves for oxidation of 1 M glycerol in crossover mode with commercial catalysts (PtRu black, 70%Pt/C, and 20%Pt/C) are shown in Figure 5.30. For PtRu black, the current rose to a limiting current density (j_{lim}) of ca. 20 mA cm^{-2} (n_{av} = 2) after 0.45 V. For the 70%Pt/C and 20%Pt/C anodes the current densities rose to a maximum of ca. 50 mA cm^{-2} (n_{av} = 5) and 35 mA cm^{-2} (n_{av} = 3.6) at 0.9 V. All tested catalyst resulted in incomplete oxidation with glycolaldehyde as an

intermediate product for PtRu black, and glycolaldehyde, and glyceric acid, or glycolic acid as intermediate products for the 70%Pt/C, and 20%Pt/C catalysts.

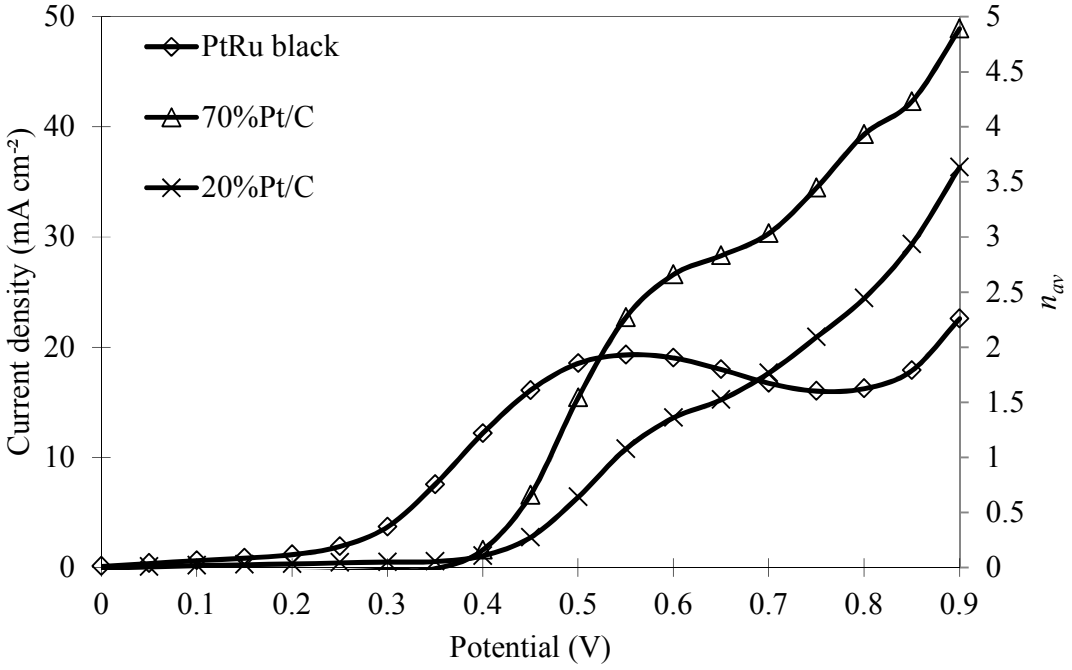

Figure 5.30: Polarization curves for the oxidation of 1 M glycerol (0.5 mL min^{-1}) at commercial PtRu black, 70%Pt/C, and 20%Pt/C anodes at 80 °C in crossover mode.

Amongst the commercial catalysts, PtRu black showed the lowest onset (0.1 V) and half-wave potential (0.4 V) whereas 70%Pt/C showed the highest current densities above 0.5 V (ca. 50 mA cm^{-2} at 0.9 V). Alloyed Ru shows a unique activating effect for CO oxidation at low potentials; however, the oxidation was limited by the diffusion of glycerol through the Nafion membrane at potentials above 0.5 V. 20%Pt/C showed similar performance compared to 70%Pt/C with significant lower current densities. The maximal current density was ca. 35 mA cm^{-2} at 0.9 V.

Polarization curves for the oxidation of 1 M glycerol were also recorded for the homemade catalysts. For clarity, only the two best-performing catalysts (Pt/$RuSnO_2$/C and Pt/$RhSnO_2$/C) are shown in Figure 5.31 in comparison to the commercial PtRu black, and 70%Pt/C catalysts. Data for all of the homemade catalysts is summarized in Figure 5.33.

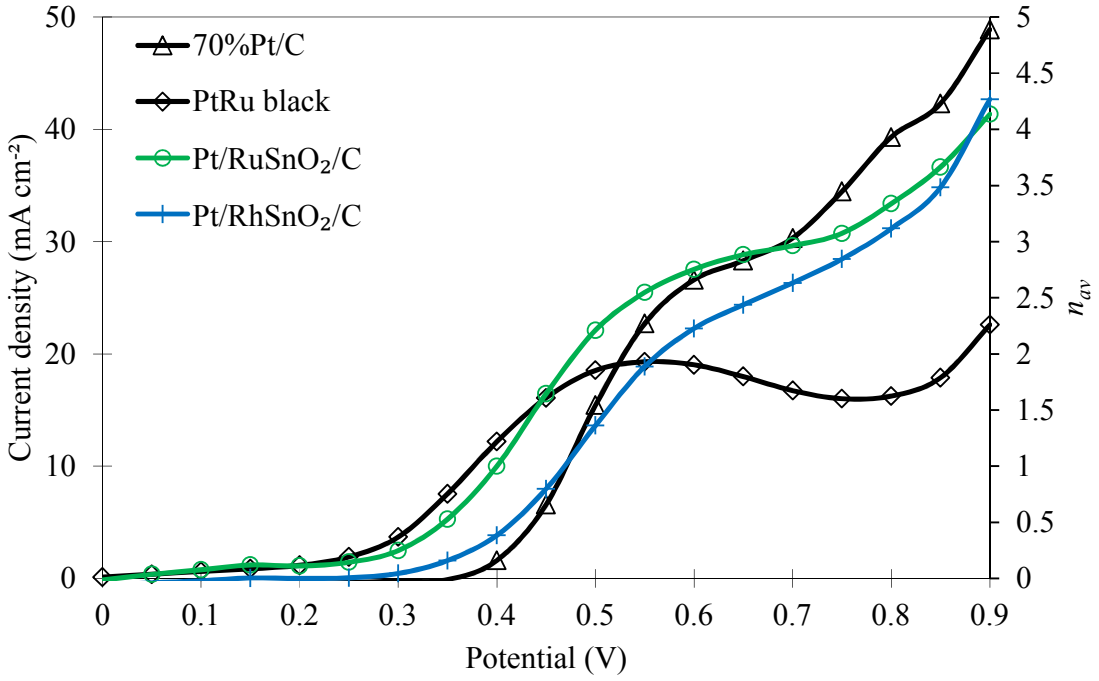

Figure 5.31: Polarization curves for the oxidation of 1 M glycerol (0.5 mL min^{-1}) at PtRu black, 70%Pt/C, 20%Pt/C, Pt/$RuSnO_2$/C, and Pt/$RhSnO_2$/C anodes at 80 °C in crossover mode.

At low potentials, the current densities at Pt/$RuSnO_2$/C anodes followed the performance of PtRu black, whereas at higher potentials it followed the performance of 70%Pt/C much more closely. The current densities at Pt/$RhSnO_2$/C anodes (Figure 5.31) were higher compared to those at the 70%Pt/C anodes at potentials (up to 0.45 V),

but lower than those for the 70%Pt/C anode at higher potentials. The current densities of both homemade catalysts at 0.9 V resulted in an n_{av} value of 4 which correlates to glyceric acid and glycolic acid as oxidation products.

Figure 5.32 shows the polarization curve results for $Ru_{54}@Pt_{46}$, and Rh@Pt nano core-shell catalysts with different shell loadings, compared to the 20%Pt/C commercial catalyst.

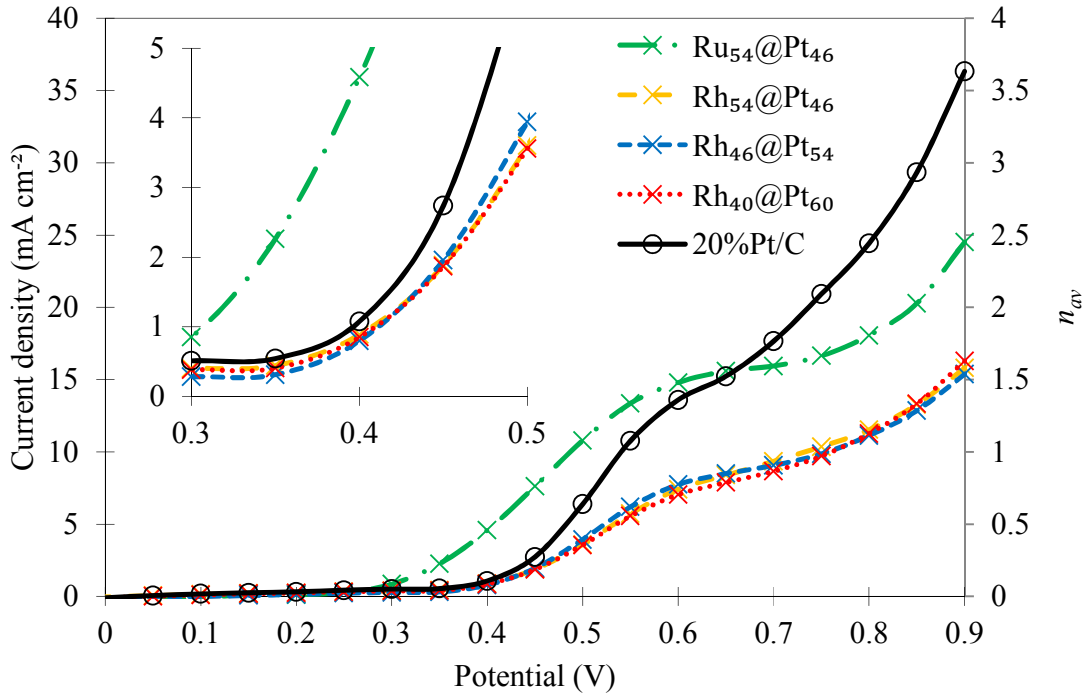

Figure 5.32: Polarization curves for the oxidation of 1 M glycerol (0.5 mL min^{-1}) at $Ru_{54}@Pt_{46}$, $Rh_{54}@Pt_{46}$, $Rh_{46}@Pt_{54}$, $Rh_{40}@Pt_{60}$ and 20%Pt/C anodes at 80 °C in crossover mode.

The $Ru_{54}@Pt_{46}$ anode in Figure 5.32 showed an increased performance compared to the 20%Pt/C anode (up to 0.65 V). At higher potentials, the current density followed the performance trend of the commercial 20%Pt/C with decreased values. The

$Ru_{54}@Pt_{46}$ catalyst showed a plateau in current density at 15 mA cm^{-2} between 0.6 V to 0.75 V. The catalyst did not reach a limiting current at high potentials similar to the 20%Pt/C catalyst. The better performance of the $Ru_{54}@Pt_{46}$ catalyst at low potentials can be attributed to the electronic effect of the Ru core which weakens the adsorption of CO [23].

The Rh@Pt anodes in Figure 5.32 showed a poor performance compared to the commercial 20%Pt/C catalyst. The different Pt shell loading showed no significance in the catalyst activity. The Rh core showed a negative effect on the glycerol oxidation performance.

Figure 5.33 illustrates the results of all investigated anode catalysts for the oxidation of 1 M glycerol in the multi-anode fuel cell. The data indicates that the screening method was useful to see significant performance differences of catalysts made in different batches or with different synthesis methods. Each bar represents the average current densities of up to three anodes of a catalyst at 0.45 V and 0.9 V. The error bars represent the standard deviations.

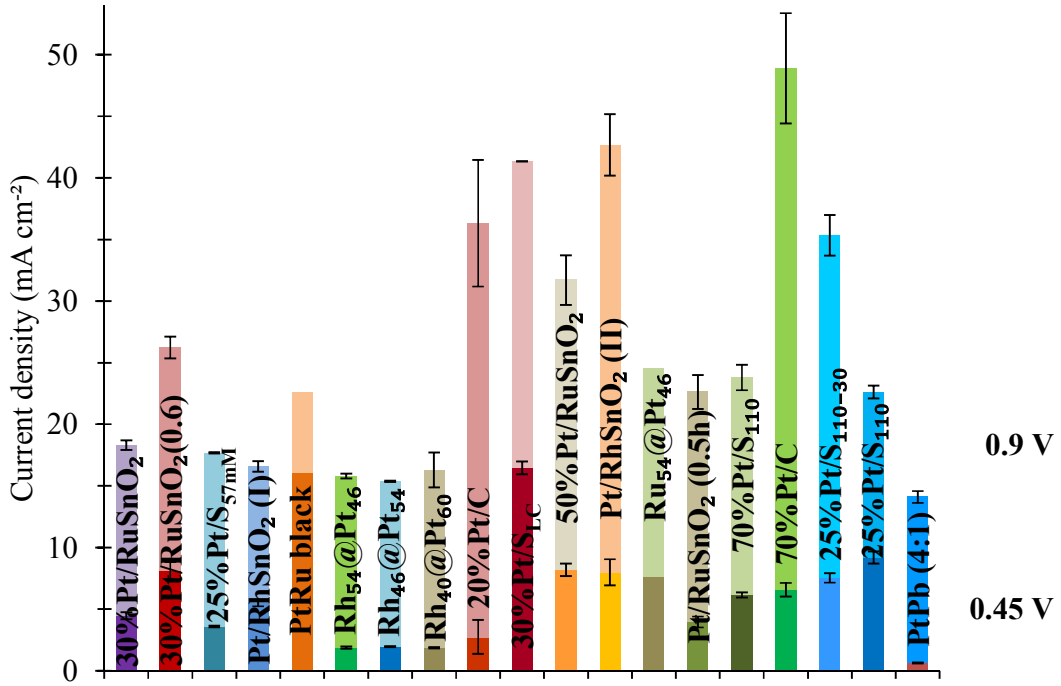

Figure 5.33: Current density bar plot of the investigated anode catalysts for the oxidation of 1 M glycerol in the multi-anode cell at 80 °C in crossover mode.

5.3.5 Acetol

Acetol was investigated as a fuel because it was a main component in pyrolysis oil enhancement (*Chapter 4*). However, the investigation was stopped as experiments showed extremely poor performance of acetol in the electrolysis cell. Polarization curves for oxidation of 1 M acetol in crossover mode with commercial catalysts (PtRu black, and Pt black) are shown in Figure 5.34.

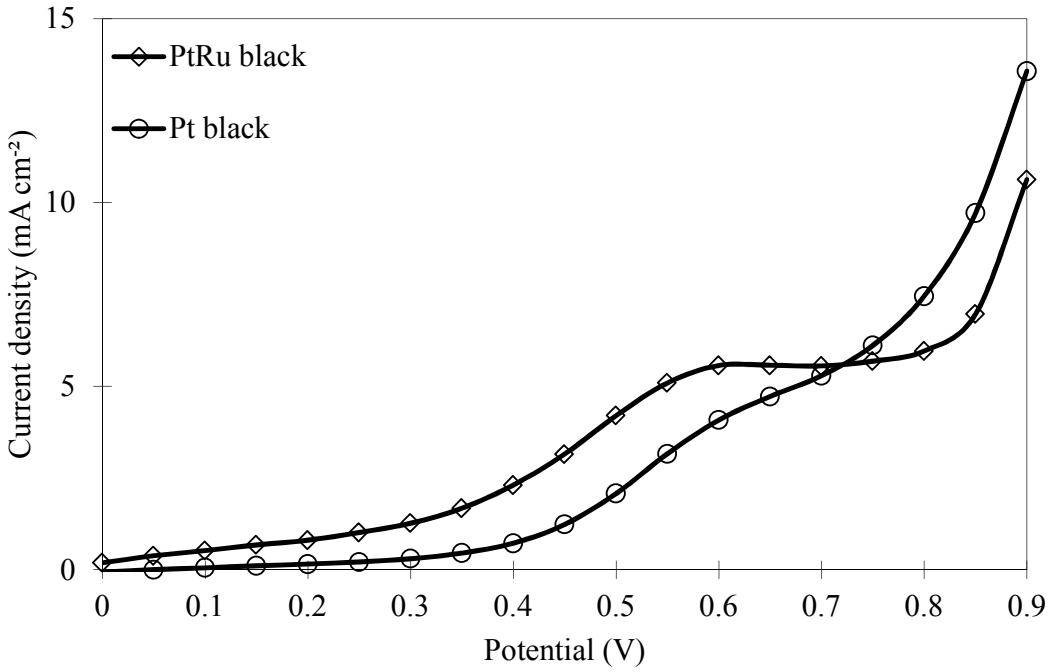

Figure 5.34: Polarization curves for the oxidation of 1 M acetol (0.5 mL min^{-1}) at commercial PtRu black and Pt black anodes at 50 °C in crossover mode.

The poor performance of both commercial Pt and PtRu black led to discontinuation of the investigation of acetol as a fuel.

5.4 Conclusions

The onset potentials, half-wave potentials, and the limiting current densities varied for each catalyst and investigated fuel. Similar electrocatalytic activities were observed for the oxidation of different fuels at the same catalyst. Overall, PtRu/C resulted in the lowest onset potentials, and Pt/C catalysts showed higher limiting currents. For the homemade catalyst, $Pt/RuSnO_2/C$ resulted in higher current densities compared to $Pt/RhSnO_2/C$. Polarization curves showed that the increased low potential activities at the homemade $Pt/RuSnO_2/C$ compared to 70%Pt/C were due to the presence of both Ru and Sn in the oxide support layer. Overall, it can be concluded that $Pt/RuSnO_2/C$ catalysts perform better than both commercial 70%Pt/C and 75%PtRu/C for use in direct liquid fuel cells and electrolysis cells for the investigated fuels.

Similar to the $Pt/RuSnO_2/C$ catalyst the $Pt/RhSnO_2/C$ catalyst showed increased low potential activities for all investigated fuels (except 0.1 M ethanol) due to Rh and Sn in the oxide support layer in comparison to 70%Pt/C anodes. However, at higher potentials, the catalyst showed a reduced performance compared to 70%Pt/C. Except for the oxidation of 1 M ethylene glycol where $Pt/RhSnO_2/C$ resulted in the highest current density of 85 mA cm^{-2} at 0.9 V.

The homemade Pt_2Ru catalyst showed a beneficial effect on the oxidation of 1 M methanol and 1 M ethanol at low potentials compared to 70%Pt/C catalyst due to the unique activation effect of Ru. At higher potentials, the performance was slightly reduced in comparison to the 70%Pt/C catalyst. Pt_2Ru is a highly active catalyst for the oxidation of ethanol.

The Ru@Pt nano core-shell catalyst showed increased activities and lower onset potentials for all investigated fuels compared to commercial 20%Pt/C catalyst. This can be attributed to the electronic, or the bi-functional effect the not fully covered Ru core [23]. The current densities at higher potentials were reduced compared to the performance at 20%Pt/C anodes. Ru@Pt only showed an improvement at higher potentials for the oxidation of 0.1 M methanol.

Varying the Pt coverage of Rh@Pt nano core-shell catalysts has provided insight into the oxidation of the investigated fuels in comparison to 20%Pt/C. The presence of the Rh core increased the onset potentials and decreased the current densities at higher potentials for all investigated fuels. The only exception was seen in the oxidation of 0.1 M methanol where the limiting current densities of the Rh@Pt catalysts were higher compared to the commercial 20%Pt/C. Overall, it can be concluded that Rh@Pt nano core-shell catalysts perform poorly compared to commercial catalysts for the use in direct liquid fuel cells and electrolysis cells for the investigated fuels.

Overall methanol was confirmed to be the most promising fuel in our electrolysis cell set-up. Ethanol's performance was approximately 50% of methanol's, with an n_{av} of 3.5 instead of 6. The best performing homemade catalyst, Pt/RuSnO$_2$/C resulted in current densities of 200 mA cm^{-2} at 0.9 V for 1 M methanol. The homemade tin oxide supported catalysts showed improved activity for all investigated fuels at low potentials compared to commercial 70%Pt/C anodes. Acetol showed a poor performance and is not a suitable fuel for applications in electrolysis or fuel cells.

5.5 Acknowledgements

This work was supported by the Centre for Forest Science and Innovation (CFSI, NL Provincial Government), the Natural Sciences and Engineering Research Council of Canada (NSERC) (grant number 2017-04260) and Memorial University of Newfoundland (MUN). E. N. El Sawy, B. Chen, and E. Wheeler developed and synthesized some of the homemade catalysts.

5.6 References

[1] Government of Canada. Canada's 7th National Communication and 3rd Biennial Report. 2017. doi:10.1002/(SICI)1520-6696(199924)35:1<63::AID-JHBS15>3.3.CO;2-O.

[2] Boudghene Stambouli A, Traversa E. Fuel cells, an alternative to standard sources of energy. Renew Sustain Energy Rev 2002;6:295–304. doi:10.1016/S1364-0321(01)00015-6.

[3] Badwal SPS, Giddey S, Kulkarni A, Goel J, Basu S. Direct ethanol fuel cells for transport and stationary applications – A comprehensive review. Appl Energy 2015;145:80–103. doi:10.1016/j.apenergy.2015.02.002.

[4] Xuan J, Leung MKH, Leung DYC, Ni M. A review of biomass-derived fuel processors for fuel cell systems. Renew Sustain Energy Rev 2009;13:1301–13. doi:10.1016/j.rser.2008.09.027.

[5] Gahleitner G. Hydrogen from renewable electricity: An international review of power-to-gas pilot plants for stationary applications. Int J Hydrogen Energy 2013;38:2039–61. doi:10.1016/j.ijhydene.2012.12.010.

[6] Hosseini SE, Abdul Wahid M, Jamil MM, Azli AAM, Misbah MF. A review on biomass-based hydrogen production for renewable energy supply. Int J Energy Res 2015;39:1597–615. doi:10.1002/er.3381.

[7] Bičáková O, Straka P. Production of hydrogen from renewable resources and its effectiveness. Int J Hydrogen Energy 2012;37:11563–78.

doi:10.1016/j.ijhydene.2012.05.047.

[8] Demirbas A. Biohydrogen generation from organic waste. Energy Sources, Part A Recover Util Environ Eff 2008;30:475–82. doi:10.1080/15567030600828909.

[9] Lamy C, Jaubert T, Baranton S, Coutanceau C. Clean hydrogen generation through the electrocatalytic oxidation of ethanol in a Proton Exchange Membrane Electrolysis Cell (PEMEC): Effect of the nature and structure of the catalytic anode. J Power Sources 2014;245:927–36. doi:10.1016/j.jpowsour.2013.07.028.

[10] Caravaca A, De Lucas-Consuegra A, Calcerrada AB, Lobato J, Valverde JL, Dorado F. From biomass to pure hydrogen: Electrochemical reforming of bio-ethanol in a PEM electrolyser. Appl Catal B Environ 2013;134–135:302–9. doi:10.1016/j.apcatb.2013.01.033.

[11] Sasikumar G, Muthumeenal A, Pethaiah S, Nachiappan N, Nalaji R. Aqueous methanol electrolysis using proton conducting membrane for hydrogen production. Int J Hydrogen Energy 2008;33:5905–10. doi:10.1016/j.ijhydene.2008.07.013.

[12] Soloveichik GL. Liquid fuel cells. Beilstein J Nanotechnol 2014;5:1399–418. doi:10.3762/bjnano.5.153.

[13] Demirci UB. Direct liquid-feed fuel cells: Thermodynamic and environmental concerns. J Power Sources 2007;169:239–46. doi:10.1016/j.jpowsour.2007.03.050.

[14] Mallick RK, Thombre SB, Shrivastava NK. Vapor feed direct methanol fuel cells (DMFCs): A review. Renew Sustain Energy Rev 2016;56:51–74. doi:10.1016/j.rser.2015.11.039.

[15] Joghee P, Malik JN, Pylypenko S, O'Hayre R. A review on direct methanol fuel cells – In the perspective of energy and sustainability. MRS Energy Sustain A Rev J 2015:1–31. doi:10.1557/mre.2015.4.

[16] Majidi P, Altarawneh RM, Ryan NDW, Pickup PG. Determination of the efficiency of methanol oxidation in a direct methanol fuel cell. Electrochim Acta 2016;199:210–7. doi:10.1016/j.electacta.2016.03.147.

[17] Taneda K, Yamazaki Y. Study of direct type ethanol fuel cells. Analysis of anode products and effect of acetaldehyde. Electrochim Acta 2006;52:1627–31. doi:10.1016/j.electacta.2006.03.093.

[18] Akhairi MAF, Kamarudin SK. Catalysts in direct ethanol fuel cell (DEFC): An overview. Int J Hydrogen Energy 2016;41:4214–28. doi:10.1016/j.ijhydene.2015.12.145.

[19] Thanh LT, Okitsu K, Boi L Van, Maeda Y. Catalytic Technologies for Biodiesel Fuel Production and Utilization of Glycerol: A Review. Catalysts 2012;2:191–222. doi:10.3390/catal2010191.

[20] Tiwari JN, Tiwari RN, Singh G, Kim KS. Recent progress in the development of anode and cathode catalysts for direct methanol fuel cells. Nano Energy

2013;2:553–78. doi:10.1016/j.nanoen.2013.06.009.

[21] Chen B, Brueckner TM, Altarawneh RM, Pickup PG. Composition Dependence of Ethanol Oxidation at Ruthenium-Tin Oxide/Carbon Supported Platinum Catalysts. J Electrochem Soc 2018;165:J3019–25. doi:10.1149/2.0041815jes.

[22] Yang J, Lee JY, Too HP. Size effect in thiol and amine binding to small Pt nanoparticles. Anal Chim Acta 2006;571:206–10. doi:10.1016/j.aca.2006.04.074.

[23] El Sawy EN, El-Sayed HA, Birss VI. Clarifying the role of Ru in methanol oxidation at Rucore@Ptshellnanoparticles. Phys Chem Chem Phys 2015;17:27509–19. doi:10.1039/c5cp04634c.

[24] El Sawy EN, Pickup PG. Carbon Monoxide and Formic Acid Oxidation at Rh@Pt Nanoparticles. Electrochim Acta 2019;302:234–40. doi:10.1016/j.electacta.2019.02.047.

[25] Brueckner TM, Pickup PG. Kinetics and Stoichiometry of Methanol and Ethanol Oxidation in Multi-Anode Proton Exchange Membrane Cells. J Electrochem Soc 2017;164:1172–8. doi:10.1149/2.1181712jes.

[26] Ren X, Springer TE, Gottesfeld S. Water and Methanol Uptakes in Nafion Membranes and Membrane Effects on Direct Methanol Cell Performance. J Electrochem Soc 2000;147:92. doi:10.1149/1.1393161.

[27] Varcoe JR, Slade RCT, Yee ELH, Poynton SD, Driscoll DJ. Investigations into the ex situ methanol, ethanol and ethylene glycol permeabilities of alkaline

polymer electrolyte membranes. J Power Sources 2007;173:194–9. doi:10.1016/j.jpowsour.2007.04.068.

[28] Majidi P, Pickup PG. Determination of the average number of electrons released during the oxidation of ethanol in a direct ethanol fuel cell. Electrochim Acta 2015;182:856–60. doi:10.1016/j.electacta.2015.09.168.

[29] Altarawneh RM, Majidi P, Pickup PG. Determination of the efficiency of ethanol oxidation in a proton exchange membrane electrolysis cell. J Power Sources 2017;351:106–14. doi:10.1016/j.jpowsour.2017.03.084.

[30] Wang Y, Zou S, Cai W-B. Recent Advances on Electro-Oxidation of Ethanol on Pt- and Pd-Based Catalysts: From Reaction Mechanisms to Catalytic Materials. Catalysts 2015;5:1507–34. doi:10.3390/catal5031507.

[31] Matsumoto T, Sadakiyo M, Ooi ML, Kitano S, Yamamoto T, Matsumura S, et al. CO2-free power generation on an iron group nanoalloy catalyst via selective oxidation of ethylene glycol to oxalic acid in alkaline media. Sci Rep 2014;4:1–6. doi:10.1038/srep05620.

[32] Huang L, Sun JY, Cao SH, Zhan M, Ni ZR, Sun HJ, et al. Combined EC-NMR and in Situ FTIR Spectroscopic Studies of Glycerol Electrooxidation on Pt/C, PtRu/C, and PtRh/C. ACS Catal 2016;6:7686–95. doi:10.1021/acscatal.6b02097.

[33] El Sawy EN, Pickup PG. Formic Acid Oxidation at Ru@Pt Core-Shell Nanoparticles. Electrocatalysis 2016;7:477–85. doi:10.1007/s12678-016-0328-8.

[34] Li G, Pickup PG. The promoting effect of Pb on carbon supported Pt and Pt / Ru catalysts for electro-oxidation of ethanol 2006;52:1033–7. doi:10.1016/j.electacta.2006.07.003.

5.7 Appendix

5.7.1 Properties of homemade catalysts

All catalyst properties, type of carbon fibre paper, metal loading and ratio, and membrane type are listed in Table 5.4.

Table 5.4: Summary of homemade catalysts and their properties.

Catalyst	Target metal load (Pt) (mg cm^{-2})	metal loading mass%	Atomic ratio of metals	Carbon fibre paper type	Solvent	Membrane type	Source	Literature reference
30%Pt/$RuSnO_2$*	3	30% Pt		not wet-proofed	1-propanol	Nafion 117	Binyu Chen	[21]
30%Pt/$RuSnO_2$(0.6) *	4	30% Pt		not wet-proofed	1-propanol	Nafion 117	Binyu Chen	[21]
25%Pt/S_{57mM} *	3	25% Pt		not wet-proofed	1-propanol	Nafion 117	Binyu Chen	[21]
Pt/$RhSnO_2$ (I)	3	25% Pt		not wet-proofed	1-propanol	Nafion 117	Evan Wheeler	
PtRu black	5.54	100%		not wet-proofed	1-propanol	Nafion 117	commercial	
Rh_{54}@Pt_{46}	3	25% Pt	54:46	not wet-proofed	1-propanol	Nafion 117	E.N. El Sawy	[24]
Rh_{46}@Pt_{54}	3	30% Pt	46:54	not wet-proofed	1-propanol	Nafion 117	E.N. El Sawy	[24]
Rh_{40}@Pt_{60}	3	33% Pt	40:60	not wet-proofed	1-propanol	Nafion 117	E.N. El Sawy	[24]
20%Pt/C	2	20%		not wet-proofed	1-propanol	Nafion 117	commercial	
30%Pt/S_{LC} *	4	30% Pt		not wet-proofed	1-propanol	Nafion 117	Binyu Chen	[21]
50%Pt/$RuSnO_2$*	4	50% Pt		not wet-proofed	1-propanol	Nafion 117	Binyu Chen	[21]
Pt/$RhSnO_2$(II)	4	25% Pt		not wet-proofed	1-propanol	Nafion 117	Evan Wheeler	
Ru_{54}@Pt_{46}	4	33.7%	54:46	not wet-proofed	1-propanol	Nafion 117	E.N. El Sawy	[33]
Pt/$RuSnO_2$(0.5h) *	4	30% Pt		not wet-proofed	1-propanol	Nafion 117	Binyu Chen	[21]
70%Pt/S_{110} *	4	70% Pt		not wet-proofed	1-propanol	Nafion 117	Binyu Chen	[21]
70%Pt/C	4	70%		not wet-proofed	1-propanol	Nafion 117	commercial	
25%Pt/$S_{110\text{-}30}$ *	4	25% Pt		not wet-proofed	1-propanol	Nafion 117	Binyu Chen	[21]
25%Pt/S_{110} *	4	25% Pt		not wet-proofed	1-propanol	Nafion 117	Binyu Chen	[21]
PtPb (4:1)	1	25%	4:1	not wet-proofed	1-propanol	Nafion 117	Guangchun Li	[34]
Ru_{62}@Pt_{38}	4	38.4%	62:38	wet-proofed	1-propanol	Nafion 115	E.N. El Sawy	[33]
Pt_2Ru	4	20%	2:1	wet-proofed	1-propanol	Nafion 115	E.N. El Sawy	[22]
Pt black	4	100%		wet-proofed	1-propanol	Nafion 115	commercial	
75%PtRu/C	4	75%		wet-proofed	1-propanol	Nafion 115	commercial	
Pt/C PtRu/C mix (1:1)	4	72%		wet-proofed	1-propanol	Nafion 115	commercial	

* Pt/$RuSnO_2$ synthesis methods are explained in [21].

Chapter 6

Summary and Outlook

6 Summary and Outlook

6.1 Summary

The scope of this work was to enhance pyrolysis oils via distillation and pervaporation to improve its properties as a fuel and produce value-added by-products. First, the methanol was separated from the pyrolysis oil via distillation in an aqueous solution with other low boiling point components. Experiments using the distillates in an electrolysis cell revealed the drawbacks of this fuel such as methanol crossover through the membrane. Therefore, pervaporation was explored as a method for pyrolysis oil enhancement. A unusable water-rich bark pyrolysis oil was enhanced to meet boiler fuel standards through pervaporation. The simultaneously generated permeate aqueous stream containing low molecular weight components was investigated as a fuel in an electrolysis cell.

6.1.1 Chapter 2- Pyrolysis oil enhancement: A design of experiment study to remove water from bark pyrolysis oil by pervaporation to improve fuel quality

Pervaporation has been studied as a process to upgrade an aqueous phase of bark pyrolysis oil to meet the ASTM pyrolysis oil boiler fuel standard. A 2^3 factorial design experiment study was performed to determine the optimal operating conditions. In this systematic method, the relationship between the factors affecting the pervaporation process and the membrane flux were determined. The investigated factors were

temperature (60 and 80 °C), feed flow rate (0.1 and 0.2 mL min^{-1}) and membrane crosslinking of two polyacrylonitrile-supported polyvinyl alcohol membranes.

The results showed that the temperature and feed flow rate were significant factors for the heating value (HHV), water content, and permeate yield models. All three investigated factors were significant for the viscosity model. None of the factors showed a significant influence on the total acid number (TAN). The highest permeate yields in the investigated system were achieved at 80 °C and a feed flow rate of 0.1 mL min^{-1}. The results demonstrated that it is possible to simultaneously dehydrate the aqueous phase of pyrolysis bark oil and separate value-added chemicals (alcohols and acids). The main outcome of this work was to improve the poorly combustible aqueous phase of a bark pyrolysis oil into a useful low viscosity oil meeting the ASTM 7544-12 standard.

The pervaporation process with the highly crosslinked Pervap 4101 membrane lowered the water content from 70.2 to 21.42 mass% and consequently increased the heating value from < 10 MJ kg^{-1} to 16.07 MJ kg^{-1}. This novel upgrading of high water content, low-quality pyrolysis oil via pervaporation broadens the types of feedstock that can be used to produce pyrolysis oil to meet the ASTM 7544-12 standard. Simultaneously to oil enhancement, the permeate by-product stream is potentially useful for several applications (including electrolysis cells see Section 6.1.3), since it contains chemicals, such as acetic and formic acid, methanol, hydroxyacetone, and furfural.

6.1.2 Chapter 3-Kinetics and stoichiometry of methanol and ethanol oxidation in multi-anode proton exchange membrane cells

A new methodology for determining the efficiency of anode catalysts based on the cell potential and the reaction stoichiometry (average number of electrons released per fuel molecule; n_{av}) was developed. The parameters were determined from polarization curves (current vs. cell potential) in a multi-anode cell. The cell was operated in crossover mode, in which fuel flows through the cathode chamber and diffuses through the membrane to be oxidized at the anode, to provide controlled mass transport conditions. Tafel analysis at low potentials provides kinetic information, while currents at high potentials provide n_{av} values and their potential dependence. Polarization curves for methanol oxidation were accurately modelled by a normal first-order electrochemical rate expression coupled with steady-state mass transport. It is shown that while PtRu alloy catalysts provide faster kinetics than Pt for both methanol and ethanol oxidation, Pt can provide much higher stoichiometries for ethanol oxidation. The accuracy of this methodology is good for ethanol oxidation at PtRu catalysts, but further assessment is required for Pt catalysts. Nevertheless, steady-state polarization curves obtained in crossover mode provide excellent data for the preliminary evaluation of catalysts for methanol and ethanol oxidation in PEMFC hardware, and kinetic data that is well suited for understanding the kinetics of these reactions in fuel cells.

6.1.3 Chapter 4-Production and electrolysis of methanol rich pyrolysis oil distillates and permeates

Fractional distillation and pervaporation processes have been investigated as methods to separate low boiling point components including water from softwood and bark pyrolysis oil to both meet ASTM D7544-12 boiler fuel standard requirements and produce a value-added by-product. The low boiling point distillate/permeates were used as a fuel in an electrolysis cell to produce renewable hydrogen, and preserve non-oxidizable value-added chemicals. Aside from water, the main identified low boiling point components by NMR were acetic acid, methanol, acetol, and formic acid. Furthermore, the mixtures contained minor components such as acrolein, glycolaldehyde, isoeugenol, and furfural. Polarization curves of the distillate as a fuel in an electrolysis cell revealed a poor performance. Therefore, the effect of single components mixed with 1 M methanol on the catalyst performance were evaluated. All impurities (acetic acid, acetol, and acrolein added to 1 M MeOH) showed a significant decrease in the electrolysis cell performance at Pt and PtRu black.

Acrolein showed a significant effect even al low concentrations. To overcome the poisoning effect through acrolein and other impurity in the distillate fractions, an upgrading process with sodium bisulfite ($NaHSO_3$) and sodium hydroxide (NaOH) was developed. $NaHSO_3$ reacts with acrolein to sodium 1-hydroxy-2-propene-1-sulfonate and NaOH reacts with acids in a neutralization reaction. The solid sodium 1-hydroxy-2-propene-1-sulfonate salt was then separated via an additional fractional distillation step. However, the treated and redistilled sample showed a poor performance

due to reforming of acrolein at the elevated distillation temperatures. The treatment was not successful and needs to be improved further.

The permeates showed an increased performance in the electrolysis cell which was limited by the low methanol content in the samples. Therefore, the methanol content of the samples was increased to 1 M by addition of reagent grade methanol. Especially, the water-rich permeate with a low impurities content produced by the highly crosslinked PVA membrane showed a significant current density improvement (63 to 317 mA cm^{-2} at 0.8°V). The results indicate a good oxidization performance of the studied components in the electrolysis cell for renewable hydrogen production at low potentials (<0.9 V). The remaining value-added components which were not oxidized to hydrogen at low potentials (acetic acid, acetol, e.g.) can be separated and sold individually for other applications.

6.1.4 Chapter 5-Catalyst screening

Finally, a catalyst screening for electrochemical oxidation of bio-fuels (from pyrolysis oil) was carried out. The screening was carried out with methanol, ethanol, ethylene glycol, glycerol, and acetol as fuels at a wide range of Pt-based precious metal catalyst and nano core-shell bimetal catalysts. The screening helped to expand the knowledge gained about characterizing, evaluating, and quantifying the performance of the various commercial catalysts. The onset potentials, half-wave potentials, and the limiting current densities varied for each catalyst and investigated fuel. Similar electrocatalytic activities were observed for the oxidation of different fuels at the same catalyst. Overall,

PtRu/C resulted in the lowest onset potentials, and Pt/C catalysts showed higher limiting currents.

For the homemade catalysts, $Pt/RuSnO_2/C$ followed by $Pt/RhSnO_2/C$ showed improved activity for all investigated fuels at low potentials compared to commercial 70%Pt/C anodes. Polarization curves showed that the increased low potential activities at the homemade $Pt/RuSnO_2/C$ compared to 70%Pt/C were due to the presence of both Ru and Sn in the oxide support layer.

For the nano core-shell catalysts Ru@Pt showed increased activities and lower onset potentials for all investigated fuels compared to Rh@Pt and commercial 20%Pt/C catalyst. This can be attributed to the electronic, or the bi-functional effect of the not fully covered Ru core. The current densities at higher potentials were reduced compared to the performance at 20%Pt/C anodes. Ru@Pt only showed an improvement at higher potentials for the oxidation of 0.1 M methanol. However, Rh@Pt nano core-shell catalysts performed poorly compared to commercial catalysts for the investigated fuels.

Overall, acetol as a fuel showed a poor performance at all investigated catalysts and is not suitable for applications in electrolysis or fuel cells.

6.2 Outlook

6.2.1 Pyrolysis oil enhancement

A laboratory scale fractional distillation column was used to separate water and low molecular weight components from the aqueous phase of bark pyrolysis oil. However, the distillation showed low separation selectivities. An improved distillation column,

such as a sieve tray column operated under vacuum conditions, could increase residence time and improve contact between the vapour and liquid phase while decreasing thermally induced reactions and therefore increase the selectivity and produce a cleaner distillate. The produced distillate with fewer impurity components could potentially perform better as a fuel in the electrolysis cell to produce hydrogen.

The investigated pervaporation proved to be an efficient method to enhance the water-rich oil to an ASTM D7544-12 boiler fuel. However, for the permeates to be useful in an electrolysis cell, the selectivity of the membranes needs to be improved. First, the optimal crosslinked PVA separation layer or a membrane with a different separation layer better suitable for pyrolysis oil should be developed. Last but not least, the pervaporation should be operated as a continuous process, to give valuable insight into long term stability of the investigated membranes.

6.2.2 Catalyst screening

Since the catalyst screening only allowed a characterization of oxidation products by the obtained n-value in the limiting current region, an online product and intermediate measuring method would give valuable insight in oxidation products and cell efficiencies. An online NMR or gas chromatograph combined with a CO_2 sensor could provide the complete product distribution of both anode and cathode sides.